Precision Measurement of Neutrino Oscillation Parameters and Investigation of Nuclear Georeactor Hypothesis with KamLAND

Thesis by

Chao Zhang

In Partial Fulfillment of the Requirements

for the Degree of

Doctor of Philosophy

California Institute of Technology

Pasadena, California

2011

(Defended June 10, 2010)

Acknowledgments

I have a lot of people to thank without whom I would not have made this far. I am deeply grateful to my advisor Bob McKeown who has supported me over the past years and brought me into the KamLAND project. His patience, encouragement and wisdom have been guiding me through my Ph.D. study. I owe my special thanks to Dan Dwyer for his constant advice and guidance to make this thesis analysis even possible. His knowledge and diligence always set an example for me. I am greatly thankful to Christopher Mauger who has been working together with me since the first day I joined KamLAND, taught me all the techniques in experimental nuclear physics, and helped me go though all the difficulties living in a foreign country, both in the United States and in Japan.

I would like to thank my fellow graduate students for all the days we spent together to get the work done. Tommy O'Donnell deserves my many thanks for the countless discussions we had about the analysis. His encouragement is essential to keep me moving on. Greg Keefer and Chris Grant are my kind roommates during my long stays in Japan. Their presence is the only thing that kept me sane. I would like to thank Kyohei Nakajima, Yuri Shimizu and Yukie Minekawa for always being my accompany in the underground mine, for making my life in Mozumi bearable.

I would like to thank all my KamLAND collaborators for their hard work. I thank Atsuto Suziki, Kunio Inoue and Stuart Freedman for leading this experiment to such a success today. Many thanks to the people who have lent me valuable knowledges about KamLAND: Brian Fujikawa, Patrick Decowski, Jason Detwiler, Lindley Winslow, Bruce Berger, Glenn Horton-Smith, Itaru Shimizu, Koichi Ichimura, Yasuhiro Kishimoto, Sei Yoshida, Yoshihito Gando, Tadao Mitsui and many others. I

would like to specially thank Masayuki Koga and Kengo Nakamura for their guidance during my work in Japan and for introducing me to the wonderful Japanese food and culture.

I would like to thank Bob Carr, Jianglai Liu, Bei Cai, Fenfang Wu and the rest of Kellogg research group for their daily help and for bearing with me for so long. Special thanks goes to Jianglai Liu who read my thesis and provided valuable feedback and discussion. The 'Ernie's Lunch Time' with the group is the most enjoyable time during my everyday life at CalTech.

Finally I would like to thank my parents Mengqiang Zhang and Renzhu Shen and my brother Gang Shen. No words can describe their love and endless support to me throughout my life for which I owe my deepest thanks.

Abstract

A combined analysis of examining the neutrino oscillation parameters and investigation of nuclear georeactor hypothesis with the KamLAND experiement is presented. With a total exposure of 2.75 kton-years, 930 $\bar{\nu}_e$ candidate events above 3.4 MeV $\bar{\nu}_e$ energy threshold were detected, with estimated 109$\pm$13 events from backgrounds. Assuming CPT invariance by combining with solar neutrino results, the best-fit value of georeactor fission power is $4.9^{+3.8}_{-4.8}$ TW. The 90% upper limit on the georeactor power is determined to be 11.2 TW using *Feldman and Cousins'* approach. This result has put a significant constraint on the contribution of a possible georeactor to the total heat from the Earth. The best-fit values of the neutrino oscillation parameters, including the georeactor power as a free parameter, are $\tan^2\theta_{12} = 0.44^{+0.05}_{-0.05}$ and $\Delta m^2_{21} = 7.59^{+0.27}_{-0.27} \times 10^{-5}$ eV^2. All oscillation parameter spaces are excluded at 99.73% C.L. except the LMA-I region. The result is consistent with KamLAND's previously published results with null-georeactor assumption.

Contents

List of Tables

List of Figures

Chapter 1 Introduction

KamLAND (Kamioka Liquid Scintillator Anti-Neutrino Detector) is the largest liquid scintillator detector built to study the neutrino oscillation phenomenon, in particular to explore the regions found by the solar neutrino experiments, but with anti-neutrinos produced by the nuclear reactors on the Earth. Meanwhile, a hypothetical nuclear georeactor [1] at the center of the Earth is also producing anti-neutrinos that will be detected by KamLAND. A combined analysis of georeactor and neutrino oscillation, performed in this dissertation, is not only going to investigate the georeactor hypothesis, but will also provide a stronger test on the current best-known neutrino oscillation theories.

In this chapter we will first review the neutrino oscillation theory and past neutrino oscillation experiments, followed by an introduction of the nuclear georeactor theory and the motivation of a combined analysis. Details of the KamLAND experiment will be discussed in Chapter 2. Analysis procedures and results will be presented in Chapter 3, 4, 5 and 6. Finally we will state the conclusion in Chapter 7.

1.1 Introduction to Neutrino Oscillation Theory

The existence of neutrinos was first proposed by Pauli [2] in 1930 to rescue the energy and angular momentum conservation in the beta decay process. It is not until 1956 that Reines and Cowan first discovered the (anti-)neutrinos ν_e in the experiment [3]. Subsequent experiments discovered two more types of neutrinos ν_μ [4] and ν_τ [5]. All three neutrinos are elementary particles in the standard model of electroweak interactions. The idea of the possible existence of neutrino oscillation was first introduced

by Pontecorvo [6], now supported by many strong experimental evidences since the late 1990s.

1.1.1 General Properties of the Neutrinos

Neutrino Flavors

Neutrinos are "elusive" particles that are neutral, do not feel the strong interactions and only interact weakly through coupling with $W^{\pm}$ (charge current) and Z^0 (neutral current) bosons. The flavor of a neutrino is defined by the corresponding charged lepton that is connected to the same charge current vertex. Three flavors of neutrino have been discovered in the lab, together with their lepton partners they form the doublets of the group SU(2) in the standard model:

$$\begin{pmatrix}\nu_e\\ e^-\end{pmatrix}, \quad \begin{pmatrix}\nu_\mu\\ \mu^-\end{pmatrix}, \quad \begin{pmatrix}\nu_\tau\\ \tau^-\end{pmatrix} \tag{1.1}$$

The number of light ($m_\nu < M_Z/2$) active neutrino species is studies by the e^+e^- annihilation at the Z-resonance peak. The $Z \to \nu\bar{\nu}$ decay channel has partial width $\Gamma_{\nu\bar{\nu}} = 166.9$ MeV, but with invisible final states. Subtracting the visible channels, interpretation of the measured Z-resonance width from the LEP experiments gives the total number of neutrino active flavors $N_\nu = 2.984 \pm 0.008$ [7]. However sterile neutrinos which do not participate in the weak interactions might still exist.

Neutrino Mass and Mixing

The neutrinos with a definite flavor are not necessarily states of a definite mass. Similar to the Cabibbo-Kobayashi-Maskawa (CKM) mixing for the quark flavors in the weak charged current, the neutrino flavor states are in general superpositions of

their mass eigenstates. For 3 neutrino flavor case, it follows:

$$|\nu_\alpha\rangle = \sum_{i=1}^{3} U^*_{\alpha i}|\nu_i\rangle. \qquad \alpha = e, \mu, \tau \tag{1.2}$$

where the unitary mixing matrix $U_{\alpha i}$ is also called Pontecorvo-Maki-Nakagawa-Sakata (PMNS) matrix. The PMNS matrix is conventionally parameterized by three mixing angles $\theta_{12}, \theta_{13}, \theta_{23}$, one CP violating phase δ and two Majorana phases α_1, α_2, as follows:

$$\begin{pmatrix} \nu_e \\ \nu_\mu \\ \nu_\tau \end{pmatrix} = \begin{pmatrix} 1 & 0 & 0 \\ 0 & c_{23} & s_{23} \\ 0 & -s_{23} & c_{23} \end{pmatrix} \begin{pmatrix} c_{13} & 0 & s_{13}e^{-i\delta} \\ 0 & 1 & 0 \\ -s_{13}e^{i\delta} & 0 & c_{13} \end{pmatrix} \begin{pmatrix} c_{12} & s_{12} & 0 \\ -s_{12} & c_{12} & 0 \\ 0 & 0 & 1 \end{pmatrix} \begin{pmatrix} \nu_1 e^{i\alpha_1/2} \\ \nu_2 e^{i\alpha_2/2} \\ \nu_3 \end{pmatrix} \tag{1.3}$$

where the notations $c_{ij} = \cos\theta_{ij}$ and $s_{ij} = \sin\theta_{ij}$ are used. The subscripts of the three mixing angles are conventionally fixed by the associated experiments which measure them, and our current best knowledge is [7]:

- $\sin^2(2\theta_{12}) = 0.87 \pm 0.03$ (solar)
- $\sin^2(2\theta_{23}) > 0.92$ (90% C.L.) (atmospheric)
- $\sin^2(2\theta_{13}) < 0.19$ (90% C.L.) (short-baseline reactor)

Except θ_{13}, the other two mixing angles are measured to be large, which is interestingly very different from the small mixings of quark flavors as one finds in the CKM matrix [7].

The absolute mass of the neutrino mass eigenstate ν_1, ν_2, ν_3 is still unknown. The best upper limit ($m_\nu < 2$ eV [7]) comes from Tritium beta decay experiments, which

measure the effective anti-electron-neutrino mass as

$$m_{\nu_e}^{2(\text{eff})} = \sum_i |U_{ei}|^2 m_{\nu_i}^2 \tag{1.4}$$

It is worth mentioning that from the current cosmological data and some cosmological assumptions, it has been concluded [8, 9] that

$$\sum_i m_i < (0.17 - 2.0)\,\text{eV} \tag{1.5}$$

where the sum is over all light neutrino mass eigenstates that may exist and were in thermal equilibrium in the early universe.

Neutrino oscillation experiments, on the other hand, are able to measure the mass-squared differences between the mass eigenstates (Section 1.1.2). In the case of three neutrino mass eigenstates, there are only two independent Δm^2. The current best-measured values are [7]:

- $\Delta m_{21}^2 = (7.59 \pm 0.20) \times 10^{-5}\,\text{eV}^2$ (long-baseline reactor, solar)
- $\Delta m_{32}^2 = (2.43 \pm 0.13) \times 10^{-3}\,\text{eV}^2$ (atmospheric, long-baseline accelerator)

As one can see, the scales of the two Δm^2 differ much. Conventionally we assign the labels such that $m_2 > m_1$. The low mass scale Δm_{21}^2 is associated with the solar neutrino oscillation (often called Δm_{sol}^2), while the high mass scale Δm_{32}^2 (or Δm_{31}^2) is associated with the atmospheric neutrino oscillation (often called Δm_{atm}^2). The sign of Δm_{32}^2, however, is still unknown. One could either have $m_3 > m_2 > m_1$, in which case is similar to the quark sector, called "normal hierarchy," or $m_2 > m_1 > m_3$, in which case is called "inverse hierarchy." Future long baseline accelerator experiments are aiming to determine which one is the correct mass hierarchy, and at the same time to measure yet another unknown parameter, the CP violating phase δ.

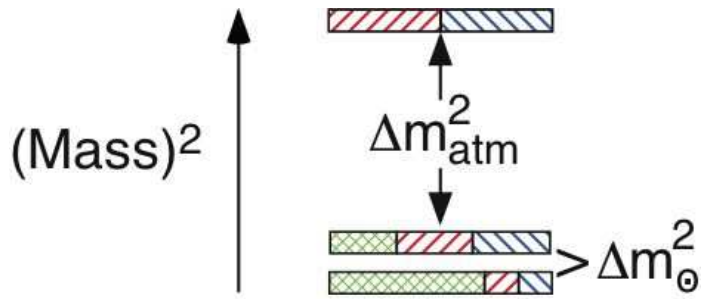

Figure 1.1: The three-neutrino mass-squared spectrum that accounts for the current experimental results (in the normal hierarchy case). The three levels correspond to the mass eigenstate ν_1, ν_2, ν_3 from bottom to top respectively (in the inverse hierarchy case, relative positions of ν_3 and (ν_1, ν_2) would exchange). The ν_e fraction of each mass eigenstate is crosshatched green, the ν_μ fraction is indicated by red right-leaning hatching, and the ν_τ fraction by blue left-leaning hatching. The absolute mass scale of the lowest mass eigenstate is yet unknown. (Figure taken from [7].)

As a summary, our current knowledges of the flavor budget of each neutrino mass eigenstate and the mass splitting between them is graphically illustrated in Fig. 1.1 (for normal hierarchy case). There are about equal fractions of ν_μ and ν_τ in each mass eigenstate, determined by the atmospheric neutrino experiments. The ν_e fraction of ν_2 is about 1/3, measured from the solar neutrino experiments. The ν_e fraction of ν_3 is known to be small from the null-oscillation observations of the short-baseline reactor experiments, which then leaves about 2/3 for the ν_e fraction in ν_1.

Dirac or Majorana Neutrino

It has been observed in many experiments and demonstrated in the standard model that the neutrino has (almost) purely negative helicity, while the anti-neutrino has (almost) purely positive helicity. The amplitude of the "wrong" helicity component is suppressed by a factor of m_ν/E. This brings up an interesting question that whether or not the differences we have observed between neutrino and anti-neutrino simply come from the strong dynamical suppression (of order $(m_\nu/E)^2$) from the helicity, and that the neutrino and anti-neutrino are in fact the same particle. If this is the case the neutrinos are "Majorana" particles, otherwise they are "Dirac" particles,

same as the quarks and charged leptons. The two Majorana phases α_1, α_2 introduced in Eqn. 1.3 are only non-zero if neutrinos are Majorana particles, otherwise they can be absorbed into the mass eigenstates by re-phasing.

The most promising way to distinguish between Dirac and Majorana neutrinos is the neutrino-less double beta decay ($0\nu\beta\beta$) experiment through the following process:

$$(Z, A) \rightarrow (Z + 2, A) + 2e^{-} \tag{1.6}$$

which obviously violates lepton number conservation and can only proceed if the neutrino is its own anti-particle. The amplitude for $0\nu\beta\beta$ decay is proportional to the effective Majorana mass:

$$A(0\nu\beta\beta) \propto |\sum_i U_{ei}^2 m_i| \equiv \langle m_{\beta\beta} \rangle \tag{1.7}$$

$0\nu\beta\beta$ decay has not been observed so far[1]. The current best upper limit of $\langle m_{\beta\beta} \rangle$ is from Heidelerg-Moscow experiment on ^{76}Ge, which reports $\langle m_{\beta\beta} \rangle < 0.35$ eV at 90% C.L. [11].

Neutrino Sources

Neutrinos are in fact very common particles in the universe. Fig. 1.2 shows the energy spectrum of neutrinos that reach the surface of the Earth. The spectra extend a large range in both the energy and the intensity. Excluding the nuclear reactors and accelerators, whose neutrino flux depends on how close one can put the detector at, from approximately high to low flux the neutrino sources are:

Cosmological neutrinos or big-bang relic neutrinos since they are the leftovers from the early universe similar to the CMB photons. They have a large number

[1] There was one controversial claim of evidence of $0\nu\beta\beta$ decay [10], which later received criticisms from various literatures.

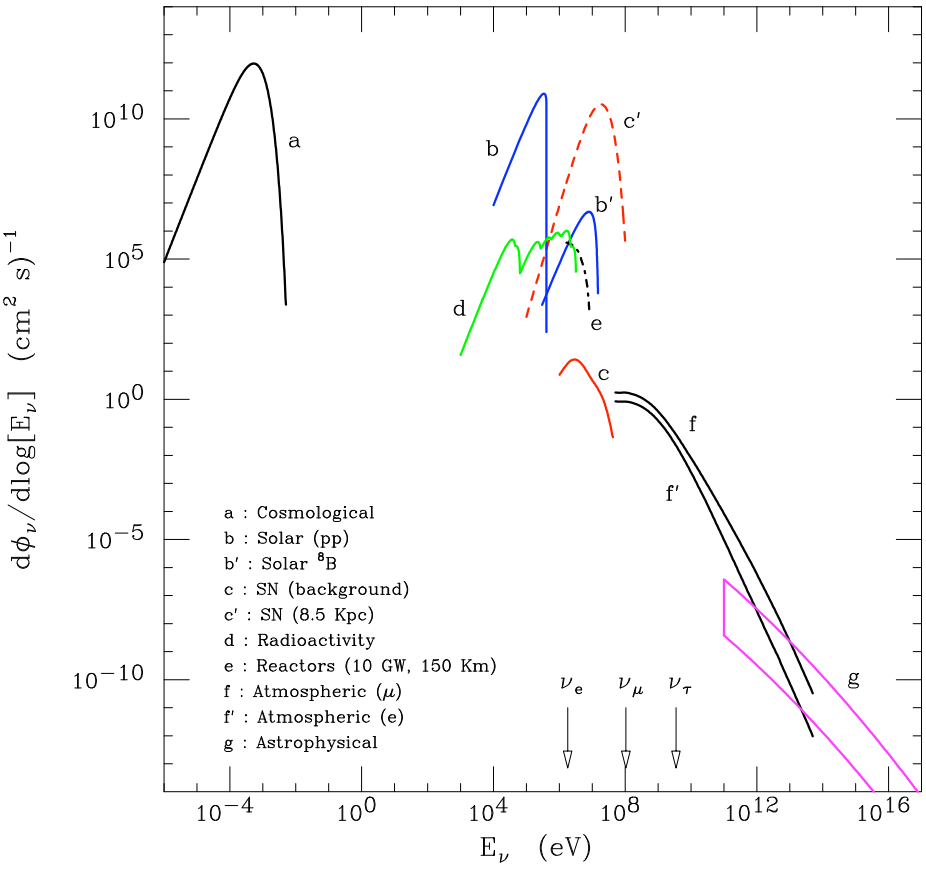

Figure 1.2: Flux of neutrinos at the surface of the Earth. The three arrows show the energy thresholds for charge current interactions on a free proton target. The geoneutrinos include the ^{238}U and ^{232}Th decay chains. The atmospheric neutrino fluxes are calculated at the Kamioka location. (Figure taken from [12].)

density of $\sim$56 cm^{-3} for each neutrino species (3 flavors and their anti-particles) with a black-body spectrum of very low temperature $T_\nu = 1.9$ K. The flux of cosmological neutrinos depends on the mass of the neutrinos. With the upper bound of $m_\nu < 2$ eV [7], the flux can be calculated to be at least $\sim 4 \times 10^{10}$ cm^{-2}s^{-1} for each neutrino species.

Solar neutrinos from the fusion reactions inside the sun. They are born as ν_e's and their flux at the Earth surface is $\sim 6 \times 10^{10}$ cm^{-2}s^{-1}, spanning an energy range up to $\sim$15 MeV. Details of solar neutrinos are discussed in Section 1.2.2. Some theories predict a $\bar{\nu}_e$ component in the solar flux through processes such as spin-flavor precession combined with neutrino oscillation. KamLAND has put an upper limit of such $\bar{\nu}_e$ flux to be less than 3.7×10^2 cm^{-2}s^{-1} at 90% C.L. in the energy window 8.3 – 14.8 MeV [13]. There are also theoretical predictions of a thermal flux of low-energy (< 5 keV) solar ν and $\bar{\nu}$'s from a variety of neutrino pair production processes. The predicted flux per flavor is $\sim 10^6$ cm^{-2}s^{-1} [14].

Supernova neutrinos from type II supernovae explosions in the Milky Way. These are rare events happening about once per 40 years. When such SN happens, enormous amount of energy ($\sim 10^{53}$ erg) is released in the form of all neutrino flavors in a timescale of $\sim$10 s, spanning an energy range up to $\sim$100 MeV. Up until now the only detected SN neutrinos are from SN1987A (55 kpc away from the Earth) on 23 February 1987. The predicted instantaneous neutrino flux from SN1987A is $\sim 10^9$ cm^{-2}s^{-1}. Kamiokande [15] and IMB [16] together detected 20 events in a time interval of 13 s. Cosmological theory also predicts a Diffuse Supernova Neutrino Background (DSNB), from an integration of estimated core-collapse supernovae rate history, to be on the order of $\sim$1 cm^{-2}s^{-1}. Super-Kamiokande has put an upper limit on DSNB to be less than 1.2 $\bar{\nu}_e$ cm^{-2}s^{-1} ($E_\nu > 19.3$ MeV) at 90% C.L. [17].

Geoneutrinos from the decay chains of natural radioactivities such as ^{238}U, ^{232}Th and ^{40}K in the Earth's crust and mantle. They are born mostly as $\bar{\nu}_e$'s from the β^- decays with energies up to 3.3 MeV. Geological models predict the radiogenic heat composes ∼19 TW or more of the total Earth heat flow [18, 19, 20]. Geoneutrinos have been observed at KamLAND [21, 22] and the $\bar{\nu}_e$ flux from ^{238}U and ^{232}Th decay chains are measured to be $(4.4 \pm 1.6) \times 10^6$ cm^{-2}s^{-1}. There is also theory predicting a natural nuclear reactor at the center of the Earth [1], called "georeactor," which will yield $\bar{\nu}_e$'s as a byproduct of the fission process, with energies up to ∼10 MeV. A hypothetical 10 TW georeactor will output a $\bar{\nu}_e$ flux of $\sim 4 \times 10^5$ cm^{-2}s^{-1} at the surface of the Earth.

Atmospheric neutrinos from the cosmic-ray interactions and decays in the Earth's atmosphere. They are born as ν_μ's and ν_e's (and their antiparticles), mostly from the decays of cosmic ray pions and muons, with energies up to ∼10 TeV. The flux falls down rapidly at high energy [23] following an approximate power law. At 1 GeV the ν_μ flux is approximately 10^{-2} cm^{-2}s^{-1}sr^{-1}. More details of atmospheric neutrinos are discussed in Section 1.2.1.

Astrophysical neutrinos with ultra high energies (> TeV) from galactic or extra-galactic sources. Possible sources of such neutrinos are extreme acceleration environments such as AGN and GRB, GZK neutrinos from proton interaction with CMB photons, and possible annihilation or decay of heavy particles. Flux of UHE neutrinos is extremely low (∼1 km^{-2}y^{-1} for GZK neutrinos), so kilometer-scale neutrino telescopes such as IceCube [24], Antares [25], Anita [26] are needed to detect them.

1.1.2 Neutrino Oscillation in Vacuum

The phenomenon of neutrino oscillation is the consequence of quantum mechanics from Eqn. 1.2. As the neutrino propagates from the source to the detector in the vacuum, it follows:

$$|\nu_\alpha(t)\rangle = \sum_{i=1}^{3} U^*_{\alpha i} e^{-iE_i t} |\nu_i\rangle. \qquad \alpha = e, \mu, \tau \tag{1.8}$$

where $E_i = \sqrt{p^2 + m_i^2} \simeq E + m_i^2/2E$ is the total energy of the mass eigenstate ν_i. Dropping the common phases to all three mass eigenstates, the probability for neutrino flavor state ν_α to oscillate into flavor state ν_β after traveling a distance L is

$$\begin{aligned} P(\nu_\alpha \to \nu_\beta) &= \left| \sum_i U_{\beta i} U^*_{\alpha i} E^{-i m_i^2 L/(2E)} \right|^2 \\ &= \delta_{\alpha\beta} - 4 \sum_{i>j} \mathbb{R}(U^*_{\alpha i} U_{\beta i} U_{\alpha j} U^*_{\beta j}) \sin^2[1.27 \Delta m^2_{ij} (L/E)] \\ &\quad + 2 \sum_{i>j} \mathbb{I}(U^*_{\alpha i} U_{\beta i} U_{\alpha j} U^*_{\beta j}) \sin[2.54 \Delta m^2_{ij} (L/E)] \end{aligned} \tag{1.9}$$

where $\Delta m^2_{ij} \equiv m_i^2 - m_j^2$, L is in km and E is in GeV. A few observations can be made from Eqn. 1.9

- Oscillation probability is independent of the Majorana phase α_1, α_2.
- For $P(\bar{\nu}_\alpha \to \bar{\nu}_\beta)$ one replaces the mixing matrix $U \to U^*$. Oscillation can violate CP if U is complex, that is if the CP violating phase δ is different from 0 or π[2].
- For $P(\nu_\beta \to \nu_\alpha)$ one exchanges the subscript $\alpha \leftrightarrow \beta$. Oscillation can violate T if δ is different from 0 or π.

[2]To violate CP it also requires that all three mixing angles and the mass splittings are different from zero. In particular θ_{13} must not be zero, since the other mixing angles have already been measured to be non-zero.

- For $P(\bar{\nu}_\beta \to \bar{\nu}_\alpha)$ one exchanges both the subscript $\alpha \leftrightarrow \beta$ and $U \to U^*$. One can see that oscillation probability remains the same and CPT is conserved independent of δ, as it should be. One application is that $P(\nu_e \to \nu_e) = P(\bar{\nu}_e \to \bar{\nu}_e)$ under the assumption of CPT invariance.

The complicated equation 1.9 can be considerably simplified given the fact that one mass splitting Δm^2_{atm} is much bigger than the other mass splitting Δm^2_{sol} ("one mass scale dominance"). As a consequence, in many neutrino oscillation experiments only two mass eigenstates are relevant ("quasi-two-neutrino oscillation"). The oscillation probability simply reduces to

$$P(\nu_\alpha \to \nu_\beta) = \sin^2 2\theta \sin^2 \left(1.27\Delta m^2[\text{eV}^2]\frac{L\,[\text{km}]}{E\,[\text{GeV}]}\right) \tag{1.10}$$

with $\beta \neq \alpha$ (appearance channel), and

$$P(\nu_\alpha \to \nu_\alpha) = 1 - \sin^2 2\theta \sin^2 \left(1.27\Delta m^2[\text{eV}^2]\frac{L\,[\text{km}]}{E\,[\text{GeV}]}\right) \tag{1.11}$$

in the disappearance channel. Here Δm^2 is the mass splitting relevant to the experiment such that $\Delta m^2 L/E = \mathcal{O}(1)$, and θ is the mixing angle relevant to the experiment, for example θ_{12} for solar and long-baseline reactor neutrino experiments, θ_{13} for short-baseline reactor neutrino experiments, and θ_{23} for atmospheric neutrino experiments. Eqn. 1.11 will be extensively used in this dissertation.

1.1.3 Neutrino Oscillation in Matter

The presence of matter provides a coherent effect of forward scattering from particles in the matter on the propagation of a neutrino. Such an effect is also known as the "MSW effect" as it is first suggested by Mikheyev, Smirnov and Wolfenstein [27, 28]. The effective potential introduced by the MSW effect receives contribution from all

target particles, i.e. electrons, protons and neutrons for ordinary matter. However, since only potential differences between the neutrino flavors play a role in the neutrino oscillation, the effective MSW potential can be written as

$$V \equiv V_{\nu_e} - V_{\nu_\mu} = V_{\nu_e} - V_{\nu_\tau} = +\sqrt{2} G_F N_e \tag{1.12}$$

which simply comes from ν_e scatters off electrons through charge current interaction, as the neutral current contribution is the same for ν_e, ν_μ and ν_τ. Here G_F is the Fermi constant and N_e is the number density of electrons. For anti-neutrinos the MSW potential reverses its sign.

The MSW effect on the neutrino oscillation is best illustrated in a two neutrino oscillation scenario (e.g. $\nu_e \rightarrow \nu_x$ as is the case for solar neutrinos). The effective Hamiltonian H, in the flavor space, is (dropping multiples of the identity matrix):

$$\begin{aligned}
H &= H_{\text{vacuum}} + H_{\text{matter}} \\
&= \begin{pmatrix} \cos\theta & \sin\theta \\ -\sin\theta & \cos\theta \end{pmatrix} \begin{pmatrix} m_1^2/2E & 0 \\ 0 & m_2^2/2E \end{pmatrix} \begin{pmatrix} \cos\theta & -\sin\theta \\ \sin\theta & \cos\theta \end{pmatrix} + \begin{pmatrix} V & 0 \\ 0 & 0 \end{pmatrix} \\
&= \frac{\Delta m^2}{4E} \begin{pmatrix} -\cos 2\theta + \xi & \sin 2\theta \\ \sin 2\theta & \cos 2\theta - \xi \end{pmatrix} \\
&= \frac{(\Delta m^2)_m}{4E} \begin{pmatrix} -\cos 2\theta_m & \sin 2\theta_m \\ \sin 2\theta_m & \cos 2\theta_m \end{pmatrix}
\end{aligned} \tag{1.13}$$

where we define

$$\xi = \frac{2VE}{\Delta m^2} \simeq \left(\frac{\pm 8 \times 10^{-5}}{\Delta m^2\,[\text{eV}^2]}\right) \left(\frac{\rho}{\text{g/cm}^3}\right) \left(\frac{E}{\text{GeV}}\right) \left(\frac{Y_e}{0.5}\right) \tag{1.14}$$

which is positive for ν_e and negative for $\bar{\nu}_e$. Here ρ is the density of the matter and Y_e is the electron number per nucleon ($\sim$0.5 on average). From Eqn. 1.13 one can see

that the presence of MSW effect can be accommodated into the vacuum oscillation by redefining $\theta \to \theta_m$ and $\Delta m^2 \to (\Delta m^2)_m$ such that

$$\sin^2 2\theta_m = \frac{\sin^2 2\theta}{\sin^2 2\theta + (\cos 2\theta - \xi)^2} \tag{1.15}$$

and

$$(\Delta m^2)_m = \Delta m^2 \sqrt{\sin^2 2\theta + (\cos 2\theta - \xi)^2} \tag{1.16}$$

As can be easily seen, when MSW effect is small, $\xi \to 0$ and vacuum oscillation is recovered. On the other hand, from Eqn. 1.14, MSW effect plays an important role for solar neutrinos since density is high ($\sim$100 g/cm^2) at the center of the sun where the neutrinos are created, and for long-baseline accelerator neutrinos traversing the Earth, with a beam energy higher than a few tens of GeV.

1.2 History of Neutrino Oscillation Experiments

There is a long history and a large number of neutrino oscillation experiments starting as early as the 1960s, using various types of neutrino sources. Early experiments were not specifically designed to look for neutrino oscillations, so when the neutrino oscillation phenomenon emerged from the data it was quite surprising, and turned out to be an even more interesting field of study. Fig. 1.3 shows a summary of regions of mass-squared splitting and mixing angle favored or excluded by various experiments, taken from PDG 2008 [7]. Some of those experiments will be discussed in this section.

1.2.1 Atmospheric Neutrinos

Despite some of the hints in the earlier experiments, the first strong evidence of neutrino oscillation comes from the study of atmospheric neutrinos by Kamiokande experiment in 1988 [29]. Atmospheric neutrinos are produced by the cosmic rays

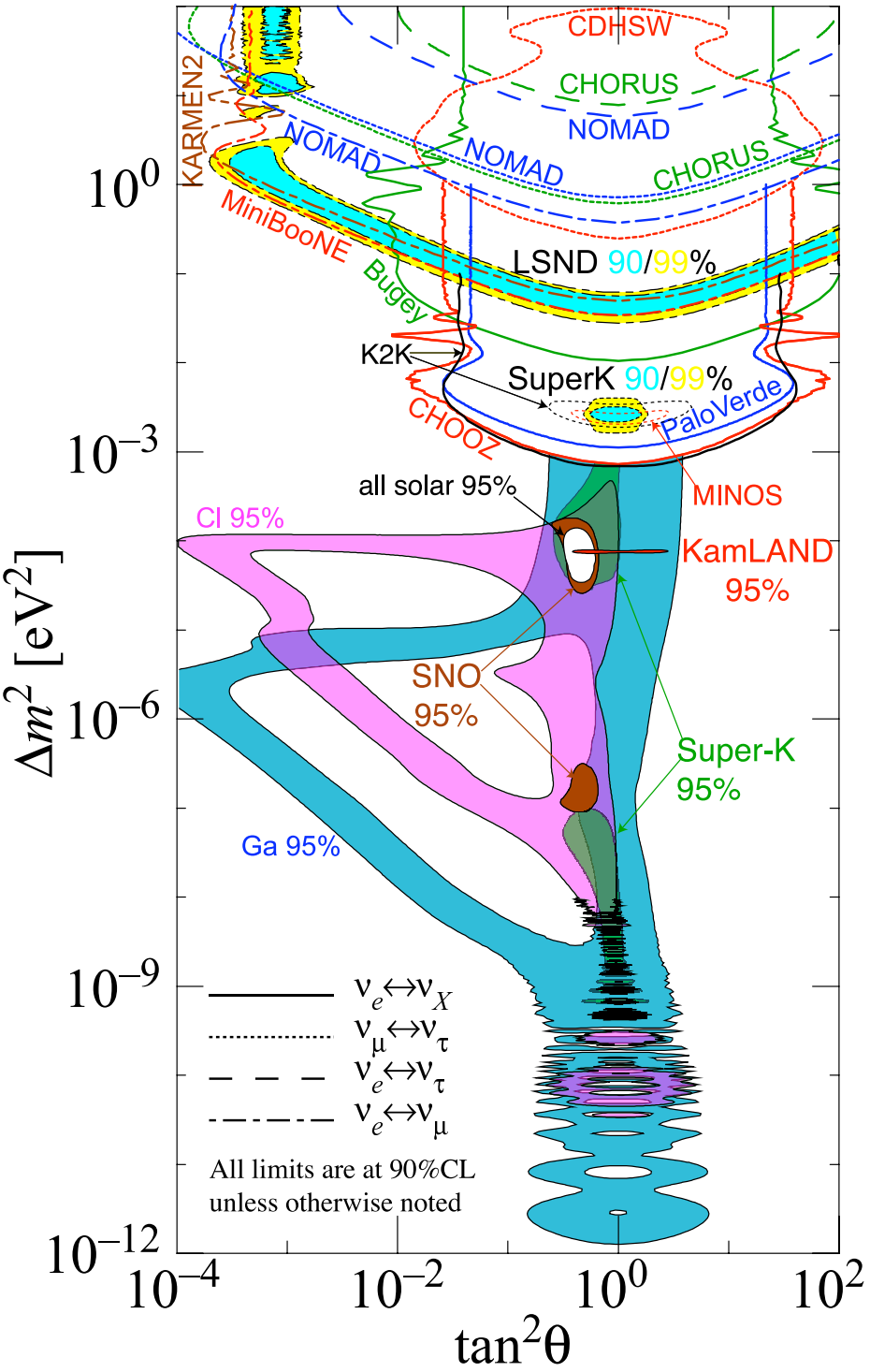

Figure 1.3: Regions of neutrino oscillation parameters favored or excluded by various experiments. Figures taken from PDG 2008 [7]. Data used in this figure can be found at http://hitoshi.berkeley.edu/neutrino/ .

interacting with the Earth atmosphere. The primary cosmic rays, mostly protons, have a spectrum approximately following a power law $\Phi(E) \propto E^{-2.7}$, extending up to extremely high energies $\sim 10^{20}$ eV. The primary cosmic ray interacts with Earth atmosphere creating abundant secondary particles, called "air showers." Among them the dominant source of neutrinos are the $\pi^{\pm}$ through their decay chains, such as:

$$\pi^+ \to \mu^+ + \nu_\mu \,, \qquad \mu^+ \to e^+ + \nu_e + \bar{\nu}_\mu \tag{1.17}$$

The calculations of the absolute atmospheric neutrino flux usually have large uncertainties $\sim$20% [23] due to the many factors involved, such as primary cosmic ray flux, solar modulation, geomagnetic cutoff, cosmic ray interaction models, etc. However, some properties have more robust estimations:

- The flux ratio of $(\nu_\mu + \bar{\nu}_\mu)/(\nu_e + \bar{\nu}_e)$ is approximately two at low energy (E $<$ 3 GeV), which is the simple consequence of the pion decay chain in Eqn. 1.17. The statement is also true for the differential flux at each neutrino energy, since the three neutrinos produced in the pion decay chain have approximately the same average energy. The flux ratio increases at higher energy because some of the muons would reach the ground before decaying away. The flux ratio is calculated to be accurate to $\sim$5%.

- The neutrino flux has an up-down symmetry:

$$\phi_{\nu_\alpha}(E, \theta) = \phi_{\nu_\alpha}(E, \pi - \theta) \tag{1.18}$$

  because the Earth is a well-defined sphere and the primary cosmic rays are isotropic. The statement is more true for high energy neutrinos (E $>$ a few GeV) where the influences from geomagnetic field is minimal.

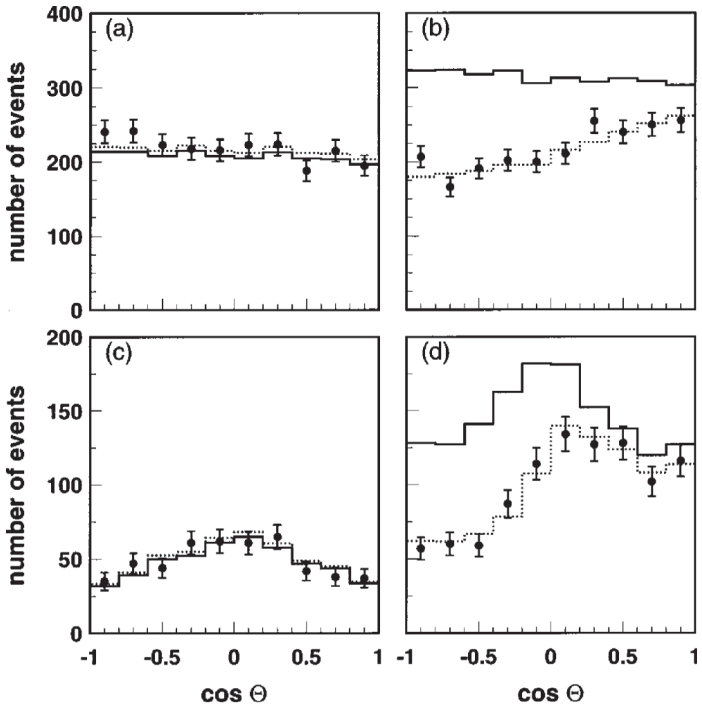

Figure 1.4: Zenith-angle distributions observed in Super-Kamiokande based on 61 kton-yr data: (a) sub-GeV e-like events; (b) sub-GeV μ-like events; (c) multi-GeV e-like events; (d) multi-GeV μ-like events including partially contained events. $\cos\theta = 1$ means upward going and $\cos\theta = -1$ means downward going. Solid lines show the Monte Carlo prediction without oscillation (normalization varied in the fit). Dashed lines show the prediction with oscillation ($\Delta m^2 = 2.8 \times 10^{-3}$ eV^2, $\sin^2 2\theta = 1.0$). Figure taken from Ref. [30].

The largest sample of atmospheric neutrino data is from the Super-Kamiokande experiment. The detector contains 50 ktons of pure water to look for the Cherenkov light produced by the charged particles passing through the detector. The atmospheric neutrinos produce e's and μ's inside the detector through CC interaction, and the directions of the leptons well represent the directions of the neutrinos at energies higher than $\sim$1 GeV. The detector is able to distinguish an electron event from a muon event by the pattern of hit PMTs: a "sharp" ring for μ-like or a "fuzzy" ring for e-like event. The events are further grouped into 4 categories: sub-GeV e-like, sub-GeV μ-like, multi-GeV e-like, multi-GeV μ-like including the partially contained events, and their zenith angle distributions are shown in Fig. 1.4 together with the Monte Carlo predictions without neutrino oscillation. It is surprising that all e-like events agree well with the Monte Carlo simulation, while μ-like events show significant deficit for up-going events only. On the other hand, the data can be well explained with neutrino oscillation because the up-going neutrinos travel much longer distances though the Earth to the detector ($\sim 10^4$ km) compared with the down-going neutrinos which only travel through the atmosphere ($\sim$20 km). Since null $\bar{\nu}_e \to \bar{\nu}_\mu$ (thus $\nu_\mu \to \nu_e$ assuming CPT invariance) oscillations have been observed by the short-baseline reactor neutrino experiments, the data agree well with the $\nu_\mu \to \nu_\tau$ oscillation explanation[3]. From Eqn. 1.11 one can immediately estimate the mixing angle θ_{23}:

$$P(\nu_\mu \to \nu_\mu) = 1 - 0.5 \sin^2 2\theta_{23} \simeq \frac{N_{\rm up}}{N_{\rm down}} \sim 0.5$$
$$\Rightarrow \quad \sin^2 2\theta_{23} \sim 1 \quad (\theta_{23} \sim 45^\circ) \tag{1.19}$$

[3]The atmospheric neutrino data by themselves do not rule out $\nu_\mu \to \nu_e$ oscillation. The observed null flux change of e-like events can be a simple cancellation between ν_e oscillating into ν_μ and ν_τ with equal probability, and ν_u oscillating into ν_e with the same probability but twice the flux.

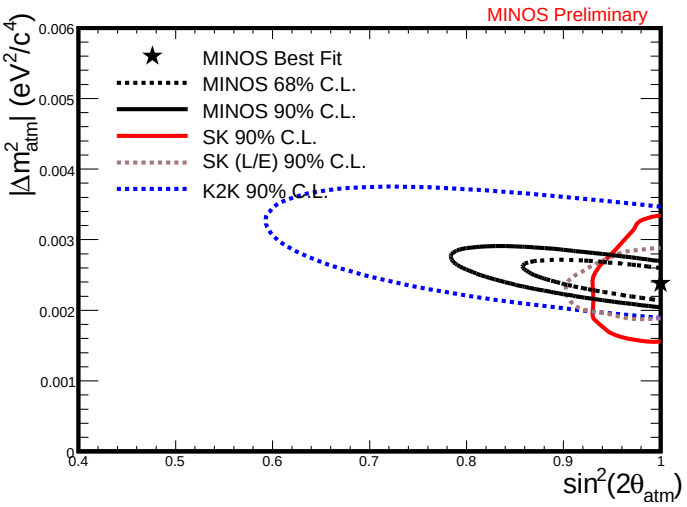

Figure 1.5: The regions of the atmospheric neutrino oscillation parameters allowed by Super-Kamiokande (SK), K2K and MINOS experiment. Figure taken from [7].

and the Δm^2_{23}:

$$\Delta m^2_{23} \sim \frac{E\,[\mathrm{GeV}]}{2.54 \cdot L\,[\mathrm{km}]} \sim \frac{3\,\mathrm{GeV}}{2.54 \cdot 500\,\mathrm{km}} \sim 2.4 \times 10^{-3}\,\mathrm{eV}^2 \tag{1.20}$$

Here the average energy $\langle E_\nu \rangle$ of $\sim$3 GeV and the horizontal path-length of $\sim$500 km are used.

The same oscillation parameter space has been explored by the long-baseline accelerator neutrino experiments such as K2K [31] and MINOS [32]. The flux of ν_μ beams is measured at a near detector before any oscillation is expected, and at a far detector, 250 km away for K2K and 735 km away for MINOS from the neutrino source. Both K2K and MINOS observed significant disappearance of the expected ν_u flux at the far detector, and distortion of the expected ν_μ energy spectrum consistent with the $\nu_\mu \rightarrow \nu_\tau$ oscillation. Fig. 1.5 shows the allowed regions by combining the Super-Kamiokande (SK), K2K and MINOS data. The constrain on Δm^2 mostly comes from the analysis of the ν_u energy spectrum distortion, while the constrain on $\sin^2 2\theta$ mostly comes from the large data set of SK atmospheric neutrino samples.

1.2.2 Solar Neutrinos

The Sun is a huge neutrino source for the Earth. Bethe [33] first pointed out in 1939 that the sun shines by the internal fusion process:

$$4p \rightarrow {}^4\mathrm{He} + 2e^+ + 2\nu_e + 26.73\,\mathrm{MeV} \tag{1.21}$$

The general fusion reaction 1.21 can proceed with different reaction cycles that produce the same final particles, but result in different energy distribution of neutrinos. In the Sun ∼98.5% of the energy is produced by the "pp" chain, while only ∼1.5% by the "CNO" chain. The pp chain reactions and the ν_e flux predictions from the Standard Solar Model (BP04 [34]) are summarized in Table 1.1. The energy spectrum of different solar neutrinos are shown in Fig. 1.6. Here we neglect "CNO" neutrinos for simplicity, as they typically have relatively low flux ($\sim 5 \times 10^8$ cm^{-2}s^{-1}) and have energies below 1 MeV, which made them difficult to be detected. The theoretical prediction for "CNO" neutrinos also have large uncertainties of ∼40% [34].

Table 1.1: The ν_e production from pp chain in the Sun. The termination percentage is the fraction of terminations of the pp chain. The predicted ν_e flux is from BP04 [34].

Source	Reaction	Termination [%]	ν_e Energy [MeV]	ν_e Flux [cm^{-2}s^{-1}]
pp	$p + p \rightarrow {}^2\mathrm{H} + e^+ + \nu_e$	99.6	< 0.43	5.94×10^{10} ($\pm$1%)
pep	$p + e^- + p \rightarrow {}^2\mathrm{H} + \nu_e$	0.4	1.44	1.40×10^8 ($\pm$2%)
	${}^2\mathrm{H} + p \rightarrow {}^3\mathrm{He} + \gamma$	100		
	${}^3\mathrm{He} + {}^3\mathrm{He} \rightarrow {}^4\mathrm{He} + 2p$	85		
	${}^3\mathrm{He} + {}^4\mathrm{He} \rightarrow {}^7\mathrm{Be} + \gamma$	15		
^{7}Be	${}^7\mathrm{Be} + e^- \rightarrow {}^7\mathrm{Li} + \nu_e$	15	0.86 (90%) 0.38 (10%)	4.86×10^9 ($\pm$12%)
	${}^7\mathrm{Li} + p \rightarrow 2\,{}^4\mathrm{He}$	15		
	${}^7\mathrm{Be} + p \rightarrow {}^8\mathrm{B} + \gamma$	0.02		
^{8}B	${}^8\mathrm{B} \rightarrow {}^8\mathrm{Be}^* + e^+ + \nu_e$	0.02	< 15	5.79×10^6 ($\pm$23%)
	${}^8\mathrm{Be}^* \rightarrow 2\,{}^4\mathrm{He}$	0.02		
hep	${}^3\mathrm{He} + p \rightarrow {}^4\mathrm{He} + e^+ + \nu_e$	2×10^{-5}	< 18.8	7.88×10^3 ($\pm$16%)

Up to present there are five main types of solar neutrino experiments using dif-

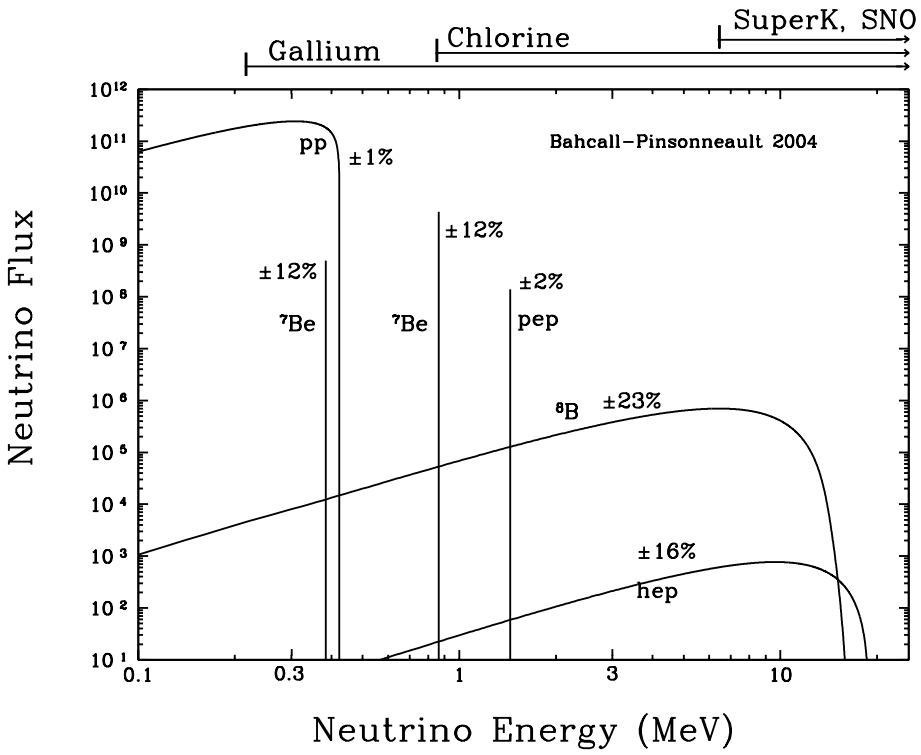

Figure 1.6: The energy spectra of solar neutrinos from the pp Chain, predicted from BP04 [34] solar model. For continuum sources, the neutrino fluxes are given in $cm^{-2}s^{-1}MeV^{-1}$ at the Earth's surface. For line sources, the units are $cm^{-2}s^{-1}$. The sensitive regions of the Gallium, Chlorine, Water and Heavy Water experiment are also shown.

ferent detector targets: Chlorine, Gallium, water, heavy water and liquid scintillator. The first two are radiochemical measurements typically involving collecting and counting the final-state radioactive isotopes periodically, while the last three are real-time measurements of the neutrino energy spectrum.

Chlorine Experiments

In the late 1960s began the first solar neutrino experiment led by Ray Davis [35] in the Homestake gold mine (depth of 4300 m.w.e) in South Dakota. The experiment uses ∼600 tons of liquid C_2Cl_4 to detect solar neutrinos through the radiochemical reaction

$$\nu_e + {}^{37}\mathrm{Cl} \rightarrow {}^{37}\mathrm{Ar} + e^- \tag{1.22}$$

The reaction has a threshold energy of 0.814 MeV and is mostly sensitive to ^{8}B neutrinos, but there is a substantial contribution from ^{7}Be neutrinos as well. The experiment was taking data for over 30 years, during when the ^{37}Ar atoms were flushed out with helium gas every ∼100 days and condensed into proportional counters for counting. As a result, the average neutrino flux observed by Homestake Chlorine experiment is 2.56 ± 0.23 solar neutrino units (SNU)[4], while the standard solar model (BP04) predicts 8.5 ± 1.8 SNU. The incompatibility between theory and experiment is well known as "The Solar Neutrino Problem."

Gallium Experiments

A lower energy threshold can be obtained with a Gallium target through the reaction

$$\nu_e + {}^{71}\mathrm{Ga} \rightarrow {}^{71}\mathrm{Ge} + e^- \tag{1.23}$$

[4] 1 SNU = 10^{-36} interactions per target atom per second.

which has a threshold energy of 0.214 MeV and is sensitive to the most abundant pp neutrinos. Such experiments have been carried out by SAGE [36] in the Baksan laboratory (depth of 4700 m.w.e) in Russia with 60 tons of liquid Ga metal, and by GALLEX/GNO [37] in the Gran Sasso laboratory (depth of 3300 m.w.e) in Italy with 30 tons of Ga in a concentrated $GaCl_3$-HCl solution. In both experiments the ^{71}Ge is extracted monthly and converted into the form of GeH_4 and counted. The measured average flux is $67.2^{+7.2+3.5}_{-7.0-3.0}$ SNU for SAGE and 69.3 $\pm$ 5.5 SNU for GALLEX+GNO. Both experiments only observed about a half of the predicted 131 SNU from the standard solar model.

Water Experiments

The first real-time solar neutrino measurement is from the Kamiokande/Super-Kamiokande experiment located in the Kamioka mine (depth of 2700 w.m.e) in Japan. As described in Section 1.2.1, the detector contains 50 ktons of pure water to look for the Cherenkov light produced by the charged particles passing through the detector, in particular for solar neutrinos through the elastic scattering on electrons:

$$\nu_x + e^- \rightarrow \nu_x + e^- \tag{1.24}$$

The elastic scattering is sensitive to all neutrino flavors, however, the cross section for ν_e ($\sim 1.0 \times 10^{-44}$ E [MeV] cm^2) is approximately 7 times larger than for ν_μ and ν_τ ($\sim 0.15 \times 10^{-44}$ E [MeV] cm^2). The direction of the electron from the elastic scattering in strongly correlated with the neutrino, pointing back to the Sun (Fig. 1.7(a)). The energy threshold is about 7 MeV for Kamiokande and 5 MeV for Super-Kamiokande, thus the sensitivity of the measurement is almost entirely to the ^{8}B neutrinos. As a result, the measured ^{8}B neutrino flux is $(2.8 \pm 0.4) \times 10^6$ cm^{-2}s^{-1} by Kamiokande [38], and $(2.35 \pm 0.08) \times 10^6$ cm^{-2}s^{-1} by Super-Kamiokande [39, 40]. Both are significantly

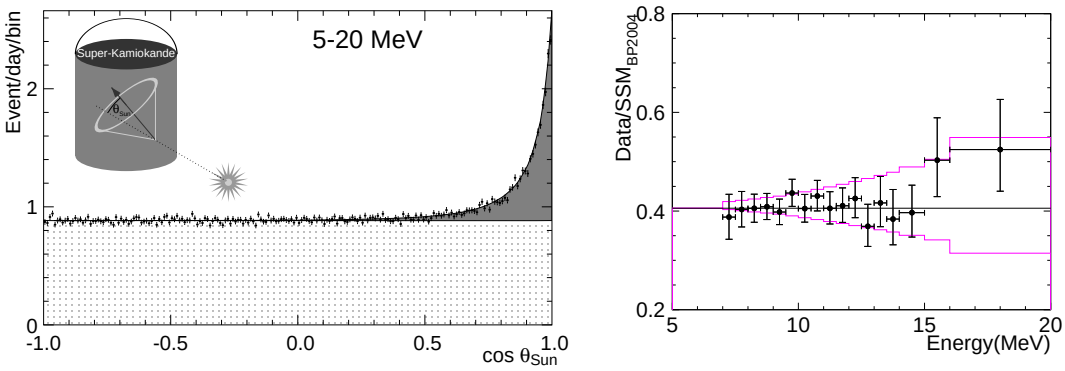

(a) (b)

Figure 1.7: The solar neutrinos measured at Super-Kamiokande: (a) Angular distribution relative to the Sun. The shaded area indicates the elastic scattering peak, the dotted area is the contribution from the background. (b) Ratio of observed and expected energy spectrum. The purple lines represent 1σ systematic error region. Figures taken from Ref. [39, 40]

less than the solar model predicted ^{8}B neutrino flux of $5.79(1 \pm 0.23) \times 10^6$ cm^{-2}s^{-1}. Furthermore, no significant distortion of the ^{8}B neutrino energy spectrum has been observed (Fig. 1.7(b)).

Heavy Water Experiments

The SNO experiment located in the Sudbury mine (depth of 6200 m.w.e) in Canada uses 1 kton of heavy water (D_2O) as a Cherenkov detector. With heavy water, three different reactions can be registered by the detector:

$$CC \;:\; \nu_e + d \rightarrow p + p + e^- \tag{1.25}$$

$$NC \;:\; \nu_x + d \rightarrow p + n + \nu_x \tag{1.26}$$

$$ES \;:\; \nu_x + e^- \rightarrow \nu_x + e^- \tag{1.27}$$

The CC reaction is sensitive only to ν_e's, while the NC reaction is sensitive to all neutrino flavors. The ES reaction is the same as in the water experiments such as Super-Kamiokande, mostly sensitive to ν_e's with reduced sensitivity to ν_μ's and ν_τ's.

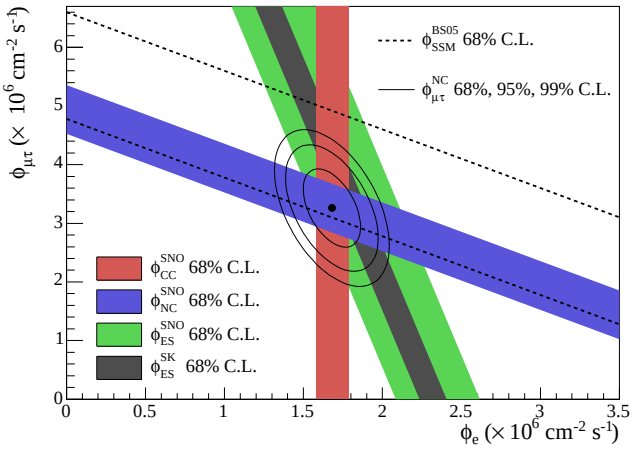

Figure 1.8: SNO measured flux of $\mu + \tau$ neutrinos versus flux of electron neutrinos. *CC*, *NC* and *ES* flux measurements are indicated by the filled bands. The total ^{8}B solar neutrino flux predicted by the standard solar model [34] is shown as dashed lines. Super-Kamiokande result is shown as the grey band. Figure taken from. [41].

The energy threshold in SNO for *CC* and *ES* reactions is about 5.5 MeV and for *NC* reaction is the reaction threshold of 2.2 MeV, thus the solar neutrino contribution is also almost entirely from the ^{8}B solar neutrinos. The different angular and energy distribution allows disentangling the three reactions on a statistical basis. The SNO experiment has been running in three phases with increasing ability of detecting the neutrons from the *NC* reactions. In the first phase with pure heavy water, neutrons are captured on deuterium giving 6.25 MeV γ-rays. In the second phase 2.7 tons of salt were added to the heavy water, which increased the neutron detection efficiency through capture on Cl and γ-rays with total energy $\sim$8.6 MeV are released. In the third phase the salt was removed and an array of ^{3}He proportional counters was installed in the detector, enabling neutron detection independent of the PMT array. The measured flux in each channel, in units of 10^6 cm^{-2}s^{-1}, is [34]:

$$\phi_{CC} = \phi_{\nu_e} = 1.68^{+0.06+0.08}_{-0.06-0.09} \quad (1.28)$$

$$\phi_{ES} = \phi_{\nu_e} + 0.155(\phi_{\nu_\mu} + \phi_{\nu_\tau}) = 2.35^{+0.22+0.15}_{-0.22-0.15} \quad (1.29)$$

$$\phi_{NC} = \phi_{\nu_e} + \phi_{\nu_\mu} + \phi_{\nu_\tau} = 4.94^{+0.21+0.38}_{-0.21-0.34} \quad (1.30)$$

where the statistical error is indicated before the systematic error. The flux in CC and ES channel shows a similar large deficit as other solar neutrino experiments. On the other hand, the NC flux measurement is in good agreement with the standard solar model prediction of $5.79(1 \pm 0.23) \times 10^6$ cm^{-2}s^{-1}. The SNO result is considered as the "smoking-gun" evidence that the neutrino oscillation is the key to solve the "Solar Neutrino Problem" that lasted for more than 30 years.

Liquid Scintillator Experiments

Liquid scintillator detector, due to its large scintillation light output, has a much lower energy threshold than the Cherenkov detectors. Carbon-based organic liquid scintillators are used in the KamLAND experiment (∼1 kton), located in the Kamioka mine (depth of 2700 w.m.e) in Japan, and in the Borexino experiment (∼300 ton) in the Gran Sasso laboratory (depth of 3300 m.w.e) in Italy. They are sensitive to the solar neutrinos through the elastic scattering process similar to Super-Kamiokande and SNO, but with energy threshold as low as a few hundred keV, thus are sensitive to the more abundant ^{7}Be solar neutrinos. One disadvantage of most liquid scintillator detectors is the lack of directional information about the neutrino event, since the scintillation light is isotropic. The greatest obstacles for low energy measurements are the radioactive backgrounds from naturally occurring or cosmogenical radioisotopes in the detector (^{14}C, ^{238}U, ^{232}Th, ^{40}K, ^{210}Pb, ^{85}Kr, ^{39}Ar, ^{11}C, etc.), thus advanced purification techniques and careful operation of the detector are needed in order to remove

the initial radioactive contaminants and to prevent introducing new contaminants. The ^{7}Be solar neutrino flux measured by Borexino [42] is $(2.8 \pm 0.2_{\rm stat} \pm 0.3_{\rm syst}) \times 10^9$ cm^{-2}s^{-1}, which is again significantly lower than the standard solar model prediction of $(5.08 \pm 0.25) \times 10^9$ cm^{-2}s^{-1}.

Interpretation of Experimental Data

All of the measurements from various solar neutrino experiments can be nicely explained by the neutrino oscillation theory, in particular the Large Mixing Angle MSW (LMA-MSW) solution. Given the small size of U_{e3}, Solar neutrino propagation is approximately a two-flavor oscillation $\nu_e \to \nu_x$, where ν_x is a 50-50 mixture of ν_μ and ν_τ if $\theta_{\rm atm} = 45^\circ$. The survival probability of ν_e in the case of 3-neutrino oscillation can be simply related to the 2-neutrino case by

$$P^{3\nu}_{\nu_e \to \nu_e} = \sin^4\theta_{13} + \cos^4\theta_{13} \cdot P^{2\nu}_{\nu_e \to \nu_e}(\Delta m^2_{21}, \theta_{12}; N_e \to \cos^2\theta_{13} N_e) \tag{1.31}$$

where N_e is the electron density at the center of the sun where the neutrinos are created.

From Eqn. 1.15 and 1.16, MSW effect is important when $\xi \gg \cos 2\theta_{12}$, and negligible when ξ is small. ξ can be calculated from the standard solar model (assuming a reasonable θ_{12}) for each type of solar neutrinos, and the result is that the MSW potential dominates for the ^{8}B neutrino, while the vacuum potential dominates for the ^{7}Be and pp neutrinos. The ν_e survival probability P_{ee} measured by the Gallium experiments and Borexino ^{7}Be experiment is $\sim$0.55, from which the mixing angle θ_{12} can be immediately estimated with the vacuum oscillation formula

$$P_{ee}(^7\mathrm{Be}, \mathrm{pp}) \simeq 1 - 0.5 \sin^2 2\theta_{12} \sim 0.55$$
$$\Rightarrow \quad \sin^2 2\theta_{12} \sim 0.9 \quad (\theta_{12} \sim 36^\circ) \tag{1.32}$$

For ^{8}B neutrinos at the center of the sun, since the MSW potential dominates, the vacuum potential can be neglected as a first approximation in Eqn. 1.13. The Hamiltonian can be then written as:

$$H = \begin{pmatrix} \sqrt{2} G_F N_e & 0 \\ 0 & 0 \end{pmatrix} \tag{1.33}$$

The diagonal Hamiltonian means that the ^{8}B ν_e is born as the higher-energy mass eigenstate. The propagation of a ^{8}B ν_e to the outer edge of the Sun is adiabatic since the electron density N_e changes slowly over the route, which means that the neutrino keeps its status as the higher-energy mass eigenstate[5] of the slowly-varying H until it reaches the outer edge of the Sun, where H becomes H_{vacuum}. The neutrino then emerges out of the sun as the higher-energy mass eigenstate of H_{vacuum}, which by definition is ν_2, until it reaches the Earth (during the journey no oscillation happens since it is a mass eigenstate) being detected as a ν_e again. The ν_e survival probability P_{ee} is then simply $U_{e2}^2 \sim \sin^2 \theta_{12}$. The pure P_{ee} for ^{8}B neutrinos is measured by the SNO CC reaction to be $\sim$0.3, from which θ_{12} can be again estimated

$$P_{ee}(^8\mathrm{B}) \simeq \sin^2 \theta_{12} \sim 0.3 \quad (\theta_{12} \sim 33^\circ) \tag{1.34}$$

which agrees well with the vacuum oscillation case for ^{7}Be and pp neutrinos. The P_{ee} for ^{8}B neutrinos measured by the water experiments and SNO ES reaction is a little higher, because they have reduced sensitivity to ν_μ and ν_τ flux as well. Finally,

[5]It can be shown that the eigenvalues of H never cross as N_e changes with r.

the SNO NC reaction measured all three neutrinos and is consistent with the standard solar model prediction. The mystery of "The Solar Neutrino Problem" is solved — Solar neutrinos are not disappearing, they are simply redistributing themselves among the three flavors.

More rigorous global analysis of the solar neutrino data has been done, for example, in Ref.[43, 44]. Historically there were four allowed regions in the (Δm^2_{21}, θ_{12}) space, namely LMA (large mixing angle, $\Delta m^2 \sim 10^{-5}$ eV^2), SMA (small mixing angle, $\Delta m^2 \sim 10^{-5}$ eV^2), LOW ($\Delta m^2 \sim 10^{-7}$ eV^2) and VACUUM ($\theta_{12} \sim 45^\circ$, $\Delta m^2_{21} \sim 10^{-10}$ eV^2) regions. It becomes clear later by combing with the KamLAND [45, 46, 22] data that the LMA-MSW solution is the solely correct solution for solar neutrinos.

1.2.3 Reactor Neutrinos

The fission processes inside the nuclear reactors typically release $\bar{\nu}_e$'s with energies up to ∼10 MeV. $\bar{\nu}_e$'s are usually detected through the inverse beta decay reaction

$$\bar{\nu}_e + \mathrm{p} \rightarrow \mathrm{n} + \mathrm{e}^+ \tag{1.35}$$

The relatively large cross section (∼10^{-42} cm^2) combined with the clean signal (prompt positron events in coincidence with delayed neutron capture event) makes the detection of $\bar{\nu}_e$ relatively easy and historically that was how the neutrinos were first detected [3]. Reactor neutrino oscillation experiments are typically disappearance experiments that measure the $\bar{\nu}_e$ flux from the reactors and compare with the theoretical predictions. The $\bar{\nu}_e$ survival probability is directly related to the ν_e survival probability assuming CPT invariance: $P(\bar{\nu}_e \rightarrow \bar{\nu}_e) = P(\nu_e \rightarrow \nu_e)$.

Short Baseline Reactor Experiments

Omitting a few very short baseline (< 100 m) reactor neutrino experiments in the early times (Savannah River [3], ILL [47], Gösgen [48], Rovno [49], Krasnoyarsk [50], Bugey [51], etc.), the first short baseline reactor neutrino experiments specifically look for oscillation parameters found by the atmospheric neutrino measurements are CHOOZ [52, 53] and Palo Verde [54]. Both experiments have a baseline ∼1 km and are suitable to look for $\bar{\nu}_e$ disappearance corresponding to

$$P(\bar{\nu}_e \to \bar{\nu}_e) = 1 - \sin^2 2\theta_{13} \sin^2 \left(1.27 \Delta m^2_{\rm atm} [\mathrm{eV}^2] \frac{L\,[\mathrm{km}]}{E\,[\mathrm{GeV}]} \right) \tag{1.36}$$

Both detectors use liquid scintillator loaded with 0.1% natural gadolinium, which has a high thermal neutron capture cross section and releases an 8 MeV γ-ray cascade that is above all natural radioactivity.

The CHOOZ detector was built at distances of 1115 m and 998 m from the two reactors of the CHOOZ power plant in France. The plant had a total thermal power of 8.5 GW, and was only commissioned after the start of the data-taking of the experiment. This gives CHOOZ a special opportunity to observe the background during the zero-power period and the slow power-ramp-up period. The CHOOZ detector consisted of a central volume of scintillator with mass of ∼5 tons, and was placed in an underground cavity with a relatively deep overburden (300 m.w.e). The measured ratio between $\bar{\nu}_e$ detected and expected is

$$R_{\rm CHOOZ} = 1.01 \pm 0.028(\mathrm{stat}) \pm 0.027(\mathrm{syst}) \tag{1.37}$$

The Palo Verde experiment was built at distances of 890m, 890m and 750m from the three reactors of the Palo Verde Nuclear Generating Station in Arizona, US. The total thermal power was 11.6 GW. The detector is located in a relatively shallow

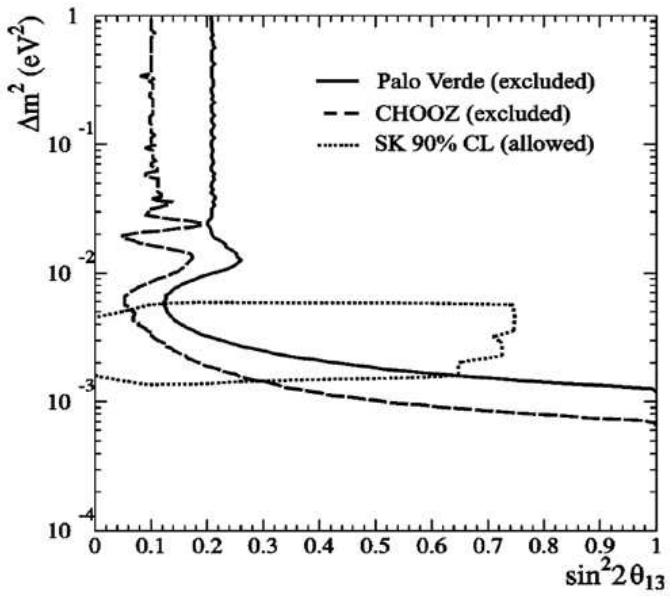

Figure 1.9: Exclusion contours on (Δm^2_{31}, $\sin^2 2\theta_{13}$) parameter space determined by CHOOZ, Palo Verde along with the allowed region obtained by Super-Kamiokande. Figure taken from. [53].

bunker (32 m.w.e). The rather large muon flux ($\sim$2 kHz) produced a substantial number of spallation neutrons, so a segmented detector design is used to take full advantage of the triple coincidence given by the positron and the subsequent annihilation γ-rays. The fiducial mass of the detector is 12 tons, but the more elaborate topological signature reduced the detection efficiency and increased the systematic errors. The measured ratio between $\bar{\nu}_e$ detected and expected is

$$R_{\text{Palo Verde}} = 1.01 \pm 0.024(\text{stat}) \pm 0.053(\text{syst}) \tag{1.38}$$

Since no $\bar{\nu}_e$ disappearance has been observed by either experiment, only upper limit of θ_{13} can be set. Fig. 1.9 shows the exclusion region on (Δm^2_{31}, $\sin^2 2\theta_{13}$) parameter space determined by CHOOZ, Palo Verde along with the allowed region obtained by Super-Kamiokande 3-neutrino analysis of the atmospheric neutrino data. The combined analysis sets the upper limit of $\sin^2(2\theta_{13}) < 0.19$ at 90% C.L.

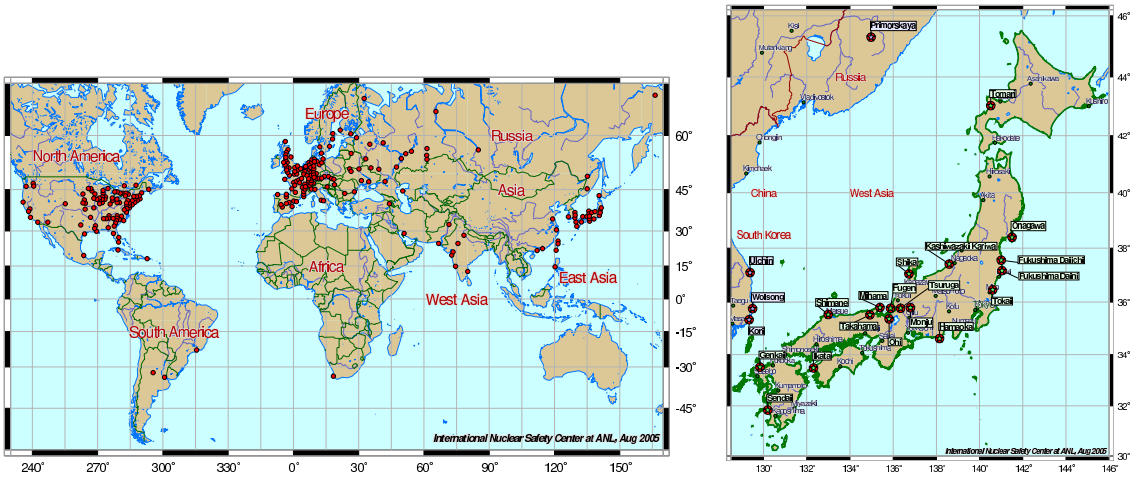

(a) (b)

Figure 1.10: The locations of nuclear power plants (a) in the world, (b) in Japan, Korea and Far East Russia. Substantial concentrations of reactors are found in Europe, Eastern US and Japan. KamLAND detector is located at (36.42 °N, 137.31 °E) in the middle of Japan. Maps can be found at http://www.insc.anl.gov/ from International Nuclear Safety Center at Argonne National Laboratory.

Long Baseline Reactor Experiments

To examine the oscillation parameters found by the solar neutrino experiments, a baseline of at least ∼100 km is needed, as can be easily seen from equation

$$P(\bar{\nu}_e \to \bar{\nu}_e) = 1 - \sin^2 2\theta_{12} \sin^2 \left(1.27 \Delta m^2_{\rm sol} [\mathrm{eV}^2] \frac{L\,[\mathrm{km}]}{E\,[\mathrm{GeV}]} \right) \tag{1.39}$$

since $\Delta m^2_{\rm sol}$ is approximately 10^{-5} eV^2 for LMA solution and even lower for other solutions (Section 1.2.2). On the other hand, the reactor $\bar{\nu}_e$ flux decreases as $1/r^2$, which means powerful nuclear reactors are needed in order to get good statistics. A quick look at the locations of nuclear power plants in the world (Fig. 1.10(a)) reveals that such a detector can be only placed in Europe, Eastern US or Japan. Historically, there was already an existing underground cavity (depth of 2700 m.w.e) built for the old Kamiokande detector, which is located in the middle of Japan surrounded by ∼55 reactor cores with total thermal power of ∼130 GW and flux averaged baseline of

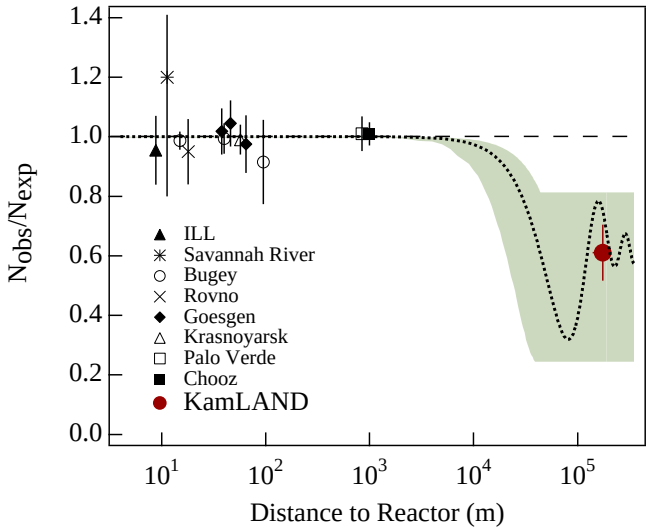

Figure 1.11: The $\bar{\nu}_e$ survival probability measured by various reactor neutrino experiments as a function of baseline distance. The shaded area indicates the 95% C.L. LMA flux predictions found in a global analysis of the solar neutrino data [43]. The dotted curve corresponds to $\sin^2 2\theta = 0.833$ and $\Delta m^2 = 5.5 \times 10^{-5}$ eV^2, while the dashed curve shows the case of small mixing angle (or no oscillation). Figure taken from [45].

$\sim$180 km (Fig. 1.10(b)). Naturally, this site was selected to house the KamLAND experiment to specifically explore the regions of neutrino oscillation parameters found by the solar neutrino experiments, but on the Earth.

The KamLAND detector consists of $\sim$1 kton of liquid scintillator and detects $\bar{\nu}_e$ through the usual inverse beta decay reaction. The predicted no-oscillation $\bar{\nu}_e$ event rate is $\sim$1 event/day/kton, modulated by the refueling and maintenance of the nuclear power plants in Japan. Details of the KamLAND experiment are discussed in Chapter 2. KamLAND for the first time observed significant deficit of the expected $\bar{\nu}_e$ flux. The measured ratio between $\bar{\nu}_e$ detected and expected is [45]

$$R_{\mathrm{KamLAND}} = 0.611 \pm 0.085(\mathrm{stat}) \pm 0.041(\mathrm{syst}) \tag{1.40}$$

Fig. 1.11 summarizes the $\bar{\nu}_e$ survival probability measured by various reactor neutrino experiments as a function of the baseline distance. As discussed in the previous

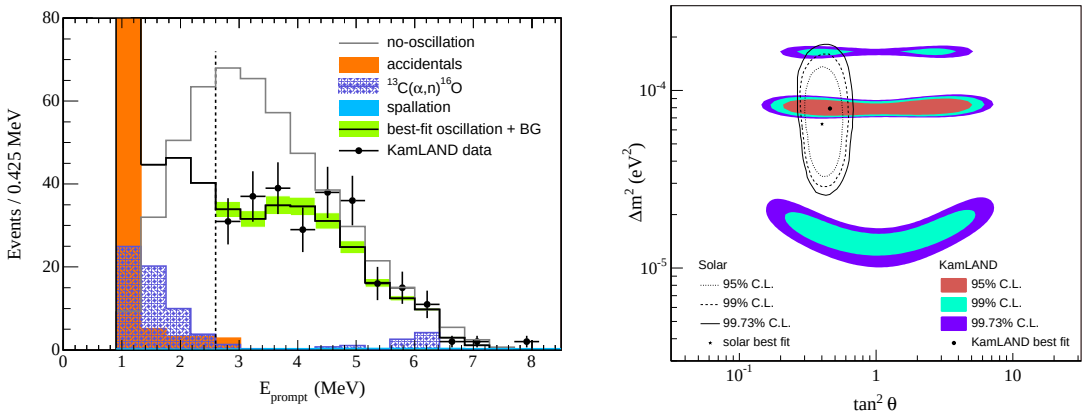

(a) (b)

Figure 1.12: (a) Prompt event energy spectrum of $\bar{\nu}_e$ candidate events at KamLAND with associated background spectra, and the predicted spectrum in case of no oscillation. (b) Neutrino oscillation parameter allowed region from KamLAND (shaded area) and solar neutrino experiments (lines). The three isolated shaded regions from bottom to top are historically called LMA-0, LMA-I and LMA-II region respectively. Figure taken from [46].

sections, the null-oscillation observation of short-baseline reactor neutrino experiments is the consequence of the smallness of θ_{13}, while the observed $\bar{\nu}_e$ flux deficit by KamLAND agrees well with the LMA-MSW oscillation parameters found by the solar neutrino experiments [43].

KamLAND has also observed significant distortion of $\bar{\nu}_e$ energy spectrum [46] as shown in Fig. 1.12(a). The observed spectrum distortion enabled KamLAND to make a very precise measurement of Δm^2_{21}. Fig. 1.12(b) shows the allowed regions of oscillation parameters from KamLAND and solar neutrino experiments [46]. The three isolated KamLAND allowed regions from bottom to top are historically called LMA-0, LMA-I and LMA-II region respectively. The recent released KamLAND result [22] shows that only the LMA-I region is allowed at 99.73% C.L. Combining with the results of solar experiments assuming CPT invariance, the neutrino oscillation parameters are measured to be $\Delta m^2_{21} = 7.59^{+0.21}_{-0.21} \times 10^{-5}$ eV^2 and $\tan^2\theta_{12} = 0.47^{+0.06}_{-0.05}$ [22].

1.3 Introduction to Nuclear Georeactor Hypothesis

It has been proposed by J.M.Herndon [1] that there could be enough ^{235}U and ^{238}U at the center of the Earth that started a natural fast breeder type nuclear reactor from 4.5 billion years ago, and sustained until present. This "georeactor" provides a source of energy that can last for a geological time scale, and possibly powers the geomagnetic fields. The georeactor model also provides alternative ways to explain the irregular geomagnetic field reversal and the ^{3}He/^{4}He anomaly problem [55]. On the other hand, this model is in contradictory with the traditional Bulk Silicate Earth (BSE) model, which disfavors any significant Uranium content in the Earth core. Although not popular in the Earth science literature, the georeactor hypothesis itself is self-consistent and is possible to be tested with a large $\bar{\nu}_e$ detector such as KamLAND.

1.3.1 Nuclear Earth Model and Substructure of the Inner Core

The Earth's chemical composition has been studied with various methods such as direct sampling from bore-holes and xenolith from lava flows, but these samples are all from above the upper mantle of the Earth. It is assumed that the the composition of non-volatile elements in the Earth should be similar to the composition of the Sun's outer layer (solar abundance), since they are formed in the same process as the entire solar system. Studies of the meteorites showed that the type I carbonaceous chondrites have very similar composition as to the solar abundance, thus they should also represent the composition of the bulk Earth in its early formation stage. This formed the basis of the traditional BSE model. In this model, the inner core of the

Earth consists of partially crystallized iron and nickel, and it is surrounded by a fluid outer core of iron, nickel and some light elements such as S, O or Si. The bulk of the Earth has the similar composition as the the type I carbonaceous chondrites, which is formed in oxygen-rich environment, and most elements formed oxide. The U and Th, being lithophile elements, like to bond with oxygen in silicates and oxides but not with metallic iron, so they can only exist in the mantle and crust.

An alternative model called "Nuclear Earth Model" was proposed by Herndon [1, 56], and the central idea is that the main composition of the bulk Earth is more similar to the enstatite chondrites (also known as E-type chondrites), which is formed under oxygen-deficient conditions and has much less oxidation. Only five elements (Fe, Mg, Si, O, S) constitute approximately 95% of the mass of each of the hundreds of known anhydrous chondrites. Herndon plotted [56] the mass ratio of metal+sulfides to silicates as a function of whole-rock molar ratio of oxygen to the three major elements (Fe, Mg, Si) with which oxygen forms compounds in anhydrous chondrites, as shown in Fig. 1.13. The core-to-mantle ratios for the earth, calculated from seismic-based data [57], show that the Earth as a whole has a state of oxidation similar to certain highly reduced enstatite chondrites (particularly the Abee enstatite chondrite) and unlike most other types of chondrites.

One prediction of the "Nuclear Earth Model" that Earth being of enstatite chondrite composition, contradictory of of the BSE model, is that the inner core of the Earth is not composed of iron-nickel metal but of nickel silicide (mainly Ni_2Si, also known as perryite), as has been found in enstatite meteorites. The normal lithophile elements such as Si, Mg, Ca and U under oxygen-deficient conditions now occur in part as non-oxides, for example sulfides, and together with S, Fe and Ni constitute the alloy portion correspond to the Earth's core. These alloy elements precipitate under gravity and one would expect the low-density precipitates such as CaS and MgS being at the core-mantle boundary, and high-density, high-temperature precipitates, most

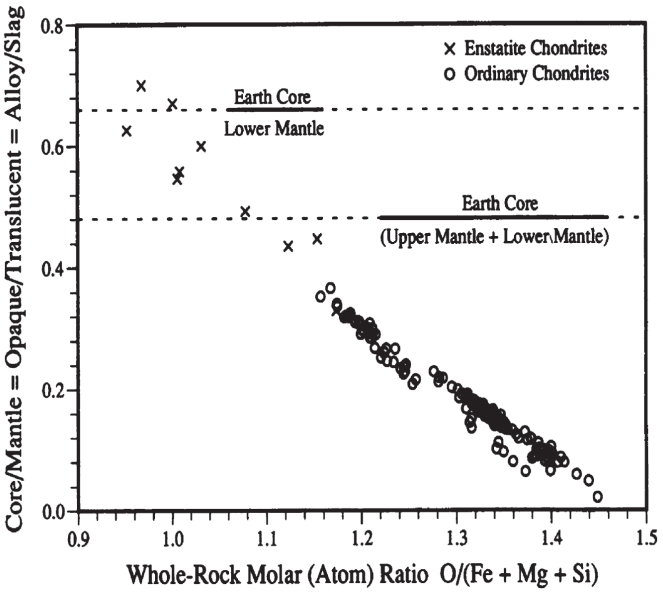

Figure 1.13: Mass ratio of (metal+sulfides) to silicates as a function of whole-rock molar ratio of oxygen to the three major elements with which oxygen forms compounds in anhydrous chondrites. the core to lower mantle ratio and the core to (upper+lower) mantle ratio are indicated by the broken lines. Figure taken from [56].

importantly uranium or its compound (mainly monosulfides), being collected at the center of the Earth. This creates an inner core substructure as shown in Fig. 1.14. The difference of the chemical composition of the Earth between the traditional BSE model and the "Nuclear Earth Model" is graphically shown in Fig. 1.15, taken from the August 2002 issue of *Discover* magazine.

1.3.2 Georeactor Feasibility

The concentration of Uranium at the center of the earth provides the feasibility of the existence of a natural self-sustaining nuclear fission reactor, or "georeactor," as suggested by Herndon [1]. The $^{235}U/^{238}U$ ratio, being $\sim$0.7% now, was much higher at the beginning life of the Earth 4.5 billion years ago because ^{235}U has a shorter half-life (0.7 billion years) than ^{238}U (4.5 billion years). With enough uranium collected at the center, a self-sustaining chain of nuclear fission reactions is possible to happen.

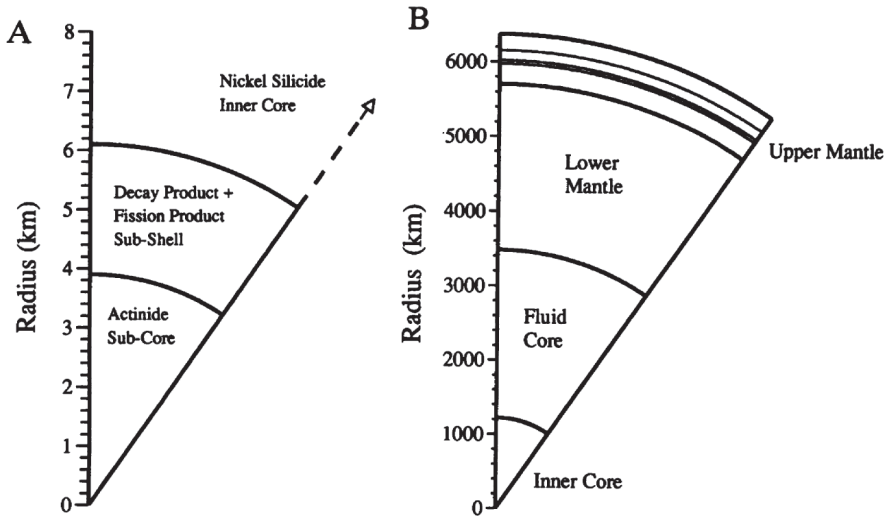

Figure 1.14: (A) Schematic representation of inner-core substructure, calculated with uranium assumed to be the mono-sulfide, present in the same relative proportion as in the alloy portion of the Abee enstatite chondrite. (B) Shell structure of the interior of the Earth. [57], shown for reference. Figure taken from [56].

Lacking of low atomic mass elements severed as neutron moderators at the center, the georeactor operates more similar to a fast breeder reactor. The fission production is mostly from ^{235}U, and partially from ^{238}U fast neutron fissions. The ^{235}U fuel is bred by ^{238}U by the following fuel production reactions, which regenerate ^{235}U that would otherwise be lost due to α decay:

$$^{238}\mathrm{U}(n,\gamma)^{239}\mathrm{U}(\beta^-)^{239}\mathrm{Np}(\beta^-)^{239}\mathrm{Pu}(\alpha)^{235}\mathrm{U} \tag{1.41}$$

Numerical simulations has been performed [60, 59] using the SAS2 sequence contained in the SCALE Code Package form Oak Ridge National Laboratory [61]. The code performs a 1-D transport analysis at selected time intervals, calculating the energy flux spectrum, updating the time-dependent weighted cross sections from the depletion analysis, and calculating the neutron multiplication factor K_{eff} of the system. The nuclear georeactor is assumed to start 4.5 billion years ago, and would cease operation when $K_{\mathrm{eff}} < 1$. All fission products were assumed to be removed upon for-

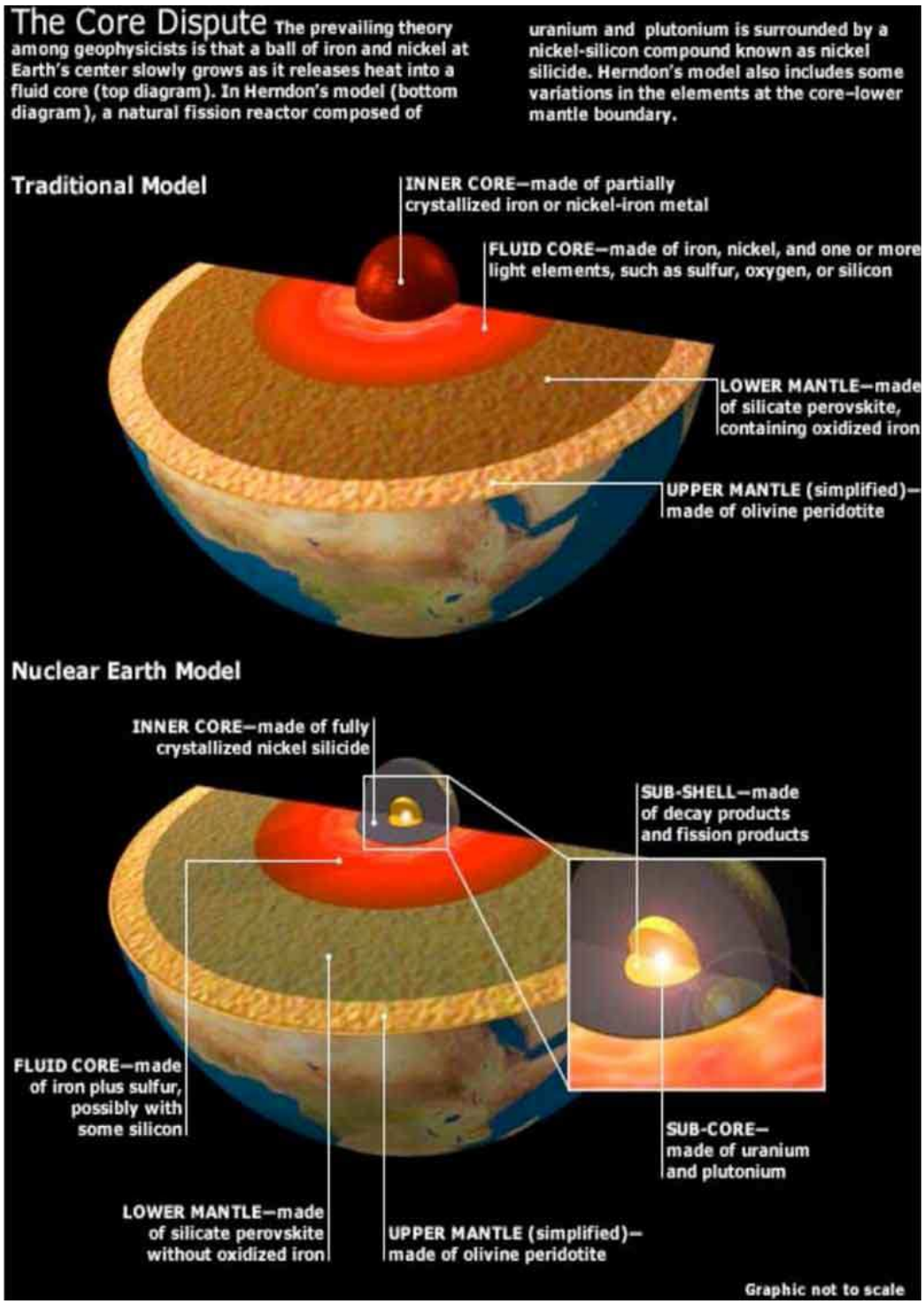

Figure 1.15: The difference of shell structure of the Earth between the traditional Earth model and the "Nuclear Earth Model." Figure taken from [58].

Table 1.2: Summary of Simulation of Georeactor with SAS2 Code. Table reformatted from [59].

Nuclide	4 TW Simulation	30 TW Simulation
Initial Mass (4.5 billion years ago) [kg]		
^{235}U	4.8672×10^{15}	2.1039×10^{16}
^{238}U	1.6060×10^{16}	6.9427×10^{16}
Present Day Fission Fraction		
^{235}U	7.46×10^{-1}	7.60×10^{-1}
^{238}U	2.49×10^{-1}	2.28×10^{-1}
^{233}U	2.60×10^{-3}	6.90×10^{-3}
^{236}U	1.38×10^{-3}	3.97×10^{-3}
^{232}Th	5.63×10^{-4}	5.77×10^{-4}
^{239}Pu	1.70×10^{-4}	3.53×10^{-4}
^{241}Pu	1.11×10^{-17}	1.97×10^{-16}

mation. As a result from the simulation, Hollenbach and Herndon showed that [60] the $K_{eff} > 1$ condition can be sustained for the whole Earth's age, and that K_{eff} and $^{235}U/^{238}U$ ratio are stabilized after reaching some minimum values at about 3 billion years ago. The maximum steady-state fission power is determined to be 30 TW, using the maximum uranium content at 4.5 billion years ago. A 4 TW simulation is also performed for reference, using a smaller amount of initial uranium. The input parameters to the simulation and the resulting present day fission fractions of selected isotopes are summarized in Table 1.2. One notable observation is that the ^{235}U and ^{238}U together contribute to ∼99% of the present-day georeactor fission[6]. This is very different from the common thermal neutron fission reactors. For example, the relative fission rate of typical reactor cores relevant to KamLAND experiment (mostly BWR and PWR) is $^{235}U : {}^{238}U : {}^{239}Pu : {}^{241}Pu = 0.56 : 0.08 : 0.30 : 0.06$, as will be discussed in Section 5.1.

As a supporting evidence, the uranium ore deposits found at Oklo (in Republic of Gabon, Africa) in 1972 are believed to be functioning at 2 billion years ago as a natural nuclear fission reactor (Bodu et al.,1972). The ^{235}U concentration in these

[6]There are other simulations that produce different fission fraction predictions, for example in Ref. [62]

samples is only 0.7171%, while the normal concentration should be $0.7202 \pm 0.0006\%$. The depletion of ^{235}U resembles the used nuclear fuel from nuclear reactors. It has been shown [63] that besides functioning as a thermal neutron reactor moderated by underground water, the Oklo reactor also functioned as a fast-neutron breeder reactor. The existence of Oklo reactor demonstrates the possibility of naturally occurring nuclear fission reactors.

1.3.3 Georeactor Implication

Herndon suggested a few implications of the existence of a georeactor at the Earth's core. One prediction is that the georeactor serves as the the energy source to sustain the geomagnetic field, and interruption of georeactor operation is the cause of the geomagnetic field reversals. The Earth's magnetic field is known to have existed for at least 2.7 billion years from the studies of the oldest rock samples. It extends a few tens of thousands of kilometers into space, known as magnetosphere, and shields the the surface of the Earth from charged particles of the solar wind. The geomagnetic field is approximately a magnetic dipole inclined by $\sim$11.3° relative to Earth's axis of rotation. The cause of the geomagnetic field is traditionally explained by the *dynamo theory* [64], stating that the rotating, convecting and electrically conducting fluid iron outer core acts to maintain the geomagnetic fields. The energy needed to sustain such geodynamo is at least 0.02 TW [65]. Herndon proposed [1] that this energy is primarily produced by the georeactor at the Earth center, with the inner core serving as heat sink, through which heat is transferred to the base of the fluid shell, creating thermal convection in the electrically conducting fluid core that generates the geomagnetic field.

The direction of the geomagnetic field, based on the study of lava flows of basalt, is known to reverse very irregularly, with average intervals of $\sim$250,000 years. The last reversal happened about 780,000 years ago. Simulation of the dynamo theory [66]

showed that the convection of the fluid core is constantly trying to reverse the field, while the inner core tries to prevent it. The frequency of the the simulated reversal, however, is ∼100,000 years and seems to be slightly too high. Herndon proposed an alternative explanation [1, 60] from the georeactor hypothesis, stating that the georeactor could be temporarily shut down if some fission fragments such as ^{149}Sm, which have a high neutron capture cross section and would poison the reactor, are not removed out of the sub-core region readily. After a period of time for the reactor poisons to diffuse to regions of lower density, the reactor output would resume, and the Earth's magnetic field would re-establish itself, either in the same direction or in the reverse direction.

Herndon also proposed that the georeactor is the origin of the ^{3}He/^{4}He anomaly problem [60, 55]. The atmospheric ^{3}He/^{4}He ratio is measured to be $R_A = 1.4 \times 10^{-6}$. It is discovered that Helium is venting from the Earth's interior [67], but the ^{3}He/^{4}He ratio of the helium released to the oceans at mid-oceanic ridges is about 8 R_A. Iceland plume ^{3}He/^{4}He ratio is found to be as high as 37 R_A. The extra ^{3}He from the Earth's interior is traditionally believed to be of primordial origin, that the ^{3}He was trapped within the mantle at the time that the Earth formed and not well outgassed. The primordial ^{3}He/^{4}He ratio however is about 100 R_A, inferred from gas-rich meteorites [68], which is too high compared with the helium released from the Earth's interior. The dilution is generally assumed to be from the ^{4}He produced by the natural radioactive decay of U and Th in the mantle and the crust. Hollenbach and Herndon instead suggested [60] that the extra ^{3}He is the product and evidence of the georeactor, since ^{3}H being one of the fission products decays to ^{3}He, which could possibly travel out of the core region and being outgassed. A simulation with the SAS2 code [61] yields the similar present-day ^{3}He/^{4}He as those measured from the basalts along the global spreading ridge system, at about 4 – 8 R_A [55].

1.4 Motivation for a Combined Analysis

One inevitable consequence of the georeactor hypothesis is the $\bar{\nu}_e$ flux coming out from the Earth core. Being the largest $\bar{\nu}_e$ detector on the Earth, KamLAND is well suited to measure this flux, or setting a limit of the georeactor power if the flux is not observed. A 10 TW hypothetical georeactor produces ∼30 events/year (oscillated) at KamLAND with the detector's efficiency (∼0.88) and ∼700 tons of fiducial mass (details discussed in Section 5.2). On the other hand, KamLAND is optimized to measure the $\bar{\nu}_e$ flux from the man-made reactors, which unfortunately becomes background source for georeactor $\bar{\nu}_e$ flux measurements. However, the neutrino oscillation causes a difference in $\bar{\nu}_e$ spectrum shape between man-made reactors and georeactor, allowing disentanglement of the two. Furthermore, the total man-made reactor power varies with time from the maintenance and refueling of different reactors. In Fig. 5.3 we can see that the maximum variation can be as large as a factor of three. A notable period of low reactor power since the summer of 2007 is due to the shutdown of the 25 GWth Kashiwazaki nuclear power plants after an earthquake of magnitude 6.8 striking in Niigata prefecture. The time variation of $\bar{\nu}_e$ flux from man-made reactors can be distinguished from the georeactor, which is assumed to provide a constant power output over the time scale of the KamLAND experiment.

The measured total heat flow from the Earth puts an upper limit on the georeactor thermal power to be 44.2 ± 1.0 TW [69]. A more recent evaluation of the same data (assuming much lower hydrothermal heat flow near mid-ocean ridges) however led to a lower value of 31 ± 1 TW [70]. From the study of chondrites the calculated radiogenic power (from the decay chains of natural radioactivities of ^{238}U, ^{232}Th and ^{40}K in the Earth) is thought to be 19 TW [18], a value that can be measured by KamLAND but currently limited by statistics [21]. Some other models of mantle convection suggest that radiogenic power is a larger fraction of the total power [19, 20]. On the other

hand, the georeactor theory itself does not have a well-predicted output power. The maximum steady-state fission power is determined to be 30 TW, using the maximum uranium content at 4.5 billion years ago [59]. The current poor constrain on the georeactor power can be much improved with KamLAND's large sample of $\bar{\nu}_e$ events from about 5 years of data-taking.

The $\bar{\nu}_e$'s coming out of the center of Earth follows the same neutrino oscillation physics laws as all other neutrinos do. A combined analysis of georeactor and neutrino oscillation is thus inevitable. On the other hand, this analysis is in turn going to put a stronger test of the neutrino oscillation theory, and demonstrating whether or not a significant change in the current best-fit neutrino oscillation results is needed by including the georeactor hypothesis. Similar work has been done before with either fewer statistics or lack of full treatment of systematic uncertainties [71, 72], issues that this dissertation is trying to resolve and improve.

Chapter 2 The KamLAND Experiment

KamLAND (Kamioka Liquid Scintillator Anti-Neutrino Detector) experiment is located in the Kamioka Underground Laboratory under the peak of Mt. Ikenoyama (36.42 °N, 137.31 °E) in Gifu Prefecture, Japan, about 50 km south of the city of Toyama. The experiment site is in the middle of Japan and surrounded by ∼55 nuclear reactor cores with total thermal power ∼130 GW and a flux weighted average distance ∼180 km. This puts KamLAND in an optimal position to directly observe the neutrino oscillation in vacuum associated with LMA-MSW solution (Section 1.2.2). KamLAND has been taking data since January 2002, and has made major discoveries in various scopes of science ever since.

2.1 Anti-neutrino Detection Method

KamLAND is a liquid scintillator detector for detecting energetic particles. The energy loss mechanism in matter varies with particle types [7], but eventually (part of) the energy of the particle is transfered to the free valence electrons of the scintillator molecules, and excite them from the lowest states (S_0) to the excited states (S^*, S^{**}). The excitations decay immediately to the S^* state without the emission of radiation ("internal degradation"). The S^* state then decays to one of the vibrational states of S_0, with emission of "fluorescence" photons. The fluorescence photon travels through the detector with the probability of incident on a photomultiplier tube (PMT) in the end. The PMT converts the light into a weak current of photoelectrons which is then further amplified by and electron-multiplier system. The resulting current signal is then analyzed by the dedicated electronics system.

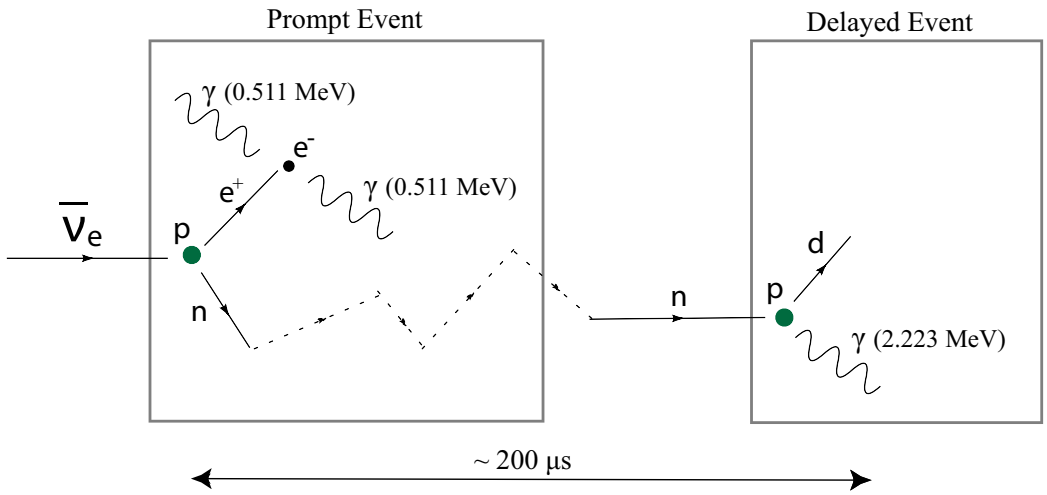

Figure 2.1: Illustration of how KamLAND detects $\bar{\nu}_e$ from inverse beta decay reaction. The prompt event from positron annihilation and the delayed events from neutron capture are correlated in $\sim 200\mu$s.

Due to the extremely weak interactions between (anti-)neutrinos and matter, KamLAND only detects $\bar{\nu}_e$ through a specific channel called *inverse beta decay*:

$$\bar{\nu}_e + \mathrm{p} \rightarrow \mathrm{n} + \mathrm{e}^+ \tag{2.1}$$

The reaction generates a neutron and a positron. The positron quickly deposits its energy (together with two annihilation γ's) in the detector and gets detected as a "prompt" event. The neutron loses its energy primarily by elastically scattering on ^{1}H ("thermalizes") until reaching thermal energy, then gets captured by ^{1}H and emits a 2.2 MeV γ-ray. The capture time follows an exponential distribution with mean capture time $\sim$206 μs (Section 4.6), so this 2.2 MeV γ-ray is detected as a "delayed" event. Fig. 2.1 shows a visual description of this process. KamLAND detects $\bar{\nu}_e$'s from reactors at a very low rate less than 1 per day, however, the "prompt-delay" coincidence signature is unique to $\bar{\nu}_e$ events and makes $\bar{\nu}_e$ detection possible even with background event rate millions times higher. Details of the $\bar{\nu}_e$ signals and backgrounds will be discussed in Chapters 4 and 5

The energy of the $\bar{\nu}_e$ must be above a threshold for the inverse beta decay reaction to happen, and is given by:

$$E_{\text{threshold}} = \frac{(M_n + M_e)^2 - M_p^2}{2M_p} = 1.806\,[\text{MeV}] \tag{2.2}$$

The cross section of inverse beta decay is given in Ref. [73] and is shown as a function of $\bar{\nu}_e$ energy in Fig. 5.2. The cross section can be expressed, neglecting terms of order of E_ν/M, in terms of the neutron lifetime and the phase-space factor $f^R_{p.s.} = 1.7152$ [74] as

$$\sigma^{(0)}_{\text{tot}} = \frac{2\pi^2/m_e^5}{f^R_{p.s.}\tau_n} E_e^{(0)} p_e^{(0)} \tag{2.3}$$

In this way, the cross section is tied directly to the neutron lifetime, known to 0.1% [7]. The small (order E_ν/M) energy-dependent outer radiative corrections to σ_{tot} [75, 76] are not negligible and are included in the calculation shown in Fig. 5.2. The total systematic uncertainty from the inverse beta decay cross section is estimated to be 0.2%.

The energy of the $\bar{\nu}_e$ can be calculated from the total energy of the prompt event, which includes the kinetic energy of the positron and two 0.511 MeV gamma-rays, as follows:

$$\begin{aligned} E_{\bar{\nu}_e} &= M_n + T_n + m_e + T_{e^+} - M_p \\ &= T_{e^+} + 2m_e + T_n + (M_n - M_p - m_e) \\ &= E_{\text{prompt}} + T_n + 0.782\,[\text{MeV}] \end{aligned} \tag{2.4}$$

The neutron recoil energy T_n depends on the scattering angle, and in current analysis the average $\langle \cos\theta \rangle$ from the positron angular distribution of inverse beta decay [73] is used. T_n is in average only $\sim$10 KeV though so it can be safely neglected.

Detection of $\bar{\nu}_e$ events at KamLAND gives a real-time measurement of the $\bar{\nu}_e$ flux

and its energy spectrum, which can be expressed by:

$$\frac{\mathrm{d}^2 N_{\bar{\nu}_e}(E_p,t)}{\mathrm{d}E_p \mathrm{d}t} = \int_0^\infty \mathrm{d}E'_{\bar{\nu}_e}\, R(E_p, E'_{\bar{\nu}_e}) \varepsilon(E_p) n_{\mathrm{target}} \sigma(E'_{\bar{\nu}_e}) \cdot \cdot \sum_i^{\mathrm{sources}} f_i(E'_{\bar{\nu}_e}, t) P_{\bar{\nu}_e \to \bar{\nu}_e}(E'_{\bar{\nu}_e}; \Delta m^2_{21}, \theta_{12}) \quad (2.5)$$

where E_p is the prompt energy deposited in the detector by the $\bar{\nu}_e$ event. $R(E_p, E'_{\bar{\nu}_e})$ is the detector energy response function, including both the conversion function from $\bar{\nu}_e$ energy to prompt energy (Eqn. 2.4) and the detector energy resolution function. $\varepsilon(E_p)$ is the possible energy dependent detection efficiency. n_{target} is the total number of target protons. $\sigma(E'_{\bar{\nu}_e})$ is the inverse beta decay cross section. $f_i(E'_{\bar{\nu}_e}, t)$ is the instantaneous flux of $\bar{\nu}_e$ source i at KamLAND, which includes $\bar{\nu}_e$'s from nuclear reactors, the hypothetical georeactor and various background events that mimic the $\bar{\nu}_e$ event (Chapter 5). $P_{\bar{\nu}_e \to \bar{\nu}_e}(E'_{\bar{\nu}_e}; \Delta m^2_{21}, \theta_{12})$ is the energy dependent $\bar{\nu}_e$ survival probability given by Eqn. 1.11. Equation 2.5 will be used to extract the neutrino oscillation parameters Δm^2_{21} and $\tan^2\theta_{12}$ from the KamLAND data.

2.2 Detector

KamLAND detector is located in the Kamioka Underground Laboratory under the peak of Mt. Ikenoyama in the existing cavity built for the old Kamiokande detector. The average vertical rock overburden is 2700 meter water equivalent (m.w.e), which reduces the cosmic-ray muon rate by a factor of $\sim 10^5$ compared to at the surface [77] to about 0.34 Hz in the detector. Besides the detector itself, other facilities such as liquid scintillator purification system, water system, material counting facilities, etc, are also located onsite as shown in Fig. 2.2.

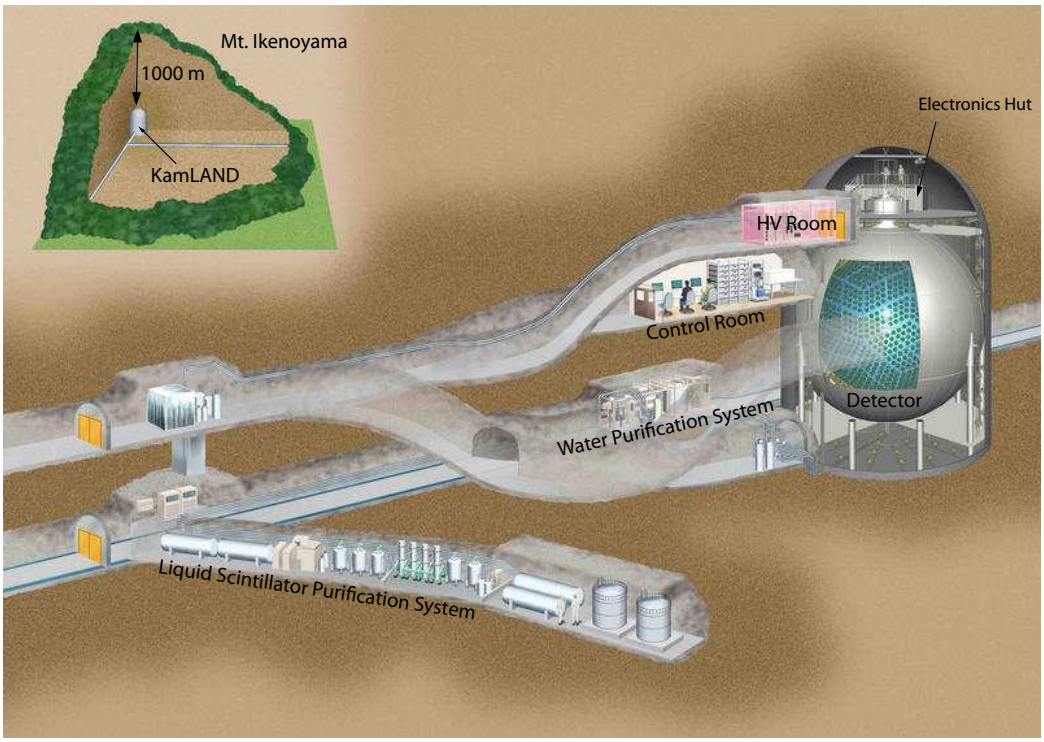

Figure 2.2: KamLAND Site

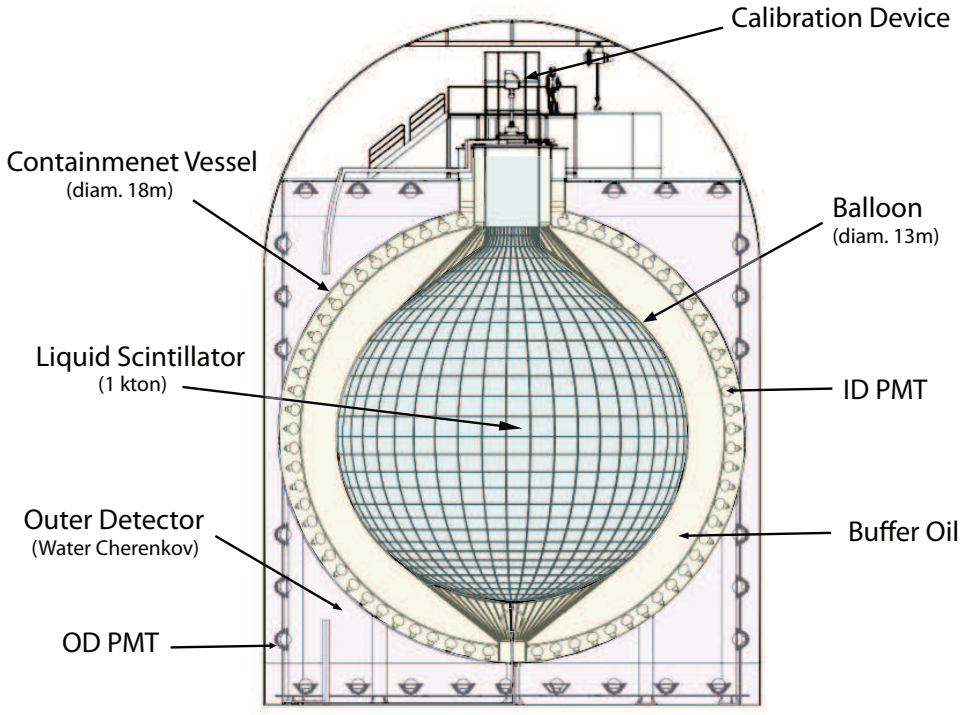

Figure 2.3: Schematic Diagram of the KamLAND detector.

2.2.1 Detector Design Overview

Fig. 2.3 shows the the schematic diagram of the KamLAND detector. The primary active region for neutrino detection is ∼1 kton of ultra-pure *liquid scintillator* (LS) at the center of the detector contained in a 13m diameter spherical balloon made of 135 μm thick transparent nylon/EVOH (ethylene vinyl alcohol copolymer) composite film and supported by a network of Kevlar ropes. The region between the balloon and the surrounding 18m diameter spherical stainless steel outer vessel is filled with ∼ 1800 m^3 *buffer oil* (BO) comprising of 57% isoparaffin and 43% dodecane to shield the LS from external radiations. An array of 1325 17-inch photomultiplier tubes (PMTs) and 554 20-inch PMTs are mounted on the inner surface of the outer containment vessel, providing 34% photocathode coverage (22% with 17-inch PMTs only). A 3mm thick spherical acrylic barrier at 16.6m diameter helps preventing Rn emanating from the PMT glass from entering the BO. The LS and BO regions together make up the *inner detector* (ID). The stainless steel vessel is surrounded by a 3.2 kton water Cherenkov detector instrumented with 225 20-inch PMTs, which is called *outer detector* (OD). The OD absorbs external γ-rays and neutrons from surrounding rock and enables the tagging and veto of cosmic-ray muons. On the top of the detector is the calibration device. Calibration sources can be lowered through the concentric *chimney* region into the LS.

2.2.2 Detector Properties

Liquid Scintillator

KamLAND liquid scintillator comprises of 80.2% normal-paraffin (Dodecane, $C_{12}H_{26}$, 0.7526 g/cm^3 at 15 °C) and 19.8% pseudocumene (1,2,4-Trimetthylbenzene, C_9H_{12}, 0.8796 g/cm^3 at 15 °C) by volume, and 1.36 ± 0.03 g/liter of the fluor PPO (2,5-Diphyenyloxazole, $C_{15}H_{11}NO$). The density of the LS is measured to be 0.7775 g/cm^3

at 15 °C (further discussion in Section 4.4). Pseudocumene is an aromatic solvent with flashing point at 54 °C. The adding of normal-paraffin increases the flashing point of the LS to 64 °C, above the (60 °C) requirement mandated by the mine operations. High purity nitrogen flow is kept on the top of the LS to prevent the oxygenation. The LS composition is adjusted to maximize the light yield for central events. The actual light output is 49% anthracene (8300 photons/MeV). The attenuation length of the LS is measured to be 10 meter at 400 nm wavelength. The light yield is ∼300 p.e./MeV for 17-inch PMTs only and ∼500 p.e./MeV for 17+20-inch PMTs. For more details of the LS properties refer to Ref. [78].

The LS is designed to have good pulse-shape discrimination (PSD) between scintillation produced by α particles, γ-rays and neutron recoils at the Test Bench Facility [78], so that further suppression of background is possible. Unfortunately, probably due to the large size of the KamLAND detector and the absorption and re-emission of the light, the PSD is not obvious from the actual KamLAND data [79] and is not implemented in the analysis described in this dissertation.

Buffer Oil

The buffer oil comprises of 57% isoparaffin (C_nH_{2n} , n∼14) and 43% normal-paraffin and is contained in a 18m diameter stainless steel vessel, separated from the LS region by the balloon. The BO shields the LS from external radiations such as from PMT glass and the stainless steel, and attenuates spallation products outside of the LS. The density difference between the LS and the BO is less than 0.04 % to maintain the spherical balloon shape. The index of refraction is 1.46 in the LS and 1% lower in the BO at 400 nm.

To reduce the internal radioactivities mainly from decay chains of ^{238}U, ^{232}Th and ^{40}K (Appendix B), both LS and BO are purified before filling into the detector. Techniques such as ultra-filtration, water extraction and nitrogen purge are utilized [80].

Table 2.1 summarizes the measured radioactivities of the LS and BO after the purification. Activities of ^{238}U, ^{232}Th and ^{40}K in the LS are measured by KamLAND detector itself with event tagging. Radioactivities of the BO are measured by the neutron activation analysis (NAA) [81]. Both meet the low background requirement for $\bar{\nu}_e$ detection.

Table 2.1: Radioactivities of ^{238}U, ^{232}Th and ^{40}K for selected materials in KamLAND.

Material	^{238}U	^{232}Th	^{40}K
Concentration			
LS [g/g]	2.7×10^{-18}	6.1×10^{-17}	1.7×10^{-16}
BO [g/g]	$< 8 \times 10^{-15}$	$< 2.8 \times 10^{-15}$	$< 1.3 \times 10^{-15}$
Balloon [ppb]	0.018	0.014	0.27
Rope [ppb]	0.08	0.8	1.2
PMT Glass [ppb]	150	240	10
SUS Tank [ppb]	0.5	0.7	0.1
Rock [ppb]	$\sim$1000	$\sim$2500	$\sim$2000
Activity			
LS [Bq/m^3]	2.6×10^{-8}	1.2×10^{-7}	3.5×10^{-5}
BO [Bq/m^3]	$< 7.7 \times 10^{-5}$	$< 5.5 \times 10^{-6}$	$< 2.7 \times 10^{-4}$
Balloon [Bq]	0.02	0.006	7.2
Rope [Bq]	0.1	0.33	31

Balloon and Ropes

The KamLAND balloon, which separates the LS region and BO region, is made of a five-layer composite film as EVOH/nylon/nylon/nylon/EVOH, with total thickness of 135 μm. The nylon provides strength and compatibility with the oil and scintillator, and the EVOH has very small gas permeability so it is used to protect the LS against the diffusion of ambient radon from the surrounding components. The light transparency of the balloon is more than 90%. There are 44 longitudinal and 30 lateral Kevlar (a light strong para-aramid synthetic fiber) ropes to support the balloon and keep the balloon's spherical shape. The tension of the ropes is monitored by a set of load cells at the top of the detector. The liquid levels of the LS and the BO are also

carefully monitored to keep enough pressure inside the balloon to maintain its shape. The radioactivities of the balloon and the Kevlar ropes are measured by inductively coupled plasma mass spectrometry (ICP-MS), and are summarized in Table 2.1.

Thermometers

Three thermometers were initially attached at the top, center and bottom of a vertical 3.5 mm diameter teflon cable slightly off the central z-axis of the detector, reaching into the 5.5m radius inside the LS. The cable and the attached thermometers were later removed on 19 April 2004 because of their slightly high radioactivities seen by the KamLAND detector.

Photomultiplier Tubes

The ID has 1325 specially developed fast PMTs (Hamamatsu R7250) masked to 17-inch diameter and 554 older 20-inch diameter PMTs (Hamamatsu R3600) reused from the Kamiokande experiment [82]. The 20-inch PMTs were not operated until after 27 February 2003. The 20-inch PMT uses venetian-blind type dynode shape and its time-transit-spread (TTS) is $\sim$5.5 ns. The 17-inch PMT uses line-focus type dynode shape and improves the TTS to $\sim$3 ns. The peak-to-valley ratio is also improved from $\sim$1.5 to $\sim$3.0. The quantum efficiency is about 22% in the wavelength from 350 nm to 400 nm.

Earth's magnetic field ($\sim$0.5 Gauss) affects the electrons' trajectories and degrades the PMT gain. A set of compensating coils is placed in the cavern surrounding the detector to cancel the magnetic field to a level well below the 50-mGauss limit necessary for proper operation of the PMTs.

Water Cherenkov Outer Detector

The OD water comes from a fountain spot and goes through the "natural" filter of the 1000m rock of Mt. Ikenoyama to reach KamLAND. It is constantly circulated at ∼5 tons/hour by the water purification system with ultra-filtration, reverse osmosis (RO) membrane, and UV sterilizer system before sending to KamLAND. The ^{238}U and ^{232}Th concentration in the water has been measured by ICP-MS to be both less than 0.5 ppt [81]. The Rn activity however is high in the water at ∼10,000 Bq/ton. The temperature of the water is quite stable ($\sim 10\,^{\circ}$C), and circulation of OD water removes excess heat produced by the PMTs in the ID and OD.

The OD is divided by the stainless steel containment vessel and Tyvek plastic sheets into four optically separate sections: top, upper, lower and bottom, mounted with 50, 60, 60 and 55 20-inch PMTs (same type 20-inch PMTs as in the ID) respectively. The OD detects cosmic-ray muons by the Cherenkov light they produced when passing through the water. The Tyvek sheets are highly reflective to optimize the light collection in each section. The tagging of muon by the OD provide extra veto against muon spallation background (Section 4.3).

Muon Tracker

A muon tracking system is installed in September 2008 on top of the KamLAND detector to track a subset of the muons incident onto the KamLAND detector. This helps to measure the OD muon tagging efficiency, and calibrate the muon reconstruction algorithms (Section 3.5). The muon tracker consists of 48 multiwire proportional chambers (MWPCs) with an active area of 5.4 m^2. It is triggered by coincidence of two plastic scintillator planes mounted on top of the higher and lower planes of MWPCs, whose relative positions are set up to be movable to allow a greater range of impact parameters relative to the center of KamLAND detector.

2.2.3 Data Acquisition

Fig. 2.4 shows the schematic diagram of the KamLAND data acquisition flow. The PMTs (or "channels") send their analog signals to the Front End Electronics (FEE) boards, and the decision of whether or not to digitize the signal is made by the trigger system based on the number of "hit" channels ($N_{channels}$) sent to the trigger system by each FEE board. The trigger system also sends a 40 MHz clock signal to each FEE board for synchronization. The DAQ system then reads out the digitized waveforms from the FEE and the trigger records from the trigger system asynchronously, compresses the data and stores them onto the disks. The DAQ also sends the run conditions to the FEE and Trigger system and can change their behaviors based on different situations.

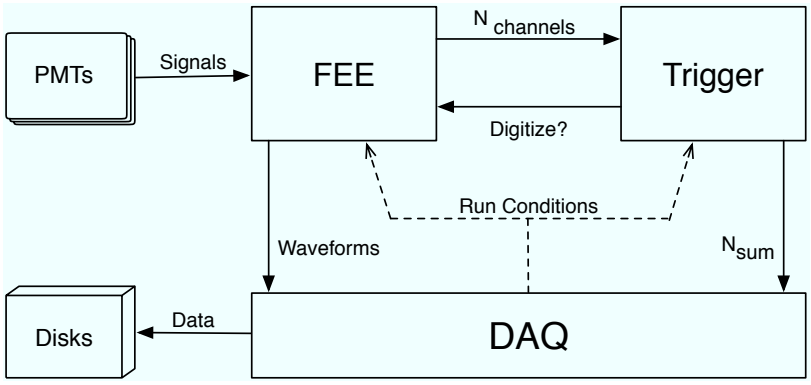

Figure 2.4: Schematic diagram of the KamLAND data acquisition process.

Front End Electronics

The KamLAND FEE system consists of 200 FEE boards hosted in 10 VME crates, and each board supports 12 channels. All FEE boards are running at 40 MHz with the internal clock distributed by the trigger system. The analog PMT signal is split and one copy is sent to a discriminator whose threshold is set at 0.15 p.e. ($\sim$0.3 mV, single p.e. efficiency >95%). The other copy is sent to a delayed line which leads to an Analog Transient Waveform Digitizer (ATWD) [83] chip on the board. If the

signal crosses the discriminator threshold, the ATWD starts to capture the PMT signal in 128 samples at ∼0.65 GHz frequency, resulting in about 200 ns of data in each waveform. The ATWD holds the waveform for 175 ns while awaiting for the trigger decision, based on which the ATWD either erases the waveform within ∼1 μs or digitizes the waveform with a 10-bit ADC in ∼27 μs. To reduce the dead time, each PMT is connected to two ATWDs, so that one can acquire a waveform when the other is busy[1].

Each ATWD has three gains (×20, ×4, ×0.5) so that a wide dynamic range of signals can be recorded. While only the high gain waveform is recorded for a typical low energy event, a high energy particle such as a muon could produce a signal as large as 1 V and saturate the high and medium gain, in which case all three waveforms are recorded[2]. Each waveform is associated with a time-stamp as the number of clock ticks (25 ns) between the start of the run and the the issuing of trigger digitization command. Each waveform is also associated with a clock tick offset of the launching of the ATWD to the trigger command (N_{launch}, which is always ≥ 0 meaning before the trigger). This time information allows for synchronizing all different waveforms and trigger records at a later offline event reconstruction stage. The digitized waveforms from all 12 channels on a FEE board are buffered onto a 32 MB on-board memory and read out through the VME bus by the DAQ system.

Trigger System

The ID PMT's dark rate is on the order of tens of kHz at the set threshold. Since each waveform requires 256 Byte of memory, it is impossible to record all the data from all channels with the current computer technology and resources. Instead, a trigger system was designed at Stanford Univ. with Field Programmable Gate Arrays

[1] A secondary electronics system named MoGURA is designed to have zero dead time through the use of free-running high-speed flash ADCs, and is installed to KamLAND in August 2009.

[2] After Oct 2007, a decision has been made that only the lowest-gain waveform is kept, in order to reduce the data transfer overhead after muon events.

(FPGAs) to allow varying complexity of triggering algorithms, and is responsible for making decisions of whether or not to record the data.

Every clock tick (25 ns) each FEE board sums up the total number of channels ($N_{channels}$) on the board that exceed the discriminator threshold in the past 5 clock ticks (125 ns), and sends to the trigger system. The trigger module calculates the sum of all $N_{channels}$ in each section of the detector: ID ($nsum_{ID}$[3]) and OD ($nsum_{ODtop}$, $nsum_{ODupper}$, $nsum_{ODlower}$, $nsum_{ODbottom}$), compares with different trigger threshold ("trigger type"), and issues digitization command to the ATWD's if the criteria of the trigger type is met. At the same time a trigger record is generated with the time-stamp, trigger type and nsum information, which is read out by the DAQ system separately.

The primary trigger type in KamLAND normal runs is the "prompt trigger," which issues a global acquisition command to FEE boards if $nsum_{ID}$ exceeds 200 or 180 (before and after 13 April 2004, respectively)[4]. This trigger threshold corresponds to ∼0.8 MeV deposited energy. The trigger module also issues "OD trigger" when $nsum_{OD}$ exceeds the threshold set for each OD section (6, 5, 6, 7 for top, upper, lower and bottom section respectively). A special trigger type is the "supernova trigger" for optimizing the detection of the rare supernova events. If the trigger module sees 8 events with $nsum_{ID} > 772$ or 1100 (before and after February 2004, respectively) in ∼0.84 s , it then sets optimal trigger parameters to collect as many supernova candidate events as possible for 1 min before returning to the initial trigger settings, during which the possible manual stopping of the run is disabled. Other common trigger types are listed below. For a complete description of trigger types and trigger electronics refer to Ref. [84, 79].

[3] $nsum_{ID}$ only includes the 17-inch PMTs in the sum.

[4] The trigger thresholds listed are taken from the nominal values used in this analysis periods only. In later runs particularly during the KamLAND solar phase, the thresholds are typically lowered, allowing for more efficiency in acquiring low energy events.

- Delayed Trigger: A global acquisition command to FEE boards if $\text{nsum}_{\text{ID}} > 120$ and a prompt trigger has occurred within 1 ms. This is useful for more efficiency in capturing coincidence events.

- Prescale Trigger: A global acquisition command to FEE boards if nsum_{ID} is above threshold and the absolute time is within the prescale time from the last 1PPS signal. This is useful when the event rate is too high for the DAQ to handle, such as in background runs when very low energy events are recorded.

- 1PPS Trigger: A global acquisition command to FEE boards (can be disabled by DAQ) when the trigger module receives a One Pulse Per Second (1PPS) input from the GPS module.

Some trigger types only output trigger records without issuing acquisition commands to the FEE boards. One example is the "history" trigger record which is generated for up to 8 clock ticks (200 ns) when nsum_{ID} exceeds 120. The maximum value of nsum_{ID} in the train of the history records accompanying an event is called *nsummax*, and is highly correlated with the energy of the event. This nsummax value is very useful in a low-level data analysis independent of the complexities of the event reconstruction algorithms, as will be discussed in later chapters.

KiNOKO DAQ System

The DAQ system is controlled by the KiNOKO software, which stands for "Kinoko Is Network distributed Object-oriented KamLAND Online-system". KiNOKO initializes all the hardware components at the beginning of the run, and sends run conditions to the FEE and trigger systems. KiNOKO asynchronously reads out the data from the FEE and trigger VME crates, compresses the data by a factor of 3 with lossless Huffman encoding [85], and stores the data onto the disks. KiNOKO also does simple online analysis and provides user interfaces for controlling and monitoring the

run behaviors in real time. For detailed information about KiNOKO system refer to Ref. [86].

Other Electronics Systems

In addition to the three main components of data acquisition system , there are some other necessary sub-systems for operating the KamLAND experiment including:

- **Trigger Backup System**: trigger records are duplicated and independently stored by the trigger backup system. This is useful in case the main DAQ system is overwhelmed by the possible high data rate, for example caused by the neutrino burst from a supernova explosion.

- **Absolute Time Acquisition System**: the absolute time is obtained from a Global Positioning System (GPS) receiver located outside of the experimental tunnel, accurate to ∼150 ns. The encoded time is sent to the GPS VME interface through optical fibers and a One Pulse Per Second (1PPS) signal is sent to the trigger system. The absolute time of an event can be calculated with the difference in the time-stamps between an event and its nearest 1PPS trigger. This is useful for (dis-)associating an event with other known astronomical transient events.

For details of the trigger backup system and absolute time acquisition system refer to Ref. [84].

2.2.4 Calibration System

Radioactive sources and light flashers (laser and LED) are periodically deployed into the KamLAND detector by the calibration system in order to understand the properties of the detector such as light output and propagation and to check the detector's stabilities. The calibrations also provide references for the event energy and position

reconstruction algorithms, and are essential to understand the event reconstruction's performances.

Table 2.2 lists the radioactive sources used for KamLAND calibrations. Among them ^{68}Ge, ^{60}Co, ^{203}Hg, ^{137}Cs and ^{65}Zn are γ sources at various energies. Unmoderated ^{241}Am^{9}Be and ^{210}Po^{13}C sources serve to calibrate the detector response to gammas and neutrons. ^{210}Po^{13}C source [87] is also specially used to understand the ^{13}C(α,n)^{16}O reaction, one of the largest background for $\bar{\nu}_e$ detection, in KamLAND (Section 5.4).

Table 2.2: Summary of Radioactive Calibration Sources at KamLAND

Source (half life)	Scheme	Particle Type & Energy [MeV]
^{68}Ge (271 d)	$^{68}\mathrm{Ge} + \mathrm{e}^- \longrightarrow {}^{68}\mathrm{Ga} + \nu_e$	
	$^{68}\mathrm{Ga} \rightarrow {}^{68}\mathrm{Zn} + \mathrm{e}^+ + \nu_e$	2γ (0.511 $\times$2)
^{60}Co (5.3 y)	$^{60}\mathrm{Co} \rightarrow {}^{60}\mathrm{Ni} + \mathrm{e}^- + \bar{\nu}_e$	2γ (1.173 + 1.332)
^{203}Hg (46.6 d)	$^{203}\mathrm{Hg} \rightarrow {}^{203}\mathrm{Ti} + \mathrm{e}^- + \bar{\nu}_e$	γ (0.279)
^{137}Cs (30.1 y)	$^{137}\mathrm{Cs} \rightarrow {}^{137}\mathrm{Ba} + \mathrm{e}^- + \bar{\nu}_e$	γ (0.661)
^{65}Zn (244.3 d)	$^{65}\mathrm{Zn} + \mathrm{e}^- \longrightarrow {}^{65}\mathrm{Cu} + \nu_e$	γ (1.116)
^{241}Am^{9}Be (432.2 y)	$^{241}\mathrm{Am} \rightarrow {}^{237}\mathrm{Np} + \alpha$	
	$\alpha + {}^{9}\mathrm{Be} \rightarrow \mathrm{X} + \mathrm{n}$	neutrons (< 10)
		γ (2.223, 4.945) from n capture
		γ (4.439, 7.654, 9.641) from ^{12}C*
^{210}Po^{13}C (138.4 d)	$^{210}\mathrm{Po} \rightarrow {}^{206}\mathrm{Pb} + \alpha$	
	$\alpha + {}^{13}\mathrm{C} \rightarrow {}^{16}\mathrm{O} + \mathrm{n}$	^{13}C(α,n)^{16}O reaction (Section 5.4)

All parts in the calibration systems that go into the KamLAND liquid scintillator need to be certified as free of radioactivities. This is done at the on-site counting facilities with rigorous certification procedures. Usually parts are soaked in acid solution and samples of the acid are counted with the on-site germanium detector. For details of the on-site material certification refer to Ref. [88].

Z-Axis System

There are two calibration systems used in the KamLAND experiment[5]. Before December 2005, all calibration sources were deployed with the Z-Axis system, which positions the sources along the central z-axis from -6m to 6m relative to the center of KamLAND. The system used a motor to unspool a stainless steel cable and a pulley encoder to measure the amount of cable payed out. The accuracy and the reproducibility of the source position is about 2 – 3 mm.

4π Full Volume System

The 4π full volume system was installed in December 2005, with the purpose of positioning radioactive sources throughout the active volume of the detector and testing the reconstruction performances in the full volume. This is achieved by attaching the sources to a segmented pole which is suspended by two cables near each end of the pole. By changing the relative length of the two cables a sweep in zenith angle can be performed. By rotating the entire glovebox (mounted on a rotary stage) on top of the detector, where the calibration system is stored, a sweep in azimuthal angle can be performed. The absolute position of the source is accurate to less than 5 cm, and the relative position between the sources in the pole segments is accurate to a few mm. For details of the 4π system refer to Ref. [88].

2.3 KamLAND History and Status

2.3.1 Achievements in Reactor Phase

KamLAND finished installing major components and started taking data in January 2002. The period between January 2002 and April 2007 is called *reactor phase*,

[5] A third calibration system named MiniCal was installed in February 2009 to meet more stringent low background requirements in the KamLAND solar phase.

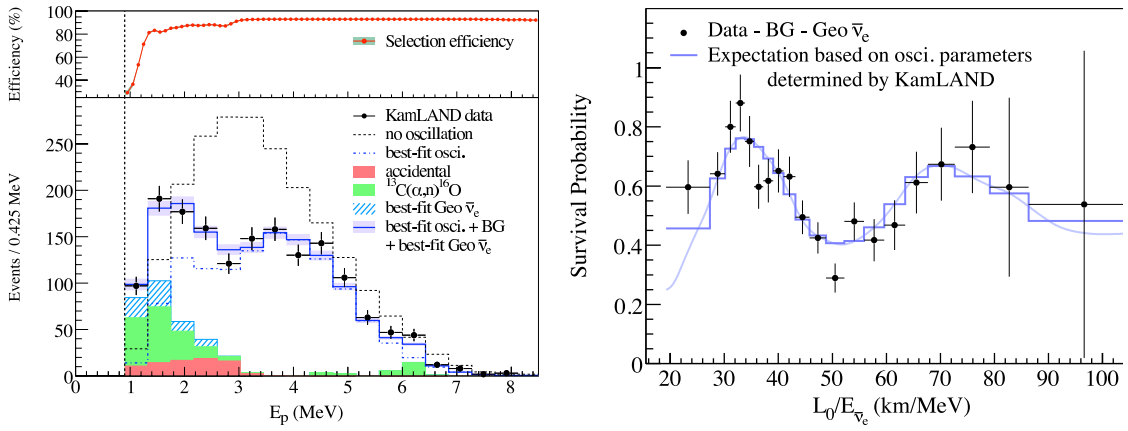

Figure 2.5: Evidence of neutrino oscillation in KamLAND [22] (a) Observed prompt energy spectrum in KamLAND compared with no-oscillation prediction. (b) The ratio of background-subtracted $\bar{\nu}_e$ events to no-oscillation expectation as a function of $L_0/E_{\bar{\nu}_e}$, where $L_0 = 180$ km is the flux-weighted effective baseline.

during when the primary goal is to detect $\bar{\nu}_e$'s from the reactors and study the neutrino oscillation theory. KamLAND has made major discoveries in the reactor phase contributing to various scopes of science including neutrino oscillation, solar anti-neutrino, earth radiogenic heat model, nucleon decay, muon spallation products, etc.

Precision Measurement of Neutrino Oscillation Parameters

KamLAND has established strong evidences of neutrino oscillation by observing a more than 5σ disappearance of reactor $\bar{\nu}_e$ flux and distortion of the reactor $\bar{\nu}_e$ spectrum [45, 46, 22]. Fig. 2.5 ([22]) shows the energy spectrum observed in KamLAND compared with no-oscillation prediction, and the ratio of background-subtracted $\bar{\nu}_e$ events to no-oscillation expectation as a function of $L/E_{\bar{\nu}_e}$. The evidence of spectrum distortion and the oscillatory behavior of the survival probability is clear.

Fig. 2.6 shows the allowed contours in $(\Delta m^2_{21}, \tan^2\theta_{12})$ space, assuming that the neutrino oscillation is the explanation of the observed results. KamLAND alone disfavors the other solar neutrino solutions at 4σ, allowing only the LMA-I region (Section 1.2.2). Combined with the results of solar experiments assuming CPT in-

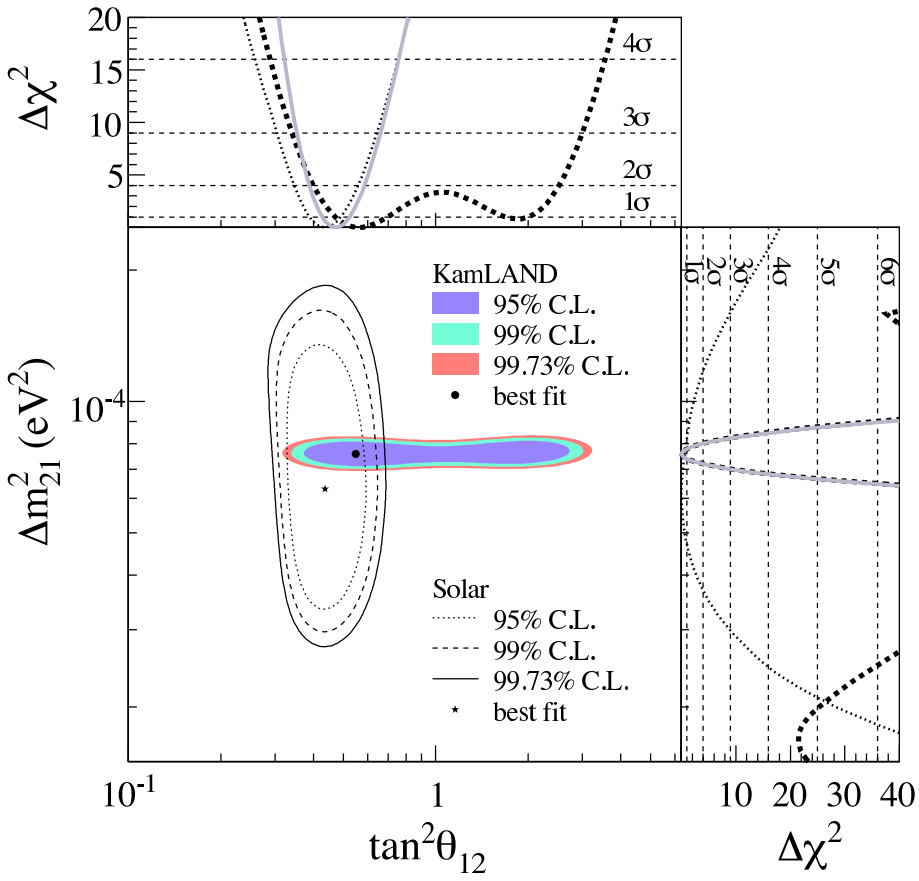

Figure 2.6: Allowed region for neutrino oscillation parameters in KamLAND and solar experiments [22]. The side-panels show the $\Delta\chi^2$-profiles for KamLAND (dashed line), solar experiments (dotted line) and the combination of the two (solid line).

variance, a precision measurement of the neutrino oscillation parameters is achieved as $\Delta m^2_{21} = 7.59^{+0.21}_{-0.21} \times 10^{-5}$ eV^2 and $\tan^2\theta_{12} = 0.47^{+0.06}_{-0.05}$.

High Sensitivity Search for Solar $\bar{\nu}_e$

KamLAND has done a high sensitivity search for $\bar{\nu}_e$ from the sun [13]. There are several conceivable mechanisms which would lead to a $\bar{\nu}_e$ component in the solar flux incident on Earth, such as spin-flavor precession combined with neutrino oscillations and neutrino decay. However the observed $\bar{\nu}_e$ events in the high energy window 8.3 MeV $< E_{\bar{\nu}_e} <$ 14.8 MeV is consistent with the background expectations, which leads to an upper limit of solar $\bar{\nu}_e$ flux of 3.7×10^2 cm^{-2}s^{-1} at 90% C.L. Combined with the

expected solar ^{8}B ν_e flux from Standard Solar Model, this $\bar{\nu}_e$ flux limit corresponds to an upper limit on the neutrino conversion probability of 2.8×10^{-4} at 90% C.L. and represents a factor of 30 improvement over the best previous measurement [89].

Investigation of Terrestrial Anti-neutrino

KamLAND has shown the first indications of the geologically produced $\bar{\nu}_e$'s, or geo-neutrinos, from the decay chains of natural radioactivities (mainly ^{238}U and ^{232}Th) in the Earth [21]. Fig. 2.7 ([21]) shows the observed $\bar{\nu}_e$ energy spectrum in KamLAND especially in the low energy window 1.8 MeV $< \bar{\nu}_e <$ 3.4 MeV where the geo-neutrinos contribute. The data fit well with the expectations from a reference model of 16 TW radiogenic power form ^{238}U and ^{232}Th, which is approximately half of the total measured heat dissipation rate from the Earth. From the data an upper limit of 60 TW for the radiogenic power of U and Th in the Earth is put, a quantity that was previously poorly constrained.

Search for Invisible Neutron Decay

Some of the possible nucleon decay modes are called *invisible modes*, such as $n \rightarrow \nu$'s and $nn \rightarrow \nu$'s, by observing which would indicate new physics beyond the Standard Model. KamLAND has good sensitivity for these invisible modes by searching for single neutron or two neutron intra-nuclear disappearance that would produce holes in the s-shell level of ^{12}C nuclei. The de-excitation of the corresponding daughter nucleus results in a sequence of time and space correlated events. The observed number of such events is consistent with the expectation from accidental coincidence background, which leads to the current best lifetime limits of the invisible nucleon decay mode $\tau(n \rightarrow inv) > 5.8 \times 10^{29}$ years and $\tau(nn \rightarrow inv) > 1.4 \times 10^{30}$ years [90].

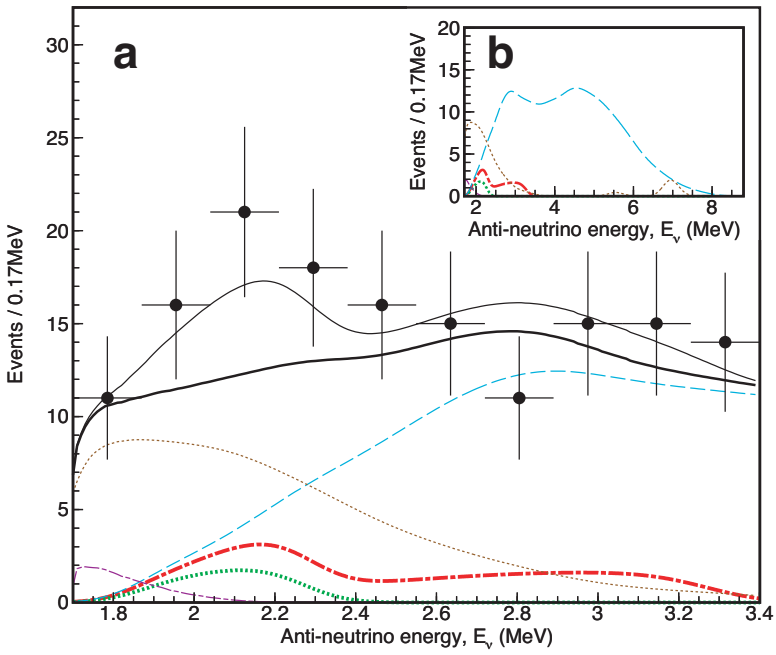

(a)

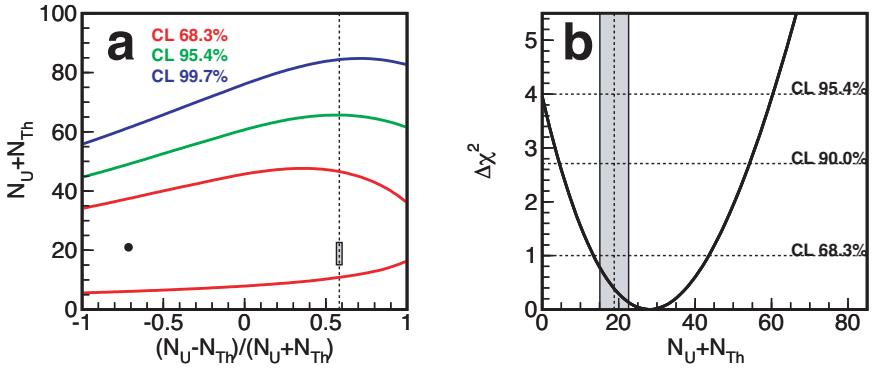

(b)

Figure 2.7: Geo-neutrinos in KamLAND [21]: (a) Observed $\bar{\nu}_e$ energy spectrum in KamLAND (black dots) with the total expectation (thin dotted black line) and total expectation excluding the geoneutrino signal (thick solid black line). The colored lines are expected ^{238}U geoneutrinos (dot-dashed red), expected ^{232}Th geoneutrinos (dotted green), reactor $\bar{\nu}_e$ background (dashed light blue), ^{13}C(α,n)^{16}O background (dotted brown) and random coincidence background (dashed purple). The inset panel extends the spectra to higher energy. (b) Confidence levels for detected ^{238}U and ^{232}Th geoneutrinos (left) and $\Delta\chi^2$-profiles for the total number of ^{238}U and ^{232}Th geoneutrinos (right). The grey band gives the prediction by geophysical model.

Study of Cosmic Muon Spallation Products

KamLAND has provided valuable data for the production yields of the isotopes from cosmic muon initiated spallation [91]. The neutron production yield is measured to be $(2.8 \pm 0.3) \times 10^{-4}\, n/(\mu \cdot (\mathrm{g/cm^2}))$, and other nuclear isotopes' production yields are listed in Table V of Ref [91]. The understanding of cosmic muon spallation products is essential for future rare event detection such as neutrino experiments, double beta decay experiments and dark matter searches.

2.3.2 Solar Phase and Purification of Liquid Scintillator

After completion of the primary goal in the *reactor phase*, KamLAND went through major purification of the liquid scintillator from May 2007, with the goal of reducing the intrinsic radioactive background in the LS mainly from ^{210}Pb and ^{85}Kr, and make a direct measurement of ^{7}Be solar neutrinos. The period from May 2007 to present is referred to as *solar phase*, or *low background phase*. It is worth mentioning that all the previous programs in the reactor phase will also benefit from the lower radioactive background, and will co-exist with the solar neutrino program with increasing sensitivities and precisions.

The ^{7}Be ν_e from the sun is mono-energetic at 862 KeV. It elastically scatters on an electron through both CC and NC interactions[6]:

$$\nu_e + e^- \longrightarrow \nu_e + e^- \tag{2.6}$$

and the recoiled electron gives a "Compton" spectrum with maximum energy of 665 KeV. The ν_e elastic scattering channel, unlike the $\bar{\nu}_e$ inverse beta decay, only gives a single e^- event, and is indistinguishable from the β and γ decays of intrinsic

[6]Same as in Super-Kamiokande experiment, the ν_μ and ν_τ from the oscillation of solar ν_e can only elastically scatter on electrons through NC interaction, with a cross section approximately 7 times smaller the ν_e.

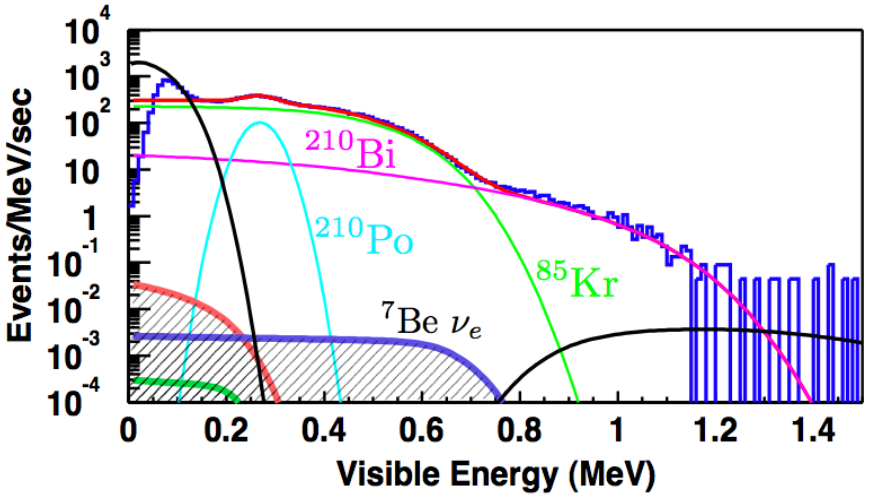

Figure 2.8: The observed singles event rate as a function of deposited energy (E_{vis}) in KamLAND in the reactor phase, overlaid with the expected un-oscillated solar ^{7}Be $\bar{\nu}_e$ spectrum from Standard Solar Model. In the expected ^{7}Be ν_e signal window 0.3MeV $< E_{vis} <$ 0.8MeV, the beta decays of ^{85}Kr (green), ^{210}Bi (magenta) and alpha decays of ^{210}Po (cyan) dominate the event rate.

radioactive impurities. Because of the lack of a good pulse shape discrimination ability, the e^- event is also indistinguishable from a radioactive α decay event. Fig. 2.8 shows the observed singles event rate as a function of deposited energy (E_{vis}) in KamLAND in the reactor phase, overlaid with the expected un-oscillated solar ^{7}Be $\bar{\nu}_e$ spectrum from the Standard Solar Model. The expected un-oscillated ^{7}Be ν_e event rate in the signal window 0.3MeV $< E_{vis} <$ 0.8MeV is ~400/day/kton, but the background event rate from beta decays of ^{85}Kr, ^{210}Bi and alpha decays of ^{210}Po overwhelms. ^{210}Bi and ^{210}Po are daughter nuclei of ^{210}Pb (Appendix B.1), who were introduced by means of ^{222}Rn contamination during the initial filling. The ^{85}Kr was also introduced at the initial filling, whose activity in the LS is ~0.6 Bq/m^3, comparable to the ^{85}Kr activity in the atmosphere (Appendix A). Both ^{210}Pb ($\tau_{1/2}$ = 22 y) and ^{85}Kr ($\tau_{1/2}$ = 10.8 y) have long half-lives, so waiting for them to decay away is not practical. Table 2.3 lists the radioimpurity levels in KamLAND LS in the reactor phase, and the requirement needed in the solar phase in order to make a ^{7}Be solar neutrino measurement. While ^{238}U and ^{232}Th already meet the solar phase low

Isotope	Concentration [g/g]	Purification Goal [g/g]	Purification Factor
^{85}Kr	5.5×10^{-20}	10^{-26}	$\sim 5 \times 10^{6}$
^{210}Pb	2.3×10^{-20}	10^{-25}	$\sim 2 \times 10^{5}$
^{40}K	1.7×10^{-16}	10^{-18}	~ 200
^{39}Ar	$< 4.3 \times 10^{-21}$	10^{-24}	~ 1000
^{232}Th	6.1×10^{-17}	10^{-16}	O.K.
^{238}U	2.7×10^{-18}	10^{-17}	O.K.

Table 2.3: Concentration of radioimpurities in KamLAND liquid scintillator in the reactor phase and purification goal for solar phase in order to make a ^{7}Be solar neutrino measurement.

background requirement, ^{85}Kr and ^{210}Pb need to be reduced by a factor of $\sim 10^{6}$ and $\sim 10^{5}$ respectively, together with a factor of 1000 and 200 reduction in ^{39}Ar and ^{40}K.

Following intensive R&D of purification method, the collaboration discovered that distillation effectively removes ^{210}Pb and ^{40}K, while ultra-pure nitrogen purging effectively removes gas contaminants such as ^{85}Kr, ^{39}Ar and ^{222}Rn. A custom LS distillation system and a nitrogen purge system (with an ultra-pure nitrogen production facility) were constructed at the KamLAND site to implement these purification techniques. Various auxiliary monitoring systems, such as Kr/Ar monitor (Appendix A), Rn monitor, light yield and attenuation length monitor, were developed to insure the purity and quality of the final purified LS products before filling them back into the KamLAND detector.

The first full-scale purification campaign started from 20 May 2007, and continued until 1 August 2007. LS was drawn from the bottom of the detector, passed through the purification system and filled back into the top of the detector. Temperature and density of the new LS were controlled (warmer and less dense) to insure the boundary between the new and old LS to reduce the mixing effects. A total of 1700 m^3 of LS was purified, among which 500 m^3 in the KamLAND LS volume was effectively purified twice. A clear boundary between the once- and twice-purified LS volume can be seen from the data as shown in Fig. 2.9. The reduction factor for ^{210}Bi, ^{85}Kr and ^{210}Po in the twice-purified volume is measured to be $\sim$ 200, 40 and 5 respectively.

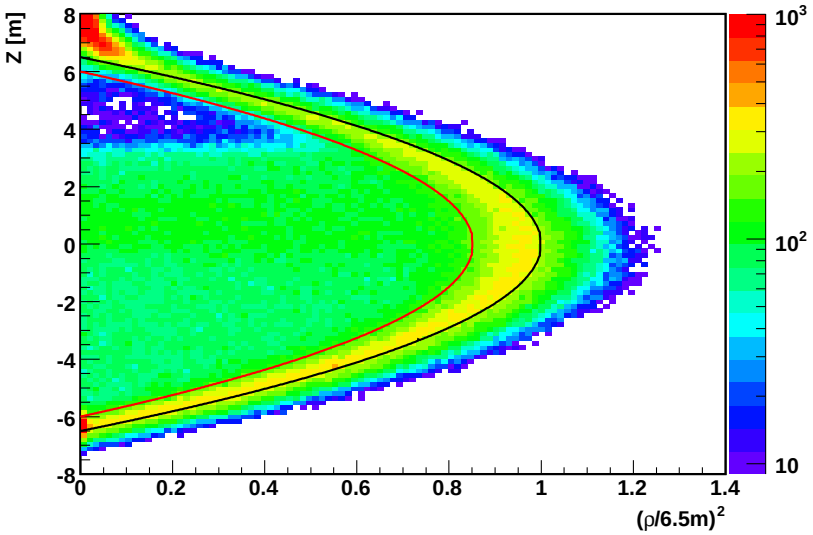

Figure 2.9: The vertex distribution of ^{85}Kr and ^{210}Bi events (0.4MeV $< E_{\rm vis} <$ 1.2MeV) after the first purification campaign, from a one-day physics run 7830. The black line indicates the balloon position at 6.5m radius. The red line indicates the edge of the 6m fiducial volume used in this analysis. A clear boundary between the once- and twice-purified LS volume can be seen.

The reduction factor does not agree well with the results from the monitoring system which samples LS emerging right after the distillation system, and shows that the ^{85}Kr and ^{222}Rn concentrations in those LS already meet the required levels for a ^{7}Be solar neutrino measurement (Appendix A). Further investigations revealed possible causes of the discrepancy including leaks around the detector chimney and convection of the LS during and after the filling.

Following important improvements of the distillation system, including an ultra-pure nitrogen over-pressured tent around the detector chimney, a heat exchanger to precisely control the LS temperature, and a new bottom-filling scheme to minimize the LS convection, the second purification campaign started on 16 June 2008 and continued until 29 January 2009. A full solar neutrino analysis is on the way and the result is promising [92].

Data Set Used in this Dissertation

The analysis described in this dissertation incorporates all the KamLAND data taken between April 2002 and June 2008, except the period between May 2007 and September 2007 during when the first purification campaign was on-going and the detector properties were unstable[7]. The first purification campaign naturally divides the whole data set into two periods: Period I (before purification) and Period II (after purification). Due to the difference in liquid scintillator properties in the two periods, such as radiopurity, light yield, uniformity, etc. the analysis treats the two periods separately and combines the results together in the end. The total live time is 1432 days in Period I and 200 days in Period II. The full definition of the data set is summarized in Table 4.1.

[7]The data taken after June 2008 is not used in this analysis, which includes the period during and after the second purification campaign.

Chapter 3 Event Reconstruction

The raw data acquired by the DAQ system (Section 2.2.3) need to be reconstructed into meaningful events before doing any physics analysis. Fig. 3.1 shows the schematic flow diagram of the KamLAND event reconstruction process. The asynchronously collected raw waveforms and trigger records are first sorted in time and grouped into events ("event building"). The analysis then extracts the charge and time information of the event from its waveforms, which are further used in the vertex and energy reconstruction algorithms ("event reconstruction"). The reconstruction algorithms use the data from calibration runs such as ^{60}Co center deployments as references. Based on either the low level (algorithm-independent) information such as charge, time and trigger record, or high level information such as reconstructed energy and position, events are further categorized ("event tagging") for future physics analysis. The properties of various events are used to check the reconstruction algorithms' performances.

3.1 Event Building

As described in Section 2.2.3, the DAQ system asynchronously reads out waveforms and trigger records and stores them onto disks. The event builder program then sorts the data and groups them into events with the same time-stamp. Given the size of each waveform (256 Byte) and the data transfer rate at a few MB/second, the memory usage of the event builder program is non-trivial. Waveforms that are read out a few minutes out-of-order (typically during noisy periods) cannot be sorted and have to be thrown away. The efficiency of the event building can be calculated from

simply counting the waveforms and trigger records for each time-stamp, and is found to be greater than 99.999%.

3.2 Waveform Analysis

The ATWD samples a PMT signal at a frequency of ∼0.65 GHz, and stores them onto an array of 128 internal capacitors. The amount of charge on each capacitor is then digitized with a 10-bit ADC. This gives an array of 128 ADC values, spanning ∼200 ns (1.5 ns ×128), which is referred to as the *waveform* of the PMT signal.

Pedestal Subtraction

The *pedestal* of an ATWD refers to the base charge variation of the ATWD's capacitors in absence of any photon signal. The pedestal adds structured-offset to the waveform and needs to be subtracted before any further waveform analysis. At the beginning of each run, 50 force-acquisition waveforms are collected for each ATWD. The pedestal waveform is obtained by simply averaging these waveforms, since most

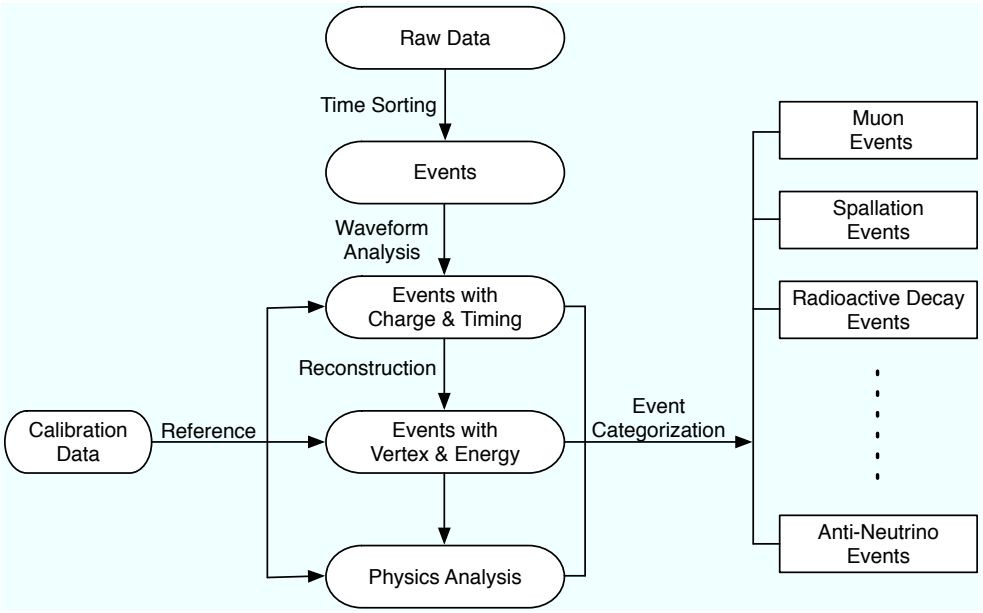

Figure 3.1: Schematic diagram of event reconstruction process

of them have zero-pulses given the PMT dark rate at ∼10 kHz[1]. A common overall offset is subtracted so that only the variation between the samples is saved. An example of a raw waveform and the pedestal waveform of corresponding ATWD is shown in Fig. 3.2.

Baseline Subtraction

After subtracting the pedestal waveform, each waveform is found to be floating above a non-zero baseline. This baseline value is related to the activities of the board at the acquiring time, and has to be calculated for each waveform and subtracted from it. For small pulses the baseline value is obtained by iteratively calculating the mean value of the waveform and throwing away large deviation samples, until the sample deviation is smaller than 2.5%. For large pulses such as from muons, the sample values might not return to the baseline before the end of the waveform window, so the baseline value is simply calculated from the mean value of the first 10 samples.

Pulse Finding

After the pedestal and baseline subtraction, the waveform is smoothed with Savitzky-Golay filter [93] to remove high-frequency noises. The pulse finding algorithm then defines a candidate pulse as any contiguous area above zero in a waveform. Noise pulses are iteratively removed if the pulse's total charge is less than 15% of the summed charges of all candidate pulses. An example of a two-pulse waveform is shown in Fig. 3.2(a). This algorithm however will count multiple pulses that overlaps above zero as one single pulse. One example is shown in Fig. 3.2(b). This algorithm is nevertheless used because of its simplicity and robustness, and further reconstruction algorithms are written in a way to minimize its drawbacks.

[1]Samples that are 4σ away from the mean of the waveform are thrown away, which removes occasional real pulses.

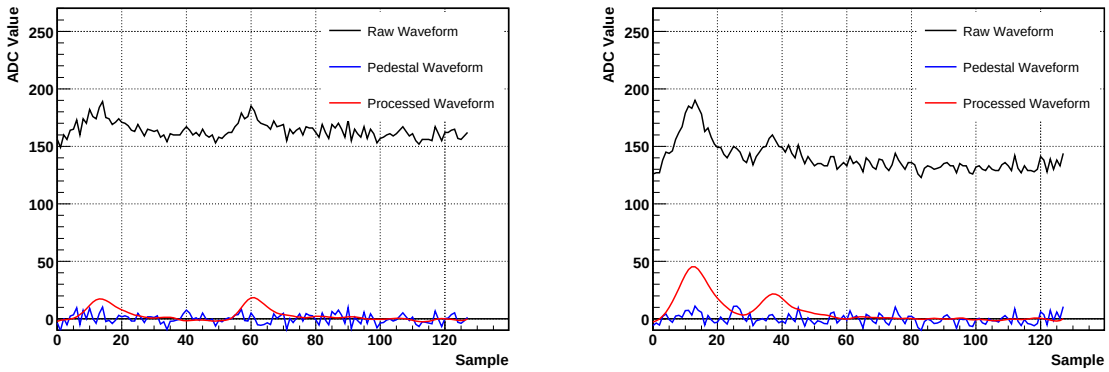

(a) (b)

Figure 3.2: Waveform analysis example: Raw waveform (black), Pedestal waveform (Blue). The processed waveform (Red) is obtained by subtracting the pedestal and baseline from the raw waveform and smoothing the waveform with Savitzky-Golay filter. (a) Two pulses are found in this waveform. (b) A waveform with two overlapping pulses. The pulse finding algorithm will only count one pulse in this case since the first pulse does not return to zero before the second pulse arrives.

Pulse Time Extraction

The time between each sample Δt_{sample} in a waveform is set by the DAQ system at the beginning of the run and is typically $\sim$1.5 ns. The sampling time however varies slightly from ATWD to ATWD and needs to be precisely obtained in order to extract the arriving time of each pulse. This is done by collecting 50 *clock waveforms*, which are the signals from the internal 40 MHz clock sent out by the trigger module, at the beginning of the run for each ATWD. After subtracting the pedestal waveform and baseline, a Fast Fourier Transform (FFT) is performed to the clock waveforms and the mean sampling frequency is calculated for each ATWD.

For a small pulse the time of the pulse, in units of number of samples, is defined as the peak position of the pulse (P_{pulse}), which comes from a quadratic fit to the three points closest to the peak. For a large pulse such as from a muon, the pulse time is estimated from its rising edge, defined as where the lowest gain waveform (Fig. 3.3) crosses 50 ADC units, since the peak comes at a much later time. A small

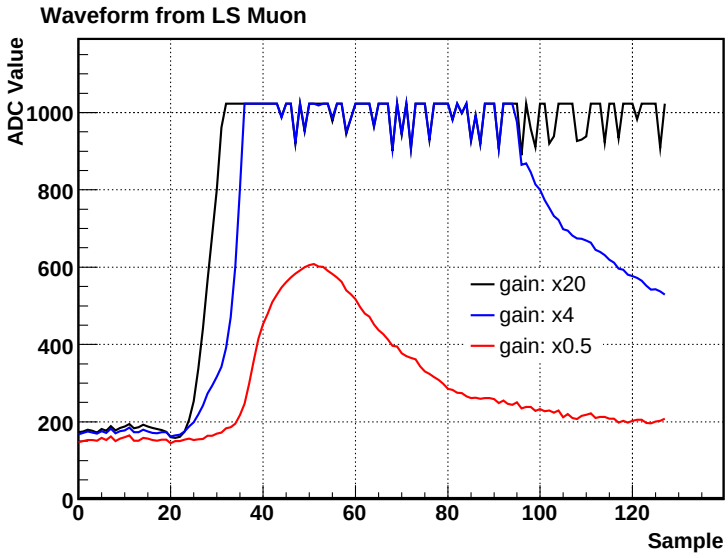

Figure 3.3: One example of raw waveforms from an LS muon event. The large muon signal saturated the two high gain channels, and the time and charge information are extracted from the lowest gain waveform.

correction $\delta t(q)$ is applied to compensate for the possible charge correlated bias in the time extraction algorithm, which is estimated from the laser calibration data where the timing and intensity of the signals are precisely controlled.

Each ATWD has a constant time offset T_0 relative to the absolute photon arriving time on the PMT, due to the different cable length or FEE channel behavior. T_0 is calculated and updated for each ATWD from the ^{60}Co center deployment every few weeks, and has a spread of $\sim$20 ns over all ATWDs. Combining with the launch offset N_{launch} (Section 2.2.3) of the ATWD recorded with each waveform, the relative timing of each pulse with respect to the the time-stamp of the event is given by:

$$t_{\text{pulse}} = P_{\text{pulse}} \times \Delta t_{\text{sample}} - N_{\text{launch}} \times 25\,[\text{ns}] - T_0 - \delta t(q) \tag{3.1}$$

Pulse Charge Extraction

The charge of a pulse is defined as the area of the pulse, in units of ADC$\times N_{\text{samples}}$. For large signals the charge is calculated from the lowest gain waveform (Fig. 3.3). The

charges are then normalized to number of photo-electrons ($N_{p.e.}$) for each ATWD by dividing the corresponding single p.e. charge (Q_0). Same as T_0, the Q_0 is calculated and updated for each ATWD from the ^{60}Co center deployment every few weeks. The distribution of the time and charge information of the pulses of an event across all PMTs in the detector is used as an input to the later event reconstruction algorithms.

3.3 Vertex Reconstruction

The vertex reconstruction algorithm uses the distribution of pulse arriving time (Eqn. 3.1) of an event to reconstruct its interaction position. Only pulses from 17-inch PMTs are used in the reconstruction because of their better timing resolution. It is assumed that the scintillation light is isotropic and that the light travels in a straight line until it reaches a PMT. Second order effects such as absorption and re-emission of the photons, or reflection of the photons off the balloon are ignored. The vertex reconstruction algorithm however only selects the pulses around the peak arriving time to minimize the drawbacks of the simplified optical model. The algorithm is thus called *peak time fitter*.

3.3.1 Algorithm

The peak time fitter finds the event vertex iteratively:

1. The starting vertex of the iteration is estimated from a "charge weighted average position"

$$\vec{r}_0 = 1.62 \frac{\sum_i N^i_{p.e.} \vec{r}_i}{\sum_i N^i_{p.e.}} \tag{3.2}$$

   where i runs over all the pulses of the event. $N^i_{p.e.}$ is the normalized charge (number of photoelectrons) of pulse i and $\vec{r}_i$ is the position of the PMT who registered pulse i. The overall scaling factor 1.62 is empirically tuned from ^{60}Co

z-axis calibration data.

2. The vertex-corrected pulse arriving time $t_i^{'}$ is calculated by subtracting the expected photon travel time $t_{\text{travel},i}$, given the event's current reconstructed vertex, from the raw pulse arriving time t_i (Eqn. 3.1) as follows:

$$\begin{aligned} t_i^{'} &= t_i - t_{\text{travel},i} \\ &= t_i - (\frac{r_{LS,i}}{c_{LS}} + \frac{r_{BO,i}}{c_{BO}}) \end{aligned} \tag{3.3}$$

where r_{LS}, r_{BO} is the expected photon traveling distance in LS and BO region, and c_{LS} = 196.1 mm/ns, c_{BO} = 220.0 mm/ns is the empirical effective speed of light in the LS and BO tuned from ^{60}Co z-axis calibration data, which does not correspond to the true speed of light in the medium due to the simplified optical model used in the algorithm.

3. The distribution of vertex-corrected pulse arriving time and the peak position $t_{\text{peak}}^{'}$ in the distribution is calculated. A "push-pull" vector $\delta\vec{r}$ is then calculated using only pulses inside the (-10ns, +5ns) window around $t_{\text{peak}}^{'}$:

$$\delta\vec{r} = \sum_i \frac{t_i^{'} - t_{\text{peak}}^{'}}{t_{\text{travel},i}} \cdot (\vec{r} - \vec{r}_i) \tag{3.4}$$

where $\vec{r}$ is the current reconstructed vertex of the event and $\vec{r}_i$ is the position of the PMT that registered pulse i. $\delta\vec{r}$ is then added to the current reconstructed vertex of the event, which essentially pushes the vertex closer the the PMTs who were hit earlier by the scintillation light.

4. Step 2 and 3 are iterated until $\delta\vec{r}$ is less than 1 mm or 100 iterations have been performed. A vertex reconstruction status is then assigned to each event. The statuses are summarized in Table 3.1.

3.3.2 Performance

The performance of the vertex reconstruction is checked by the z-axis calibration data from different radioactive sources at various energies, as shown in Fig. 3.4. The peak time fitter works very well for events with energies higher than 0.6 MeV, with the typical bias less than 3 cm between -6 m and 6 m along the z-axis. The peak time fitter's performance decreases at lower energies since the number of pulses in the peak time window becomes smaller and the contribution of pulses from dark hits, which are uncorrelated with the event, becomes larger. This can be clearly seen from ^{203}Hg (0.279 MeV γ-ray) data, where the inward vertex bias is as large as 10 cm at z = 6m. The vertex reconstruction bias is slightly worse in Period II (after purification). The effective speed of light c_{LS} and c_{BO} are tuned in early Period I and fixed afterwards. The change of LS properties and the non-uniformity of the LS after purification (Fig. 2.9) could have caused the change of c_{LS} and c_{BO} and consequently reduced the peak time fitter's performance in Period II.

Table 3.1: Summary of vertex reconstruction status. t'_{RMS}, $t'_{\mathrm{peak}RMS}$ and f_{pulse} refer to the RMS of the vertex-corrected pulse time distribution, the RMS of the vertex-corrected pulse time distribution in the peak time window, and the fraction of pulses in the peak time window, respectively. An event can have multiple statuses.

Status	Description
Valid	Fit is successful
Unknown	Event has less than 4 pulses
Not Valid	Reconstructed vertex is unphysical ($r > 10$ m)
Bad Fit	Fit does not converge
Bad RMS	$t'_{RMS} < 35$ ns or $t'_{RMS} > 90$ ns
Bad Peak RMS	$t'_{\mathrm{peak}RMS} < 1.7$ ns or $t'_{\mathrm{peak}RMS} > 4$ ns
Bad Pulse Ratio	$f_{\mathrm{pulse}} < 0.22$ or $f_{\mathrm{pulse}} > 0.55$

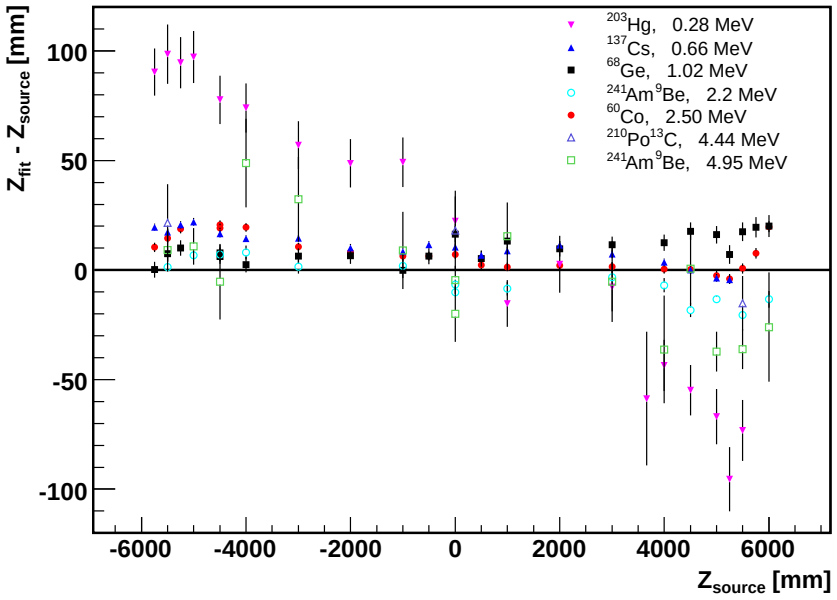

(a) in Period I (before purification)

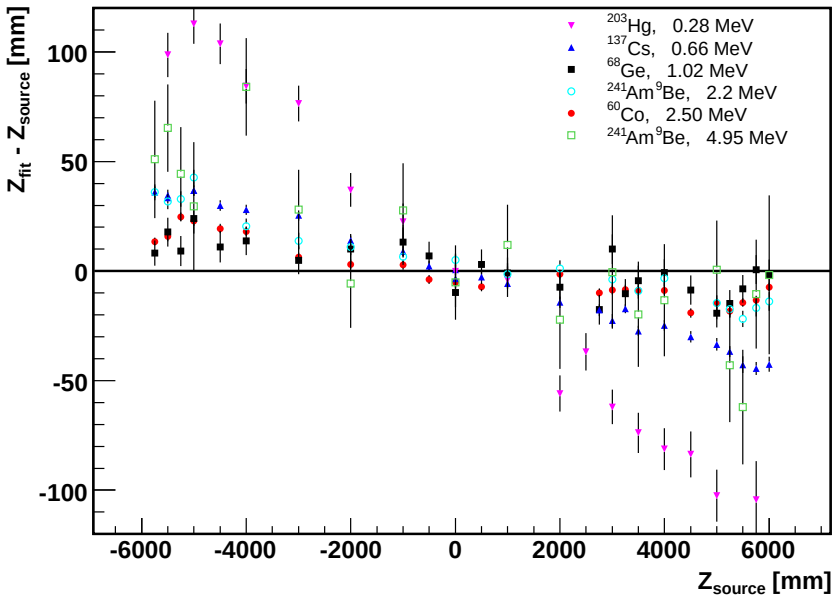

(b) in Period II (after purification)

Figure 3.4: The vertex reconstruction performance in (a) Period I and (b) Period II, checked with z-axis calibration data from different radioactive sources at various energies.

3.4 Energy Reconstruction

The KamLAND detector can be viewed as a calorimeter that measures the total energies deposited by a particle, which is partially transferred to the scintillation light-output, regardless of the particle's type. It is then convenient to work with the *visible energy* of an event, instead of its real energy. The scale of the visible energy is defined such that the sum of the two gamma-ray energies from ^{60}Co at the detector center has the same value (2.506 MeV) in real and reconstructed energy.

The energy reconstruction algorithm used in this analysis is called multi-photoelectron (MPE) fitter, which uses the distribution of number of photoelectrons on each PMT to estimate the event's energy. The MPE fitter relies on the reconstructed position of the event as an input, so its performance is directly correlated with the vertex reconstruction.

3.4.1 Algorithm

The MPE fitter first constructs an energy likelihood function from all active inner detector 17-inch PMTs:

$$L(E) = \prod_{i}^{\text{PMTs}} L_i(E; q_i) \tag{3.5}$$

where $L_i(E; q_i)$ is the probability of PMT$_i$ producing charge q_i from an event having visible energy E at reconstructed position $\vec{r}$. This probability follows Poisson statistics $f(n; \mu)$ where n is the observed number of photoelectrons and μ is the expected number of photoelectrons on the PMT. The probability of charge q_i being n photoelectrons is assumed to follow Gaussian distribution:

$$P(n|q_i) = \frac{1}{\sqrt{2\pi n\sigma_i^2}} e^{-(q_i - n\cdot q_{0i})^2/(2n\sigma_i^2)} \tag{3.6}$$

where q_{0i} and σ_i are the mean and variance of the single photoelectron charge dis-

tribution, calculated and updated for each PMT from ^{60}Co center deployment about once a month. $L_i(E;q_i)$ can then be written as:

$$L_i(E;q_i) = \begin{cases} f(0;\mu_i) + \sum_{n=1}^{\infty} f(n;\mu_i) \cdot P(q_i < q_{\rm th}|n) & \text{if not hit.} \\ \sum_{n=1}^{\infty} f(n;\mu_i) \cdot P(n|q_i) & \text{if hit.} \end{cases} \tag{3.7}$$

where the second term in the "not-hit" case accounts for the probability of photoelectrons not producing enough charge to cross the discriminator's threshold $q_{\rm th}$. The expected number of photoelectrons μ_i is directly related to the energy of the event and the vertex $\vec{r}$ of the event relative to the PMT position. The factors that can affect μ_i are:

- η_i: number of photoelectrons per MeV for events at the detector center.
- Λ: effective attenuation length of the LS and BO, which is fixed from ^{60}Co data to be 30 m.
- δ_i: number of dark photoelectrons uncorrelated with the event.
- $\Omega_i(\vec{r})$: solid angle extended from the event position to the PMT cathode area.
- $S_i(\vec{r})$: the shadowing correction due to the balloon and ropes, calculated from KamLAND detector simulation package (KLG4sim).

μ_i can be then written as:

$$\mu_i = \eta_i \cdot \frac{\Omega_i(\vec{r}) \cdot S_i(\vec{r}) \cdot e^{-l_i(\vec{r})/\Lambda}}{\Omega_i(0) \cdot S_i(0) \cdot e^{-l_i(0)/\Lambda}} \cdot E + \delta_i \tag{3.8}$$

where all the geometry factors are normalized to the detector center. The two constants η_i and δ_i are calculated and updated from ^{60}Co center deployments for each PMT, by free floating η_i and δ_i until $L_i(\eta_i, \delta_i; E = 2.506 \text{ MeV})$ is maximized.

With the full likelihood function $L(E)$ in Eqn. 3.5 defined, the effective $\chi^2 = -2\ln L$ is minimized using the Minuit Package [94] with respect to the unknown parameter E. The reconstructed visible energy of the event is taken to be the best-fit value of E if the minimization succeeds. If the minimization fails the energy reconstruction status is set to "not valid."

3.4.2 Performance

The performance of the energy reconstruction is again checked by the z-axis calibration data from different radioactive sources at various energies, as shown in Fig. 3.5. The reconstructed energy bias relative to the detector center is generally less than 3% between -6 m and 6 m along the z-axis. The shape of the bias however indicates some systematic biases in the fitter's algorithm, and is similar at all energies. This shape is different in Period II and is believed to be caused by the change of LS light yield (Fig. 3.6) and the non-uniformity of the LS (Fig. 2.9) after purification.

Spallation neutron events are uniformly distributed in the detector volume and can be used to check the energy reconstruction bias in the full volume, as shown in Fig. 3.7. Spallation neutron capture events are selected along the x-, y-, z-axis, and similar shapes of reconstruction bias are observed. The angular dependence of the bias is also checked and the variation is only $\sim$0.3%. Combing these observations the MPE fitter's bias is considered to be mainly coming from the the radial dependence of the events' positions, and the volume weighted variation is within $\sim$1% at all calibration energies. Details of selections of spallation neutron events are discussed in Appendix C.4.1.

The ^{60}Co source is deployed to the center of the detector about twice a month. Half of these runs are used for updating the energy reconstruction's constants, and the other half are used to monitor the stability of reconstruction's performance in time. The time variation of the reconstructed energy is checked with calibration sources

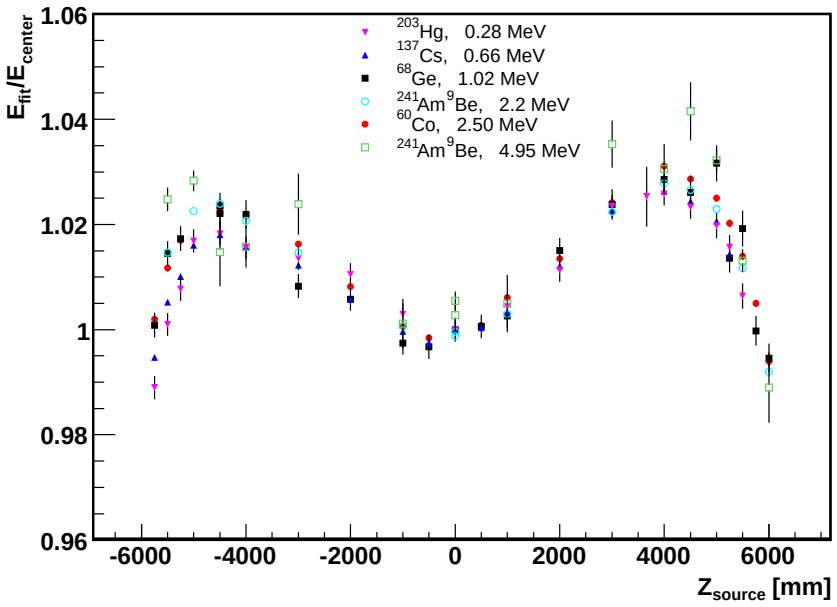

(a) in Period I (before purification)

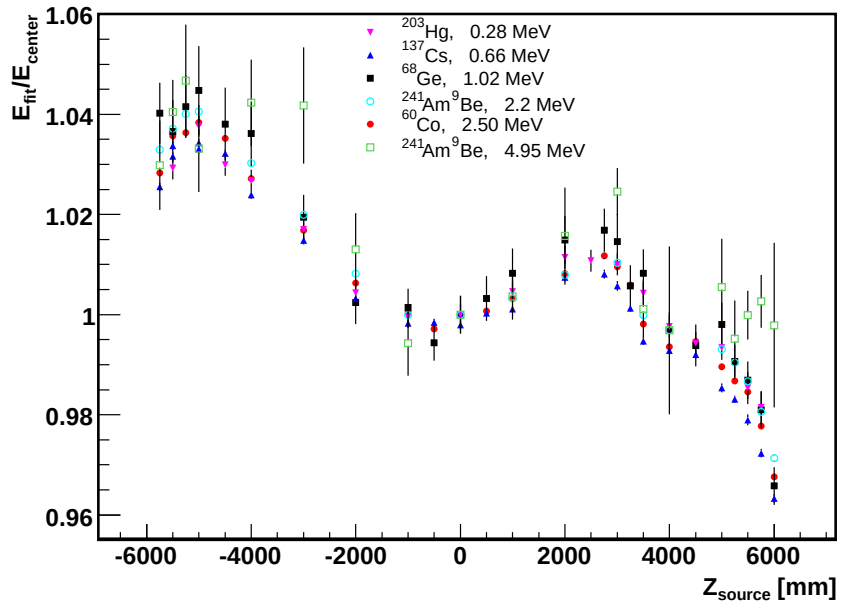

(b) in Period II (after purification)

Figure 3.5: The energy reconstruction performance in (a) Period I and (b) Period II, checked with z-axis calibration data from different radioactive sources at various energies.

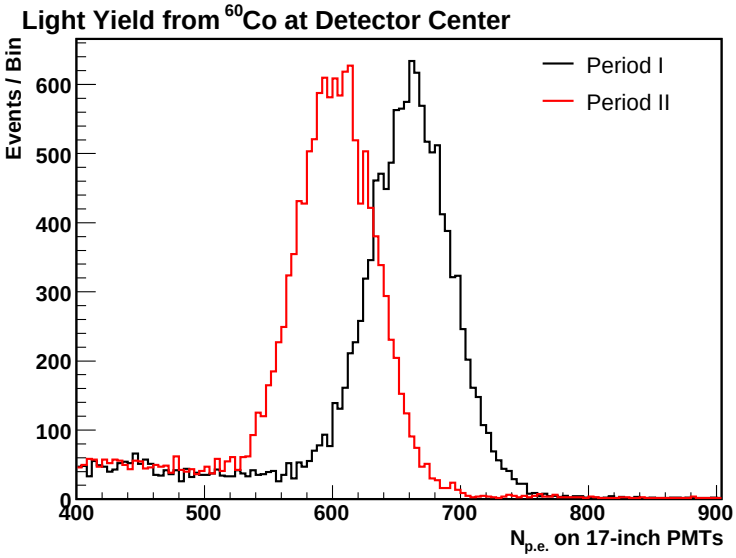

Figure 3.6: The distribution of total number of photoelectrons on all 17-inch PMTs from ^{60}Co events (2.506 MeV) at the detector center in Period I (black) and Period II (red). There is about 10% light yield decrease in the LS after the purification.

and is found to be within 0.5%, as shown in Fig. 3.8. Spallation neutrons and alpha decay events are also used to check the time variation of reconstructed energy. Details can be found in Appendix C.

3.4.3 Detector Energy Response

The reconstructed visible energy of an event is related to the scintillation light output from the energies deposited by the particle in the detector and in general is not equalling or proportional to the real energy of the particle. The conversion from real energy to visible energy is called "energy scale," and is parametrized by the following equation:

$$\frac{E_{\rm vis}}{E} = a_0[1 - \delta_B(E, k_B) + k_c\delta_c(E) + k_0\delta_0(E)] \tag{3.9}$$

where each term corresponds to a process which would lead to the non-linearity of the energy scale:

- $\delta_B(E, k_B)$: The light-output suppression due to the quenching interactions be-

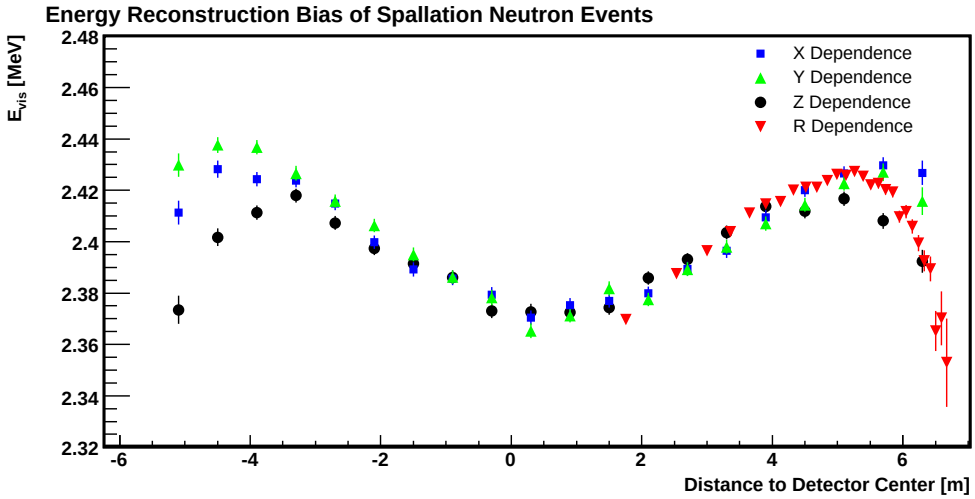

(a) Energy Reconstruction Bias in X, Y, Z and R

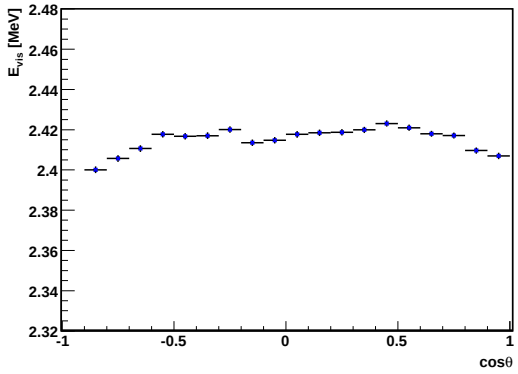

(b) Energy Reconstruction Bias in $\cos\theta$

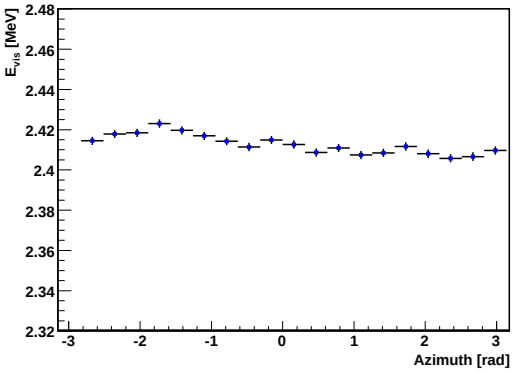

(c) Energy Reconstruction Bias in ϕ

Figure 3.7: Energy reconstruction bias in the full volume checked by spallation neutron capture events (in Period I only): (a) Bias in X, Y, Z and R for events in a 2.5 m radius cylinder along the corresponding axis. (b) Bias in $\cos\theta$ for events inside 6m radius. (c) Bias in ϕ for events in a 2.5 m radius cylinder along z-axis ($-5m < z < 5m$). Combining all three figures, the major systematic bias of the energy reconstruction comes from the radial dependence of the events' positions.

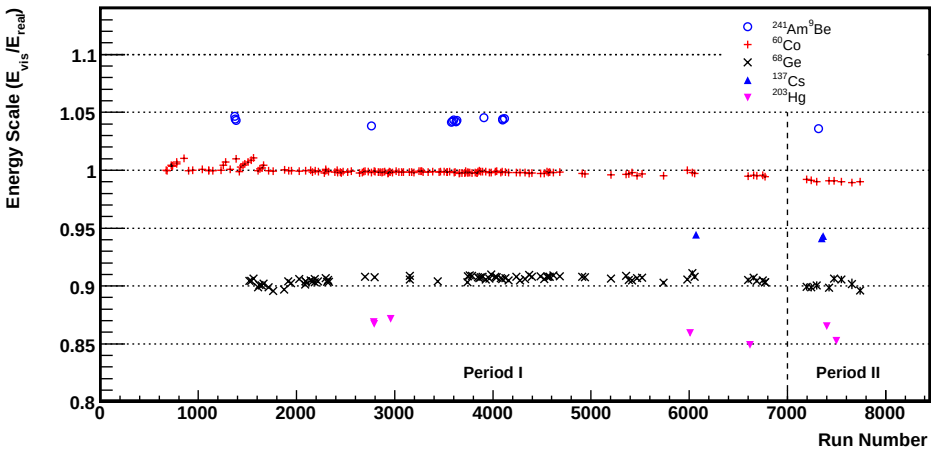

Figure 3.8: The time variation of energy scale from calibration sources. The reconstructed visible energy is divided by the expected real energy of the γ-rays from the source. All the center calibration runs throughout the analysis periods are included. The average time variation is $\sim$0.5%.

tween the excited molecules along the path of the incident particle, which drain energy that would otherwise go into fluorescence photons [95]. This *quenching effect* is more obvious for high ionizing power particles such as α particles, since they would produce a higher density of excited molecules. The *Birk's formula* introduces a positive *Birk's constant* k_B to semi-empirically correct for the quenching effect as follows:

$$\frac{\mathrm{d}L}{\mathrm{d}x} \propto \frac{\mathrm{d}E/\mathrm{d}x}{1 + k_B \cdot (\mathrm{d}E/\mathrm{d}x)} \tag{3.10}$$

where $\mathrm{d}L/\mathrm{d}x$ and $\mathrm{d}E/\mathrm{d}x$ are the light output per unit length and the particle stopping power respectively. For small $\mathrm{d}E/\mathrm{d}x$ Eqn. 3.10 reduces to a linear relationship, but for large $\mathrm{d}E/\mathrm{d}x$ such as for α particles the light output is saturated and is only related to the particle range.

The Birk's formula Eqn. 3.10 is used to calculate $\delta_B(E, k_B)$ for α particles and protons, together with the SRIM package [96] to calculate $\mathrm{d}E/\mathrm{d}x$ of the particle given KamLAND LS's composition. For γ and $e^{\pm}$ particles, the EGSnrc

package [97] is used, which does a Monte Carlo simulation and tracks the energy deposited per tracking length. The Birk's constant k_B is limited to 5 – 15 mg/(cm^2 MeV) in calculating and extrapolating the $\delta_B(E, k_B)$ function. k_B outside of the range would be unphysical for KamLAND LS.

- $k_c\delta_c(E)$: The light output from Cherenkov radiation, which is emitted when a particle travels in a medium faster than the speed of light in the same medium. The Cherenkov radiation is an electromagnetic shock wave, whose coherent wavefront is conical in shape and is emitted at a well-defined angle θ_c

$$\cos\theta_c = \frac{c}{nv} \tag{3.11}$$

  with respect to the track of the particle, where c is the speed of light in vacuum and n is the index refraction of the medium. $\delta_c(E)$ is again calculated from the EGSnrc Monte Carlo package and is proportional to $\sin^2\theta_c$. The constant k_c represents the detector's response in collecting the Cherenkov photons.

- $k_0\delta_0(E)$: A byproduct from the EGSnrc Monte Carlo simulation, which keeps track of the energy that is lost when it is below the simulation tracking threshold. The constant k_0 allows for the recovery of some of this energy.

- a_0: An overall normalization factor such that the sum of the two γ-ray energy from ^{60}Co at the detector center is 2.506 MeV in both visible energy and real energy.

The four energy scale parameters a_0, k_B, k_0 and k_c and their error matrices have to be extracted from the KamLAND data. The data points that are used are taken from various known energy events and are summarized in Table 3.2. Besides the events from radioactive calibration sources, the γ-rays from spallation neutron capture on ^{1}H and ^{12}C and the α decays from ^{214}Po and ^{212}Po are also used. Details of the

Table 3.2: Data Points for Determine Energy Scale Parameters

Events		E_{real} [MeV]	E_{vis} [MeV]	
α	γ		Period I	Period II
	^{203}Hg	0.279	0.244 ± 0.003	0.238 ± 0.003
	^{68}Ge	1.022/2	0.941 ± 0.012	0.913 ± 0.010
	^{137}Cs	0.662	0.637 ± 0.008	0.616 ± 0.010
	^{65}Zn	1.116	1.120 ± 0.013	-
	^{60}Co	1.173 + 1.332	2.539 ± 0.030	2.462 ± 0.030
	^{1}H(n,γ)^{2}H	2.225	2.414 ± 0.030	2.436 ± 0.048
	^{12}C(n,γ)^{13}C	4.946	5.485 ± 0.056	5.585 ± 0.056
^{214}Po		7.687	0.630 ± 0.016	0.640 ± 0.016
^{212}Po		8.785	0.827 ± 0.023	0.806 ± 0.023

Table 3.3: Best-fit Energy Scale Parameters

Parameter	Period I	Period II
a_0	1.08 ± 0.02	1.00 ± 0.03
k_B [mg/(cm^2 MeV)]	9.8 ± 0.3	9.0 ± 0.3
k_0	0.85 ± 0.10	1.01 ± 0.13
k_c	0.43 ± 0.10	0.81 ± 0.15

selection and properties of these events can be found in Appendix C. The E_{vis} value in Table 3.2 is the volume weighted mean value for the correspond events inside a 6 m radius sphere from the detector center, which is the fiducial volume used in this analysis (Section 4.4). E_{vis}'s error comes from a combination of its spacial variation inside the fiducial volume and time variation over each period. The errors on the alpha events are manually enlarged by a factor of 1.2 to partially compensate the higher order quenching effects [98] which are not included in the current energy response model.

These data points are then fitted to the energy scale function (Eqn. 3.9) as shown in Fig. 3.9, where the shaded area indicates the 68.3% C.L. region of the fit. Because of the change of LS properties after purification, the energy scale parameters are estimated in Period I and Period II separately. The χ^2/ndf from the fit is 4.8/5 for Period I and 3.9/4 for Period II. The best-fit values are summarized in Table 3.3.

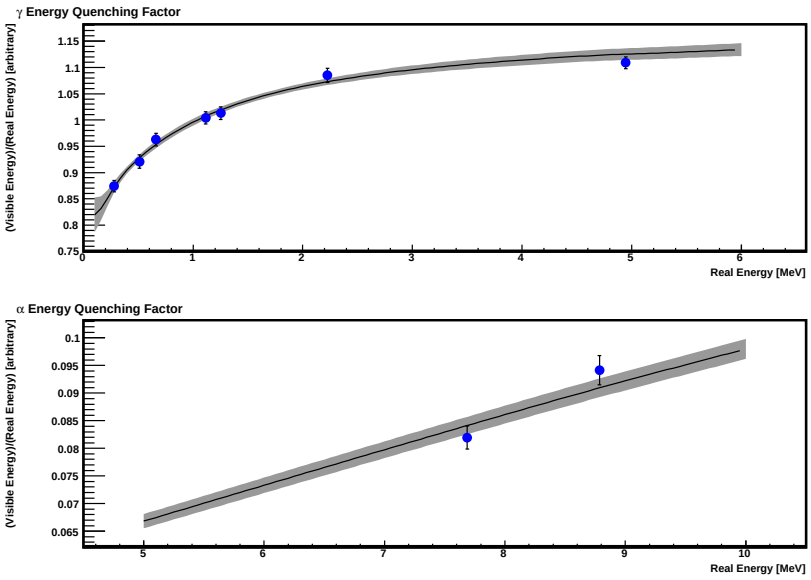

(a) in Period I (before purification)

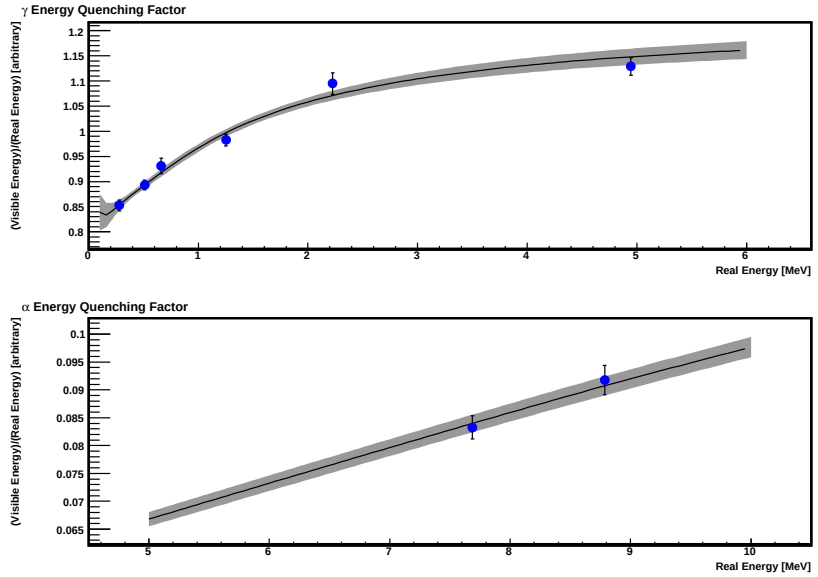

(b) in Period II (after purification)

Figure 3.9: The fit to the energy scale function (Eqn. 3.9) in (a) Period I and (b) Period II. The top panel is for γ particles and the bottom panel is for α particles. The shaded area is the 68.3% C.L. region from the fit. The χ^2/ndf from the fit is 4.8/5 for Period I and 3.9/4 for Period II.

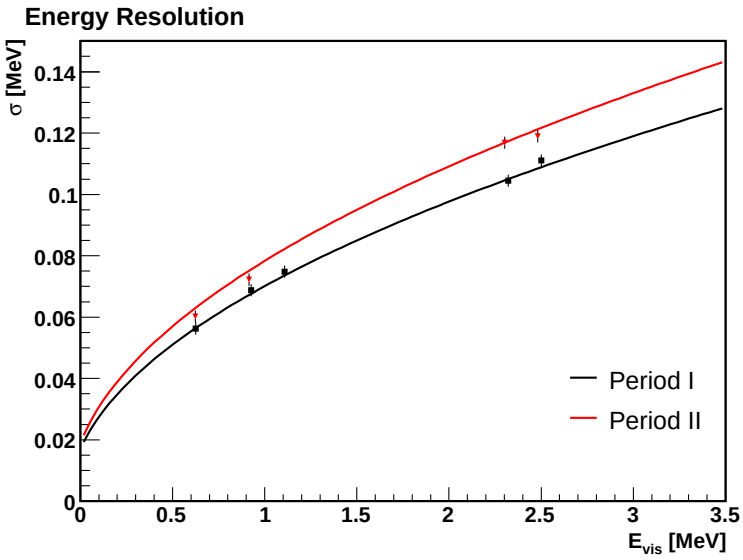

Figure 3.10: The detector energy resolution as a function of reconstructed energy in Period I (black) and Period II (red). The data points are from radioactive γ-ray sources' reconstructed energy widths. The worse energy resolution in Period II is caused by the decrease of light yield in the LS after the purification.

The energy resolution of the detector is dominated by the Poisson statistics of the total number of photoelectrons collected. It can be approximated by a Gaussian function with width $\sigma_{E_{\rm vis}}$

$$\sigma_{E_{\rm vis}} = \sqrt{\sigma_0^2 + \sigma_1^2 \cdot \frac{E_{\rm vis}}{1{\rm MeV}}} \tag{3.12}$$

where σ_0 accounts for the background photoelectrons uncorrelated with the event and σ_1 accounts for the photoelectrons from the event. Eqn. 3.12 is then fitted from calibration γ-rays' reconstructed energy widths (e.g. Fig. C.2) for Period I and Period II separately. Fig. 3.10 shows the fitting results, which are $\sigma_0 = 0.0169 \pm 0.0016$ MeV, $\sigma_1 = 0.0681 \pm 0.0004$ MeV in Period I, and $\sigma_0 = 0.0189 \pm 0.0016$ MeV, $\sigma_1 = 0.0763 \pm 0.0004$ MeV in Period II. The light yield decrease after purification (Fig. 3.6) caused the worse energy resolution in Period II.

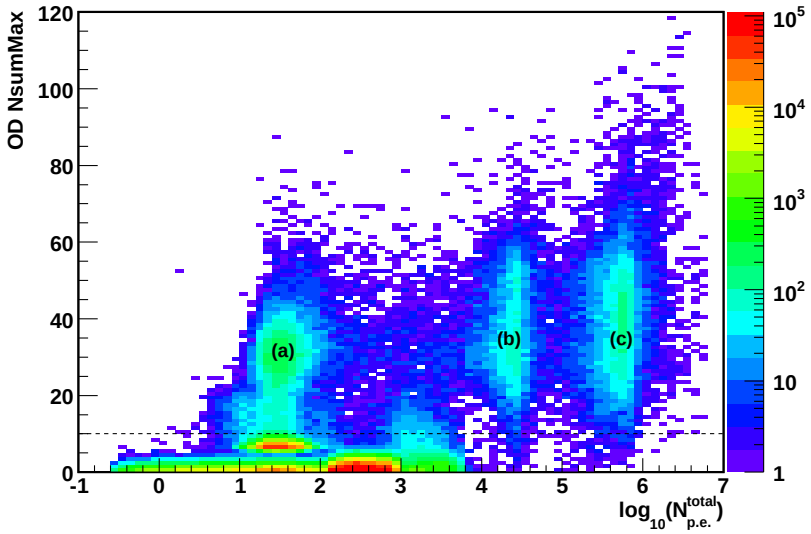

Figure 3.11: The light yields of muon events plotted as $\mathrm{OD}_{\mathrm{nsummax}}$ v.s. total number of photoelectrons collected by the ID 17-inch PMTs. Three distinct regions can be identified: (a) muons that only pass through the OD; (b) muons that pass through the BO without entering LS; (c) muons that pass through the LS, which produce the most light outputs. The dotted line indicates the OD muon tagging threshold at $\mathrm{OD}_{\mathrm{nsummax}} > 10$.

3.5 Muon Track Reconstruction

The muons that incident on KamLAND detector have typical energies above 10 GeV (average energy ∼268 GeV [99]). Most of them traverse the detector without stopping and produce scintillation light and Cherenkov light along their tracks. At such energies the muons are approximately *minimum ionizing* with stopping power of ∼2 MeV/(g cm^{-2}) [7]. This causes high light yields for typical muon events, as can be seen in Fig. 3.11. The muons also produce secondary spallation products along their tracks which are potential backgrounds for $\bar{\nu}_e$ detection. It is thus necessary to reconstruct the tracks of muons for efficient vetoing of the spallation events after the muons (Section 4.3).

The high light yield of the muon event results in photoelectrons on almost every PMT. The muon track reconstruction algorithm use the *fastest-light model*, which

takes advantage of the fact that the first-arriving photons on a PMT are always coming from the direct light on the muon track at the Cherenkov angle θ_c, even true for scintillation light. The algorithm then construct a likelihood function

$$L(\vec{x}) = \prod_{i}^{\text{PMTs}} P(t_i - t_{\text{fastest},i}(\vec{x})) \tag{3.13}$$

where $\vec{x}$ is the vector of muon track, i runs over all ID 17-inch PMTs, t_i is the earliest hit time of PMT$_i$, and $t_{\text{fastest},i}$ is the predicted earliest hit time of PMT$_i$ given the muon track geometry. The hit time distribution $P(\Delta t)$ is modeled by a Gaussian with an exponential tail from the KamLAND data. The effective $\chi^2 = -2 \ln L$ is then minimized using the Minuit Package [94] to extract the best-fit value of the muon track vector $\vec{x}$. If the minimization converges with a good χ^2, a "good track" status is assigned. The "good track" reconstruction efficiency is 99.7% for both LS and Oil muons.

The result of the muon track reconstruction is compared with the MUSIC and MUSUN Monte Carlo simulations [100]. The simulations use the detailed shape of the KamLAND overburden to calculate the muon flux at KamLAND detector. The distribution of muon tracks in zenith angle and azimuth angle from the simulation shows good agreement with KamLAND data [99].

Chapter 4 Anti-neutrino Candidate Selection

In order to efficiently select the real $\bar{\nu}_e$ events and reject irrelevant background events, selection rules for $\bar{\nu}_e$ candidate events are defined as follows :

- The event must be from a good quality run period
- The event must have a good reconstruction status
- The event must pass the muon spallation cut
- $|(\vec{R}_p + \vec{R}_d)/2| < 6\,m$
- $2.7\,\mathrm{MeV} < E_p < 15\,\mathrm{MeV}$
- $2.04\,\mathrm{MeV} < E_d < 2.82\,\mathrm{MeV}$
- $0.5\,\mu s < \Delta T_{p-d} < 660\,\mu s$
- $\Delta R_{p-d} < 1.6\,m$
- The event must pass the probability density estimator (PDE) cut

The definitions and efficiencies of these selection rules will be discussed in detail in the subsequent sections in this chapter. The remaining background events after the selection will be discussed in Chapter 5.

4.1 Run Selection and Live Time

As discussed in Section 2.3, two periods are defined in this analysis as before the purification and after the purification. Due to the unstable condition of the detector, the data during the purification period are not used in this analysis. The run range

Table 4.1: Summary of Run Range and Live Time.

	Run Range	Time Range	Live Time [Days]	Live Time [Days] (After Spallation Cut)
Period I	394 – 6756	2002/04 – 2007/04	1432.09	1261.35
Period II	7116 – 7830	2007/10 – 2008/06	200.41	178.52
Total			1632.50	1439.87

and time range of each period are summarized in Table 4.1. Some runs are specially taken only to understand the properties and status of the detector, such as calibration runs and background runs. Data from these runs are not included in the $\bar{\nu}_e$ analysis.

Much effort has been put by KamLAND collaborators to maximize the the total live time of the detector. Except for a few minutes between the daily run change, and the occasional trouble-shooting of the detector when problem occurs, the data-taking is almost continuous. In addition to increasing the size of the data for analysis, maximizing the live time is also idea for catching rare events such as a type II supernova in the Milky Way, which happens only about once per 40 years.

After the raw data of each run has been reconstructed into "physics events" (Chapter 3), rigorous checks of the quality of the data are performed by qualified collaborators. Based on the results of the quality checks, the entire run or sub-periods of the run could be vetoed as "bad" and are not used in the analysis. Examples of the causes of a "bad run" are high voltage failures, abnormal DAQ errors, unstable event rate, unusual noisy periods, etc. The live time of each run is then calculated by adding up the data taking time from all the clean periods, minus the short trigger disable gaps (if no trigger records are issued for more than 0.1s) when the data flow rate is too high. Given the normal trigger rate of over $\sim$100 Hz, this subtraction wrongly removes less than 0.05% of the live time and is treated as a systematic uncertainty. Summing over all the selected good runs, the total live time is 1432.09 days in Period I and 200.41 days in Period II, which is $\sim$80% of the possible maximum time. Muon spallation cut at the analysis stage effectively reduces the total live time and will be

discussed in section 4.3.

4.2 Reconstruction Quality

The event reconstruction algorithms described in Chapter 3 occasionally fail to return a good status on either the energy or the position of the event. The reason of the failure varies from the noisy unphysical events to issues that are not very-well addressed by the algorithms such as the dark hits on the PMTs. Those bad-reconstructed events are not used in this analysis. The percentage of those bad-reconstructed events vary with energy, and is more prominent at energies below 1 MeV where the "dark hits" contribute a non-negligible amount to the total PMT hits. For the energy range of $\bar{\nu}_e$ events between 2 MeV and 15 MeV though, the reconstruction is very efficient. Fig. 4.1 shows the nsummax distribution from a typical physics run for all reconstructed events and bad-reconstructed events. The typical $\bar{\nu}_e$ events have nsummax distribution from 250 to 700. An integration in this range results a conservative estimation of reconstruction efficiency of physics events being 0.9939 ± 0.0001. The reconstruction efficiency is also calculated with ^{60}Co events at 2.5 MeV and ^{68}Ge events at 1.0 MeV from calibration runs, which gives 0.9994 ± 0.0001 and 0.9989 ± 0.0001 respectively. The cumulative reconstruction efficiency for physics events is taken to be the average of the two as 0.9992 ± 0.0001.

The event is also required to have a minimum nsummax 200 to avoid occasional low nsummmax events that are acquired with special trigger types and unknown trigger efficiency. The trigger efficiency at nsummax ≥ 200 is energy dependent and can be calculated from special low-trigger-threshold runs for each energy bin as:

$$\varepsilon_{200}(E) = \frac{\text{number of events with nsummmax} \geq 200}{\text{number of total events}} \tag{4.1}$$

Fig. 4.2 shows the trigger efficiency at nsummax ≥ 200 as a function of visible energy,

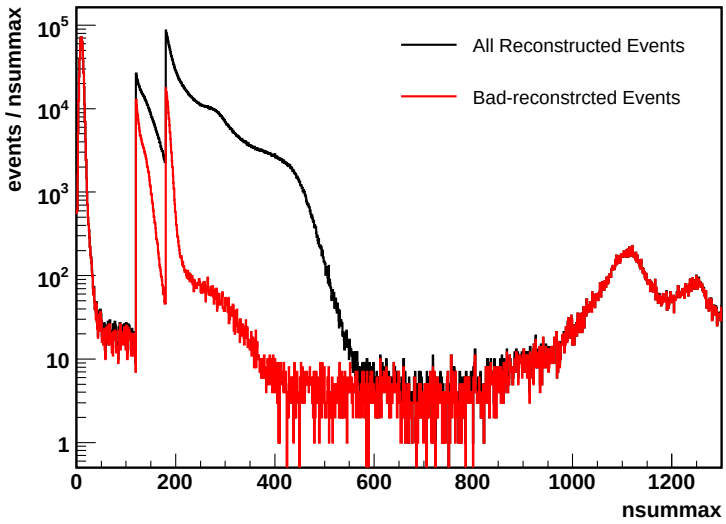

Figure 4.1: An example of the nsummax distribution from run 4274 for all reconstructed events (black) and bad-reconstructed events (red). The two vertical lines at nsummax 120 and 200 correspond to the delayed and prompt trigger thresholds. The peak at very low nsummax is due to calibration triggers and is not related to physics events. the peaks above nsummax 1000 are from muon events and post-muon noises. The efficiency of good reconstructed events for nsummax from 250 to 700 is 0.9939 ± 0.0001.

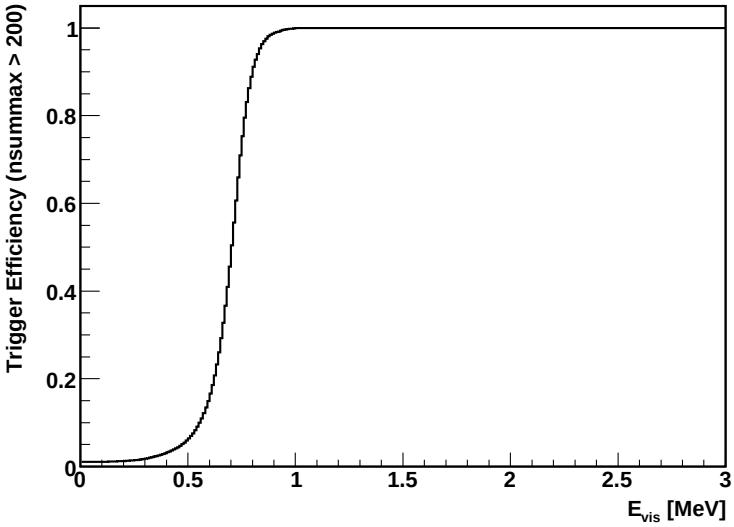

Figure 4.2: Trigger efficiency at nsummax $\geq$ 200 as a function of visible energy, calculated from a special low-threshold run 3888 with prompt trigger set at nsummax = 35.

calculated from a special low-threshold run 3888 with prompt trigger set at $\mathrm{nsum_{ID}} = 35$. Above 2.0 MeV, which is the lowest energy of the $\bar{\nu}_e$ events (from delayed neutron capture events), the trigger efficiency is essentially 100%, with negligible errors.

4.3 Muon Spallation Cut and Live Time Correction

Cosmic muons entering the KamLAND detector produce large amount of spallation products [91]. Among them the spallation neutrons and the spallation ^{9}Li's could give prompt-delayed signals and mimic the $\bar{\nu}_e$ events, so they are potential background for $\bar{\nu}_e$ detection. The high energy spallation neutrons predominantly lose energies by elastically scattering on ^{1}H nuclei. The recoiled protons inside the liquid scintillator could give prompt signals with visible energies above the analysis threshold at 2.7 MeV. The thermalized neutrons then capture on protons and give delayed signals. It is also possible that a pair of neutron captures will coincide in time given that

the neutrons are essentially created at the same time. To remove those spallation neutrons the following muon spallation cut rule is applied:

- For all inner and outer detector muons[1] the whole detector is vetoed for 2 milliseconds after the muon.

Since the neutron capture time is only $\sim$206 μs (Section 4.6), this cut essentially removes all the correlated spallation neutron background after identified muons. The remaining fast neutron background after unidentified muons will be discussed in Section 5.6. The loss of live time due to the 2 ms veto is only 0.1%. This 2 ms veto also removes the short post-muon noisy period due to the electronic effects, typically less than $10\mu s$.

The spallation ^{9}Li beta decays ($\tau_{1/2} = 178.3\,\mathrm{ms}, Q = 13.6\,\mathrm{MeV}$) to ^{9}Be and the beta particle gives a prompt signal. The excited states of ^{9}Be however are neutron unstable and could decay to ^{8}Be with emitting a neutron. This neutron then thermalizes, captures on ^{1}H and gives a delayed signal. The beta particles are not as penetrating as fast neutrons thus the ^{9}Li events are predominantly produced by muons traversing the liquid scintillator. Due to the long decay time of ^{9}Li, a 2 second veto is needed to remove 99.96% of the ^{9}Li events. Given the LS muon rate of $\sim$0.2 Hz, vetoing the whole detector after every LS muon will greatly reduce the live time of the experiment. However, as will be discussed in Section 5.5, the majority of the ^{9}Li's are produced by shower muons (a subset of LS Muons, which have the highest light yields. Appendix. C.1) and along the tracks of the muons. Thus more efficient muon spallation cut rules are applied as follows:

- For all shower muons and muons with mis-reconstructed tracks, the whole detector is vetoed for 2 seconds after the muon.

[1] Refer to Section 3.5 for definition of the muon types

- For all LS muons with well-reconstructed tracks, a 2-second veto after the muon is applied only to the 3-m cylinder volume along the muon track

The remaining number of ^{9}Li background events after these cuts will be discussed in Section 5.5.

The loss of live time due to the muon spallation cut, because of the complicated geometry dependent cut efficiency, is calculated from a simple Monte Carlo simulation on a run-by-run basis. Simulated $\bar{\nu}_e$ events are generated uniformly inside the detector volume, and events after and before the muon spallation cut are calculated. The ratio between the two is defined as "muon spallation cut efficiency" and treated as a correction to the live time of run. Fig. 4.3 shows the time variation of the muon spallation cut efficiency and it is 0.881 ± 0.004 in Period I and 0.891 ± 0.003 in Period II. The efficiency is fairly constant over time except for the jump from Period I to Period II, which is due to the decrease of rate of "shower muons" (defined as $N_{p.e}^{\text{total}} > 7 \times 10^5$) because of the $\sim 10\%$ loss of the light yield after the purification of the liquid scintillator. The total live time after the muon spallation cut, summing up all the runs used in this analysis, is 1261.35 days in Period I and 178.52 days in Period II.

4.4 Fiducial Volume Cut and Number of Target Protons

Fig. 4.4 shows the typical event vertex distribution from a normal physics run. The high event rate near the balloon edge is clearly visible. These events mostly come from the radioactive impurities on the balloon material, or from outside of the liquid scintillator such as in the buffer oil or on the PMTs. To avoid the accidental coincidence (Section 4.8.1) from these high rate background events, we take advantage of the large detector itself as a shield and only use the very inside spherical liquid

Figure 4.3: The live time fraction after spallation cut for each run. The increase in Period II is due to the decrease of number of "shower muons" because of the $\sim 10\%$ loss of the light yield after the purification of the liquid scintillator, which effectively reduced the spallation cut vetoing time.

scintillator volume with a 6 meter radius, defined as the *fiducial volume* for the analysis. Since each $\bar{\nu}_e$ detection refers to a prompt-delayed event pair, we require that the average reconstructed position of the event pair be within the fiducial volume:

- $|(\vec{R}_p + \vec{R}_d)/2| < 6m$

The total number of target protons depend on the the physical size of the fiducial volume, which could be different from the geometric size of a 6-m radius sphere due to the energy dependent reconstruction biases and uncertainties on event positions. Two methods are combined to estimate the size and the uncertainty of the fiducial volume, one with the 4π calibration data, another with the spallation ^{12}B beta decay events. The two methods are described in the following sections.

4π Calibration Measurements

The 4π calibration system, introduced in Section 2.2.4, is specifically designed to test the vertex reconstruction performance across the full detector volume. Fig. 4.5 shows

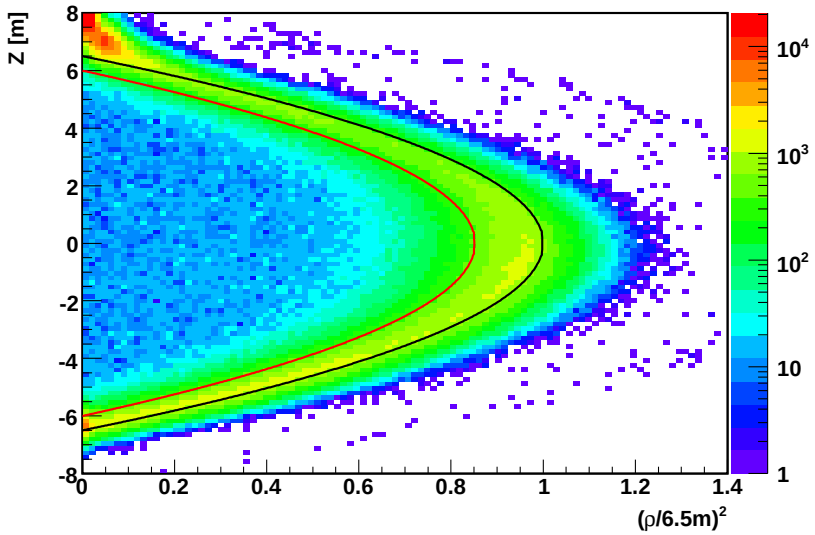

Figure 4.4: The vertex distribution of all the events with reconstructed energy higher than 1 MeV, from a one-day physics run 6756. The black line indicates the balloon position at 6.5m radius. The red line indicates the edge of the 6m fiducial volume used in this analysis.

an illustration of the 4π calibration system and an example of ^{60}Co data taken with a 4π deployment.

Excluding the initial commissioning period, sets of of 4π calibration runs were performed around Oct 2006 to systematically scan the full detector volume. For each pole configuration, data were taken at a range of zenith positions while pivoting the pole about the detector center. Fig. 4.6 shows the radial distribution of all off-axis source deployments with the composite ^{60}Co^{68}Ge source in a single azimuthal plane. The maximum radial reach at the equator was 4.6 m. Additional points were probed along the equatorial plane and near the polar regions by translating the pole up and down, allowing a maximum radial reach of 5.5 m. To study the energy dependence of reconstruction deviations, deployments were also made to a subset of the points using other sources.

The 4π calibration data were analyzed in detail in Ref. [85]. Table 4.2 summarizes the radial position reconstruction bias and the corresponding volume bias at 5.5

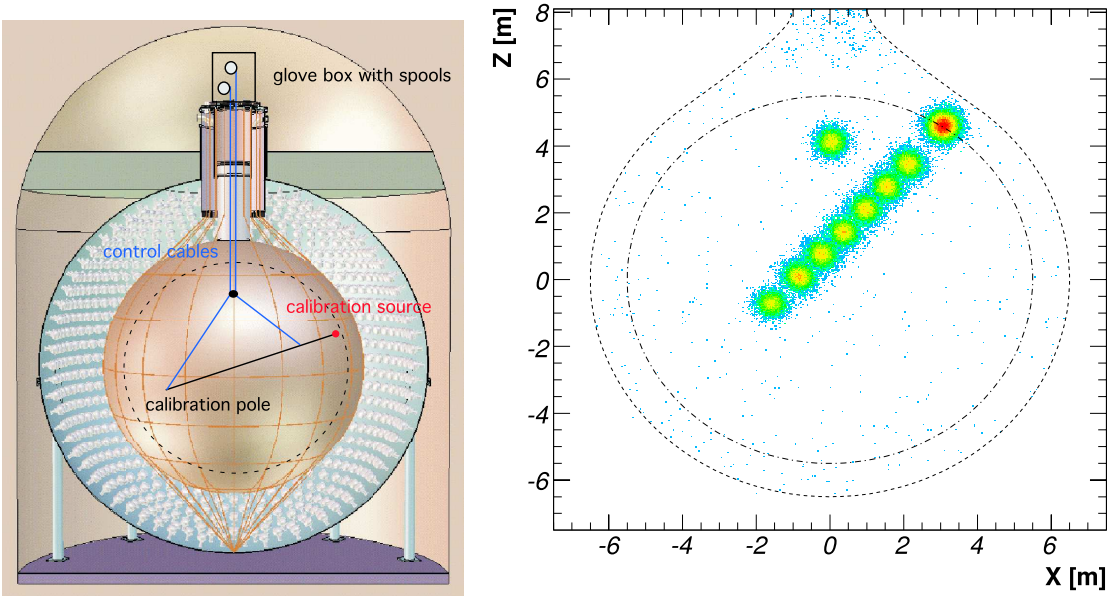

(a) (b)

Figure 4.5: (a) Illustration of the 4π calibration system in the KamLAND detector. A radioactive source was attached to one end of the pole, and was positioned throughout the fiducial volume by adjusting the orientation and the length of the pole. Additional ^{60}Co pin sources were located along the pole for monitoring the pole position. Two cables and a spool system manipulated the pole position. (b) An example of ^{60}Co data taken with a 4π deployment (run 6167).

Source	Radial Bias [mm]	Volume Deviation [%]
^{60}Co, 2.5 MeV	-5 ± 17	0.3 ± 0.9
^{68}Ge, 1.0 MeV	15 ± 20	-0.8 ± 1.1
^{241}Am^{9}Be, 2.2 MeV	-5 ± 18	0.3 ± 1.0
^{241}Am^{9}Be, 4.5–7 MeV	25 ± 26	-1.4 ± 1.5
^{210}Po^{13}C, 4.4 MeV	25 ± 28	-1.4 ± 1.6
^{210}Po^{13}C, 6.1 MeV	105 ± 34	-5.7 ± 1.9

Table 4.2: The fiducial volume measurements from 4π calibrations with different sources. The radial bias and volume deviation is evaluated at 5.5 m radius.

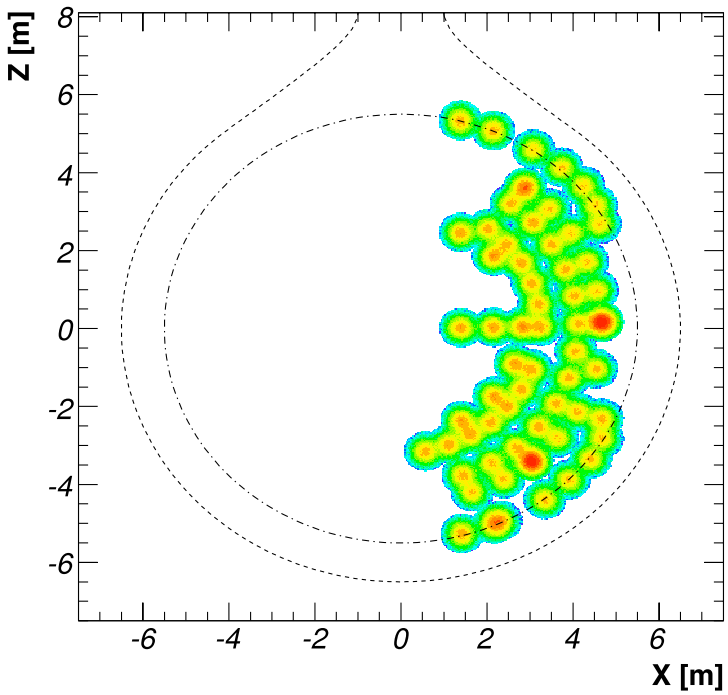

Figure 4.6: The radial distribution of all off-axis source deployments with the composite ^{60}Co^{68}Ge source excluding the initial commissioning runs, in a single azimuthal plane.

m radius, measured with different sources at different energies. The mean fiducial volume $\langle f \rangle$ and its uncertainty $\langle \sigma_f \rangle$ for $\bar{\nu}_e$ events is obtained by integrating $f(E)$ across the expected unoscillated $\bar{\nu}_e$ spectrum $S(E)$. Using the best fit oscillated $\bar{\nu}_e$ energy spectrum resulted in negligible changes in the results.

$$\langle f \rangle = \frac{\int_{E_0}^{E_1} f(E) \cdot S(E) \mathrm{d}E}{\int_{E_0}^{E_1} S(E) \mathrm{d}E} \tag{4.2}$$

and

$$\langle \sigma_f \rangle = \frac{\int_{E_0}^{E_1} \sigma_f(E) \cdot S(E) \mathrm{d}E}{\int_{E_0}^{E_1} S(E) \mathrm{d}E} \tag{4.3}$$

$f(E)$ is obtained from a linear fit to the data summarized in Table 4.2. It is found that the result is insensitive to the choice of model of $f(E)$. Comparing with geometric size of a 5.5 m radius sphere, the fiducial volume at radius 5.5 m is reduced by 1.0% to be 689.9 ± 13.8 m^3. The relative uncertainty is 2.0%.

Spallation ^{12}B Measurements

The maximum radial reach of the 4π calibration is 5.5 m. This is determined mainly to ensure the safety of the balloon, which is located at radius of 6.5 m. The fiducial volume used in this analysis is however at radius 6 m. It is non-trivial to extrapolate the 4π calibration data directly to 6 m. Instead, we use a separate method to evaluate the fiducial volume between 5.5 m and 6 m.

The spallation ^{12}B events are generated by the cosmic muons uniformly over the detector volume. We define the fiducial volume ratio R_{fv} as the number of the spallation ^{12}B beta decay events inside the fiducial volume divided by the number of the spallation ^{12}B events in the whole detector. The fiducial volume V_{fv} can then be simply expressed as:

$$V_{fv} = V_{\mathrm{LS}} \cdot R_{\mathrm{fv}} \tag{4.4}$$

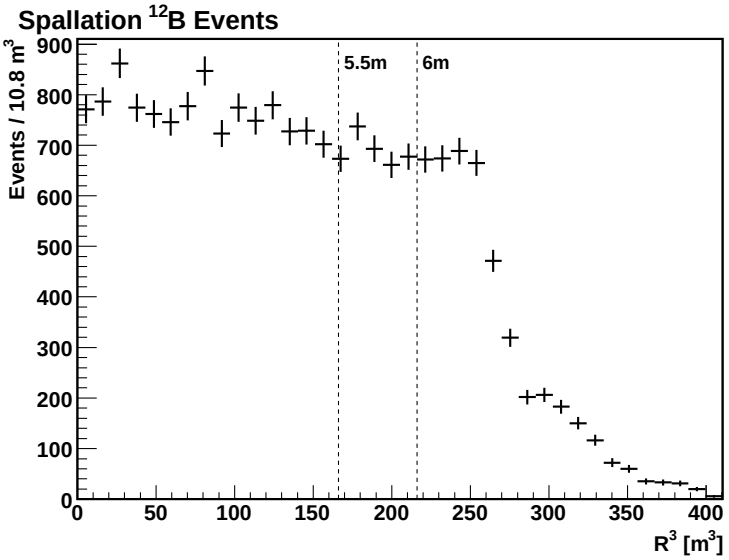

Figure 4.7: The background subtracted spacial distribution of spallation ^{12}B Events. The dotted line indicates the fiducial volume boundary at radius 5.5 m and 6 m.

where $V_{\rm LS}$ is the total volume of the liquid scintillator measured with flow-meter during the filling of the LS to be 1171 ± 25 m^3. One crucial assumption of the ^{12}B method is that KamLAND detects the ^{12}B events with 100% efficiency inside liquid scintillator volume and zero efficiency outside. Simulation shows that the portion of the beta particles from ^{12}B decay that are generated outside of the liquid scintillator but deposit part of the energies inside the LS near the boundary introduces a 0.5% systematic uncertainty.

The selection of spallation ^{12}B events is summarized in Appendix C.4.2. The spacial distribution of all ^{12}B events in Period I with visible energies between 4 MeV and 14 MeV are shown in Fig. 4.7. The distortion from uniform distribution near the balloon edge is caused by the reconstruction resolution, imperfect shape of the balloon, and decrease of efficiency at the very edge of the balloon. The fiducial volume ratio $R_{\rm fv}^{5.5m}$ for radius less than 5.5 m is calculated to be $0.602 \cdot (1 \pm 1.2\%)$ where the uncertainty is statistical only. This results a fiducial volume of 704.9 m^3 for $R < 5.5$ m. Comparing with the 4π calibration results (689.9 m^3), the two measurements

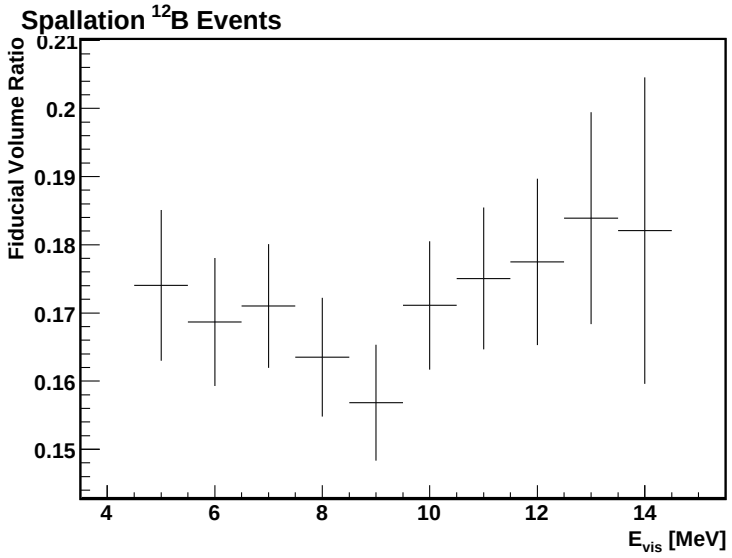

Figure 4.8: The ratio of fiducial volume between radius 5.5 m and 6 m to all liquid scintillator volume as a function of reconstructed energy, calculated from spallation ^{12}B events.

agreed to within 2.2%.

The fiducial volume between radius 5.5 m and 6 m is measured with the ^{12}B method only. The fiducial volume ratio $R_{\rm fv}^{5.5m-6m}$ is calculated to be $0.173 \cdot (1 \pm 0.02_{\rm stat.})$. To further investigate the energy dependent systematic uncertainties on fiducial volume, the spallation ^{12}B events are binned into 1 MeV bins. $R_{\rm fv}^{5.5m-6m}$ is calculated for each bin and is shown in Fig. 4.8. The systematic uncertainties from energy dependency is calculated to be 4.5% using Eqn. 4.3 with a linear fit to the data. The uncertainty is found to be insensitive to the choice of the fit functions. Combining together, the fiducial volume between radius 5.5 m and 6 m from the ^{12}B measurement is 202.6 ± 10.9 m^3. The relative uncertainty is 5.4%.

The total fiducial volume inside 6 m radius is obtained by combining the 4π calibration measurements and the spallation ^{12}B measurement to be 892.5 ± 17.6 m^3. The relative uncertainty is 2.0%. Comparing with geometric size of a 6 m radius sphere, the fiducial volume is reduced by 1.4%.

In Period II, the change of liquid scintillator properties after the purification sys-

tematically affects the quality of the event reconstructions. For this reason the results from the 4π calibrations, which were only deployed in Period I, are not applied to Period II. The fiducial volume inside 6 m radius is measured by the ^{12}B data in Period II only. The fiducial volume in Period II is measured to be 907.0 ± 59.7 m^3. The relative uncertainty is 6.6%.

Number of Target Protons

The total number of target protons can be calculated as

$$N_{\rm p} = I_{^1{\rm H}} \cdot n_{\rm H} \cdot \rho_{\rm LS} \cdot V_{\rm fv} \tag{4.5}$$

where $I_{^1{\rm H}} = 0.99985$ is the isotopic abundance of ^{1}H, $n_{\rm H}$ is the number density of hydrogen atoms per unit mass, $\rho_{\rm LS}$ is the density of the liquid scintillator, and $V_{\rm fv}$ is the fiducial volume defined by the analysis and measured with the 4π calibration and spallation ^{12}B events.

The number density of hydrogen atoms per unit mass is calculated as follows:

$$\begin{aligned} n_{\rm H} &= \frac{N_A}{m_H + m_C/(H/C) + m_N/(H/N) + m_O/(H/O)} \\ &= 8.4708 \times 10^{22}/g \end{aligned} \tag{4.6}$$

where the masses are referring to the atomic mass of H, C, N and O. The ratio of H/C , H/N and H/O are calculated from the composition of the liquid scintillator to be 1.96908, 17842.0 and 17842.0 where the small amount of nitrogen and oxygen come from the fluor PPO. The H to C ratio was verified by elemental analysis to within $\pm 2\%$, which translates into $\pm 0.1\%$ in the uncertainty of $n_{\rm H}$.

The density of KamLAND liquid scintillator is measured to be 0.7775 ± 0.0001 g/cm^3 at 15 °C in both periods. The actual temperature distribution in KamLAND is

not uniform, and is measured to be $11.5 \pm 1.5\,^{\circ}\mathrm{C}$ with the instrument units during the 4π calibration system deployments [88]. The temperature of the liquid scintillator in Period II is a little higher during the filling to keep the new LS in separate with the old LS, and an conservative estimation of $\pm 4\,^{\circ}\mathrm{C}$ is assigned to the systematic uncertainty. Given the temperature coefficient of density of the liquid scintillator measured to be -7.41×10^{-4} g/cm^3/K, the actual density of KamLAND liquid scintillator is 0.7796 g/cm^3 with 0.1% uncertainty in Period I and 0.4% uncertainty in Period II.

Putting all the values and uncertainties into Eqn. 4.5, the total number of target protons is calculated to be $5.89 \times 10^{31} \cdot (1 \pm 2.0\%)$ in Period I and $5.99 \times 10^{31} \cdot (1 \pm 6.6\%)$ in Period II. The contributions of uncertainties are summarized in Table 4.3.

Table 4.3: Summary of Uncertainties on Target Protons

Description	Uncertainty [%]	
	Period I	Period II
Fiducial Volume	2.0	6.6
Density variation from composition	0.1	0.1
Density variation from temperature	0.1	0.4
Total	2.0	6.6

Combining with the live time measurement discussed in Section 4.1 and 4.3, the total exposure for this analysis is 8.50×10^{34} proton-days, or $\sim$2.75 kiloton-years.

4.5 Prompt and Delayed Energy Cut

The following selection rules on the visible energy of prompt and delayed events are applied in this analysis:

- $2.7\,\mathrm{MeV} < E_p < 15\,\mathrm{MeV}$
- $2.04\,\mathrm{MeV} < E_d < 2.82\,\mathrm{MeV}$

The prompt events are required to have visible energies higher than 2.7 MeV to specifically avoid the $\bar{\nu}_e$ background from the decay chains of natural radioactivities,

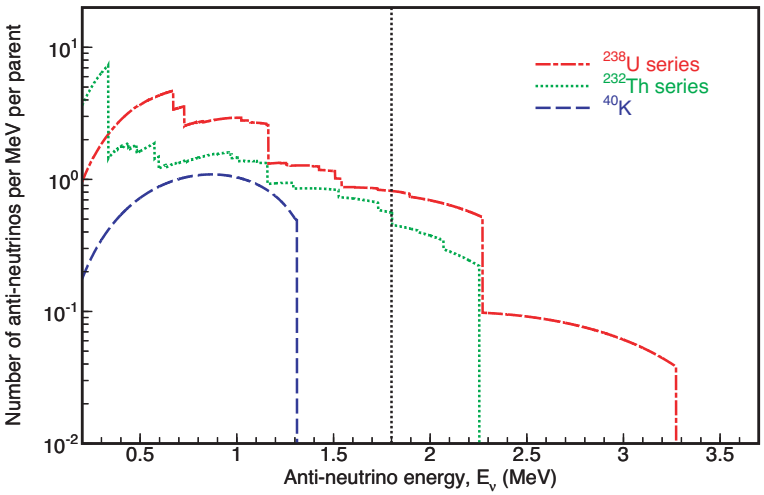

Figure 4.9: The energy spectrum of $\bar{\nu}_e$ from ^{238}U, ^{232}Th and ^{40}K decay chains, which are the natural radioactivities in the Earth. The dotted line indicates the inverse beta decay threshold at 1.8 MeV. KamLAND is insensitive of detecting $\bar{\nu}_e$'s below this threshold. Figure taken from [21].

mainly ^{238}U, ^{232}Th and ^{40}K, in the Earth. These $\bar{\nu}_e$'s are often referred to as "geo-neutrinos." Fig. 4.9 shows the energy spectra of $\bar{\nu}_e$ from ^{238}U, ^{232}Th and ^{40}K decay chains. The maximum energy of these $\bar{\nu}_e$'s is 3.3 MeV, corresponding to 2.5 MeV for the prompt positron event. Given the energy response model and detector resolution (Section 3.4), a cut at $E_p > 2.7$MeV removes the contribution from geo-neutrinos with 100% efficiency and negligible uncertainties. The geo-neutrinos are however very interesting and important topics in geology. Geological models predict the radiogenic heat composes ~19 TW or more of the total Earth's heat flow [18, 19, 20]. A dedicated analysis on KamLAND low energy data [21] is now putting good constrains on the radiogenic power of uranium and thorium in the Earth.

The $\bar{\nu}_e$ flux from the fission reactions from nuclear reactors and the georeactor is negligible above 8.5 MeV (Fig. 5.2). We, however, include higher energy events up to $E_p = 15$ MeV in this analysis to constrain the number of fast neutron and atmospheric neutrino background events from the shape of the spectrum at high energies. Details of those backgrounds will be discussed in Section 5.6 and 5.7.

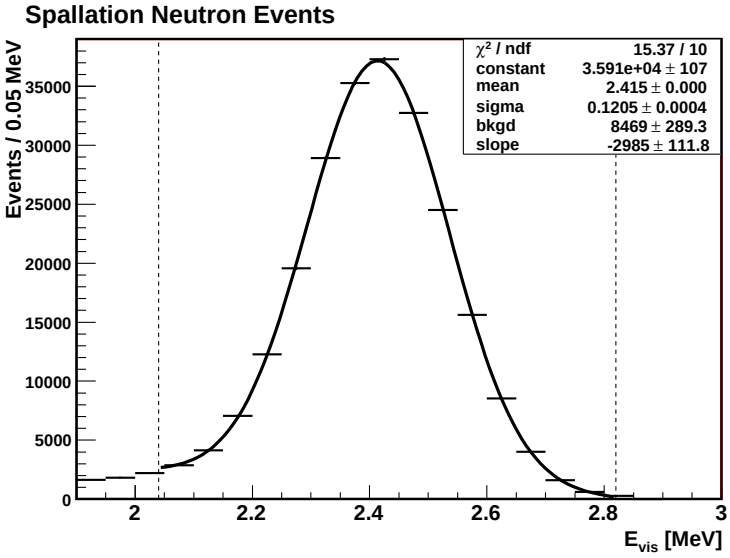

Figure 4.10: The reconstructed energy distribution of the spallation neutron capture events. The efficiency of the delayed energy cut 2.04MeV $< E_d <$ 2.82MeV is calculated from the fitted Gaussian peak to be 0.9987 ± 0.0003. The dotted lines indicate the delayed energy cut thresholds.

The delayed event from neutron capture on ^{1}H is a monochromatic gamma-ray at 2.2 MeV. The visible energy cut on the delayed events is set to be 2.04MeV $< E_d <$ 2.82MeV for historical reasons to agree with the older analysis [85]. The efficiency of this cut is calculated from the reconstructed energy distribution of the spallation neutron capture events (Fig. 4.10) to be 0.9987 ± 0.0003.

The neutrons can, however, capture on other nuclei besides ^{1}H. Table 4.4 lists the possible target nuclei in KamLAND liquid scintillator for (n,γ) reaction and the corresponding cross sections and γ-ray energies, in decreasing order of number densities of the nuclei. Besides ^{1}H, only ^{12}C contributes non-negligibly to the neutron capture process. The efficiency of only selecting neutron capture on ^{1}H is calculated to be 0.9946 ± 0.0010.

Table 4.4: Target Nuclei for (n,γ) Reaction in KamLAND

Target Nuclei	Cross Section [mb]	E_γ [MeV]	Density [nuclei/cm^3]
^{1}H	332.6 (7)	2.22	6.603×10^{22}
^{12}C	3.53 (5)	4.95	3.316×10^{22}
^{13}C	1.37 (4)	8.17	3.723×10^{20}
^{2}H	0.519 (7)	6.25	9.905×10^{18}
^{16}O	0.19 (2)	4.14	3.692×10^{18}
^{14}N	80 (2)	10.83	3.687×10^{18}

4.6 Time Correlation Cut

The temporal correlation between the prompt and delayed event from the inverse beta decay is a very powerful tool to reject background from the $\bar{\nu}_e$ events. The following selection rule on the time correlation is applied in this analysis:

- $0.5\,\mu s < \Delta T_{p-d} < 660\,\mu s$

The probability of a thermalized neutron get captured in a time interval dt is constant over time ("lack of aging"), thus the neutron capture time follows an exponential distribution. The mean neutron capture time τ can be estimated on the first order as following:

$$\frac{1}{\tau} = \frac{v}{\lambda} = v \cdot \sum_i n_i \sigma_i(v) \tag{4.7}$$

where v is the velocity of the neutron, λ is the mean free path of the neutron, n_i and σ_i are the number density and cross section of target nuclei i as listed in Table 4.4. The cross sections in Table 4.4 are measured at neutron velocity $v_0 = 2200$ m/s [101], however, if we assume that the neutron capture cross section is inversely proportional to its velocity (which is true at neutron energies below ~10 keV), then

$$v \cdot \sigma(v) = v_0 \cdot \sigma(v_0) \tag{4.8}$$

and the capture time becomes independent of the neutron energy. The time it takes to slow down an energetic neutron to below 10 keV is less than 0.1 μs and can

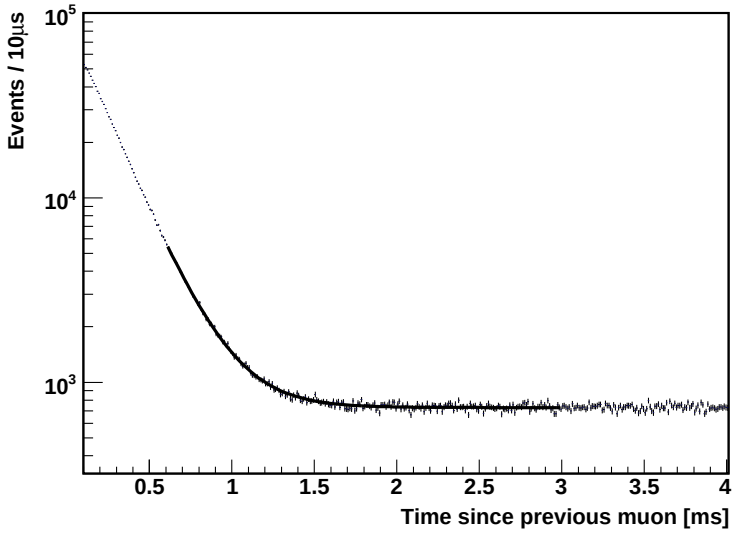

Figure 4.11: The distribution of time to the previous muon for all spallation neutrons inside 6m fiducial volume. A fit from 0.6 ms to 3 ms to exponential distribution plus a flat background results the mean neutron capture time $\tau = 206.4 \pm 1.3\mu s$. The χ^2/ndf from the fit is 227/237.

be neglected here. Using the values from Table 4.4, this simple estimation gives $\tau \sim 206\,\mu s$.

A better estimation comes from the study of spallation neutron events in the detector. Fig. 4.11 shows the distribution of time to the previous muon for all spallation neutrons in the analysis periods inside 6m fiducial volume. As shown in Fig. C.8(a), muons with high multiplicity (number of events within 0.15 – 10 ms following a muon) result in severe loss of waveforms and spallation events immediately following the muon. For this reason only muons with multiplicity less than 75 are included. We fit the distribution to an exponential distribution plus a flat background from 0.6 ms to 3 ms and avoid the earlier time since the loss of neutron events immediately after muon will distort the distribution. This yields the mean neutron capture time $\tau = 206.4 \pm 1.3\mu s$. The efficiency of time correlation cut can be then calculated from:

$$\varepsilon_{\Delta T} = \int_{0.5\mu s}^{660\mu s} \frac{1}{\tau} e^{-t/\tau} \mathrm{d}t \tag{4.9}$$

to be 0.9567 ± 0.0008.

The neutron capture time from spallation neutron study is cross-checked with the data from ^{241}Am^{9}Be z-axis calibration runs. The measured neutron capture time from combining all the ^{241}Am^{9}Be data is $205.2 \pm 0.5\,\mu s$ [91]. The discrepancy between this value and the one from the spallation neutron measurement is not completely understood, but is suspected to be caused by neutrons from the ^{241}Am^{9}Be source that capture on the stainless-steel source capsule, which has mostly iron whose neutron capture cross section is $\sim$10 times higher than ^{1}H. The efficiency of the time correlation cut is insensitive to this discrepancy though.

4.7 Spacial Correlation Cut

The prompt positron event and delayed neutron capture gamma event are also correlated in space. The following spacial correlation cut is applied to further reject background events:

- $\Delta R_{p-d} < 1.6\,m$

The distribution of the distance of the prompt/delayed event position to the $\bar{\nu}_e$ inverse beta decay interaction position is approximated from the ^{68}Ge and AmBe z-axis calibration data respectively. The ^{68}Ge event radial spread may be taken as an upper limit for prompt event since the absorption length is much shorter for positrons than for the (annihilation) γ's. Fig. 4.12 shows the distribution of the distance of the ^{68}Ge event (two annihilation γ's) position to the ^{68}Ge source position (black line), and the AmBe neutron capture gamma event position to the AmBe source position (blue line), from summing up all the corresponding z-axis calibration runs across the liquid scintillator volume in the analysis periods. These distributions are then taken as an input into a simple simulation where the positions of the prompt and delayed events are generated assuming no angular correlation. The distribution of the distance

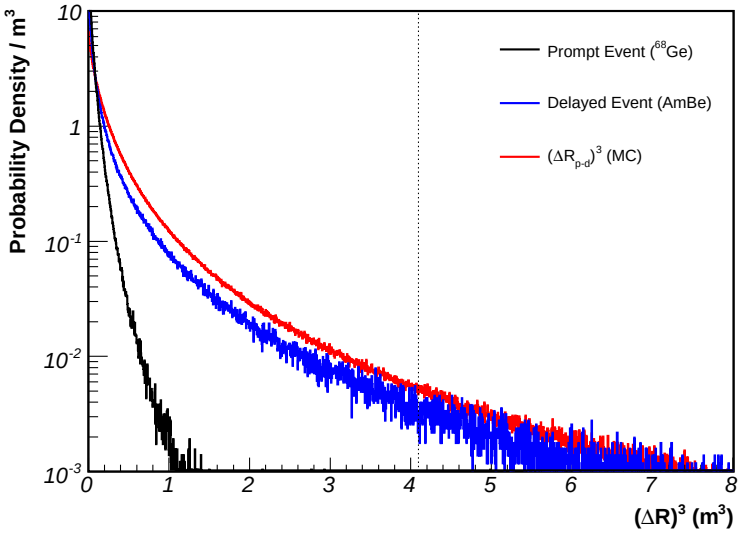

Figure 4.12: The distribution of the distance of the ^{68}Ge event position to the ^{68}Ge source position (black line) and the AmBe neutron capture gamma event position to the AmBe source position (blue line), calculated from z-axis calibration runs. Also shown is the distribution of the distances between prompt and delayed events (red line) from monte carlo simulations. The dotted line indicates the spacial correlation cut at $(\Delta R_{p-d})^3 = 4.096$ m^3.

between the two is plotted in Fig. 4.12 (red line). Since the ^{68}Ge event distribution gives a maximal absorption length for the prompt event, the fraction of the simulated events within 1.6 m of each other can be taken as an upper limit of the efficiency. The lower limit is obtained by assuming no smearing of prompt event, in other words by integrating the AmBe distribution. The efficiency of the $\Delta R_{p-d} < 1.6\,m$ cut is calculated in this way to be 0.9881 ± 0.0057.

The efficiency on spacial correlation cut is cross-checked with the result using GEANT4 [102] based KLG4sim (KamLAND Monte Carlo Simulation) full detector simulation package, where inverse beta decay events were simulated uniformly inside the detector and distribution of ΔR_{p-d} is calculated. KLG4sim simulation yields the efficiency being 0.9887 ± 0.0051 [84]. The results of the two methods agree well with each other.

4.8 Probability Density Estimator (PDE) Cut

The so far discussed "box-cuts" combined all together are very efficient in selecting $\bar{\nu}_e$ signals and rejecting background events, and were actually all one needed for a 5.5m-radius or less fiducial volume analysis, for example in Ref. [85, 84]. However, when we enlarge the fiducial volume to 6m radius, the accidental coincidence background starts to become significant and further rejection method is needed.

4.8.1 Accidental Coincidence Background

The normal trigger rate of KamLAND is just over ∼100 Hz. Most of these events are uncorrelated in time and do not cause background for $\bar{\nu}_e$ detection and are referred to as "singles events." Fig. 4.13 shows the singles event rate of each run for all good-reconstructed events that have nsummax higher than 200 (or 180 for runs before 3753) and have passed the muon spallation cuts (Section 4.3). The jumps in singles rate are mostly correlated with electronics upgrades, while the sudden drop between Period I and II comes from the decrease of the radioactive impurities are purification.

Although singles events themselves do not cause background for $\bar{\nu}_e$ detection, because of the high event rate, two events can accidentally coincide in time and be wrongly tagged as a prompt-delayed pair. The probability of seeing two random singles events inside the time correlation cut window ΔT_{p-d} follows Poisson distribution and can be calculated on a run-by-run basis as follows:

$$P_{\text{coincidence}} = f(n;\nu) = f(1; R_{\text{singles}} \cdot \Delta T_{p-d}) \tag{4.10}$$

where ν is the expected number of singles events inside the ΔT_{p-d} window, and R_{singles} is the singles rate of the run. For a 20 Hz singles rate, $P_{\text{coincidence}}$ is ∼1.3%.

The accidentally temporal correlated events need to pass the other "box-cuts" selection rules in order to be considered as "$\bar{\nu}_e$ candidate events." The probability

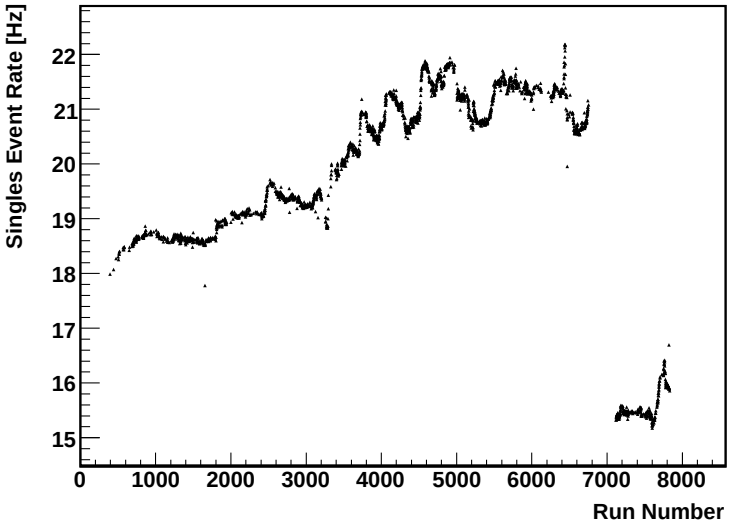

Figure 4.13: The singles event rate per run, where "singles" refers to all good-reconstructed events in the detector with nsummax > 200 and have passed the muon spallation cuts.

that this could happen is calculated on a run-by-run basis. Singles events in each run are randomly paired with each other and the probability P_{cuts} is defined as the number the event pairs that satisfy the prompt and delayed energy cut, spacial correlation cut and fiducial volume cut, divided by the total number of event pairs. To avoid the possible correlations during event pairing, each event is used once and only once, so the total number of event pairs is just half of the total number of singles events.

The total number of accidental background events can be then calculated as:

$$N_{\text{accidentals}} = \sum_{\text{run}} T_{\text{run}} \cdot R_{\text{singles}} \cdot P_{\text{coincidence}} \cdot P_{\text{cuts}} \tag{4.11}$$

where T_{run} is the live time of each run and we sum over all the runs in the analysis period. For the 6m fiducial volume, the number of accidental background events is calculated to be 438.7 ± 3.8 in Period I and 84.7 ± 1.5 in Period II. The accidental background is about half of the number of expected reactor $\bar{\nu}_e$'s (Section 5.1) and

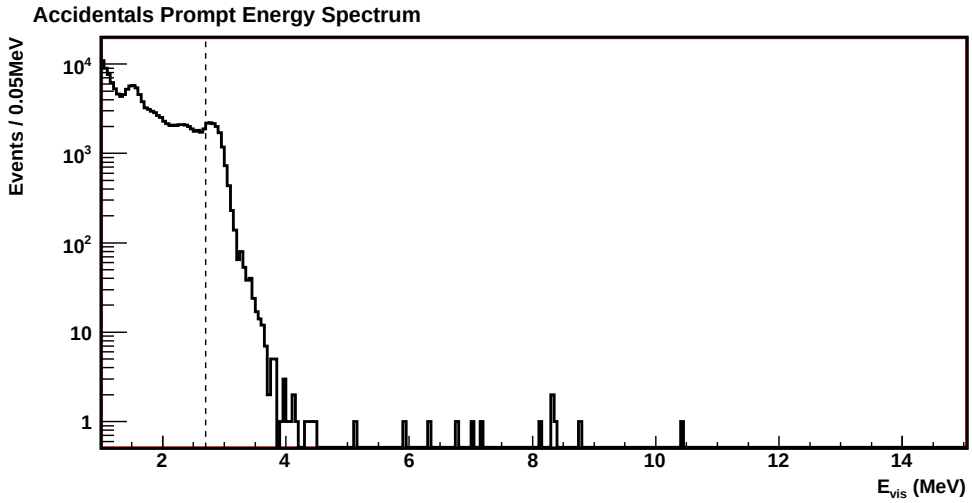

(a)

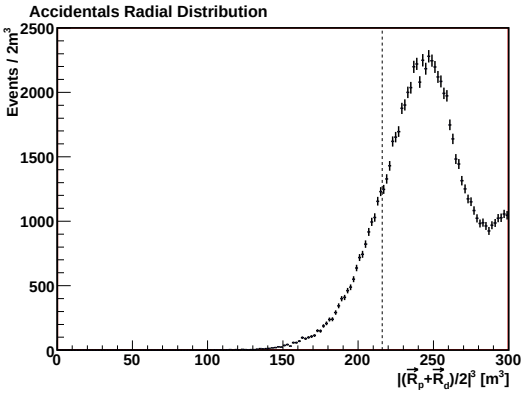

(b)

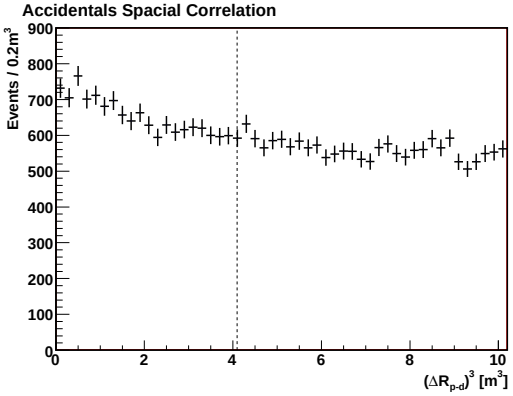

(c)

Figure 4.14: Statistically measured properties of accidental coincidence background: (a) Prompt visible energy spectrum. The dotted line indicates the analysis threshold at 2.7 MeV. (b) Radial distribution of average position of prompt and delayed events. The dotted line indicates the fiducial volume boundary at 6m. (c) Distribution of distance between prompt and delayed events. The dotted line indicates the spacial correlation cut at $(\Delta R_{p-d})^3 = 4.096$ m^3.

requires further reduction in order to get a good signal to background ratio [2].

Fig. 4.14 shows some of the properties of the accidental coincidence background from the statistical measurement. The prompt visible energy spectrum is shown in Fig. 4.14(a). The peak near the analysis threshold 2.7 MeV is caused by the

[2]For a 5.5m fiducial volume, the number of the accidental coincidence events is greatly reduced to 22.5 ± 0.9 in Period I and 4.3 ± 0.3 in Period II. This is the reason why smaller fiducial volumes are chosen in the earlier KamLAND analysis, for example in Ref. [45, 46].

external gamma-ray from ^{208}Tl concentrated on the balloon surface and outside of liquid scintillator, which beta decays (Q = 5.0 MeV) to ^{208}Pb and emits a 2.6 MeV gamma-ray. The accidentals event rate drops sharply as energy increases and becomes negligible above 4 MeV.

Fig. 4.14(b) shows the radial distribution of the average position of the prompt and delayed events from the accidental coincidence background. The distribution follows a Gaussian shape with the mean position at the balloon surface, which is very different from the uniformly distributed $\bar{\nu}_e$ events. The accidentals event rate becomes negligible at radius less than 5m, but is still significant near the 6m fiducial volume boundary. Fig. 4.14(c) shows the distribution of distance between prompt and delayed events. Compared with the $\bar{\nu}_e$ events (Fig. 4.12), the temporal correlated accidental coincidence events are only weakly correlated in space. The differences in the spacial distributions between accidental coincidence events and $\bar{\nu}_e$ events make further background rejection possible with a multivariate analysis method, as will be discussed in Section 4.8.2.

4.8.2 PDE Cut Definition

Compared with traditional "box cut" methods, multivariate data analysis tries to extract a maximum of the available information from the data by combining different properties ("variables") of the data. The systematic uncertainties from the multivariate analysis, however, are generally complicated and extensive Monte Carlo simulations are needed to extract the full error matrix, if a lot of variables are used. To avoid the complication, we construct the probability density estimator (PDE) using only two spacial variables:

- R_{mean} : The mean radial position of the prompt and delayed events.
- ΔR : The distance between the prompt and delayed events.

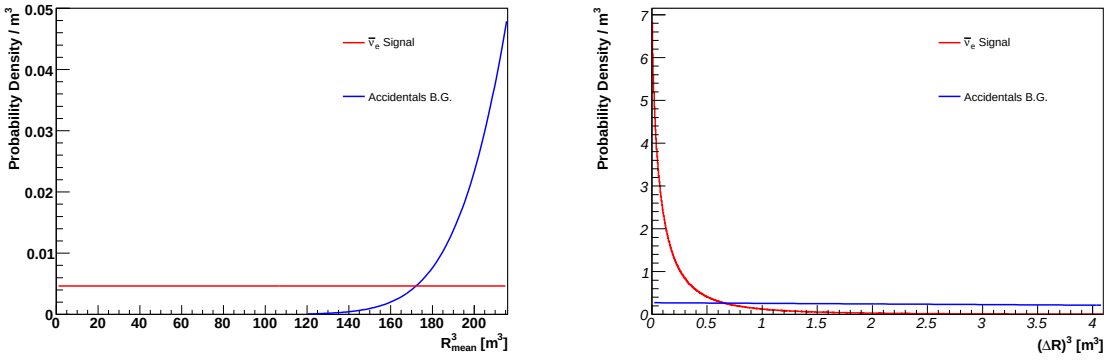

(a) (b)

Figure 4.15: Probability density function for $\bar{\nu}_e$ signal and accidental background events. (a) Pdf's of mean position of the prompt and delayed events, normalized inside the 6m fiducial volume. (b) Pdf's of distance between the prompt and delayed events, normalized insidethe $\Delta R_{p-d} < 1.6m$ cut.

and define the PDE, following the likelihood ratio method, as:

$$\text{PDE} = \frac{L_{\text{signal}}}{L_{\text{signal}} + L_{\text{background}}} \tag{4.12}$$

where L_{signal} or $L_{\text{background}}$ is the likelihood (probability) that an event is a $\bar{\nu}_e$ signal event or an accidental coincidence background event. The likelihood can be calculated by:

$$L^{\alpha} = \prod_i (\text{pdf})_i^{\alpha} \qquad \alpha = \text{Signal or B.G.} \tag{4.13}$$

where the subscript i runs over all the variables used in the multivariate analysis and $(\text{pdf})_i^{\alpha}$ stands for the probability density function of variable i, for signal events or background events respectively. With this definition, a signal-like event will have a PDE close to 1 and a background-like event will have a PDE close to 0.

The probability density functions of R^3_{mean} and $(\Delta R)^3$ for signal and background events are shown in Fig. 4.15. The $\bar{\nu}_e$ signal events are taken to be uniformly distributed in the detector so their R^3_{mean} distribution is flat, while the R^3_{mean} distribution for accidental backgrounds is calculated from a fit to a Gaussian function from

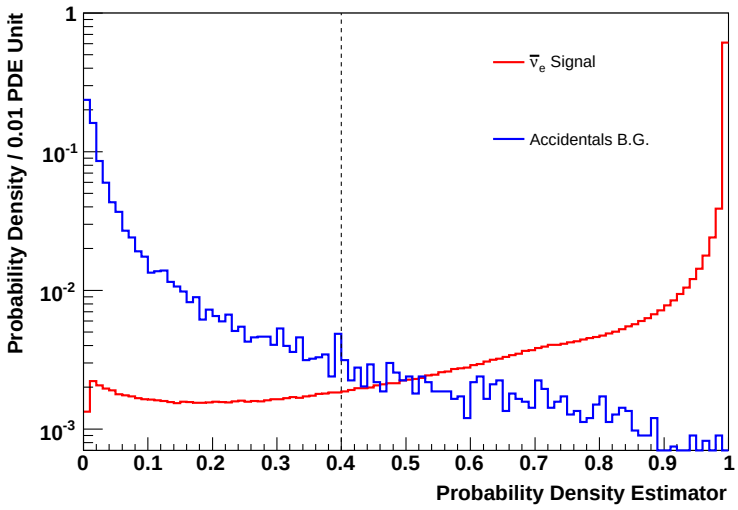

Figure 4.16: The distribution of probability density estimator (PDE) for simulated $\bar{\nu}_e$ signal and accidentals background events. Signal and background events are strongly peaked at 1 and 0 respectively. The dotted line indicates the PDE cut at PDE > 0.4.

Fig. 4.14(b) (χ^2/ndf = 34.1/44). These distributions are then normalized to unity inside the 6m fiducial volume. $(\Delta R)^3$ distribution for $\bar{\nu}_e$ signal events has been shown in Fig. 4.12, and for accidental backgrounds is calculated from a linear fit to the distribution shown in Fig. 4.14(c) (χ^2/ndf = 13.6/19). The $(\Delta R)^3$ distributions are then normalized to unity inside the $\Delta R_{p-d} < 1.6$ m cut.

With the pdf of each variable defined, the PDE can be calculated from Eqn. 4.12 for each simulated $\bar{\nu}_e$ event and accidental coincidence event. The normalized distribution of PDE is shown in Fig. 4.16. As expected, the $\bar{\nu}_e$ signal events' PDEs are strongly peaked at 1 and the accidental background events' PDEs are strongly peaked at 0.

To determine where the PDE cut threshold should be placed, three "figure of merit" rules are considered:

1. High signal acceptance efficiency.

2. High background rejection efficiency.

3. High $S/\sqrt{S+B}$ for good statistical performance.

Rule 1 and 2 are in general contradictory with each other and some prior decisions need to be made. The decision in this analysis is set such that the PDE cut will reduce the accidentals background to equal or below the background from other sources ($\sim$40 events, Table 5.4), while keeping the signal efficiency above 90%. Fig. 4.17(a) plots the signal efficiency and number of accidental background events as a function of PDE cut threshold. A PDE cut placed at 0.4 will have a 93.30% signal efficiency, while reducing the accidentals background from 438.7 to 42.0 events (in Period I), a 90.43% background rejection efficiency. This satisfies our prior requirements.

It's always a good idea to maximize $S/\sqrt{S+B}$ (rule 3) to reduce the statistical uncertainties. The total number of signal events, however, is unclear in prior because of the suppression by neutrino oscillation and unknown amount of georeactor $\bar{\nu}_e$ events. If we take the oscillation parameters from Ref. [22] and assume null georeactor contribution, the $S/\sqrt{S+B}$ can be estimated and used as a cross-check on the PDE cut decision. Fig. 4.17(b) shows $S/\sqrt{S+B}$ as a function of PDE cut threshold, and a plateau exists for optimum performance of $S/\sqrt{S+B}$. The PDE cut placed at 0.4 will put us in the middle of the plateau and satisfies all three "figure of merit" rules, thus is used in this analysis:

- Events must have probability density estimator (PDE) higher than 0.4

The total efficiency of PDE > 0.4 cut is calculated to be 0.9330 ± 0.0047 where the uncertainty comes from allowing the ΔR distribution of $\bar{\nu}_e$ events to vary within its uncertainty from the Monte Carlo simulation (Section 4.7). Fig. 4.18. shows the PDE cut efficiency as a function of $R^3_{\rm mean}$. The efficiency drops quickly near the fiducial volume boundary as the accidental backgrounds start to dominate. The total number of accidental coincidence events, after the PDE cut, is 40.2 ± 1.2 in Period I and 8.2 ± 0.5 in Period II. It is worthing emphasizing that the efficiency of the PDE

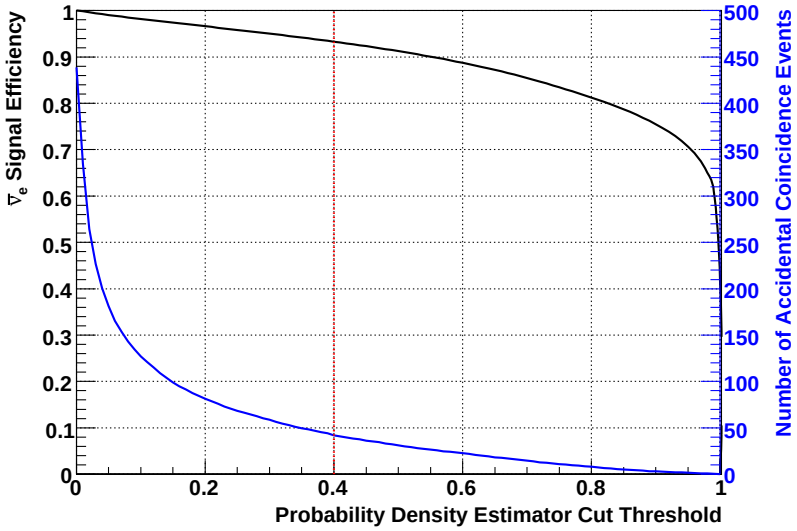

(a)

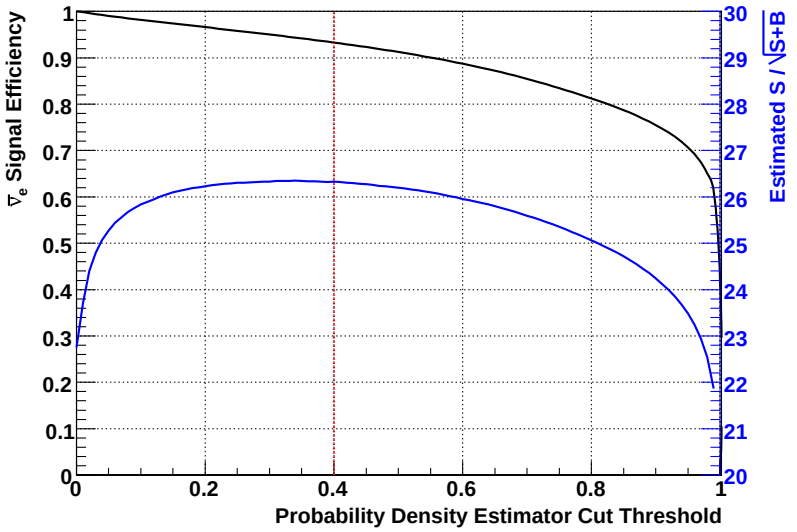

(b)

Figure 4.17: Figure of Merit in determining the PDE cut: (a) signal efficiency and number of accidental background events vs. PDE cut threshold. (b) signal efficiency and $S/\sqrt{S+B}$ vs. PDE cut threshold. The optimum PDE cut threshold is set to 0.4, indicated by the dotted red line.

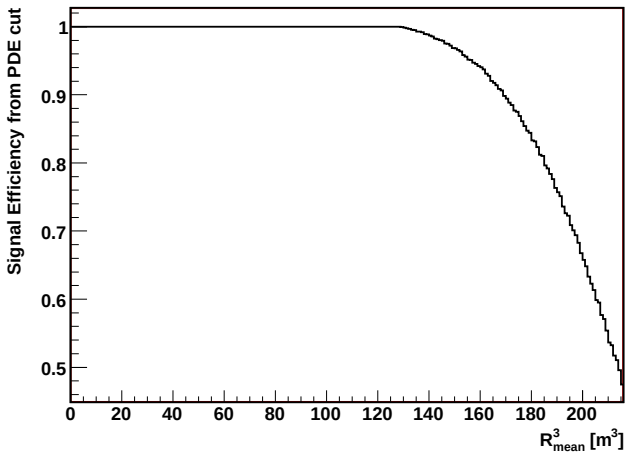

Figure 4.18: The PDE cut efficiency as a function of $R^3_{\rm mean}$. The efficiency drops quickly near the fiducial volume boundary ($R^3_{\rm mean} = 216$m) as the accidental backgrounds start to dominate.

cut is energy independent, as long as the probability density functions of $R^3_{\rm mean}$ and $(\Delta R)^3$ for $\bar{\nu}_e$ events do not depend on the $\bar{\nu}_e$ energy, which is assumed to be the case.

4.9 Summary of $\bar{\nu}_e$ Candidate Selection Efficiency

Table 4.5 summarizes the $\bar{\nu}_e$ candidate selection efficiency from each selection rule. The total efficiency is $0.875(1 \pm 0.9\%)$ and the uncertainty is mostly coming from the PDE cut and the ΔR_{p-d} cut.

Table 4.5: Summary of $\bar{\nu}_e$ Selection Efficiency

Description	Efficiency	Uncertainty
Reconstruction Quality	0.9992	0.0001
2.04MeV $< E_d <$ 2.82MeV	0.9987	0.0003
Neutron Capture on ^{1}H	0.9946	0.0010
$0.5\mu s < \Delta T_{p-d} < 660\mu s$	0.9567	0.0008
$\Delta R_{p-d} <$ 1.6 m	0.9881	0.0057
PDE > 0.4	0.9330	0.0047
Total	0.8754	0.0075

4.10 Final Sample of $\bar{\nu}_e$ Candidate

After applying all the selection rules discussed in this section, 930 $\bar{\nu}_e$ candidate events were extracted out of the total ∼12 billion raw events from the 1439.87 live-day's data. This apparent $10^7 : 1$ background rejection ratio shows the power of inverse beta decay coincidence technique.

Fig. 4.19 shows the vertex distribution of the $\bar{\nu}_e$ candidate events, by applying all the cuts except the fiducial volume cut. We emphasize that the PDE cut is only applied to events inside the 6m fiducial volume since the pdf of $R^3_{\rm mean}$ distribution is normalized inside the fiducial volume only (Fig. 4.15(a)). As can be seen, the $\bar{\nu}_e$ candidates appear to be uniformly distributed inside the fiducial volume, and the accidental coincidence background dominates outside of the fiducial volume.

Fig. 4.20 shows the energy distributions of $\bar{\nu}_e$ candidate events, by applying all the cuts except the prompt and/or delayed energy cuts. The events with prompt energy below the analysis threshold 2.7 MeV are mostly accidental coincidence events, with some contributions from ^{13}C(α,n)^{16}O events (Section 5.4) and possible geo-neutrino events from natural radio-activities in the Earth (Section 4.5). The events with delayed energy below 2 MeV are also from accidentals. The 5 events with delayed visible energy around 5.5 MeV agree in number with neutron capture on ^{12}C, comparing with the number of neutron capture on ^{1}H events (Table 4.4).

Fig. 4.21 shows the ΔT_{p-d} distribution of $\bar{\nu}_e$ candidate events, by applying all the cuts except the time correlation cut. A fit to an exponential function plus a flat background yields the neutron capture time being $199.7 \pm 12.4 \mu s$. This agrees with the neutron capture time measurement from spallation neutrons ($206.4 \pm 1.3 \mu s$, Section 4.6). The flat background comes from the accidental coincidence events since they have no natural time correlation. Within the $0.5 \mu s < \Delta T_{p-d} < 660 \mu s$ window, the fitted total number of accidental events is 40.7 ± 19, which agrees with the

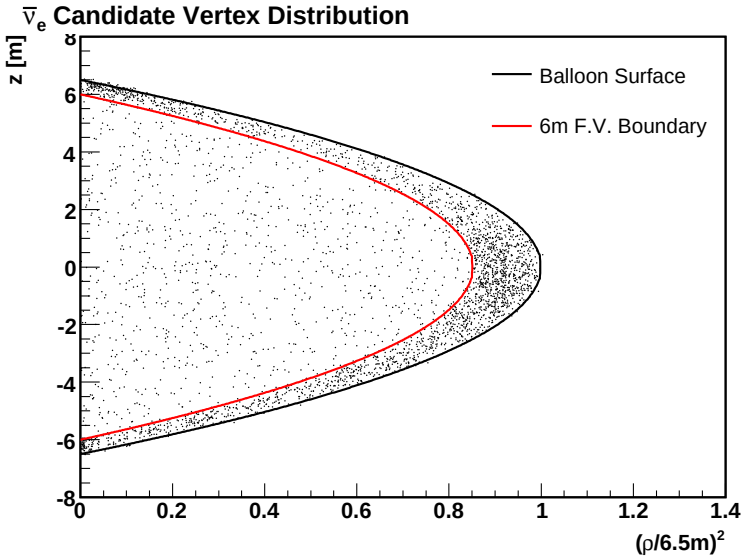

(a)

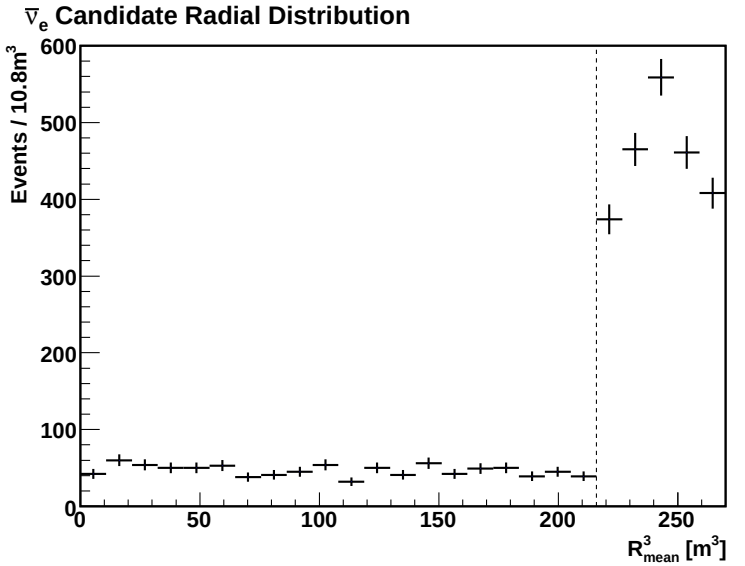

(b)

Figure 4.19: (a) Scatter plot of $\bar{\nu}_e$ candidate's vertex. (b) Radial distribution of $\bar{\nu}_e$ candidate. All vertexes refer to the average positions of the prompt and delayed event pairs. Outside of the 6m fiducial volume (dotted line), the PDE cut is not applied, so the accidental coincidence background dominates. Inside the fiducial volume the $\bar{\nu}_e$ candidates appear to be uniformly distributed.

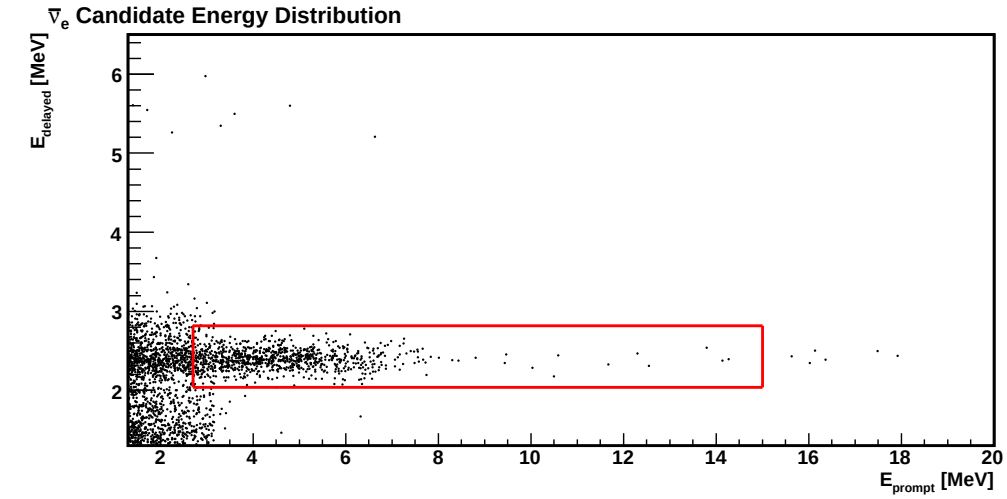

(a)

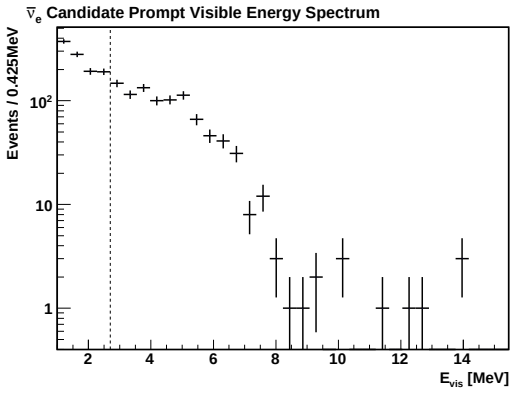

(b)

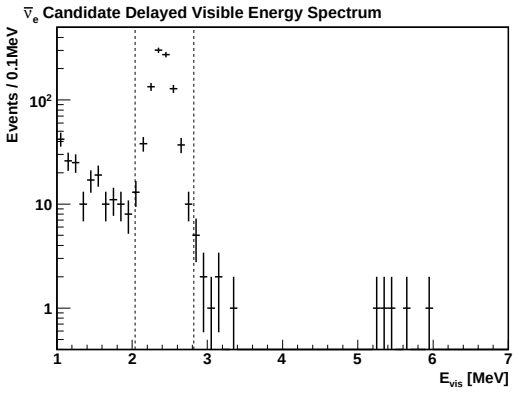

(c)

Figure 4.20: The energy distributions of $\bar{\nu}_e$ candidate events: (a) Delayed energy vs. prompt energy. The red box is the candidate window. (b) Prompt visible energy spectrum. Events below 2.7 MeV are dominated by accidentals and have contributions from geoneutrinos. (c) Delayed visible energy spectrum. The 5 events around 5.5 MeV agree with neutron capture on ^{12}C. The dotted lines indicate the prompt and delayed energy threshold used in this analysis.

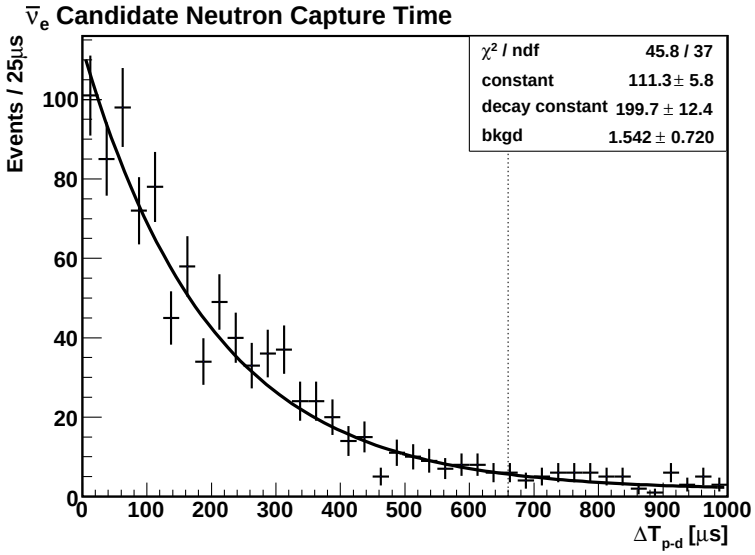

Figure 4.21: The ΔT_{p-d} distribution of $\bar{\nu}_e$ candidate events. A fit to an exponential function plus a flat background yields the neutron capture time being $199.7 \pm 12.4 \mu s$. The χ^2/ndf of the fit is 45.8/37. The dotted line indicates the time correlation cut at 660 μs. The fitted total flat background within the cut is 40.7 ± 19.

estimation (48.4 ± 1.3) from the statistical calculation in Section 4.8.

Chapter 5 Signals and Backgrounds

5.1 Anti-neutrino from Nuclear Reactor

Most of the $\bar{\nu}_e$'s detected in KamLAND come from the man-made nuclear reactors. Besides providing $\bar{\nu}_e$'s for scientists, these nuclear power plants produce a large amount of electric power. In Japan, nuclear power contributes to 34.5% of the total electricity. Since the $\bar{\nu}_e$ flux goes down as inverse square of the distance, only reactors nearby KamLAND, namely reactors in Japan and Korea, contribute significantly. Table 5.1 summarizes the information of the 57 reactor cores in Japan and the 20 reactor cores in Korea, including their types, distances to the KamLAND detector and thermal powers. Most of the reactors are boiling water reactors (BWR) and pressurized water reactors (PWR). There are two research-type test reactors including an advanced thermal reactor (ATR) and a fast breeder reactor (FBR). The contribution of Korean reactors to the total $\bar{\nu}_e$ flux is estimated to be $3.2 \pm 0.3\%$, where the uncertainty comes from the conservative uncertainty (10%) of converting reported electric power to thermal power. Reactors from other countries are included assuming one effective reactor at one distance for each country, and is estimated to contribute $1.0 \pm 0.5\%$ of the total $\bar{\nu}_e$ flux. The positions of Japanese reactors were given by Tokyo Electric Power Company (TEPCO), and are accurate to within 70 m. The distances range from 80 km to 900 km, with a flux-weighted average baseline of $\sim$180 km (Fig. 5.1). The $\bar{\nu}_e$ flux uncertainty from baseline is less than 0.1% . The reactor thermal power is monitored at each reactor from the heat balance of the reactor cores and the uncertainty is conservatively assigned as 2.0%, which is dominated

by the accuracy of the feed-water flowmeters[1].

Table 5.1: Summary of Japanese and Korean Reactors

Site	Distance [km]	Cores	Type	Power [GWth]
		Japan		
Hamaoka	214	5	BWR	14.5
Shimane	401	2	BWR	3.8
Tokai2	295	1	BWR	3.3
Tsuruga-1	138	1	BWR	1.1
Tsuruga-2	138	1	PWR	3.4
Tomari	783	2	PWR	3.3
Shika	88	2	BWR	5.5
Fugen	139	1	ATR	0.6
Monju	142	1	FBR	0.7
Mihama	146	3	PWR	4.9
Ohi	179	4	PWR	13.7
Takahama	191	4	PWR	10.2
Genkai	754	4	PWR	10.1
Sendai	830	2	PWR	5.3
Ikata	561	3	PWR	6.0
Onagawa	431	3	BWR	6.4
Higashidori	636	1	BWR	3.3
Fukushima1	349	6	BWR	14.2
Fukushima2	345	4	BWR	13.2
KashiwazakiKariwa	160	7	BWR	24.3
		Korea		
Kori	736	4	PWR	9.2
Ulchin	712	6	PWR	17.3
Wolsong	709	4	PWR	8.2
Yonggwang	986	6	PWR	17.7

Four main fissile nuclei ^{235}U, ^{238}U, ^{239}Pu and ^{241}Pu contribute to 99.9% of the $\bar{\nu}_e$'s from the nuclear reactors. ^{235}U is the initial fuel enriched to ∼3–4% of the uranium. It fissions with thermal neutrons as follows:

$$^{235}\mathrm{U} + n \longrightarrow X_1 + X_2 + 6.1e^- + 6.1\bar{\nu}_e + xn + 202\mathrm{MeV} \tag{5.1}$$

where X_1 an X_2 are the daughter fission fragment nuclei such as ^{94}Zn and ^{140}Ce. ^{238}U,

[1]The reactor thermal power uncertainty might be reduced to ∼0.8%, from the random cancellation as described in Ref. [103].

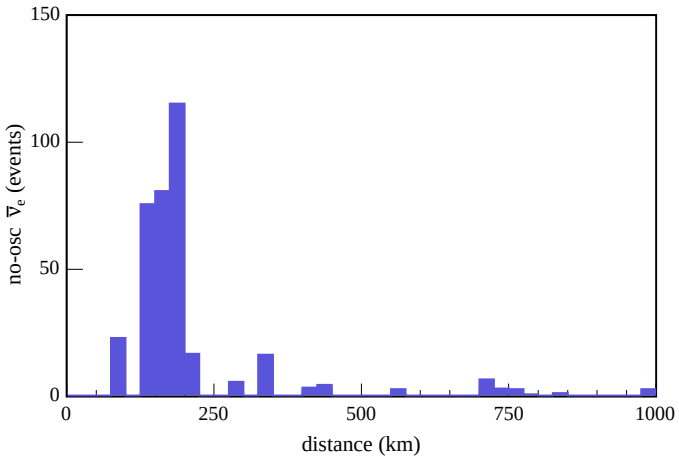

Figure 5.1: Baseline distribution of the expected on-oscillation anti-neutrino event rate (arbitrary unit) at KamLAND. The flux-weighted average baseline is ∼180 km. Figure taken from [46].

on the other hand, can only fission with fast neutrons:

$$^{238}\mathrm{U} + n(> 1\mathrm{MeV}) \longrightarrow X_3 + X_4 + 5 \sim 7e^- + 5 \sim 7\bar{\nu}_e + yn + 205\mathrm{MeV} \tag{5.2}$$

^{238}U can also capture a neutron and through subsequent β decays breeds another fissionable isotope ^{239}Pu:

$$^{238}\mathrm{U}(n,\gamma)^{239}\mathrm{U}(\beta^-)^{239}\mathrm{Np}(\beta^-)^{239}\mathrm{Pu} \tag{5.3}$$

^{239}Pu fissions with thermal neutrons as follows:

$$^{239}\mathrm{Pu} + n \longrightarrow X_5 + X_6 + 5.6e^- + 5.6\bar{\nu}_e + zn + 210\mathrm{MeV} \tag{5.4}$$

Or it could sequentially capture two neutrons and produce another fissionable isotope ^{241}Pu, which then fissions with thermal neutron as follows:

$$^{241}\mathrm{Pu} + n \longrightarrow X_7 + X_8 + 6.4e^- + 6.4\bar{\nu}_e + wn + 212\mathrm{MeV} \tag{5.5}$$

On average, 6 $\bar{\nu}_e$'s and 200 MeV energy are released in each fission. A typical 3 GWth reactor produces $\sim 5 \times 10^{20} \bar{\nu}_e$'s per second. The $\bar{\nu}_e$ energy spectra from fissions of ^{235}U, ^{239}Pu, ^{241}Pu are deduced from the measured beta spectra at ILL high flux reactor in Grenoble [104, 105]. The $\bar{\nu}_e$ spectrum from fission of ^{238}U is calculated theoretically [106], since ^{238}U only fissions with fast neutrons and lacks experimental data. These $\bar{\nu}_e$ spectra are shown in Fig. 5.2. In typical reactor cores relevant to KamLAND, the relative fission rate of the isotopes is ^{235}U : ^{238}U : ^{239}Pu : ^{241}Pu = 0.56 : 0.08 : 0.30 : 0.06. The uncertainty of the total $\bar{\nu}_e$ spectrum shape is estimated from the rate-weighted sum of the uncertainty of each spectrum of the isotope [104, 105, 106] to be 2.5%. The shapes of $\bar{\nu}_e$ spectra are checked by the Bugey [51, 107] experiment and agree well with the measurement within 1.4%.

The existence of 1.8 MeV threshold in the inverse beta decay detection process ensures that only $\bar{\nu}_e$'s from large-Q-valued (short half life) β decays can be detected. Two long-lived isotopes ^{106}Ru ($T_{1/2}$ = 373.6 days) and ^{144}Ce ($T_{1/2}$ = 284.9 days) are from the fission products and their daughters ^{106}Rh and ^{144}Pr can beta decay and produce $\bar{\nu}_e$'s above inverse beta decay threshold. They are important for the periods immediately following reactor shutdowns, and for the contribution from spent fuels which are stored near the reactors for a long period of time. The contribution from these long-lived isotopes is estimated to be $\sim$0.04% above the analysis energy threshold 2.7 MeV [108] and is negligible.

To accurately calculate the total $\bar{\nu}_e$ rates at KamLAND site, it is necessary to trace the time variation of fission rate of all the reactors. Detailed simulations exist that can calculate the fuel component in accordance with the burn-up, but it is very computationally intensive. Instead, a simple model of reactor cores [109] is constructed by TEPCO and Tohoku University to calculate the instantaneous fission rate of different isotopes. The input to this model are the initial fuel composition and the instantaneous and integrated thermal power of the reactor. These data for

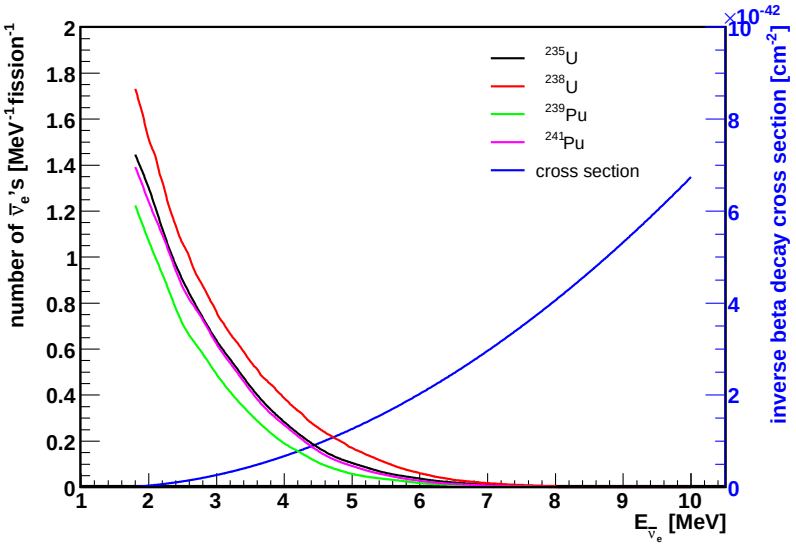

Figure 5.2: The $\bar{\nu}_e$ energy spectrum from different fission isotope ^{235}U, ^{238}U, ^{239}Pu and ^{241}Pu. The inverse beta decay cross section as a function of $\bar{\nu}_e$ is show in blue line.

all 57 reactor cores are provided weekly (hourly on reactor starting or stopping) by TEMPCO on a special agreement exchanged between Tohoku university and the power agencies as a member of KamLAND. The accuracy of this simple model is estimated to be 1% compared to the detailed simulations.

The instantaneous $\bar{\nu}_e$ energy spectrum at KamLAND site can be calculated as follows:

$$\frac{\mathrm{d}N_{\bar{\nu}_e}(E,t)}{\mathrm{d}E} = \sum_{\text{reactors}} \frac{P(E, L_{\text{reactor}})}{4\pi L^2_{\text{reactor}}} \cdot \sum_{\text{isotopes}} \frac{\mathrm{d}N^{\text{isotope}}_{\bar{\nu}_e}(E)}{\mathrm{d}E} f^{\text{isotope}}_{\text{reactor}}(t) \tag{5.6}$$

where E is the energy of the $\bar{\nu}_e$, L_{reactor} is the distance from the reactor to KamLAND, $P(E, L_{\text{reactor}})$ is the survival probability of the $\bar{\nu}_e$, and $f^{\text{isotope}}_{\text{reactor}}(t)$ is the instantaneous fission rate of each isotope in each reactor. KamLAND then detects these $\bar{\nu}_e$ through the inverse beta decay process described in Section 2.1. The expected un-oscillated $\bar{\nu}_e$ event rate at KamLAND as a function of time is shown in Fig. 5.3. The noticeable drop of event rate during Period II is due to the shutdown of Kashiwazaki Kariwa

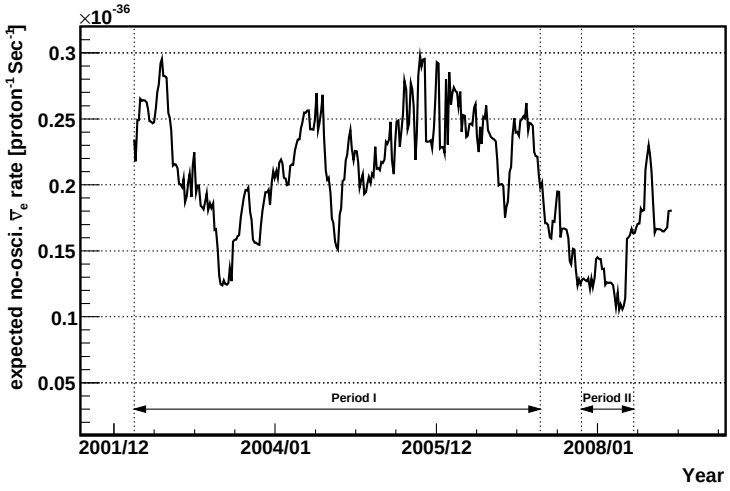

Figure 5.3: The expected un-oscillated $\bar{\nu}_e$ event rate at KamLAND as a function of time.

reactors after an earthquake of magnitude 6.8 striking in Niigata prefecture on 16 July 2007.

The expected prompt visible energy spectrum at KamLAND from reactors can then be calculated with Eqn. 2.5, and is shown in Fig. 5.4 in case of no-oscillation, and oscillation with LMA-0, LMA-I and LMA-II solutions (Section 1.2.3). The total expected un-oscillated reactor $\bar{\nu}_e$'s within the analysis energy window and fiducial volume, with the detection efficiency of 87.5% (Section 4.9), is 1267.6 events in Period I and 104.8 events in Period II.

Table 5.2 summarizes the reactor related systematic uncertainties discussed in this section.

5.2 Anti-neutrino from Nuclear Georeactor

As described in Section 1.3, a hypothetical georeactor at the core of the earth could produce sizable amount of $\bar{\nu}_e$'s and be detected at KamLAND. The georeactor model predicts that ^{235}U comprises 76% of the present-day georeactor fission and ^{238}U comprises 24% [59]. Based on this fuel composition, the normalized prompt visible energy

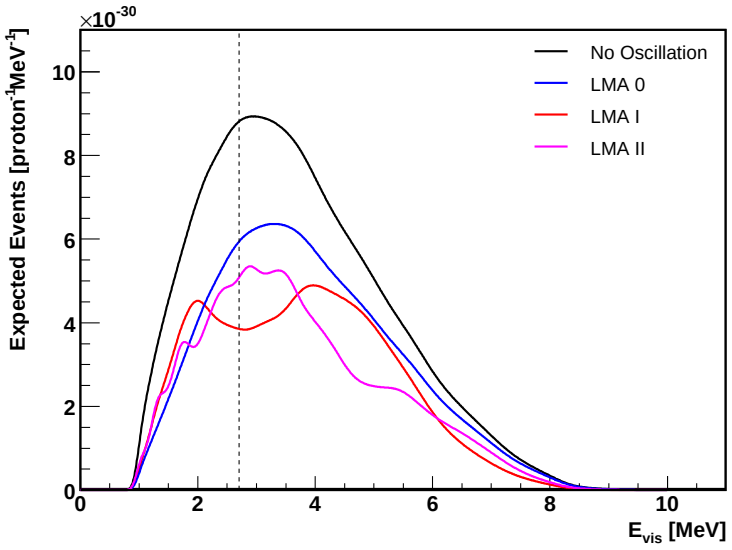

Figure 5.4: The expected prompt visible energy spectrum in Period I in case of no-oscillation, and oscillation with LMA-0 ($\Delta m^2_{21} = 1.0 \times 10^{-5}\mathrm{eV}^2$), LMA-I ($\Delta m^2_{21} = 7.59 \times 10^{-5}\mathrm{eV}^2$) and LMA-II ($\Delta m^2_{21} = 2.0 \times 10^{-4}\mathrm{eV}^2$) solutions. $\tan^2\theta_{12}$ is fixed at 0.47 in the calculation. The dotted line indicates the analysis threshold at 2.7 MeV.

Table 5.2: Summary of Reactor Related Systematic Uncertainties

Description	Uncertainty
Thermal Power	
Japanese Reactors	2.0%
Korean Reactors	0.3%
Other Reactors	0.5%
$\bar{\nu}_e$ Spectra	2.5%
Distance	0.1%
Fuel Composition	1.0%
Total	3.4%

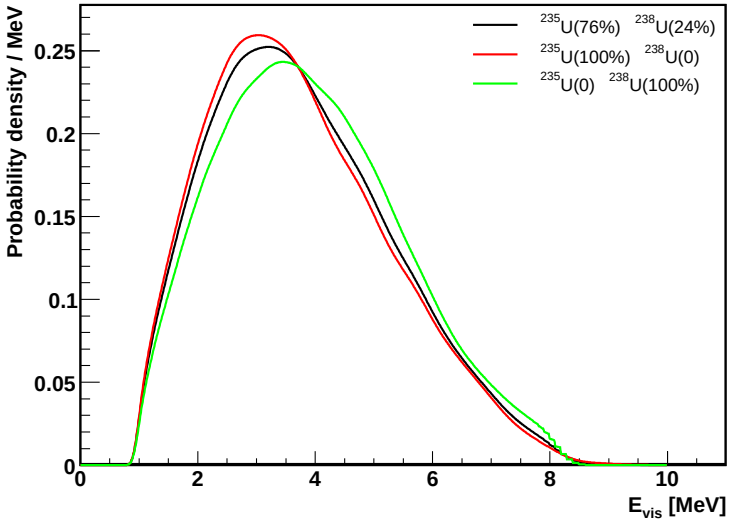

Figure 5.5: The prompt visible energy spectrum at KamLAND from georeactor $\bar{\nu}_e$'s. The georeactor model predicts the present-day fuel composition of 76% ^{235}U and 24% ^{238}U. Two other extreme case of 100% ^{235}U or 100% ^{238}U are also calculated. All three spectra are normalized to unity to compare their shapes. The shape difference due to the fuel composition uncertainty is small.

spectrum from georeactor $\bar{\nu}_e$ is calculated similarly as in Section 5.1 and shown in Fig. 5.5. Two other extreme cases of 100% ^{235}U or 100% ^{238}U are also calculated to compare their shapes. Even in the extreme cases, the fuel composition uncertainty only causes a small difference in the spectrum shape and is ignored in the subsequent analysis.

The $\bar{\nu}_e$'s from georeactor undergo the same oscillation as described in Section 1.1 as they travel through the Earth. The matter effect, as can be calculated from Eqn. 1.14, is small because of the low energy of the neutrinos and the relative low density of the Earth and is neglected here. The survival probability of the $\bar{\nu}_e$ is:

$$P(\bar{\nu}_e \to \bar{\nu}_e) = 1 - \sin^2\theta_{12}\sin^2\left[1.27\Delta m^2_{21}(\mathrm{eV}^2)\frac{R_\oplus(\mathrm{km})}{E_{\bar{\nu}_e}(\mathrm{GeV})}\right] \tag{5.7}$$

where $R_\oplus = 6370$ km is the radius of the Earth. The size of the model-predicted georeactor is $\sim$5 km in radius [59], thus can be treated as a point source compared with the

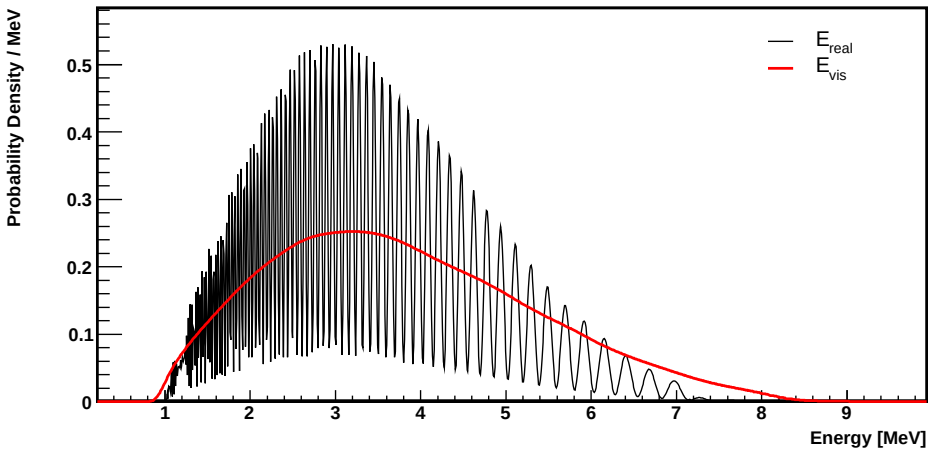

Figure 5.6: The calculated oscillation effect ($\Delta m^2_{21} = 7.59 \times 10^{-5}\mathrm{eV}^2$ [22]) on the prompt energy spectrum at KamLAND from georeactor $\bar{\nu}_e$. The fine structure of the oscillation (E_{real} spectrum, black line) is smeared out after applying detector resolution (E_{vis} spectrum, red line).

oscillation length (∼100 km) if we take the LMA solutions for Δm^2_{21}. Because of the long distance of $R_\oplus$, the energy related oscillatory part undergoes many oscillations within the georeactor $\bar{\nu}_e$ energy range from 1 to 10 MeV. The fine structure of the oscillated energy spectrum, however, is smeared out by the finite size of the energy resolution ($\sim 7\%/\sqrt{E/1\mathrm{MeV}}$, Section 3.4) of KamLAND detector. This smearing effect can be visually seen from Fig. 5.6, where $\Delta m^2_{21} = 7.59 \times 10^{-5}\mathrm{eV}^2$ is used for the simulation. The survival probability is then simply given by $P(\bar{\nu}_e \to \bar{\nu}_e) = 1 - 0.5 \sin^2\theta_{12}$ and is used in the subsequent analysis. The oscillation only results in a total rate suppression and does not distort the $\bar{\nu}_e$ spectrum shape of the georeactor.

To calculate the georeactor $\bar{\nu}_e$ event rate at KamLAND, we assume that each georeactor fission reaction releases 200 MeV energy and that the fission rate is constant over the time scale of the KamLAND experiment. The event rate of georeactor $\bar{\nu}_e$ can be then calculated from the fission rate similarly as described in Section 5.1. Fig. 5.7 shows the expected prompt visible energy spectrum in Period I from a hypothetical 10 TW georeactor, in comparison with the expected $\bar{\nu}_e$ events from the

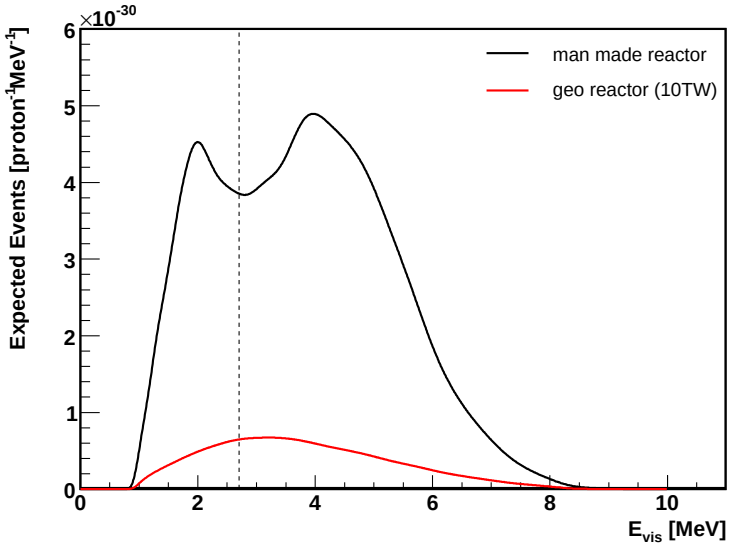

Figure 5.7: The expected prompt visible energy spectrum at KamLAND in Period I from a hypothetical 10 TW georeactor (red line), in comparison with the expected $\bar{\nu}_e$ events from the man-made reactor (black line). The oscillation parameters are taken from Ref. [22]. The dotted line indicates the analysis threshold at 2.7 MeV.

man-made reactors (Section 5.1), calculated with the oscillation parameters taken from Ref. [22]. With the same detection efficiency and analysis threshold as reactor $\bar{\nu}_e$, for a 10 TW georeactor we expect to see 102 events in Period I and 14.5 events in Period II within the 6m fiducial volume. This is ∼13.4% of the expected oscillated man-made reactor $\bar{\nu}_e$ signal. The normalized oscillated georeactor $\bar{\nu}_e$ event rate is ∼0.012 event/(day·kton·TW).

The georeactor model [59] only loosely constrains its fission power from 3 TW to 30 TW. Thus, the number of georeactor $\bar{\nu}_e$ events is treated as a free parameter in the analysis. Its spectrum shape and time variation signatures are however very different from the reactor $\bar{\nu}_e$, which helps to distinguish them from the large reactor $\bar{\nu}_e$ background and a well constraint on the georeactor power can be put.

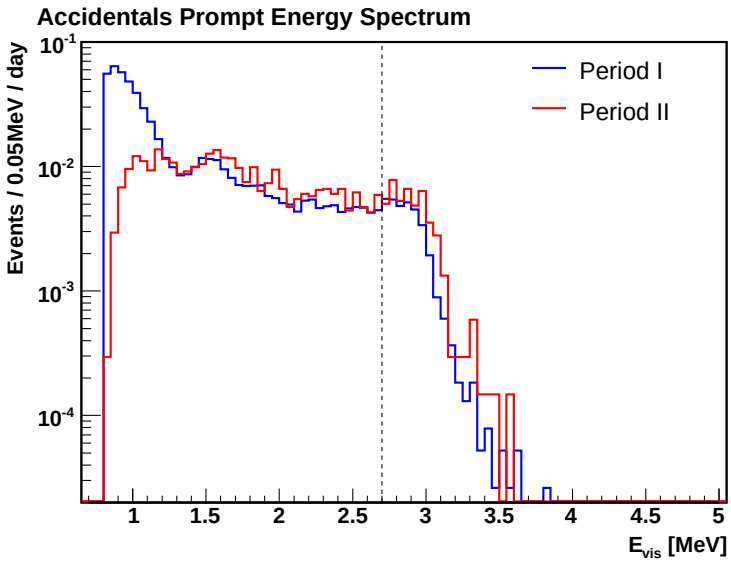

Figure 5.8: The prompt visible energy spectrum of accidental background in Period I (blue) and Period II (red). The dotted line indicates the analysis threshold at 2.7 MeV.

5.3 Accidental Coincidence Background

Accidental coincidence background has already been discussed in detail in Section 4.8. In summary, the total number of estimated accidental background events is 42.0 $\pm$ 1.2 in Period I, and 8.2 $\pm$ 0.5 in Period II.

Fig. 5.8 shows the expected prompt visible energy spectrum of accidental coincidence events from simulation (Section 4.8). Comparing Period I and II, after the purification the accidental event rate below 1 MeV was reduced by a factor of $\sim$5, which is dominated by the ^{210}Bi decay in the liquid scintillator. Above the analysis threshold at 2.7 MeV though, the event rate did not decrease after purification, probably because it's dominated by the ^{208}Tl decay on the balloon surface and outside of the liquid scintillator. In fact, due to the change in energy scale, the accidental event rate slightly increased in Period II.

5.4 ^{13}C(α,n)^{16}O Background

Radioactive impurities in KamLAND liquid scintillator, during their decay chains, emit α particles (Appendix B). The visible energies of these α particles are heavily quenched down to below 1 MeV, however, the second order (α,n) reactions could produce fast neutrons. The thermalization and capture of those fast neutrons then give prompt-delayed signals and mimic the $\bar{\nu}_e$ events. More than 99% of the α activity in KamLAND comes from the decay of ^{210}Po [108], who is the daughter nucleus of ^{210}Pb (Table B.1) and was introduced by means of ^{222}Rn contamination during the initial filling. ^{210}Po has a half life of 138 days and emits an α particle with kinetic energy of 5.304 MeV. Table 5.3 lists the possible target nuclei for (α,n) reaction, in decreasing order of number densities of the nuclei. The maximum α energy in KamLAND is 8.785 MeV from ^{212}Po. Below this threshold, the only dominant target nucleus is ^{13}C. Therefore only ^{13}C(α,n)^{16}O reactions from ^{210}Po decay is considered in the following analysis.

Table 5.3: Target Nuclei for (α,n) Reaction in KamLAND

Target Nuclei	Q value [MeV]	Threshold [MeV]	Density [nuclei/cm^3]
^{1}H	-23.68	115.4	6.603×10^{22}
^{12}C	-8.50	11.34	3.316×10^{22}
^{13}C	2.22	0	3.723×10^{20}
^{2}H	-4.19	12.5	9.905×10^{18}
^{16}O	-12.13	15.17	3.692×10^{18}
^{14}N	-4.74	6.09	3.687×10^{18}

^{210}Po Decay Rate in KamLAND

The α particle from ^{210}Po decay has a kinetic energy 5.304 MeV, but is quenched down to $\sim$0.3 MeV, which is below the trigger threshold during normal run ($\sim$0.7 MeV), so the ^{210}Po activity is estimated from special low threshold background runs taken at about once a week during the running of the KamLAND experiment. The

energy reconstruction algorithm (Section 3.4) has known issues at such low energy and often returns invalid reconstruction status. To avoid this inefficiency, the low-level nsummax distribution is used for the estimation of ^{210}Po decay rate instead of the reconstructed energy distribution. The nsummax of an event , however, does not tell the vertex of the event, which is needed to estimate ^{210}Po's activity inside the 6m fiducial volume. To reduce the reconstruction inefficiency, a more loose "acceptably reconstructed event" selection is used, which includes events with somewhat degraded position reconstruction quality unless "unknown," "not valid" or "bad" position reconstruction status is set (Table 3.1). Fig. 5.9 shows the nsummax distribution of the good reconstructed, acceptably reconstructed and all events near ^{210}Po α energy in the whole KamLAND detector. As can be seen, the "good reconstructed events" have energy dependent inefficiency and distort the nsummax spectrum, so they are not used in the analysis. The efficiency of "acceptably reconstructed event" is 98% $\pm$ 2% by comparing with all the events in the detector. To estimate the ^{210}Po activity, the nsummax spectrum for events inside 6m fiducial volume is modeled by a Gaussian function for the ^{210}Po peak around nsummax 85, plus a second order polynomial for the background under the ^{210}Po peak (mainly from ^{85}Kr β decay), plus an exponential decay function for the rise at low nsummax (mainly from ^{14}C β decay). The systematic error from the fitting is estimated to be 16%, which comes from trying different fitting ranges and assuming different background functions.

The low threshold background runs are usually as short as 5 minutes[2]. To study the time dependence of ^{210}Po decay rate with enough statistics, those background runs are grouped into 8 periods with running time $\sim$8 hours each. The nsummax spectra inside 6m fiducial volume are fitted in each period and the result is shown in Fig. 5.10. The first 7 points are from Period I. The ^{210}Po activity inside the fiducial volume in Period I is consistent with a fitted constant 40.7 $\pm$ 7.2 Bq over time. The

[2]There are three special 8-hour background runs (run 3888, 5757 and 5767).

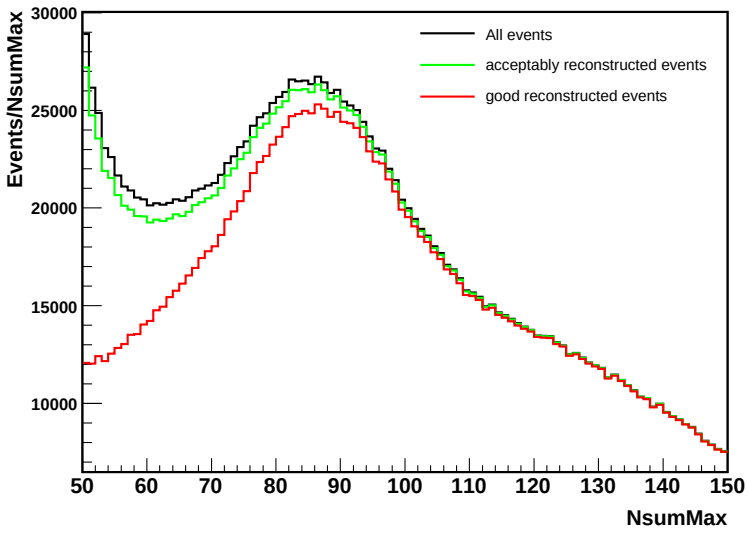

Figure 5.9: Nsummax distribution of good reconstructed, acceptably reconstructed and all events in KamLAND detector near ^{210}Po alpha energy (5.304 MeV, quenched down to ∼0.3 MeV in visible energy), taken from a special low threshold background run 3888.

last point shows the ^{210}Po activity in Period II after the purification. The ^{210}Po activity is reduced by about a factor of four to 11.3 ± 2.6 Bq inside the 6m fiducial volume.

To study the position distribution of ^{210}Po decay rate, the nsummax spectrum is fitted in different equal-volume regions of the detector and the result is shown in Fig. 5.11. As can be seen, the ^{210}Po activity rises near the balloon boundary, which indicates the contamination from the balloon surface. But inside the 6m fiducial volume the ^{210}Po activity is consistent with constant over the volume. Since the ^{210}Po α events have the same radial distribution as the $\bar{\nu}_e$ events, the detection efficiency of ^{13}C(α,n)^{16}O events is taken to be the same as $\bar{\nu}_e$ events, which is 0.875 (1±0.9%) (Section 4.9).

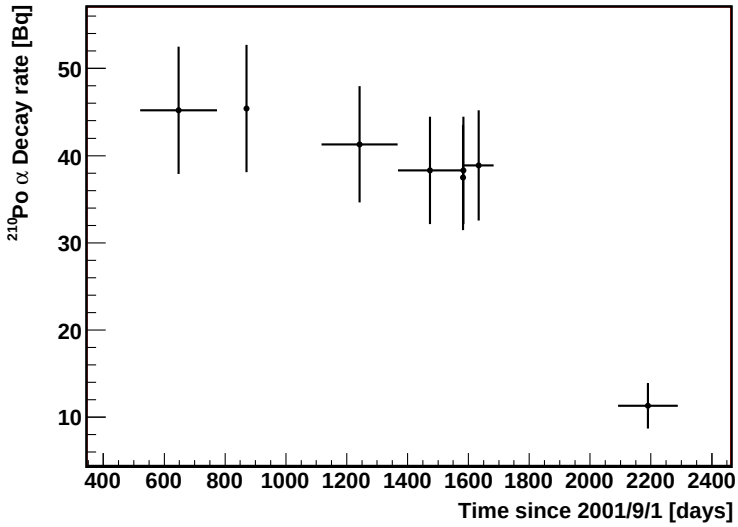

Figure 5.10: Time dependence of ^{210}Po decay rate inside 6m fiducial volume, estimated from the low threshold background runs throughout the KamLAND running time. The ^{210}Po activity in Period I is consistent with a fitted constant 40.7 ± 7.2 Bq over time. In Period II, due to the purification, the ^{210}Po activity is reduced to 11.3 ± 2.6 Bq inside the 6m fiducial volume.

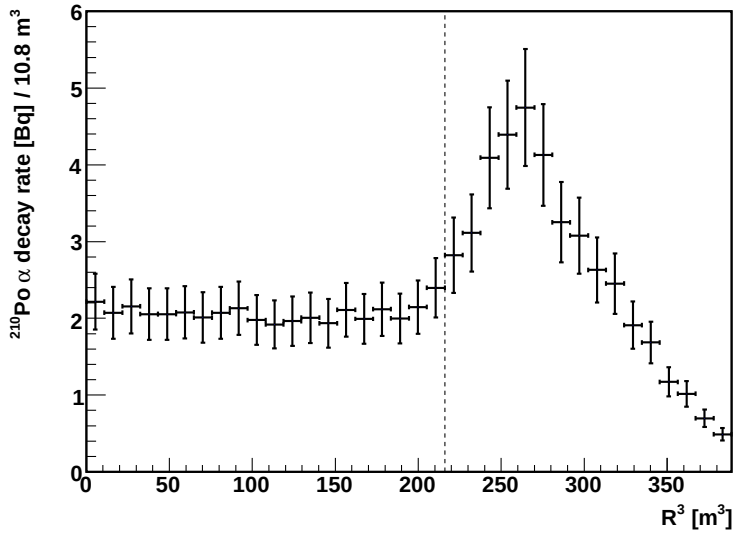

Figure 5.11: Radial distribution of ^{210}Po Activities. The dashed line indicates the 6m fiducial volume boundary. Inside the fiducial volume, the ^{210}Po activity is consistent with constant over the radius. The activity rises near the balloon boundary, which indicates the contamination from the balloon surface.

^{13}C(α,n)^{16}O Reaction Rate and Prompt Energy Spectrum

Fig. 5.12 shows the cross section of ^{13}C(α,n)^{16}O reaction as a function of α energy [110]. At ^{210}Po α particle energy of 5.304 MeV, the final state of ^{16}O can be its ground state, first excited state or second excited state. The prompt signal from ^{13}C(α,n)^{16}O background thus consists of the following events:

- The neutrons from the ^{13}C(α,n)^{16}O$^{\text{g.s.}}$ reaction typically have energies from 3 MeV to 7 MeV. Most of them lose energy by elastically scattering on ^{1}H nuclei during thermalization, and the recoiled protons could give visible energies above the analysis threshold of 2.7 MeV. The neutrons from reactions involving ^{16}O 1st or 2nd excited state typically have energies below 1 MeV and do not contribute to the prompt signal.

- High energy neutrons sometimes inelastically scatter on ^{12}C and excite the nucleus to its first excited state. The ^{12}C* then emits a 4.438 MeV γ particle during de-excitation.

- If the final state of ^{16}O is its 1st exited state, the ^{16}O* returns to its ground state by emitting an e^+e^- pair with total energy of 6.049 MeV.

- If the final state of ^{16}O is its second exited state, the ^{16}O* returns to its ground state by emitting a 6.129 MeV γ ray.

The energy loss function of α particles in KamLAND detector is calculated from the SRIM software package [96], with the composition of KamLAND liquid scintillator given in Section 2.2. The result is shown in Fig. 5.13. The ^{13}C(α,n)^{16}O reaction rate is then calculated through:

$$R_{\text{n}}^{i} = \int_{E_0}^{0} \mathrm{d}E_\alpha \, n_{\text{target}} R_\alpha \sigma^i(E_\alpha) \left(-\frac{\mathrm{d}X}{\mathrm{d}E_\alpha}\right) \quad , \quad i = 0, 1, 2 \tag{5.8}$$

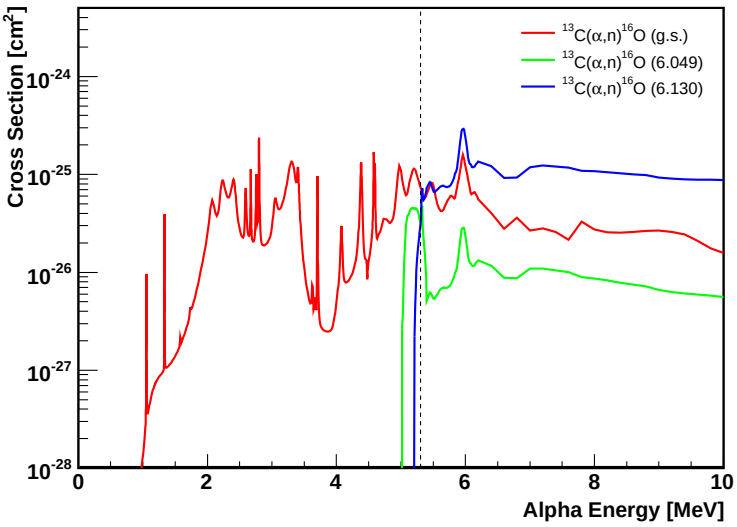

Figure 5.12: Cross section of ^{13}C(α,n)^{16}O reaction [110] in case of ^{16}O ground state (red), first excited state (green) and second excited state (blue). The dashed line indicates the ^{210}Po α particle energy at 5.304 MeV.

where E_α is the energy of the α particle, E_0 is the initial ^{210}Po α energy 5.304 MeV, n_{target} is ^{13}C density in the KamLAND liquid scintillator (3.723×10^{20} atoms/cm^3), R_α is the ^{210}Po α decay rate in the fiducial volume, $\sigma^i(E_\alpha)$ is the cross section of ^{13}C(α,n)^{16}O reaction with ^{16}O at i^{th} final state, and dE_α/dX is the energy loss function of α particles in the KamLAND detector.

The energy of the neutron coming out from the ^{13}C(α,n)^{16}O reaction in the lab frame is calculated from the kinematics of the two body scattering ^{13}C + ^{4}He $\longrightarrow$ n + ^{16}O

$$\begin{aligned} E_{\rm n}^{\rm lab} &= \gamma E_{\rm n}^{\rm CM} + \gamma\beta P_{\rm n}^{\rm CM}\cos\theta_{\rm CM} \\ \beta &= P_\alpha^{\rm lab}/(E_\alpha^{\rm lab} + M_{\rm C}) \quad , \quad \gamma = 1/\sqrt{1-\beta^2} \\ E_{\rm n}^{\rm CM} &= \frac{M_\alpha^2 + M_{\rm C}^2 + 2M_{\rm C}E_\alpha^{\rm lab} + M_n^2 - M_{\rm O}^2}{2\sqrt{M_\alpha^2 + M_{\rm C}^2 + 2M_{\rm C}E_\alpha^{\rm lab}}} \end{aligned} \tag{5.9}$$

As seen from Eqn. 5.9, the energy of the neutron depends on the scattering angle. In this analysis, the differential cross section of ^{13}C(α,n)^{16}O reaction is parameterized

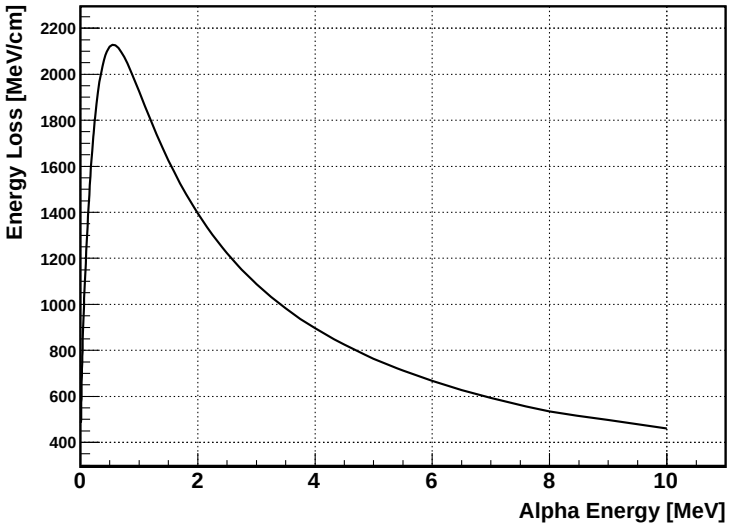

Figure 5.13: dE/dX function of α particles in KamLAND, calculated from the SRIM software package [96].

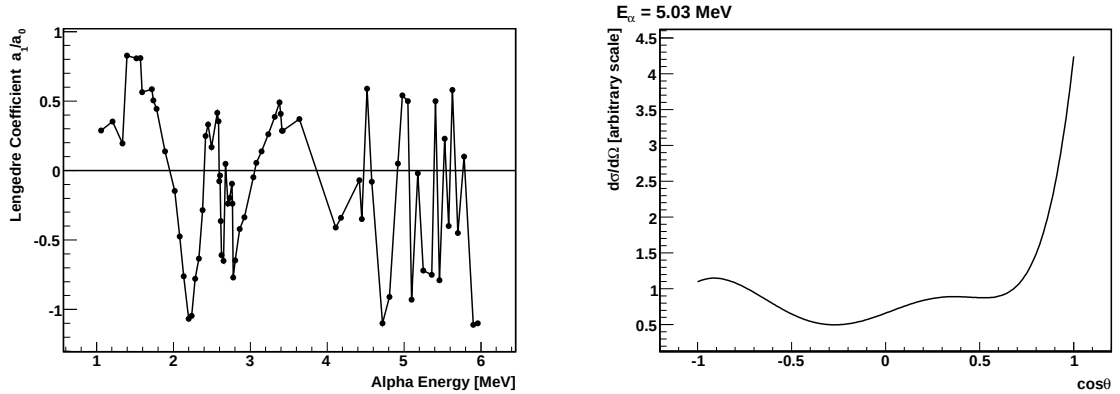

(a) (b)

Figure 5.14: (a) Legendre Polynomial coefficient a_1/a_0 as a function of α energy. (b) ^{13}C(α,n)^{16}O differential cross section at α energy 5.03 MeV.

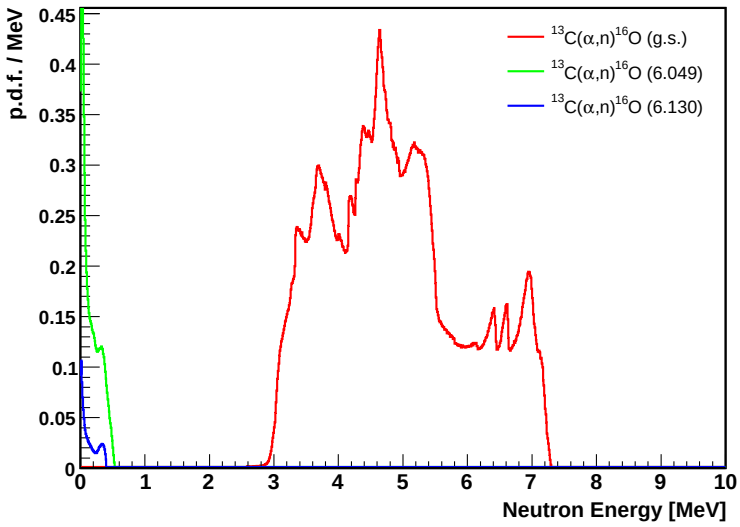

Figure 5.15: Normalized Neutron energy spectrum from ^{13}C(α,n)^{16}O reaction in the KamLAND detector.

by Legendre Polynomials to the 8$^{\text{th}}$ power as:

$$\frac{d\sigma}{d\Omega} = \sum_{l=0}^{8} a_l(E_\alpha) P_l(\cos\theta) \tag{5.10}$$

where the coefficient a_l is taken from Ref. [111, 112]. Fig. 5.14 shows an example of a_1 as a function of α energy and the differential cross section at α energy 5.03 MeV. The neutron energy spectrum is then calculated from:

$$R^i_{\text{n}}(E_{\text{n}}) = \int_{E_0}^{0} \mathrm{d}E_\alpha \int \mathrm{d}\Omega\, \delta(E_{\text{n}};\Omega,E_\alpha) n_{\text{target}} R_\alpha \frac{\mathrm{d}\sigma^i}{\mathrm{d}\Omega} \left(-\frac{\mathrm{d}X}{\mathrm{d}E_\alpha}\right) \quad , \quad i = 0,1,2 \tag{5.11}$$

where the parameters are the same as in Eqn. 5.8, with the δ function $\delta(E_{\text{n}};\Omega,E_\alpha)$ calculated from Eqn. 5.9. The resulting normalized neutron energy spectrum is shown in Fig. 5.15.

Finally, to calculate the prompt visible energy spectrum, a monte carlo simulation of ^{13}C(α,n)^{16}O interactions are performed according to the cross section of ^{13}C(α,n)^{16}O reaction and the p.d.f of the neutron energy spectrum. The neutrons are

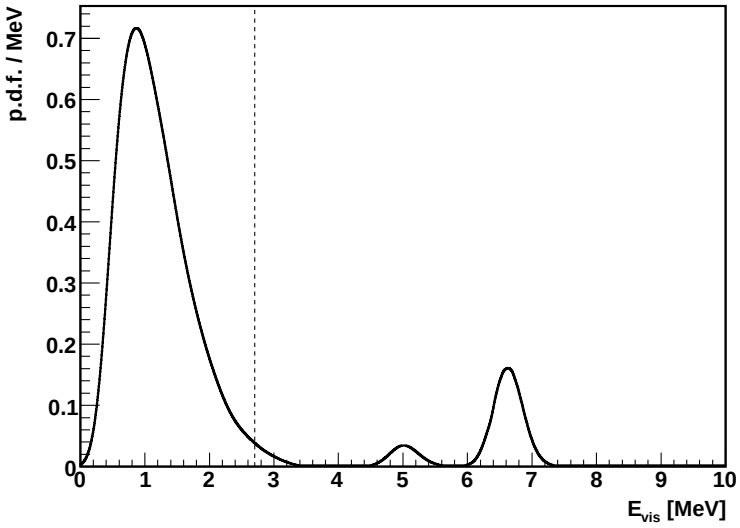

Figure 5.16: Normalized visible prompt energy Spectrum of ^{13}C(α,n)^{16}O background in KamLAND. The dashed line indicates the analysis energy threshold 2.7 MeV.

then thermalized and the visible energies of the various prompt events discussed at the beginning of this subsection are summed together. After applying the detector resolution, the normalized prompt energy spectrum is shown in Fig. 5.16. The first peak in the spectrum comes from the recoiled protons during neutron thermalization, the second peak comes from the inelastic scattering of neutrons on ^{12}C and subsequent de-excitation of ^{12}C* nuclei, and the last peak comes from the de-excitation of ^{16}O first and second excited states. Because of the different systematic errors of the cross sections, the number of events under each peak is estimated separately in the analysis. The cross section of ^{13}C(α,n)^{16}O* reaction is not very well measured and a 50% uncertainty is assigned. Given the ^{210}Po α decay rate, the detection efficiency and the exposure of Period I and II, the total number of ^{13}C(α,n)^{16}O background events under each peak above the analysis threshold 2.7 MeV is estimated to be 2.7 $\pm$ 0.5 , 4.8 $\pm$ 2.4, 22.4 $\pm$ 11.2 for Period I, and 0.1 $\pm$ 0.0, 0.2 $\pm$ 0.1, 0.9 $\pm$ 0.4 for Period II respectively.

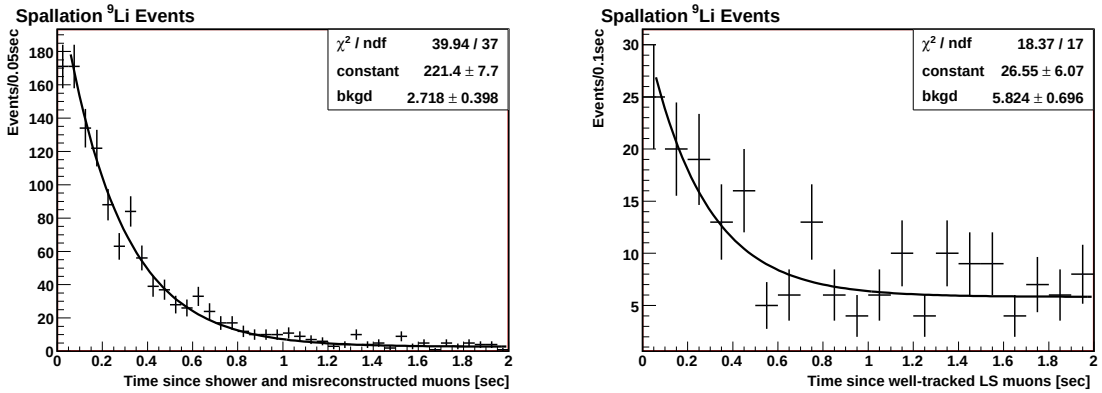

(a) (b)

Figure 5.17: (a) Time between spallation ^{9}Li events and associated shower or misreconstructed muons. (b) Time between spallation ^{9}Li events and associated well-tracked non-show LS muons within 3-m of the muon track. Both distributions are fitted to an exponential decay function with fixed half life of 178.3 ms. The fitted functions are integrated from 0 sec to infinity, resulting a total number of 1139.3 ± 39.8 ^{9}Li events after shower and misreconstructed muons, and 68.3 ± 15.6 ^{9}Li events after well-tracked non-shower LS muons.

5.5 ^{9}Li Background

As discussed in Section 4.3, ^{9}Li produced by muon spallation could give a prompt-delayed signal and mimic the $\bar{\nu}_e$ event. The muon spallation cuts are designed to reject these events, however, a fraction of ^{9}Li events still remains due to inefficiency of the cuts.

A 2-second veto on the full detector is applied after a shower muon or a muon with misreconstructed track. Given the half life of ^{9}Li (178.3 msec), this veto rejects 99.96% of the ^{9}Li background. To estimate the remaining, ^{9}Li events after showering or misreconstructed muon are selected by applying the same $\bar{\nu}_e$ selection cuts except inverting the muon spallation cuts. The distribution of time between ^{9}Li event and associated muon is shown in Fig. 5.17(a). This time distribution is fitted to an exponential decay function with a fixed half life of 178.3 ms, resulting a total number of 1139.3 ± 39.8 events integrated from 0 second to infinity. After the 2-second veto, the remaining ^{9}Li background events are 0.48 ± 0.02.

For well-tracked non-shower LS muons, a 2-second veto is applied only to the 3-m cylinder volume along the muon track. The distribution of time between spallation ^{9}Li events inside the 3-m cylinder and associated well-tracked non-shower LS muons is shown in Fig. 5.17(b). This time distribution is again fitted to an exponential decay function with a fixed half life of 178.3 ms, resulting a total number of 68.3 $\pm$ 15.6 events from the fit. After the 2-second veto, the remaining ^{9}Li background events are 0.03 $\pm$ 0.01.

For the volume outside of the 3-m cylinder along the muon track, only a 2ms veto is applied (Section 4.3). Given the half life of ^{9}Li (178.3 msec), this veto only rejects 0.77% of the ^{9}Li background. The inefficiency of the 3-m cylinder cut is investigated through the ^{12}B spallation events. The selection of ^{12}B events is described in Appendix C.4.2. The distribution of distance between ^{12}B events and the associated LS muon track is shown in Fig. 5.18. 11.7% $\pm$ 2.8% of the ^{12}B events have reconstructed positions outside of the 3-m cylinder along the muon track. The result agrees with a FLUKA [113] based simulation in Ref. [114]. Assuming a similar vertex distribution for ^{9}Li events, given 68.3 $\pm$ 15.6 ^{9}Li events inside the 3-m cylinder along the muon track, 9.0 $\pm$ 3.0 ^{9}Li events lie outside of the 3-m cylinder and are not rejected by the muon spallation cuts.

The above analysis is performed for Period I and II separately because of the observed changes in muon spallation cut efficiency between the two periods (Fig. 4.3), which is caused by the decrease of "shower muons" (defined as $N_{p.e}^{\text{total}} > 7 \times 10^5$) rate because of the $\sim$ 10% loss of the light yield after the purification of the liquid scintillator. Combining all contributions together, the total number of spallation ^{9}Li background events is estimated to be 9.5 $\pm$ 3.1 in Period I and 1.3 $\pm$ 0.6 in Period II.

A separate estimation of ^{9}Li background is performed by studying the distribution of time between the $\bar{\nu}_e$ candidate and the previous muon event, shown in Fig. 5.19.

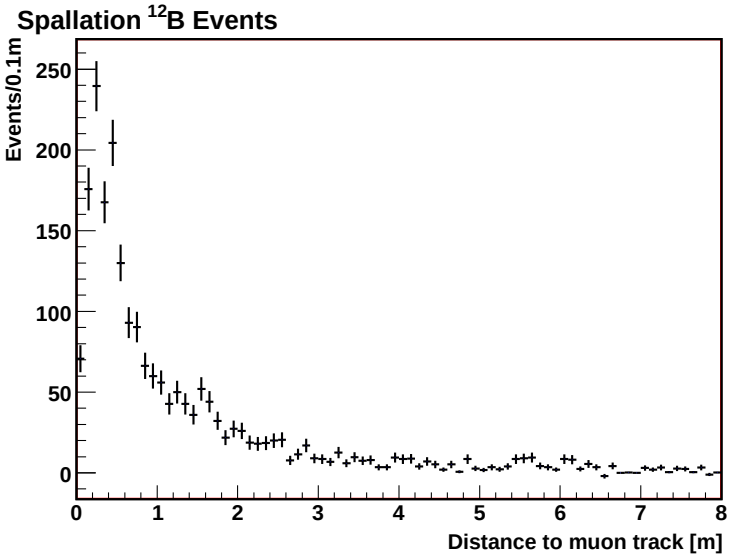

Figure 5.18: The distance between spallation ^{12}B events and associated muon track. The percentage of the ^{12}B events inside the 3-m cylinder along the muon track is 88.3% ± 2.8%.

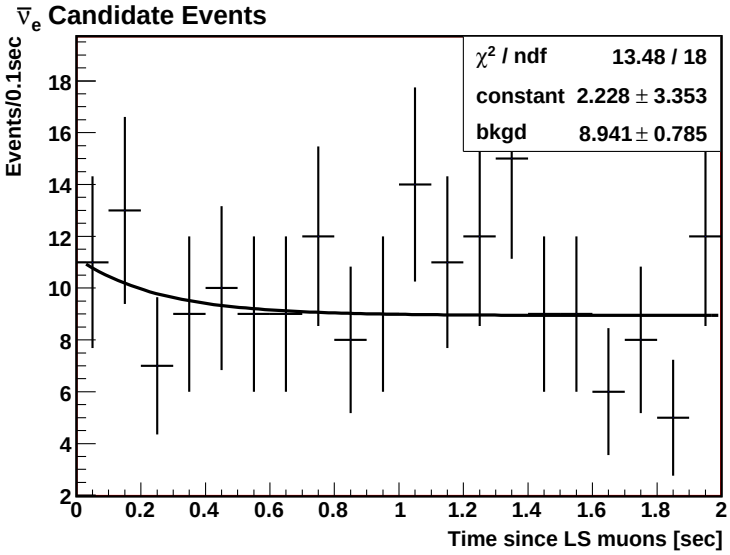

Figure 5.19: Time between $\bar{\nu}_e$ candidate events and previous LS muons. The distribution is fitted to an exponential decay function with fixed ^{9}Li half life of 178.3 ms. The fitted function is integrated from 0 sec to infinity, resulting a total number of 5.7 ± 8.6 ^{9}Li events in the $\bar{\nu}_e$ candidates.

Any time correlation with the muon should be coming from the spallation ^{9}Li background. This time distribution is fitted to an exponential decay function with a fixed ^{9}Li half life of 178.3 ms, resulting in a total number of 5.7 ± 8.9 events from the fit. This number is consistent with the previous more precise estimation and is only used as a consistency cross-check.

5.6 Fast Neutron Background

Fast neutrons produced by muons could enter the KamLAND detector and give coincidence events that mimic the $\bar{\nu}_e$ events (Section 4.3). They are easily removed by the 2 ms spallation cut after each muon, if the associated muon is detected. However, due to the OD inefficiency, muons going through OD only might not be efficiently tagged. Furthermore, muons passing outside the detector, for example in the surrounding rocks, produce fast neutrons that could travel inside the detector without being detected by the OD.

The property of the fast neutron background is studied by applying all the cuts same as the $\bar{\nu}_e$ candidate selection, except reversing the 2 ms OD muon cut by requiring that the prompt event must happen within 2 ms of an OD-only muon. This predominantly selects the fast neutrons that are produced by muons passing through outer detector only. As a result, a total of 39 fast-neutron-like events were tagged by the OD. The OD inefficiency in tagging ID muons can be studied by counting ID muons that do not register enough OD hits (OD nsummmax > 10), as shown in Fig. 5.20. The inefficiency is in average $\sim$1%, but is increasing with time due to the dying of OD PMTs. However, It can not be assumed that this inefficiency is the same as for tagging non-ID muons, since they might produce less light in the OD, especially for muons only passing through the rock. For this reason the number of fast neutron events in the $\bar{\nu}_e$ candidates can not be estimated directly, and is treated as a free

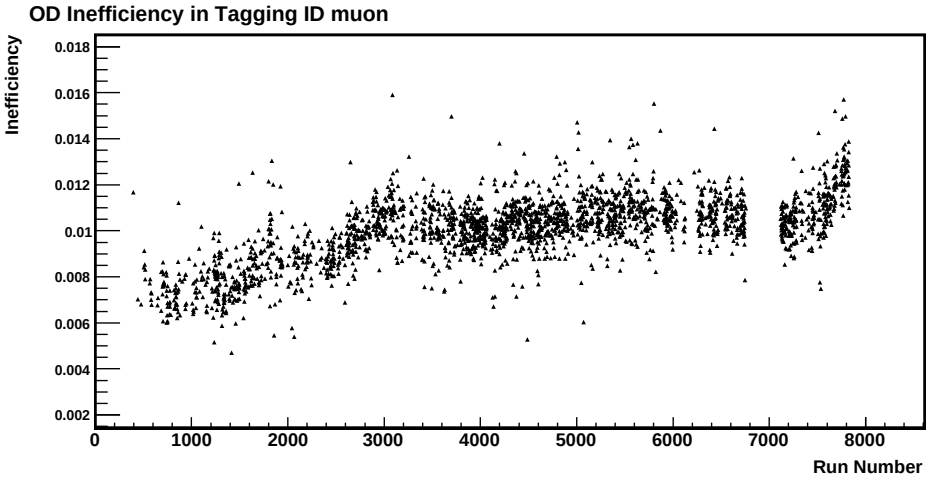

Figure 5.20: The OD inefficiency in tagging ID muons. The increasing of inefficiency over time is due to the wear-out of OD PMTs.

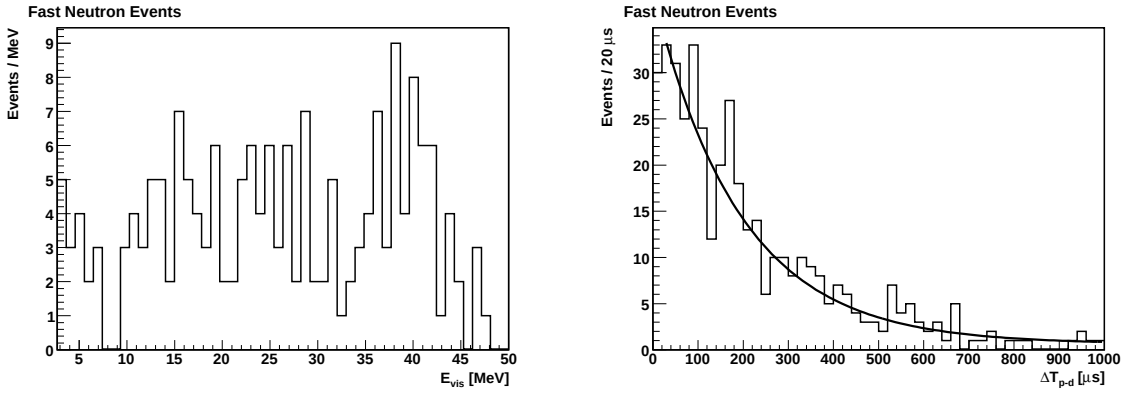

(a) Fast Neutron Energy Spectrum

(b) Neutron Capture Time of Fast Neutron

Figure 5.21: The fast neutron events are selected the same as $\bar{\nu}_e$ events except requiring that the prompt event happens within 2 ms of an OD-only muon. (a) Prompt visible energy spectrum ($E_{vis} > 2.7$ MeV) of fast neutron events. There is no apparent structure in the spectrum and the spectrum is assumed to be flat in the analysis. (b) The distribution of time between prompt and delayed events. The distribution is fitted to an exponential decay function plus a flat background. The neutron capture time from the fit is 193.5 ± 21.9 μs. The χ^2/ndf from the fit is 29.7/40.

parameter in this analysis, confined only by the shape of its energy spectrum.

Fig. 5.21(a) shows the energy spectrum of the OD-tagged fast neutrons after applying all $\bar{\nu}_e$ selection rules but reversing the 2 ms OD muon cut. The spectrum is rather flat in the energy region up to ∼30 MeV, and a flat spectrum is assumed for

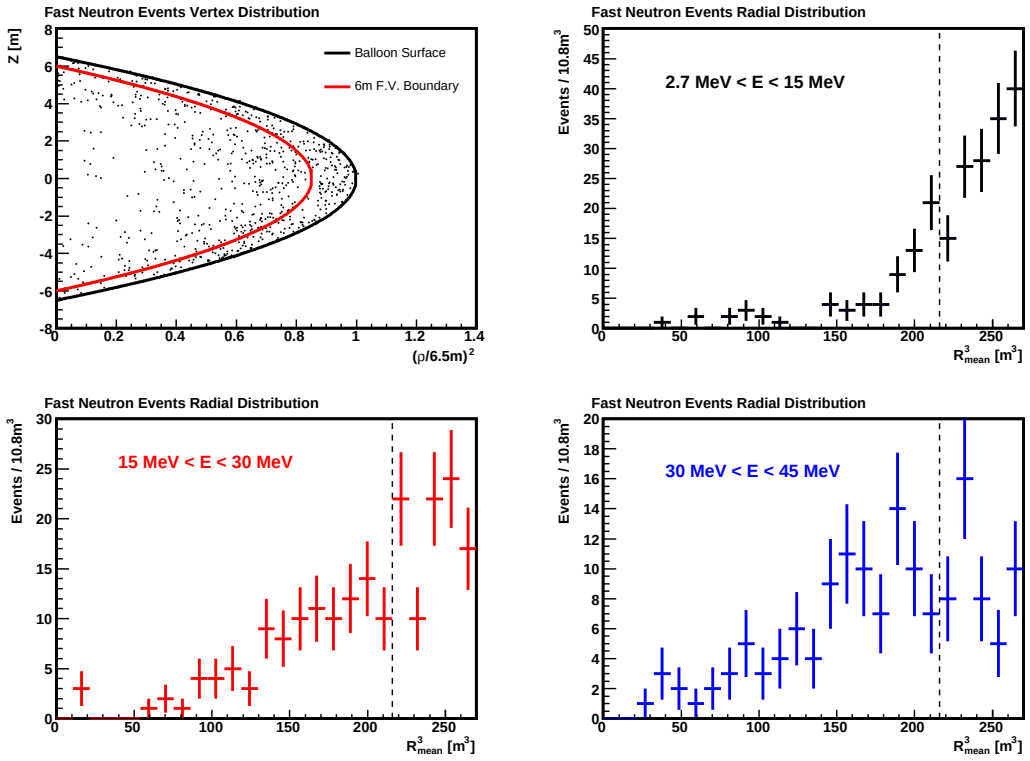

Figure 5.22: The vertex distribution of OD-tagged fast neutron events (PDE cut is not applied). In the top left figure the prompt energy is only required to be higher than 2.7 MeV. The radial distribution of the fast neutrons are shown in three different energy ranges: 2.7 – 15 MeV, 15 – 30 MeV and 30 - 45 MeV. The vertical dotted line indicate the 6m fiducial volume boundary.

the OD-missed fast neutrons as well in the following analysis. Fig. 5.21(b) shows the distribution of time between prompt and delayed events. To increase the statistics the prompt energy is only required to be higher than 2.7 MeV and no upper limit is required. The distribution is fitted to an exponential decay function plus a flat background and the neutron capture time from the fit is 193.5 ± 21.9 μs.

A study of the vertex distribution of fast neutron events is shown in Fig. 5.22. Here the PDE cut is not applied since it preferentially removes events near the fiducial volume boundary. The prompt energy is only required to be higher than 2.7 MeV, and the radial distribution of the fast neutrons are shown in three different energy ranges: 2.7 – 15 MeV, 15 – 30 MeV and 30 – 45 MeV. The attenuation of fast neutrons

by the liquid scintillator is clear, and higher energy neutrons are more penetrating than the lower energy ones. In the analysis energy range 2.7 – 15 MeV, the radial distribution is very similar to the accidental background (Fig. 4.14(b)), thus the PDE cut is expected to be removing a lot of fast neutron events as well (Fig. 4.18, 66 events $\rightarrow$ 39 events after applying the PDE cut). Nevertheless, we treat the number of fast neutron background events as a free parameter and do not estimate the efficiency directly.

5.7 Atmospheric Neutrino Background

The quasi-elastic neutral current interactions between atmospheric neutrinos and neutrons in the liquid scintillator produce energetic neutrons and could become a potential background source. This background has been conservatively estimated in Ref. [115], by using the calculated maximum atmospheric neutrino flux (solar minimum case) $\mathrm{d}\phi/\mathrm{d}E_\nu$ at KamLAND site from Ref. [23] and neutrino-neutron elastic scattering cross section $\mathrm{d}\sigma/\mathrm{d}Q^2$ (modified from Ref. [116] by changing the isovector form factor) and neglecting the nuclear effects of carbon (including which lowers the cross-section by $\sim$15%). The recoiled neutron energy spectrum can be then calculated from

$$\frac{\mathrm{d}N}{\mathrm{d}T} = N_n \cdot T_{\mathrm{live}} \cdot \sum_i \int \frac{\mathrm{d}\phi^i}{\mathrm{d}E_\nu} \frac{\mathrm{d}\sigma^i}{\mathrm{d}Q^2} \frac{\mathrm{d}Q^2}{\mathrm{d}T} \, \mathrm{d}E_\nu \tag{5.12}$$

where $N_n = 1.8 \times 10^{32}$ is the number of the neutrons (from ^{12}C) in the 6m fiducial volume, and $T_{\mathrm{live}} = 1440$ days is the total live time. The sum is over the 4 types of atmospheric neutrinos ν_μ, $\bar{\nu}_\mu$, ν_e and $\bar{\nu}_e$, and the neutron recoil energy T is related to the squared momentum transfer Q^2 simply by $T = Q^2/2M_n$. This neutron energy spectrum is then used as an input to a GEANT4 based simulation of KamLAND detector and the expected prompt visible energy spectrum is generated as shown in Fig. 5.23. Within the analysis threshold from 2.7 MeV to 15 MeV, a maximum

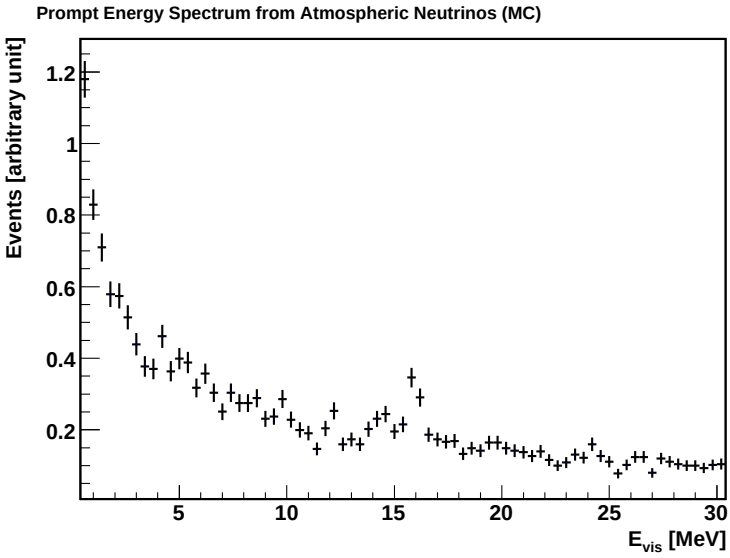

Figure 5.23: The prompt visible energy spectrum from atmospheric neutrino interacting in KamLAND detector, simulated by KLG4sim in Ref [115].

number of 9 events are expected.

In the current analysis, the atmospheric neutrino background is treated the same as the fast neutron background by allowing the total number free floating but assuming a flat energy spectrum in the analysis energy window 2.7 – 15 MeV. Assuming the correctness of the Monte Carlo spectrum in Fig. 5.23, this treatment systematically underestimates the number of atmospheric neutrinos at the lower energy. The maximum deviation is less than 2 events though, assuming that the total number of atmospheric neutrino events is less than 9 as estimated above.

5.8 Summary of Signals and Backgrounds

Table 5.4 summarizes the number of expected signal and background events discussed in this chapter. Accidentals are the dominant background in both periods, while ^{13}C(α,n)^{16}O background, being significant in Period I, is significantly reduced in Period II due to the purification of the liquid scintillator.

Table 5.5 summarizes the estimated sources of systematic uncertainties on deter-

mining the number of expected reactor $\bar{\nu}_e$ events. The systematic uncertainty in the energy scale (Section 3.4.3) at the 2.7 MeV prompt visible energy threshold is 1.2%, which corresponds to a 1.2% uncertainty in integrating the number of events in an un-oscillated reactor $\bar{\nu}_e$ spectrum. The total systematic uncertainty is 4.2% and is dominated by the uncertainties of $\bar{\nu}_e$ spectra, reactor power and fiducial volume.

Table 5.4: Summary of Signal and Background Events

	Period I	Period II
live time (days)	1261.35	178.52
expected reactor $\bar{\nu}_e$ (no osci.)	1267.6	104.8
georeactor $\bar{\nu}_e$	free parameter	
observed $\bar{\nu}_e$ candidate events	844	86
Background Events		
accidentals	40.2 ± 1.2	8.2 ± 0.5
^{13}C(α,n)^{16}O (recoiled protons)	2.7 ± 0.5	0.1 ± 0.0
^{13}C(α,n)^{16}O (^{12}C* de-excitation)	4.8 ± 2.4	0.2 ± 0.1
^{13}C(α,n)^{16}O* (^{16}O* de-excitation)	22.4 ± 11.2	0.9 ± 0.4
^{9}Li	9.5 ± 3.1	1.3 ± 0.6
fast neutron and atmospheric $\bar{\nu}_e$	free parameter	
Total Backgrounds	79.6 ± 11.9	10.7 ± 0.9

Table 5.5: Summary of estimated systematic uncertainties (%).

Fiducial volume	2.0	Reactor power	2.1
Energy threshold	1.2	Fuel composition	1.0
Efficiency of cuts	0.9	$\bar{\nu}_e$ spectra	2.5
Cross section	0.2		
Total Systematic Uncertainty			4.2

Chapter 6 Analysis and Results

An unbinned *maximum likelihood* (ML) method is used in this dissertation to estimate the set of *model parameters* $\boldsymbol{\theta} = (\theta_1, \ldots, \theta_m)$ whose values are unknown. The model parameters are divided into two sets: *free parameters* whose values are allowed to be free floating in the analysis, and *nuisance parameters* whose values are constrained by independent measurements. Table 6.1 summarizes all the free model parameters and nuisance model parameters used in this analysis. The neutrino oscillation parameters ($\tan^2\theta_{12}$, Δm^2_{21}) and the georeactor fission power $P_{\rm geo}$ are treated as free parameters, and a combined fit of them is performed. $\epsilon_{\rm reactor}$ denotes the efficiency of detecting reactor $\bar{\nu}_e$ events, summarized in Table 4.5. The uncertainties on $\epsilon_{\rm reactor}$ is summarized in Table 5.2. $\epsilon_{\rm common}$ denotes the common efficiency of detecting all signal and background events. Its uncertainty includes those on the number of target protons, and is summarized in Table 4.3. α_i^j denotes the four detector energy response parameters in period j, discussed in Section 3.4. $N^j_{\rm acc}$, $N^{j,k}_{(\alpha,{\rm n})}$ and $N^j_{\rm Li9}$ indicate the number of corresponding background events in period j, summarized in Section 5.8. $N_{\rm fn,atm}$, the total number of fast neutron and atmospheric ν background events is allowed to be free floating but assuming a flat energy spectrum (Section 5.6, 5.7).

6.1 Likelihood Function

At the beginning of the analysis, a *likelihood function* $L(\boldsymbol{\theta}) = f(\vec{x};\boldsymbol{\theta})$ is constructed, which defines the joint probability density function (p.d.f.) of the data $\vec{x} = (x_1, \ldots, x_n)$, evaluated with the measurements obtained from the experiments, predicted by the set of model parameters $\boldsymbol{\theta}$. The likelihood function is regarded as a function of the

Table 6.1: Model parameters used in this analysis. The number in the parenthesis indicates the total number of parameters in the corresponding category

Free Model Parameters	
$\tan^2\theta_{12}$	Neutrino oscillation mixing angle
Δm^2_{21}	Neutrino oscillation mass square difference
$P_{\rm geo}$	Georeactor fission power
$N_{\rm fn,atm}$	Number of fast neutron and atmospheric ν background events
Nuisance Model Parameters	
$\epsilon_{\rm common}$	Common Efficiency for $\bar{\nu}_e$ and background events detection
$\epsilon_{\rm reactor}$	Efficiency for reactor and georeactor $\bar{\nu}_e$ detection only
α_i^j	Detector energy response parameters in period j (8)
$N^j_{\rm acc}$	Number of accidental coincidence background events in period j (2)
$N^{j,k}_{(\alpha,{\rm n})}$	Number of type k ^{13}C(α,n)^{16}O background events in period j (6)
$N^j_{\rm Li9}$	Number of ^{9}Li background events in period j (2)

model parameters, and the ML method takes the estimators $\widehat{\boldsymbol{\theta}}$ to be those values of $\boldsymbol{\theta}$ that maximize $L(\boldsymbol{\theta})$. Unbinned ML method is often used when the experiment is limited by low statistics, especially when a multi-dimensional binning is needed for the binned analysis. Meanwhile, $\widehat{\boldsymbol{\theta}}$, known as *maximum likelihood estimator* (MLE) has the nice properties of being asymptotically consistent, unbiased and efficient.

The likelihood function $L(\boldsymbol{\theta})$ can be written as a product of independent pdfs, and evaluated separately:

$$L(\boldsymbol{\theta}) = \prod_l L_l(\boldsymbol{\theta};\vec{x}) \tag{6.1}$$

$$= L_{\rm penalty}\cdot L_{\rm rate}\cdot L_{\rm shape}\cdot L_{\rm time}\cdot L_{\rm solar} \tag{6.2}$$

In this analysis, the likelihood function consists of several pdf terms including penalty terms for nuisance parameters, absolute event rate, shape of the prompt visible energy spectrum, time variation of event rate and solar experiment term. Details will be discussed in the following subsections.

It is equivalent and often easier to work with $\ln L$ instead of L. It can be shown that in the large sample limit, L has a Gaussian shape and $\ln L$ is parabolic. In this

case, one often defines

$$\chi^2(\boldsymbol{\theta}) = -2[\ln L - \ln L_{\max}] \quad (6.3)$$

$$= \chi^2_{\text{penalty}} + \chi^2_{\text{rate}} + \chi^2_{\text{shape}} + \chi^2_{\text{time}} + \chi^2_{\text{solar}} - \chi^2_{min} \quad (6.4)$$

where L_{max} is the value of maximized likelihood function, or, $L(\widehat{\boldsymbol{\theta}})$. The variance of the MLE $\widehat{\theta_i}$ can then be numerically determined by the fact that the contour in parameter space defined by $\chi^2(\boldsymbol{\theta}) = s^2$ has tangent planes located at s-standard-deviation away from the MLE $\widehat{\theta_i}$.

Penalty Term

Each nuisance parameter θ_i in Table 6.1 is treated as a Gaussian distributed random variable, whose mean μ_i and standard deviation σ_i is determined from independent measurements. They then introduce a χ^2_{penalty} term in Eqn. 6.4

$$\chi^2_{\text{penalty}} = \sum_i \left(\frac{\theta_i - \mu_i}{\sigma_i} \right)^2 \quad (6.5)$$

where the subscript i runs over all the independent nuisance parameters. Some nuisance parameters, namely the four detector energy response parameters α_i, are correlated. In this case, the covariance error matrix is applied, and the χ^2_{penalty} becomes

$$\chi^2_{\text{penalty}}(\boldsymbol{\alpha}) = \sum_{i,j} (\alpha_i - \mu_i)(V^{-1})_{ij}(\alpha_j - \mu_j) \quad (6.6)$$

where the covariance matrix $V_{ij} = \text{cov}[\alpha_i, \alpha_j]$ is calculated in Section 3.4 from the fit to the detector energy response model.

Rate Term

$L_{\rm rate}$ defines the probability of detecting n events, when expecting ν events. This simply follows the Poisson distribution:

$$\begin{aligned} L_{\rm rate}(\boldsymbol{\theta}) &= f(n;\nu) \\ &= \frac{\nu^n e^{-\nu}}{n!} \end{aligned} \tag{6.7}$$

where $n = 930$ is the total number of observed $\bar{\nu}_e$ candidate events in the two analysis periods. The total number of expected events ν is the sum of the number of expected reactor $\bar{\nu}_e$ events, the number of expected georeactor $\bar{\nu}_e$ events and the number of all other background events in both analysis periods, predicted by model parameters $\boldsymbol{\theta}$.

Shape Term

The visible energy spectrum of prompt events is also model parameter $\boldsymbol{\theta}$ dependent. $L_{\rm shape}$ defines the probability of detecting the event set with prompt visible energies $\vec{E} = (E_1, \ldots, E_n)$. We consider the normalized prompt visible energy spectrum as a pdf $f(E;\boldsymbol{\theta})$, and define

$$L_{\rm shape}(\boldsymbol{\theta}) = \prod_i^{\rm events} f(E_i;\boldsymbol{\theta}) \tag{6.8}$$

$$= \prod_i^{\rm events} \left(\frac{1}{\nu} \sum_{j={\rm I}}^{\rm II} \sum_k \frac{{\rm d}N_k^j(E;\boldsymbol{\theta})}{{\rm d}E} \right) \Bigg|_{E=E_i} \tag{6.9}$$

where i runs over all the observed 930 event pairs, j runs over Period I and II and k runs over all the signal and background components of the energy spectrum (because of the change of the detector energy response between Period I and II, the visible energy spectrum of each component has to be evaluated separately in each period). ν is the same total number of expected events as in the $L_{\rm rate}$ term. In particular, the

prompt visible energy spectrum is normalized in such a way that

$$\int_{E_{\min}}^{E_{\max}} \mathrm{d}E \, \frac{\mathrm{d}N_k^j(E;\boldsymbol{\theta})}{\mathrm{d}E} = \nu_k^j \tag{6.10}$$

and

$$\int_{E_{\min}}^{E_{\max}} \mathrm{d}E \, \sum_{j=\mathrm{I}}^{\mathrm{II}} \sum_k \frac{\mathrm{d}N_k^j(E;\boldsymbol{\theta})}{\mathrm{d}E} = \nu \tag{6.11}$$

where $(E_{\min}, E_{\max}) = (2.7\mathrm{MeV}, 15\mathrm{MeV})$ is the analysis range of prompt energy, and ν_k^j is the expected number of signal or background events ν_k in period j.

Shape + Time Term

The time information of the observed events provides another powerful tool for evaluating the model parameters $\boldsymbol{\theta}$. In particular, the reactor $\bar{\nu}_e$ events are correlated with reactor power and varies with time, while the georeactor and other background type events are typically constant over time. On the other hand, the two terms L_{time} and L_{shape} are not independent of each other. This is because the relative of change of signal and background event rate with time will also affect the normalization of the energy spectrum, thus makes the shape time-dependent. In this case, a joint likelihood function $L_{\mathrm{shape+time}}$ is defined as the probability of detecting the event set with prompt visible energies $\vec{E} = (E_1, \ldots, E_n)$ at time $\vec{t} = (t_1, \ldots, t_n)$. We can then write down the normalized instantaneous prompt energy spectrum as a joint pdf $f(E, t; \boldsymbol{\theta})$, and define $L_{\mathrm{shape+time}}$ as

$$L_{\mathrm{shape+time}}(\boldsymbol{\theta}) = \prod_{i=1}^{930} f(E_i, t_i; \boldsymbol{\theta}) \tag{6.12}$$

$$= \prod_{i}^{930} \left(\frac{1}{\nu} \sum_{j=\mathrm{I}}^{\mathrm{II}} \sum_k \frac{\mathrm{d}N_k^j(E, t; \boldsymbol{\theta})}{\mathrm{d}E\mathrm{d}t} \right) \Bigg|_{E=E_i,\, t=t_i} \tag{6.13}$$

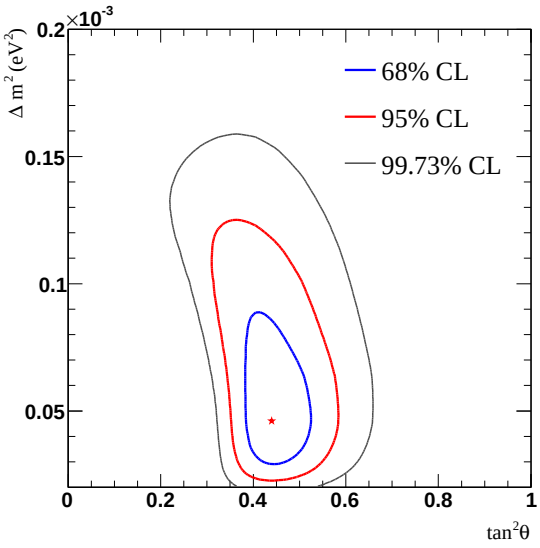

Figure 6.1: The SNO-only contour plot on neutrino oscillation parameters, which includes a combined fit from SNO D2O & salt phase day and night spectra and NCD phase flux information [117]

where the subscripts are the same as in Eqn. 6.9 and the instantaneous reactor $\bar{\nu}_e$ rate is evaluated from Eqn. 5.6. Georeactor $\bar{\nu}_e$ rate and all other background ground event rates, on the other hand, are considered to be time-invariant over period j, such that:

$$\frac{\mathrm{d}N_k^j(E,t;\boldsymbol{\theta})}{\mathrm{d}E\mathrm{d}t} = \frac{1}{T_j}\frac{\mathrm{d}N_k^j(E;\boldsymbol{\theta})}{\mathrm{d}E} \tag{6.14}$$

where T_j is the total live time of period j, and k runs over all the signal and background components except the reactor $\bar{\nu}_e$ component. The normalization then, after integrating over the live time in each period, becomes the same as in Eqn. 6.10 and 6.11

Solar Term

Solar neutrino experiments, discussed in Section 1.2.2, probe the same neutrino oscillation parameters region as KamLAND does, assuming CPT invariance. In particular, as will be shown, they provide better constraint on $\tan^2\theta_{12}$ than KamLAND-only analysis.

The SNO-only χ^2 table [118] is used in this analysis, which includes a combined fit from SNO D2O & salt phase day and night spectra and NCD phase flux information [117]. Fig. 6.1 shows the SNO-only contour plot on (Δm^2_{21}, $\tan^2\theta_{12}$) parameter space. Since including other solar neutrino experiment results into the global fit does not improve significantly on the contour, while introducing non-trivia correlated systematic errors, it is avoided in this analysis. The solar term then introduces a $\chi^2_{\rm solar}$ term which only depends on model parameter $\tan^2\theta_{12}$ and Δm^2_{21}:

$$\chi^2_{\rm solar}(\boldsymbol{\theta}) = \chi^2_{\rm SNO}(\tan^2\theta_{12}, \Delta m^2_{21}) \tag{6.15}$$

6.2 Analysis Modes

Four analysis modes are performed in this dissertation by including all or part of the likelihood function terms defined in Eqn. 6.2. The four modes are defined as follows:

KL-RS KamLAND-only (rate + shape)

$$L_{\rm KL-RS} = L_{\rm penalty} \cdot L_{\rm rate} \cdot L_{\rm shape} \tag{6.16}$$

KL-RST KamLAND-only (rate + shape + time)

$$L_{\rm KL-RST} = L_{\rm penalty} \cdot L_{\rm rate} \cdot L_{\rm shape+time} \tag{6.17}$$

KL-RS-Solar KamLAND (rate + shape) + Solar

$$L_{\rm KL-RS-Solar} = L_{\rm penalty} \cdot L_{\rm rate} \cdot L_{\rm shape} \cdot L_{\rm solar} \tag{6.18}$$

KL-RST-Solar KamLAND (rate + shape + time) + Solar

$$L_{\mathrm{KL-RST-Solar}} = L_{\mathrm{penalty}} \cdot L_{\mathrm{rate}} \cdot L_{\mathrm{shape+time}} \cdot L_{\mathrm{solar}} \tag{6.19}$$

6.3 Best Fit Parameters

The best-fit model parameters $\boldsymbol{\theta}$ were extracted from the two KamLAND-only analysis modes "KL-RS" and "KL-RST". In each analysis mode, the effective $\chi^2 = -2 \ln L$ is minimized using the Minuit Package [94], which is equivalent to maximize the likelihood function. The best-fit values of free model parameters are summarized in Table 6.2. Notice that in the "KL-RS" analysis mode, the best-fit value of georeactor power comes out to be zero (with large uncertainties).

Fig. 6.2 shows the prompt visible energy spectra from signal and background components, predicted by the best-fit model parameters from each analysis mode. Also shown on the plot is the binned observed events' energy spectrum for visual comparison.

Fig. 6.3 shows the time variation of event rate from signal and background components, predicted by the best-fit model parameters. KamLAND data are binned into 8 equal live-time bins with 180 live-days each. The filled area shows the expected total events in each bin (reactor + georeactor + all backgrounds). The best-fit average event rate is ∼0.6/day from oscillated reactor $\bar{\nu}_e$, and ∼0.05/day from oscillated

Table 6.2: Summary of best-fit values of free model parameters, in the "rate + shape" (KL-RS) and "rate + shape + time" (KL-RST) analysis modes. Shown in the parenthesis is the uncertainty of each parameter returned by the Minuit package.

Parameter	KL-RS	KL-RST	Description
$\tan^2\theta_{12}$	0.40(07)	0.51(20)	ν oscillation mixing angle
Δm^2_{21} [$\times 10^{-5}\mathrm{eV}^2$]	7.58(24)	7.56(27)	ν oscillation mass square difference
P_{geo} [TW]	0(5.4)	6.6(7.4)	Georeactor fission power
$N_{\mathrm{fn,atm}}$	19(6)	19(6)	fast neutron + atmospheric ν events

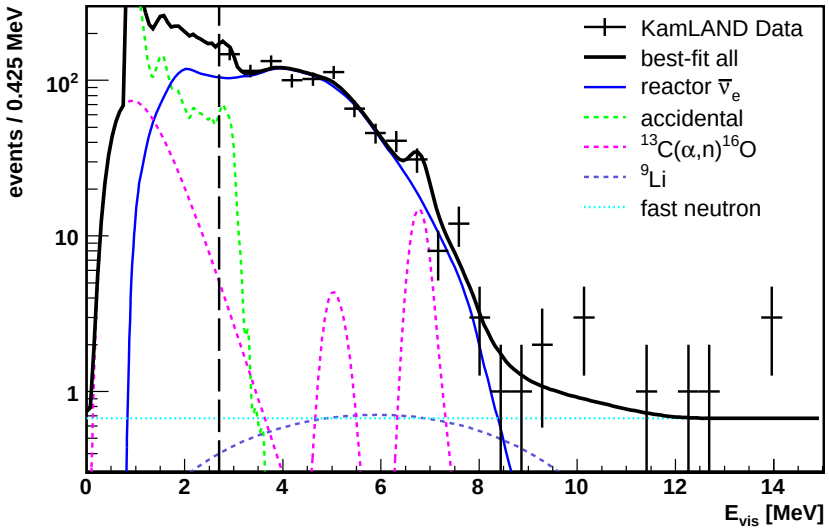

(a) Rate + Shape

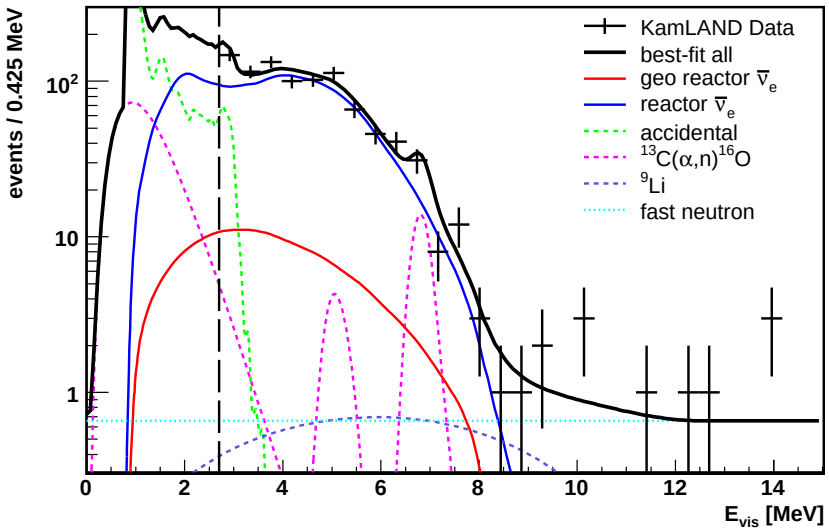

(b) Rate + Shape + Time

Figure 6.2: The prompt visible energy spectra predicted from the best-fit model parameters, with binned $\bar{\nu}_e$ candidate data overlaid, in (a) "rate + shape" analysis mode; (b) "rate + shape + time" analysis mode. The energy spectrum components shown on the graph are: best-fit total energy spectrum (black solid), oscillated georeactor $\bar{\nu}_e$ (solid red), oscillated reactor $\bar{\nu}_e$ (solid blue), accidentals (dashed green), $^{13}C(\alpha,n)^{16}O$ (dashed magenta), ^{9}Li (dashed light blue) and fast neutron (dashed cyan). The best-fit georeactor power is zero in "rate + shape" analysis mode. The vertical long-dashed line indicates the analysis threshold at 2.7 MeV.

georeactor $\bar{\nu}_e$ events in the KL-RST analysis mode.

6.4 Goodness-of-fit Test

The maximum likelihood method, however, does not provide a direct way to evaluate the goodness of fit. In particular, the effective $\chi^2 = -2\ln L$ does not indicate the quality of the fit. Instead, a binned goodness-of-fit test is performed following the statistical techniques described in Ref. [119].

Goodness-of-fit of Energy Spectrum

A goodness-of-fit test is performed to the best-fit prompt visible energy spectrum (from the KL-RS mode) as follows. First, N equal probability bins are constructed from the expected total energy spectrum (Fig. 6.2(a)) in the analysis range 2.7 – 15 MeV. The Pearson χ^2 is then defined by :

$$\chi^2_{\text{Person}}(\text{shape}) = \sum_{i=1}^{N_{\text{bins}}} (n_i - \mu_i)^2/\mu_i \tag{6.20}$$

where n_i is the number of observed events in the i^{th} bin, and μ_i is the number of expected events in the i^{th} bin. Then, the χ^2_{penalty} term from nuisance model parameters (Eqn. 6.5) is added to the total Pearson χ^2 :

$$\chi^2_{\text{test}} = \chi^2_{\text{Person}}(\text{shape}) + \chi^2_{\text{penalty}} \tag{6.21}$$

The remaining four free model parameters ($\tan^2\theta_{12}$, Δm^2_{21}, P_{geo}, $N_{\text{fn,atm}}$) decrease the total number of degree of freedom (ndf) by 4. The p-value is then looked up from the χ^2 distribution with $N-4$ degree of freedom, and plotted against the number of bins, shown in Fig. 6.4.

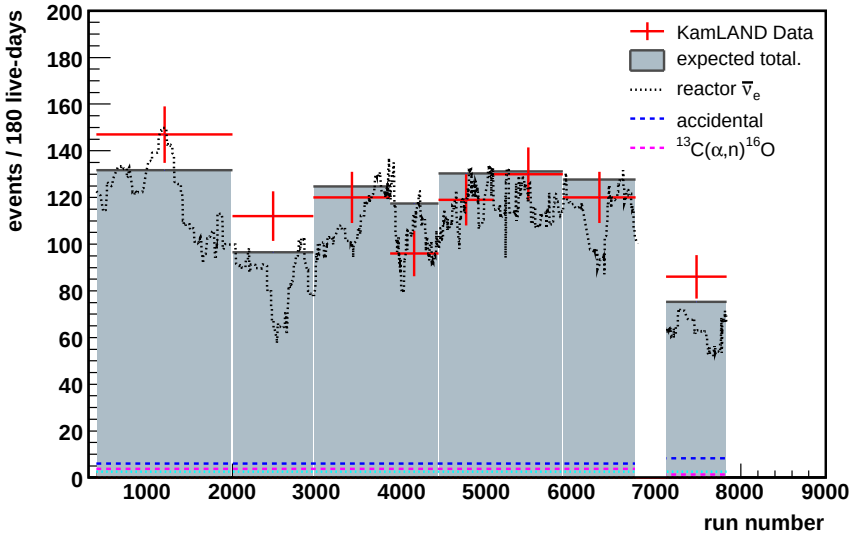

(a) Rate + Shape

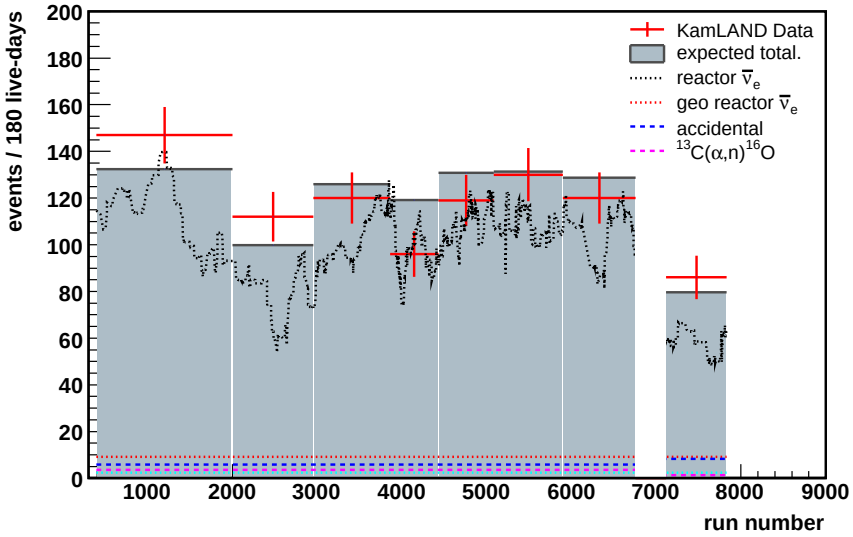

(b) Rate + Shape + Time

Figure 6.3: Time variation of event rate predicted by the best-fit model parameters in (a) "rate + shape" analysis mode; (b) "rate + shape + time" analysis mode. KamLAND data (solid red) are binned into 8 equal live-time bins with 180 live-days each. The filled light blue area shows the expected total events in each bin (reactor + georeactor + all BG). Also shown on the figures are : oscillated reactor $\bar{\nu}_e$ (dotted black), oscillated georeactor $\bar{\nu}_e$ (dotted red), accidentals (dashed blue) and $^{13}C(\alpha,n)^{16}O$ (dashed magenta). ^{9}Li and fast neutron background are too small to be shown. The best-fit georeactor power is zero in the "rate + shape" analysis mode.

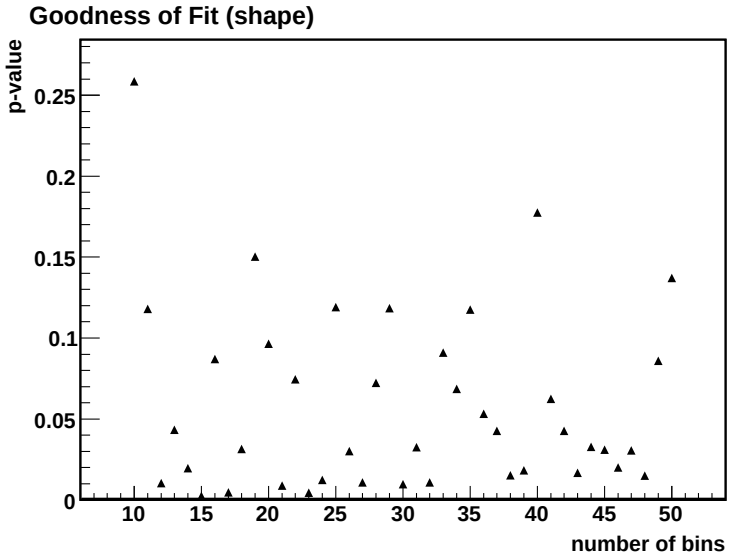

Figure 6.4: Goodness-of-fit of the prompt visible energy spectrum. The p-value is plotted against the number of bins used to construct the goodness-of-fit test.

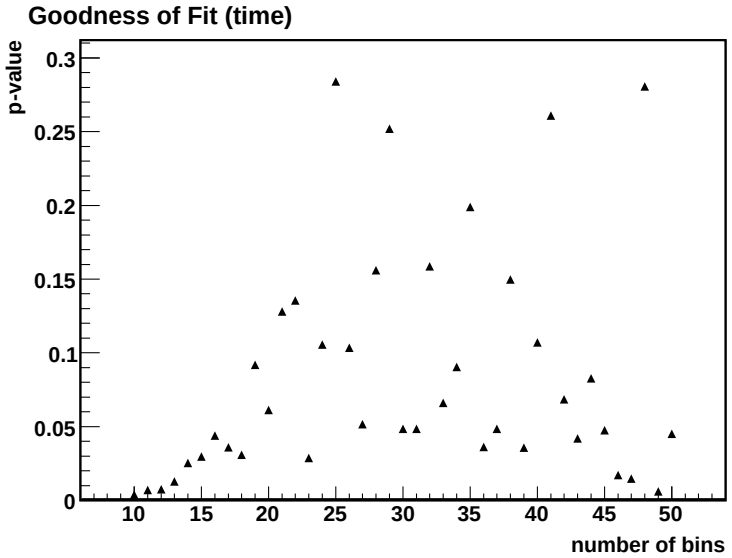

Figure 6.5: Goodness-of-fit of the time variation spectrum. The p-value is plotted against the number of bins used to construct the goodness-of-fit test.

Goodness-of-fit of Time Variation Spectrum

A goodness-of-fit test is also performed to the best-fit time variation spectrum (from the KL-RST mode). N equal probability bins are constructed from the expected total event rate time-variation spectrum shown in Fig. 6.3(b). The χ^2 test is then defined by :

$$\chi^2_{\text{test}} = \chi^2_{\text{Person}}(\text{time}) + \chi^2_{\text{penalty}} \tag{6.22}$$

where χ^2_{penalty} is defined the same as in goodness-of-fit test of energy spectrum. The four free model parameters ($\tan^2\theta_{12}$, Δm^2_{21}, P_{geo}, $N_{\text{fn,atm}}$) decrease ndf by 4. The p-value is then looked up from the χ^2 distribution with $N-4$ degree of freedom, and plotted against the number of bins, shown in Fig. 6.5.

The number of equal probability bins used to construct the χ^2 test is subjective and need to be chosen based on the data set. From Eqn 25.62 in Ref. [119], the recommended number of bins is approximately proportional to $n^{0.4}$, where n is the total number of events. For this analysis, a recommended range of 25 – 50 bins is calculated following Ref. [119]. Increasing the number of bins would make the fit more sensitive to the high frequency components of the spectrum. If we choose 40 equal probability bins, the p-value is 0.18 for the energy spectrum χ^2 test and 0.11 for the time variation spectrum χ^2 test. The goodness-of-fit test finds no issues with the fit and the result for the unbinned likelihood analysis is reasonable.

6.5 Significance of Energy Spectrum Distortion

In Fig. 6.6(a) we plot the observed prompt visible energy spectrum together with the expected spectrum without neutrino oscillation. As can be seen the two spectra are inconsistent with each other, in particular due to the large deficit of the observed event rate. One alternative explanation of this inconsistence is that some unknown factors

cause a larger decrease of $\bar{\nu}_e$ detection efficiency than expected. A no-oscillation shape-only analysis is performed to test this hypothesis, by fixing θ_{12} at zero but allowing the efficiency $\epsilon_{\text{reactor}}$ to float freely. The $\bar{\nu}_e$'s from man-made reactors and from the georeactor are treated together since their spectra essentially become the same in the no-oscillation case. The resulting best-fit spectra are shown in Fig. 6.6(b).

As can be visually seen, the best-fit prompt energy spectrum in the on-oscillation case does not agree well with the data. A goodness-of-fit χ^2 test is constructed the same as in Section 6.4. The two free model parameters ($\epsilon_{\text{reactor}}$, $N_{\text{fn,atm}}$) decrease the ndf by 2. The resulting p-value is plotted against the number of bins used to construct the χ^2 test, shown in Fig. 6.7. One can compare this with the goodness-of-fit test from oscillation analysis (Fig. 6.4). Although the p-values are sensitive to the number of bins chosen, the majority of them are below 0.1%, corresponding to the no-oscillation hypothesis being disfavored at more than 3σ from the distortion of the shape of prompt energy spectrum.

6.6 Correlation with Reactor $\bar{\nu}_e$ Flux

In Fig. 6.8(b) we show the correlation of the data with the reactor $\bar{\nu}_e$ flux by plotting the observed event rate against the expected reactor $\bar{\nu}_e$ rate without oscillation. A positive correlation is clearly visible. If the survival probability and background rate is constant over time, then one would expect a perfect linear correlation between the two. A linear fit and the 1σ C.L. region from the fit is shown as the gray shaded area in Fig. 6.8(b). The fitting result seems to suggest an extra event rate above the expected background level at zero reactor power, a hint of the existence of non-negligible georeactor $\bar{\nu}_e$ flux.

However, the above conclusion is incorrect because the survival probability of $\bar{\nu}_e$ varies with time too. From Eqn. 1.11, the survival probability depends on the

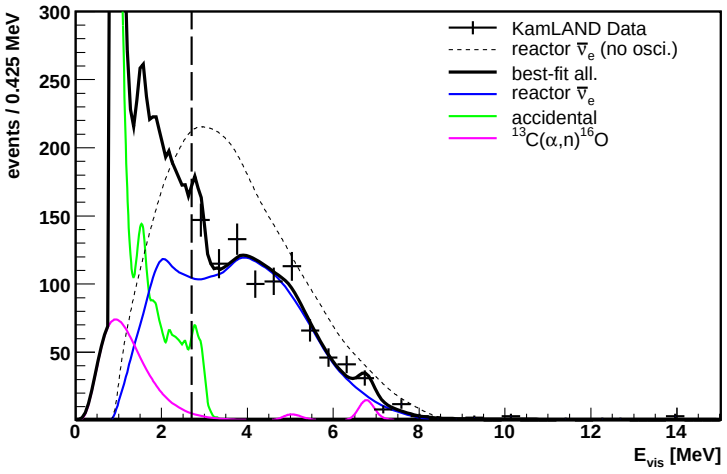

(a) Oscillation Analysis

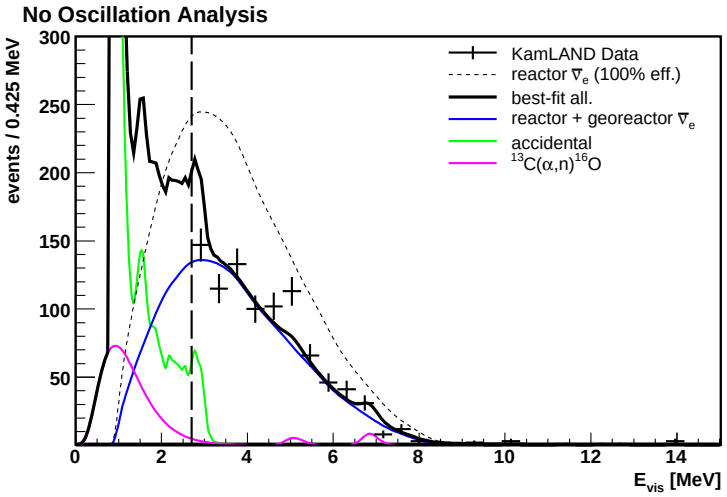

(b) No Oscillation Analysis

Figure 6.6: The best-fit prompt visible energy spectra from (a) KamLAND-only oscillation (rate + shape) analysis, (b) KamLAND-only no-oscillation (shape-only) analysis. In both cases, ^{9}Li and fast neutron backgrounds are too small to be shown. The vertical long-dashed line indicates the analysis threshold at 2.7 MeV. The best-fit total prompt energy spectrum from no-oscillation analysis does not agree well with the data.

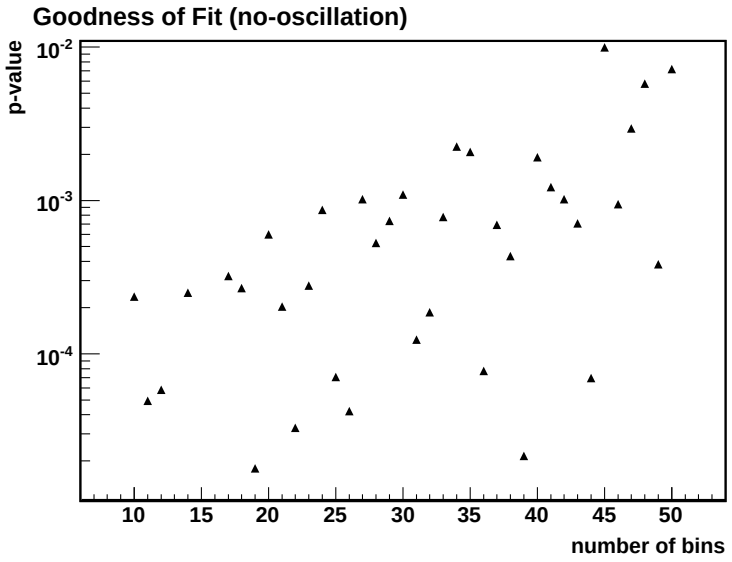

Figure 6.7: Goodness-of-fit of no-oscillation analysis. The p-value is plotted against the number of bins used to construct the $\chi^2_{\rm Person}$ test.

distances of the reactors to the detector. With different reactors turned on and off at different times, the relative contribution of $\bar{\nu}_e$ flux from each reactor changes, which causes the survival probability to be time-dependent. With the oscillation parameters from Ref. [22], the survival probability is calculated as a function of time as shown in Fig. 6.8(a). On average, a $\sim$10% variation of the survival probability is seen over time. In particular, the Shika reactors are at a much closer distance (88 km) than the average (180 km). When they were in full operation, a noticeable decrease of the survival probability was observed.

We can account for the time variation of survival probability by plotting the observed event rate against the expected oscillated reactor $\bar{\nu}_e$ rate, as shown in Fig. 6.8(c). A linear fit yields $\chi^2/{\rm ndf} = 9.8/15$. The allowed 68.3% C.L. region from the fit is shown as the grey shaded area. The correlation coefficient (slope) from the fit is 0.784 ± 0.211. The rather large uncertainty comes from the limited statistics, and reflects the fact that KamLAND by itself does not constrain the θ_{12} very well.

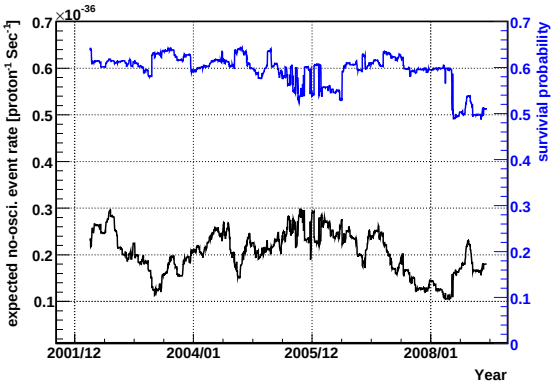

(a) Time Variation of Survival Probability

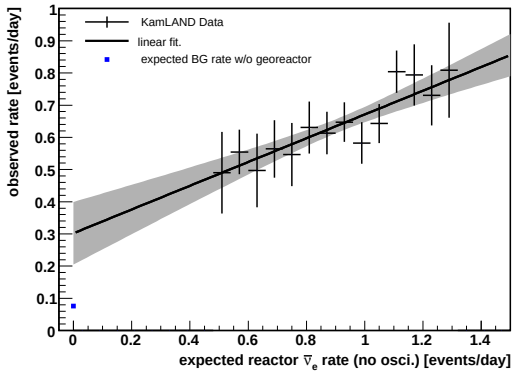

(b) Correlation with Un-oscillated Reactor $\bar{\nu}_e$ Flux

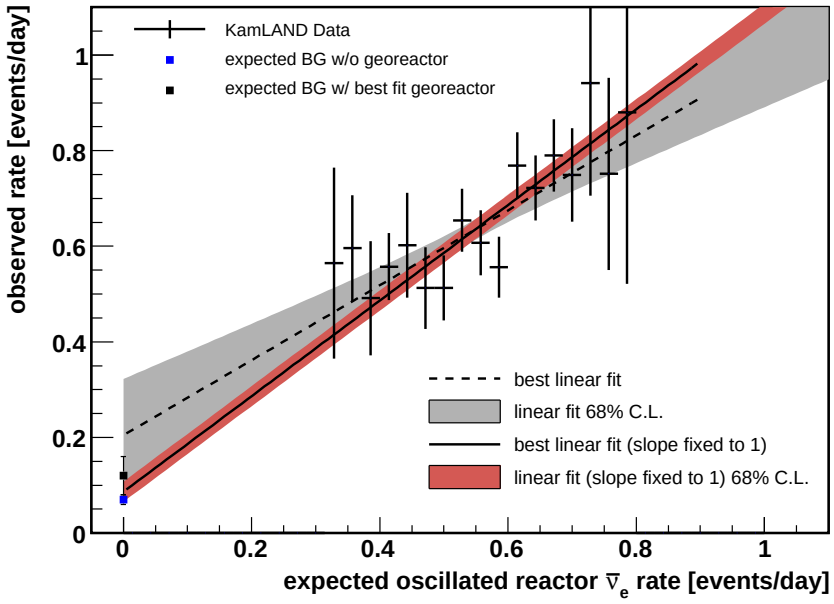

(c) Correlation with Oscillated Reactor $\bar{\nu}_e$ Flux

Figure 6.8: (a) Time variation of survival probability calculated with the oscillation parameters from Ref. [22]. (b) Correlation of observed event rate with expected un-oscillated reactor $\bar{\nu}_e$ flux. (c) Correlation of observed event rate with expected oscillated reactor $\bar{\nu}_e$ flux. In case (c), a linear fit yields $\chi^2/\text{ndf} = 9.8/15$, with the allowed 68.3% C.L. region shown as the grey shaded area. The correlation coefficient (slope) from the fit is 0.784 ± 0.211. A linear fit with the slope fixed to 1 yields $\chi^2/\text{ndf} = 10.8/15$ with the allowed 68.3% C.L. region shown as the red shaded area. The event rate at zero reactor $\bar{\nu}_e$ flux is 0.09 ± 0.02 from the fit. The expected background event rate without georeactor is 0.07 ± 0.01 events/day (blue marker). The expected background event rate including best fit georeactor $\bar{\nu}_e$ is 0.12 ± 0.04 events/day (black marker) from the "rate + shape + time" unbinned likelihood analysis.

If we take as a priori the precision of the oscillation parameters from Ref. [22], a linear fit can be performed with the slope fixed to expected value 1. The result from the fit is $\chi^2/\text{ndf} = 10.8/16$ with the allowed 68.3% C.L. region shown as the red shaded area in Fig. 6.8(c). The expected background event rate without georeactor is 0.07 ± 0.01 events/day (blue marker), which agrees with the fitted event rate at zero reactor $\bar{\nu}_e$ flux (0.09 ± 0.02 events/day) within 1σ, and no clear evidence of the existence of the georeactor is observed. As a comparison, the expected background event rate including best fit georeactor $\bar{\nu}_e$ is 0.12 ± 0.04 events/day (black marker) from the KL-RST unbinned likelihood analysis.

6.7 Results on Georeactor Fission Power

All four analysis modes described in Section 6.2 have been performed on the data to estimate the georeactor fission power. In each analysis mode, a global scan on (P_{geo}, $\tan^2\theta_{12}$) parameter space is performed, where for each pair of values of (P_{geo}, $\tan^2\theta_{12}$), a best fit is obtained by varying other model parameters until the effective χ^2 is minimized. The 68.3%, 90% and 99% confidence regions are given as all points that have a χ^2 within 2.30, 4.61 and 9.21 of the global minimum value. The results are shown in Fig. 6.9. A positive correlation between P_{geo} and $\tan^2\theta_{12}$ is clear in all four analyses. The positive correlation mainly comes from the following two facts:

1. The higher the $\tan^2\theta_{12}$ is, the more georeactor $\bar{\nu}_e$ events disappeared by oscillation before getting to the detector, thus for the same number of observed georeactor $\bar{\nu}_e$ events, the higher the georeactor power is.

2. The higher the $\tan^2\theta_{12}$ is, the more reactor $\bar{\nu}_e$ events disappear by oscillation. For the same number of total observed events, this implies more among them could be georeactor $\bar{\nu}_e$ events, which leads to a higher georeactor power.

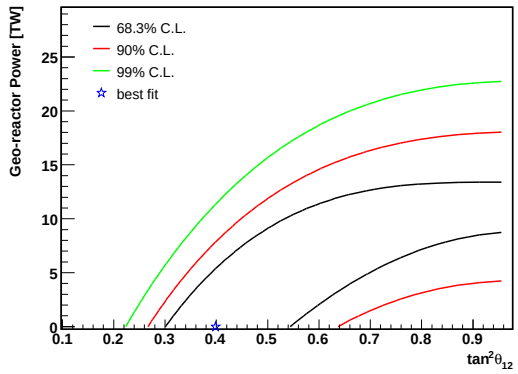

(a) KamLAND-only (rate + shape)

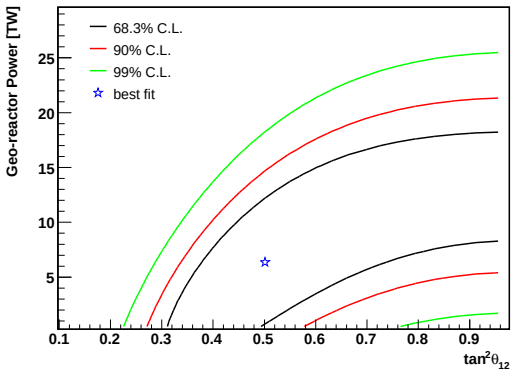

(b) KamLAND-only (rate + shape + time)

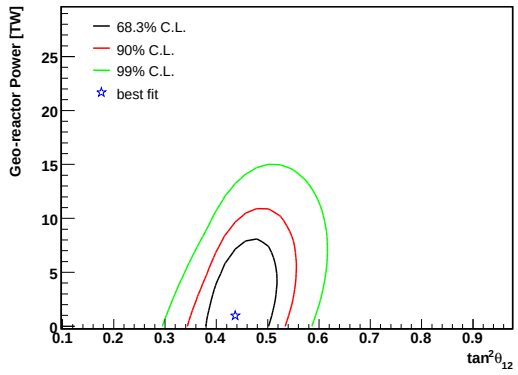

(c) KamLAND (rate + shape) + Solar

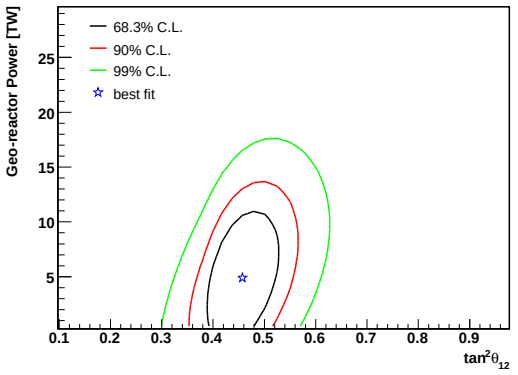

(d) KamLAND (rate + shape + time) + Solar

Figure 6.9: The 68.3%, 90% and 99% confidence regions of ($P_{\rm geo}$, $\tan^2\theta_{12}$) from (a) KamLAND-only (rate + shape + time) analysis; (b) KamLAND-only (rate + shape + time); (c) KamLAND (rate + shape + time) + Solar analysis; (d) KamLAND (rate + shape + time) + Solar analysis.

The positive correlation between $P_{\rm geo}$ and $\tan^2\theta_{12}$ implies that a better constraint on $\tan^2\theta_{12}$ will also give a better constraint on $P_{\rm geo}$. KamLAND-only analysis, while giving the best constraint on Δm^2_{21} (from distortion of energy spectrum), does not constrain $\tan^2\theta_{12}$ very well (Section 6.8), especially on the higher end of $\tan^2\theta_{12}$. The situation becomes worse when including the georeactor in the analysis since too large a deficit caused by a large $\tan^2\theta_{12}$ can now be partially compensated for by the georeactor $\bar{\nu}_e$ flux. On the other hand, the solar neutrino experiments give a much better constraint on $\tan^2\theta_{12}$ [117], especially on the higher end of $\tan^2\theta_{12}$. By including the solar χ^2 term in the analysis, the constraint on georeactor power is largely improved.

The χ^2 distribution of georeactor fission power is obtained by performing a one-dimensional scan on $P_{\rm geo}$. For each value of $P_{\rm geo}$, a best fit is obtained by varying other model parameters. The global minimum $\chi^2_{\rm min}$ is subtracted from each best-fit χ^2, and the $\Delta\chi^2$ profile is shown in Fig. 6.10. As expected, the best constraint comes from including the solar term in the analysis. The best fit value of georeactor fission power is at $1.0^{+4.8}_{-1.0}$ TW from the KL-RS-Solar analysis, and $4.9^{+3.8}_{-4.8}$ TW from the KL-RST-Solar analysis. By including the time variation information of expected event rate, the best-fit value of georeactor power moved from 1.0 TW to 4.9 TW which is approximately 1σ away from zero. The reason is best illustrated from the best-fit time variation spectrum in Fig. 6.3. The few extra observed events in bin 1, 2 and 8 slightly prefer a sizable georeactor $\bar{\nu}_e$ flux which is constant over time.

Nevertheless zero georeactor power is still allowed at 1σ even in the KL-RST-Solar analysis, indicating a small signal. For this reason we follow Feldman and Cousins' unified approach [120] to construct the confidence intervals. The 68.3%, 90%, and 99% confidence intervals of georeactor fission power in units of TW are (0, 5.8), (0, 8.8) and (0, 13.3) from the KL-RS-Solar analysis and (1.1, 8.7), (0, 11.2), and (0, 14.7) from KL-RST-Solar analysis, respectively.

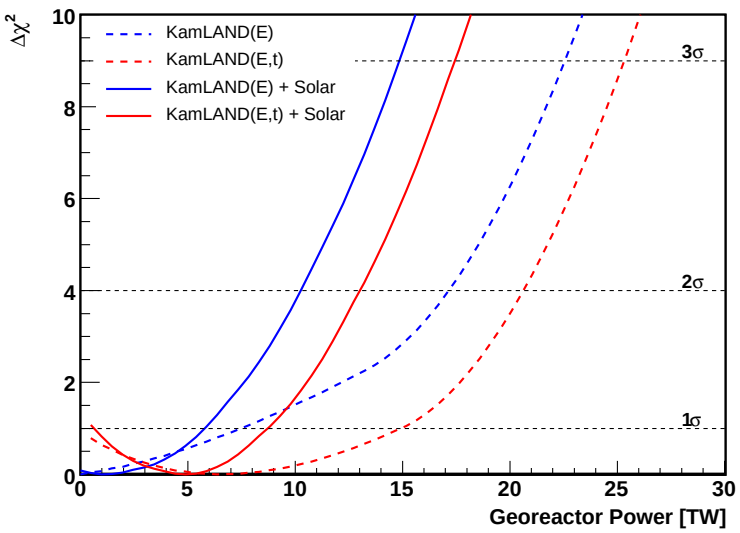

Figure 6.10: 1-D χ^2 distribution of georeactor fission power. The results comes from 4 different analysis modes: "KamLAND-only (rate + shape)" (dashed blue), "KamLAND-only (rate + shape + time)" (dashed red), "KamLAND (rate + shape) + solar" (solid blue) and "KamLAND (rate + shape + time) + solar" (solid red). The best fit value of georeactor fission power is at $1.0^{+4.8}_{-1.0}$ TW with "KamLAND (rate + shape) + solar" analysis, and $4.9^{+3.8}_{-4.8}$ TW with "KamLAND (rate + shape + time) + solar" analysis.

Period-I-Only Analysis

As mentioned in the previous chapters, the ∼180-live-day data from Period II is important to the analysis because of the reduced reactor $\bar{\nu}_e$ flux (Fig. 5.3) due to the shut-down of Kashiwazaki reactors. However, due to the change of liquid scintillator properties after the purification, the data from Period II have different systematics from Period I. Even though they are properly treated as described in the previous chapters, as a consistency check, a period-I-only analysis is performed by only including the data from Period I. The results are shown in Fig. 6.11. The best fit value of georeactor fission power is at $2.8^{+4.6}_{-2.8}$ TW in the KL-RST-Solar analysis. The 68.3%, 90%, and 99% confidence intervals of georeactor fission power in units of TW are (0.3, 7.4), (0, 10.3) and (0, 14.6) following Feldman and Cousins' unified approach [120].

Comparing with the results from full-data-set analysis, the best-fit georeactor signal is less than 1σ from zero in the period-I-only analysis. The result is quite interesting and suggests that for future improvement on the georeactor detection, a longer low-reactor-power period is necessary. If possible, a new experiment set up far away from any man-made nuclear reactors is preferred.

Heat Balance of the Earth

Fig. 6.12 shows the heat balance of the Earth plotted as georeactor heat output v.s. radiogenic (and other residual) heat output. The 90% C.L region of total heat flow of the Earth comes from a combination of two models [69, 70], which predicts 44.2 ± 1.0 TW and 31 ± 1 TW respectively. The expected radiogenic heat from Ref. [18, 19, 20] predicts 19 TW to 31 TW. The geoneutrino measurement by KamLAND[21, 22] infers the radiogenic heat from uranium and thorium decay chains to be within (7, 27) TW at 90% C.L. if fixing the Th/U mass ratio to 3.9 as derived from chondritic meteorites [121]. The allowed region of heat flow generated by georeactor, derived from KL-RST-Solar analysis in this dissertation, is shown as the red shaded area.

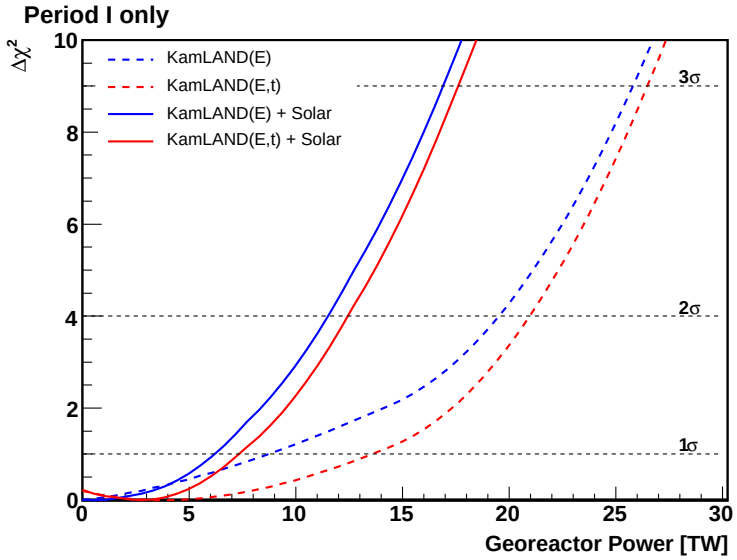

Figure 6.11: 1-D χ^2 distribution of georeactor fission power, including only the data from Period I.

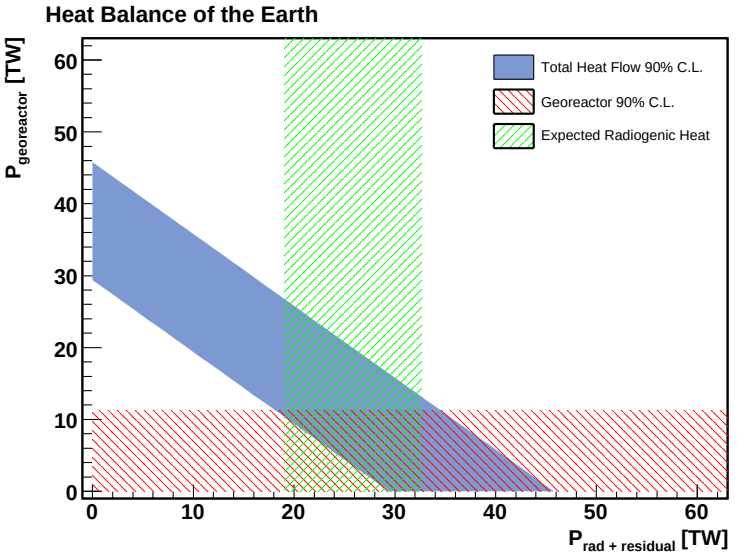

Figure 6.12: Heat balance of the Earth plotted as georeactor heat output v.s. radiogenic (and other residual) heat output. The light blue filled area is the total heat flow of the Earth at 90% C.L. [69, 70], the green hatched area is the expected radiogenic heat output [18, 19, 20], and the red hatched area is the allowed 90% region from the analysis described in this dissertation.

6.8 Results on Neutrino Oscillation Parameters

Null Georeactor Analysis

KamLAND's previous published results [45, 46, 22] on neutrino oscillation all assumed non-existence of georeactor in the analysis. To cross-check with these results, a null-georeactor analysis is performed with the same analysis method as described in this thesis except fixing the georeactor power at zero. In the absence of $\bar{\nu}_e$ disappearance, we expect to observe $1372.4 \pm 57.6(\text{syst.})$ reactor $\bar{\nu}_e$ events above 2.7 MeV, where the systematic uncertainty is summarized in Table 5.5. We observed 930 events, among which the total number of background events is 109.4 ± 13.5. The average survival probability of $\bar{\nu}_e$ is calculated to be

$$R = \frac{N_{\text{obs}} - N_{\text{BG}}}{N_{\text{expected}}} = 0.598 \pm 0.022(\text{stat.}) \pm 0.027(\text{syst.}) \tag{6.23}$$

The probability of no-oscillation is rejected at $(1 - 5 \times 10^{-17})$ C.L. (8.3σ).

The allowed region in $(\Delta m^2_{21}, \tan^2\theta_{12})$ space from null-georeactor analysis is shown in Fig. 6.13. In KL-RST analysis, there are still small allowed regions in the LMA-II region at 99% C.L. The recent released KamLAND results [22] lowered the analysis energy threshold to 0.9 MeV, which helped to exclude LMA-0 and LMA-II at 99.73% C.L. with "KamLAND only" analysis. In either case, when combining with solar results, only LMA-I solution is allowed at 99.73% C.L.

From the null-georeactor analysis, the best-fit values of neutrino oscillation parameters are $\tan^2\theta_{12} = 0.38^{+0.08}_{-0.06}$, $\Delta m^2_{21} = 7.59^{+0.28}_{-0.27} \times 10^{-5}$ eV^2 in KL-RST analysis, and $\tan^2\theta_{12} = 0.42^{+0.04}_{-0.04}$, $\Delta m^2_{21} = 7.50^{+0.26}_{-0.21} \times 10^{-5}$ eV^2 in KL-RST-Solar analysis. This is consistent with KamLAND's previous published results.

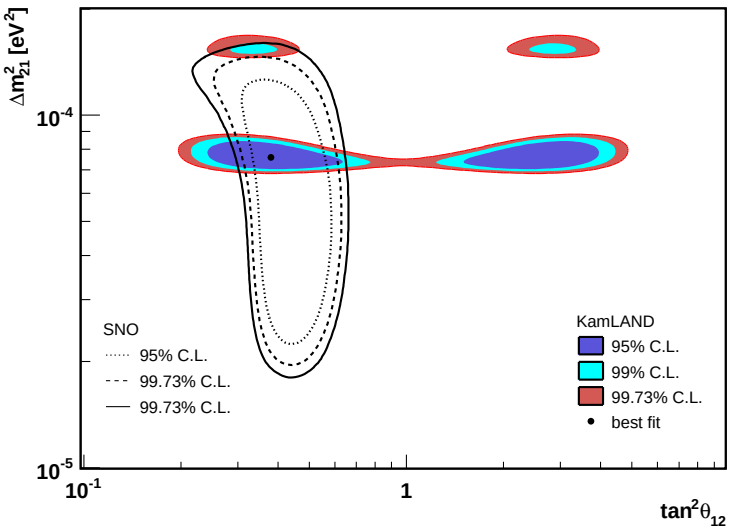

(a) KamLAND-only, Null Georeactor

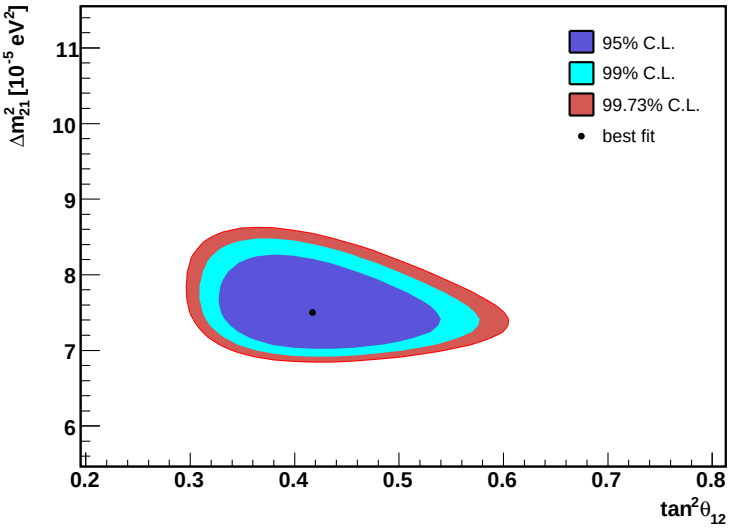

(b) KamLAND + Solar, Null Georeactor

Figure 6.13: The 95%, 99% and 99.73% confidence regions of (Δm^2_{21}, $\tan^2\theta_{12}$) from (a) KamLAND-only (rate + shape + time) analysis, (b) KamLAND (rate + shape + time) + Solar analysis. In both analyses, a null georeactor hypothesis is assumed.

Combined Analysis of Neutrino Oscillation and Georeactor

The Best-fit georeactor fission power from the KL-RST-Solar analysis is $4.9^{+3.8}_{-4.8}$ TW, which corresponds to $58.5^{+45.4}_{-56.1}$ oscillated georeactor $\bar{\nu}_e$ events at KamLAND. The total number of background events, including the georeactor $\bar{\nu}_e$'s, is $167.9^{+47.3}_{-57.7}$. The $\bar{\nu}_e$ survival probability is calculated to be

$$R = \frac{N_{\rm obs} - N_{\rm BG}}{N_{\rm expected}} = 0.555 \pm 0.022({\rm stat.}) \pm 0.048({\rm syst.}) \tag{6.24}$$

The probability of no-oscillation is rejected at $(1 - 10^{-12})$ C.L. (7.0σ).

Fig. 6.14 shows the allowed region in (Δm^2_{21}, $\tan^2\theta_{12}$) space from the combined analysis of neutrino oscillation and georeactor with the method described in this thesis. Comparing with null-georeactor analysis, in KL-RST case, because of the greater freedom introduced by the existence of georeactor $\bar{\nu}_e$, more areas are allowed especially in the LMA-0 (lower) and LMA-II (upper) regions. In particular, the uncertainty in the large $\tan^2\theta_{12}$ region becomes larger for the reason discussed in Section 6.7. However by including solar neutrino results in the analysis, still only LMA-I solution is allowed at 99.73% confidence level.

From the combined analysis, the best-fit values of neutrino oscillation parameters are $\tan^2\theta_{12} = 0.50^{+0.14}_{-0.14}$, $\Delta m^2_{21} = 7.59^{+0.29}_{-0.26} \times 10^{-5}$ eV^2 in KL-RST analysis, and $\tan^2\theta_{12} = 0.44^{+0.05}_{-0.05}$, $\Delta m^2_{21} = 7.59^{+0.27}_{-0.27} \times 10^{-5}$ eV^2 in KL-RST-Solar analysis. This is consistent with KamLAND's previously published results with null-georeactor hypothesis, and shows that including the georeactor does not significantly change the current best measured values of neutrino oscillation parameters.

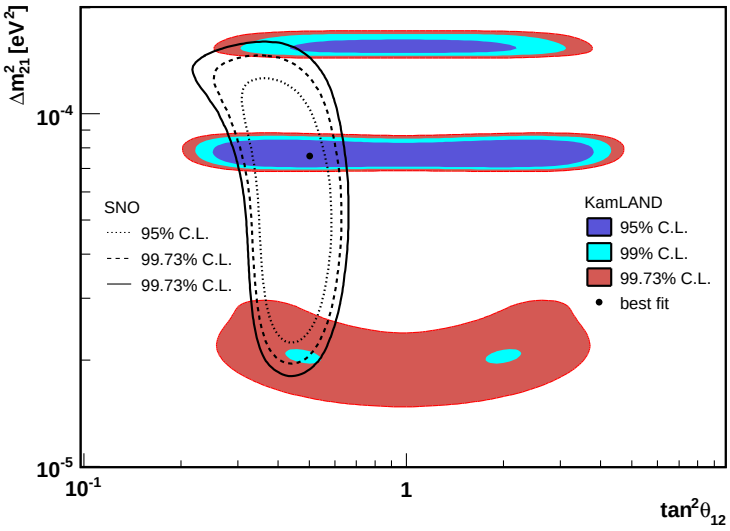

(a) KamLAND-only

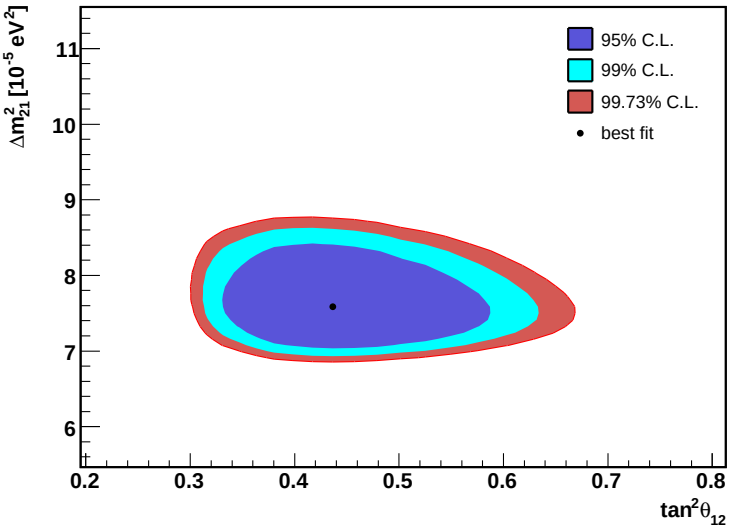

(b) KamLAND + Solar

Figure 6.14: The 95%, 99% and 99.73% confidence regions of (Δm^2_{21}, $\tan^2\theta_{12}$) from (a) KamLAND-only (rate + shape + time) analysis, (b) KamLAND (rate + shape + time) + Solar analysis. The result comes from the combined analysis of neutrino oscillation and georeactor with the method described in this thesis.

Chapter 7 Conclusions

The KamLAND experiment, being on the surface of the Earth, provides a unique tool to investigate the georeactor hypothesis which predicts a natural fast breeder type nuclear reactor at the center of the Earth. The anti-electron-neutrinos from a georeactor have a constant flux over time that is rather distinguishable from man-made reactors whose powers may vary over time due to the operations. They also have a different energy spectrum from the man-made reactors when reaching the KamLAND detector due to the neutrino oscillation effects. Combining with the solar neutrino experiments, KamLAND for the first time can provide a strong test on the georeactor hypothesis, measuring or setting a limit on its fission power.

The analysis presented in this dissertation includes all the data taken from Apr 2002 to Jun 2008, except the six months from Apr 2007 to Oct 2007 during which the detector upgrading work was on-going. Since July 2007, the 25 GWth Kashiwazaki nuclear plant has been shut down due to damage from an earthquake, which resulted in about 25% of the reduction of reactor anti-neutrino signal in KamLAND when it is fully operational. The reduced event rate enables a more precise determination of the extrapolated zero power rate, which helps to set the limit on the georeactor power. The total live time for the analysis is 1439.87 days after muon veto. The fiducial volume for the analysis has been extended to 6 meter radius compared with the previous US analysis (5.5 m), which enlarges the fiducial mass to 0.7 ktons and gives a total exposure of 2.75 kton-years (8.50×10^{34} proton-days).

From the data set 930 $\bar{\nu}_e$ candidate events above 3.4 MeV $\bar{\nu}_e$ energy threshold were extracted, with estimated 109 ± 13 events from backgrounds. The overall $\bar{\nu}_e$ detection efficiency is estimated to be $87.5 \pm 0.8\%$. An unbinned maximum likelihood analysis

was performed using the event rate, spectrum shape and time variation information. Combined with the solar neutrino experiments assuming CPT invariance, the best-fit value of georeactor power is $4.9^{+3.8}_{-4.8}$ TW. Using *Feldman and Cousins'* approach, the 90% upper limit on georeactor power is determined to be 11.2 TW. Since the total heat from the Earth is known to be between 30 and 45 TW, this result has put a significant constraint on the contribution of a possible georeactor to the total power. The 1σ georeactor signal requires additional future statistics for verification. Periods with low man-made reactor power will be especially helpful.

A combined fit to the neutrino oscillation parameters is also performed, including the georeactor power as a free parameter. Combining with the solar neutrino experiments, the best-fit values of the oscillation parameters are $\tan^2\theta_{12} = 0.44^{+0.05}_{-0.05}$ and $\Delta m^2_{21} = 7.59^{+0.27}_{-0.27} \times 10^{-5}$ eV^2. All parameter spaces are excluded at 99.73% C.L. except the LMA-I region. The result is consistent with KamLAND's previously published results with null-georeactor analysis, and shows that including the georeactor does not significantly change the current best measured values of neutrino oscillation parameters.

Appendix A KamLAND Kr/Ar Monitor

A.1 Motivation and Methodology

Since 2007, the KamLAND collaboration started to upgrade the detector by purifying the liquid scintillator to reduce low energy backgrounds due to the radioactive contaminants, with the primary goal of observing solar ^{7}Be neutrinos. As discussed in Section 2.3.2, the signal from a ν_e elastic scattering is a single recoiled e^- event with maximum energy of 665 keV which is indistinguishable from a radioactive β^- decay event at similar energies. Table 2.3 lists the most concerned radioimpurity levels in KamLAND LS before the purification, and the requirement needed in solar phase in order to make a ^{7}Be solar neutrino measurement. Among them the ^{85}Kr and ^{39}Ar are especially harmful through their β^- decays

$$^{85}_{36}\mathrm{Kr} \longrightarrow {}^{85}_{37}\mathrm{Rb} + e^- + \bar{\nu}_e \qquad \mathrm{Q} = 687 \text{ keV}, \, t_{1/2} = 10.76 \text{ y} \tag{A.1}$$

and

$$^{39}_{18}\mathrm{Ar} \longrightarrow {}^{39}_{18}\mathrm{K} + e^- + \bar{\nu}_e \qquad \mathrm{Q} = 565 \text{ keV}, \, t_{1/2} = 269 \text{ y} \tag{A.2}$$

because of their long half-lives and the end-point Q values that are similar to end-point of the recoiled e^- spectrum from solar ^{7}Be ν_e elastic scattering. It is therefore necessary to have a Kr/Ar monitoring system that operates in-line with the purification system to ensure that the required purification factors are always achieved ($\sim 10^6$ for ^{85}Kr and $\sim 10^3$ for ^{39}Ar). Such a system must meet the following requirements:

- A high detection sensitivity. The system should be able to detect $1 - 10$ μBq/m^3 level of activity for dissolved ^{85}Kr and ^{39}Ar in the liquid scintillator, in order to

Isotope	$T_{1/2}$ [yr]	A_{air} [Bq/m^3]	$^{nat}N_{air}$ [mol/mol]	$^{iso}N/^{nat}N$
^{85}Kr	10.76	1.4	1.099×10^{-6}	2.8×10^{-11}
^{39}Ar	269	16.6×10^{-3}	0.933×10^{-2}	8.1×10^{-16}

Table A.1: Summary of characteristic properties of ^{85}Kr and ^{39}Ar. The symbols stand for: $T_{1/2}$: half life; A_{air}: activity in the atmosphere; $^{nat}N_{air}$: natural gas abundance in the atmosphere; $^{iso}N/^{nat}N$: isotopic abundance. The values are taken from [122, 123, 124, 125].

ensure the required purification factors.

- A fast measurement cycle. The system should provide measurement result in a relatively short time scale, in order for timely operation to be performed on the purification system.

- A low need for liquid scintillator sample volume. The system should be able to achieve the required sensitivity with a relatively small LS sample volume, in order to reduce the time and cost of LS production.

The above requirements make any radioassay techniques impractical for evaluating the reduction factors because of the low activities of ^{85}Kr and ^{39}Ar. However, by making a reasonable assumption that the purification techniques (distillation plus nitrogen purging) removes all isotopes of Kr or Ar with equal efficiency, it is more practical to measure the concentration of ^{nat}Kr and ^{nat}Ar in the LS, and infer the ^{85}Kr and ^{39}Ar activity provided that the ^{85}Kr/^{nat}Kr and ^{39}Ar/^{nat}Ar ratios are known.

The natural argon concentration in the air is measured to be $0.933 \pm 0.003\%$ [122], and for natural krypton it is 1.099 ± 0.009 ppm [123]. In nature, ^{39}Ar is mainly produced by cosmic-ray induced ^{40}Ar(n,2n)^{39}Ar reactions in the atmosphere. The activity of ^{39}Ar in the atmosphere is measured to be 16.6 ± 0.6 mBq/m^3 [124], which corresponds to the ^{39}Ar/^{nat}Ar ratio of $(8.1 \pm 0.3) \times 10^{-16}$. ^{85}Kr, on the other hand, is mostly anthropogenic. It is amply produced by the fissions of uranium and plutonium in the nuclear reactors and is released to the atmosphere when spent fuels are repro-

cessed. The anthropogenic production of ^{85}Kr has resulted in an order of magnitude increase of the isotope in the atmosphere since the early 1950s and a non-uniform geological distribution. The ^{85}Kr activity in the atmosphere at several locations in Japan has been monitored monthly from 1996–2001 [125], and an annual increasing of $\sim$0.03 Bq/m^3 has been observed. The averaged activity 1.4 Bq/m^3 with an uncertainty of 50% is adopted in our work, which corresponds to the ^{85}Kr/$^{\rm nat}$Kr ratio of 2.8×10^{-11}. These characteristic properties are summarized in Table A.1.

Extensive work has been done at CalTech to develop such a detecting system that meets all the requirement. The central idea is to turn the measurement of the low concentration of $^{\rm nat}$Kr and $^{\rm nat}$Ar into a partial pressure measurement, and use a residual gas analyzer (RGA) as a detector to take advantage of its high sensitivity and fine mass resolution. The schematic design of KamKAM (KamLAND Kr/Ar Monitor) is shown in Fig. A.1. A picture of the on-site setup is shown in Fig. A.2. Details will be discussed in Section A.2. The relatively low cost and fast operation cycle makes this detecting system competitive to other alternative systems such as ATTA (Atom Trap Trace Analysis) [126]. It is also worth noting that there are growing interests and active R&D's in using liquid scintillator detectors, in particular the noble gas detectors such as Xenon and Argon, for dark matter search, solar neutrino and double beta decay experiments. All these experiments demand low contaminations from ^{85}Kr and ^{39}Ar, for which having a Kr/Ar monitoring system such as KamKAM will be very beneficial.

A.2 Detector Design and Operation

The first part of the KamKAM system is the Kr and Ar extraction and trapping system. The method is inspired by Ray Davis' famous solar neutrino experiment [35] where the ^{37}Ar atoms produced by solar neutrinos were flushed out with helium

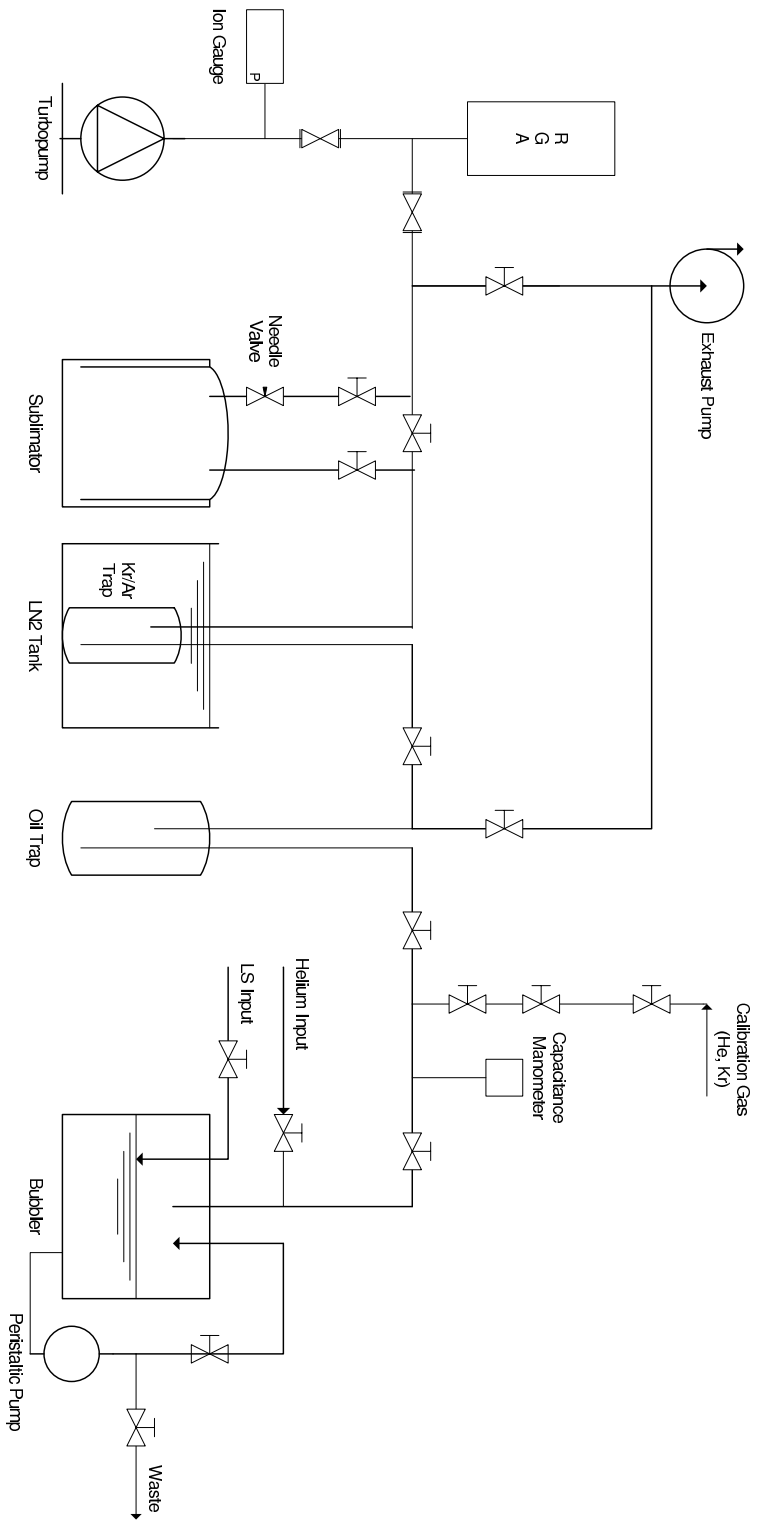

Figure A.1: Schematic design of the KamLAND Kr/Ar monitor.

Figure A.2: A picture of the on-site KamKAM setup. Various components are labeled.

gas every ∼100 days and condensed into proportional counters for counting. In the KamKAM system, the Kr/Ar extraction part (The Bubbler) is a stainless steel vacuum chamber with a volume of 8.3 liters and is pumped down to below 0.1 torr before any measurement starts. At the beginning of each measurement, 5 liters of liquid scintillator sample is input either from a direct line right after the purification system, or from a sampling port at the top of the bubbler. A helium carrier gas (99.9999% pure) is then inserted from the gas line on top of the liquid until pressure reaches 800 torr. Next we use a peristaltic pump (Masterflex I/P system) to pump the liquid from the bottom to the top and sparge into the helium gas at 0.2 liter/min for 2 hours in a closed re-circulation loop. This procedure establishes equilibrium concentrations of the dissolved gas in the helium carrier gas and the liquid scintillator. The percentage of dissolved Kr and Ar gas extracted from the LS at equilibrium is calibrated to be $79 \pm 6\%$.

After the bubbling stage is finished the helium gas is released into the bottom of a molecular sieve trap held in a liquid nitrogen bath at 77K to freeze the krypton (BP = 120 K) and argon (BP = 87 K) gas. The molecular sieve trap contains type 13X (pore size of 8 Angström) synthetic zeolite beads which effectively enlarges the surface area for trapping large molecules. Many other gases and organic vapors with a high boiling point are also trapped and become potential background in later measurements. On the other hand, most of the helium carrier gas (BP = 4 K) simply passes the trap and is pumped out.

After all the helium carrier gas has been passed through the cold trap, the bubbler sub-system is closed and the cold trap is heated up to release the trapped gases into the the second part of the system, which is a vacuum line that leads to a Residual Gas Analyzer (RGA) for measuring the partial pressure of Kr and Ar in the vacuum system. This part of the system is initially under ultra-high vacuum below 10^{-7} torr and is continuously pumped down by a turbo-molecular pump (Varian Turbo-V 70).

The pressure goes up when the trapped gases are released into the system. The partial pressure of each gas species integrated over the release time is directly proportional to the amount of the gas that has been released from the trap, and hence is proportional to the concentration of the gas which is originally dissolved in the liquid scintillator.

The partial pressure is continuously measured by the RGA (SRS RGA100), which is essentially a mass-spectrometer that ionizes the gases, separates the ion paths of different gas species by their mass-to-charge ratio through a quadrupole filter, and collects the ions at the end of the filter rods. The RGA can be operated in two modes depending on which type of ion collector being used: the faraday cup (FC) mode which has a dynamic range of (10^{-9} torr – 10^{-4} torr), or the electron multiplier (EM) mode which has a dynamic range of (10^{-12} torr – 10^{-6} torr). By combining the two modes a wide dynamic range and a high sensitivity can be achieved.

The RGA signal is in general directly proportional to the partial pressure. However, at total pressure higher than 10^{-5} torr, this linear relationship breaks. The nonlinearity arises from the space charge effect in the ion source which causes the difficulty of transmitting ions from the source to the detector and decreases the signal strength at high pressures [127]. The gas release flow rate from the cold trap increases as the the temperature goes up. Because of the multitude of trapped gases including all background gases such as N_2 (from the N_2 purge tower), O_2 (from the residual air), and oil vapors, the total pressure of the system at a certain point would exceed the RGA linearity region. The problem is solved by inserting a titanium sublimation pump (NEC sublimators) between the cold trap and the RGA. The pump contains a titanium filament which under high current sublimates and deposits highly reactive thin films of titanium on the inner surface of the chamber surrounding the filaments. Most of the N_2, O_2 and oil vapors are chemically absorbed by the titanium films before they reach the RGA, while the noble gases such as Kr and Ar are not affected. In this way the resulting gas being sampled by the RGA is primarily the trace amount

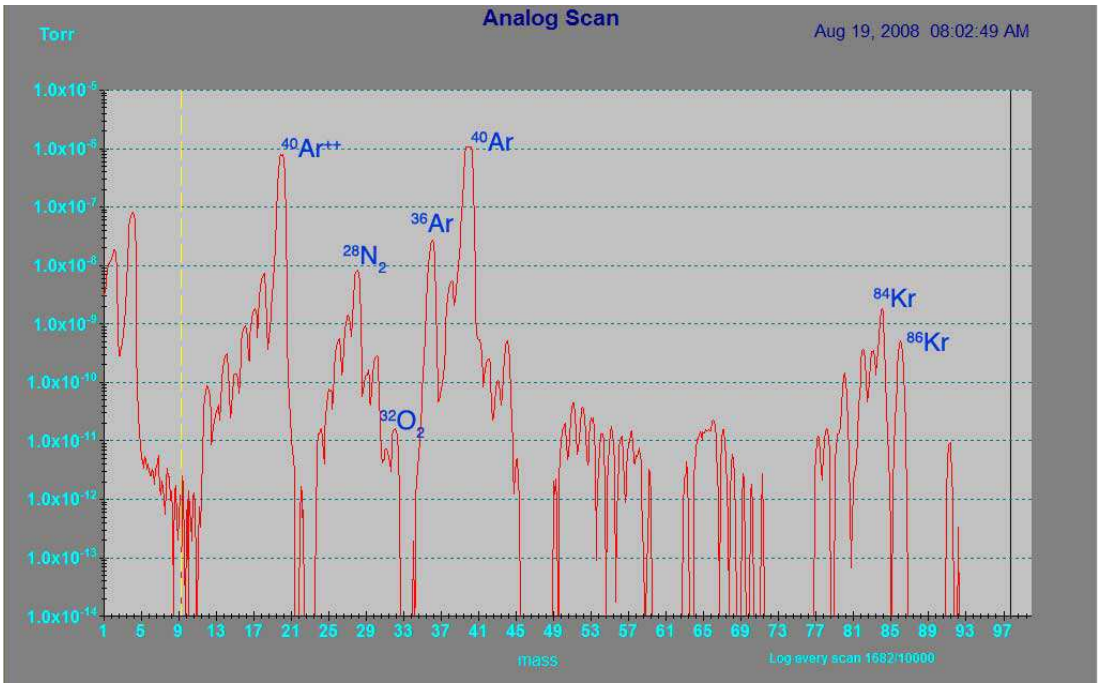

Figure A.3: Partial-pressure vs. mass-to-charge-ratio measured by the RGA (analog scan mode) from a relatively air-rich LS sample. The gases passed through a sublimator before being sampled by the RGA. The various residual gas peaks are identified and labeled.

of noble gasses of interest.

Fig. A.3 shows a plot of partial-pressure versus mass-to-charge-ratio measured by the RGA from a relatively air-rich LS sample. The various residual gas peaks are identified and labeled in the plot. Since the gases passed through the sublimator before being sampled by the RGA, the partial pressure of N_2, O_2 and other Ti-active background gases are greatly reduced, and the total pressure of the system is well within the RGA linearity region (below 10^{-5} torr). The peaks from krypton and argon are easily identifiable because of the rich isotopic feature of $^{\mathrm{nat}}$Kr (^{84}Kr 57%, ^{86}Kr 17.3%, ^{83}Kr 11.5%, ^{82}Kr 11.6%) and $^{\mathrm{nat}}$Ar (^{40}Ar 99.6%, ^{36}Ar 0.34%, ^{38}Ar 0.06%), which provide unambiguous signals over background gases at similar mass-to-charge-ratios.

After the measurement procedure is finished, the partial pressures of krypton and argon together with other background gases recorded by the RGA are plotted against

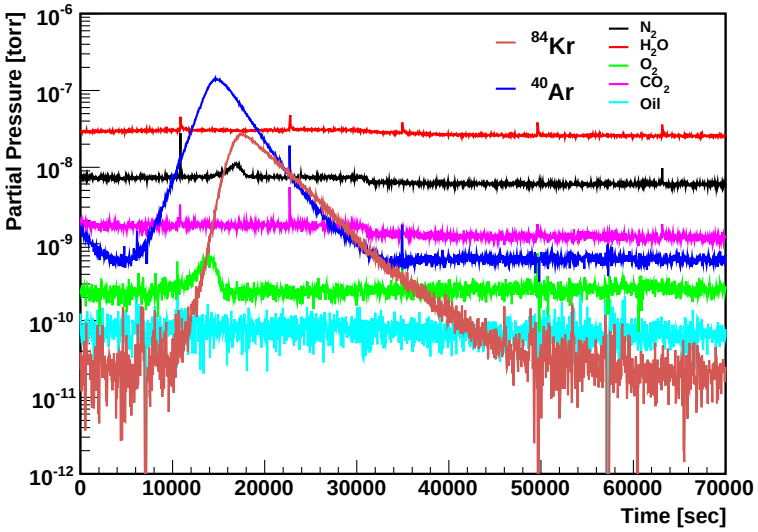

(a) Partial Pressure Trend

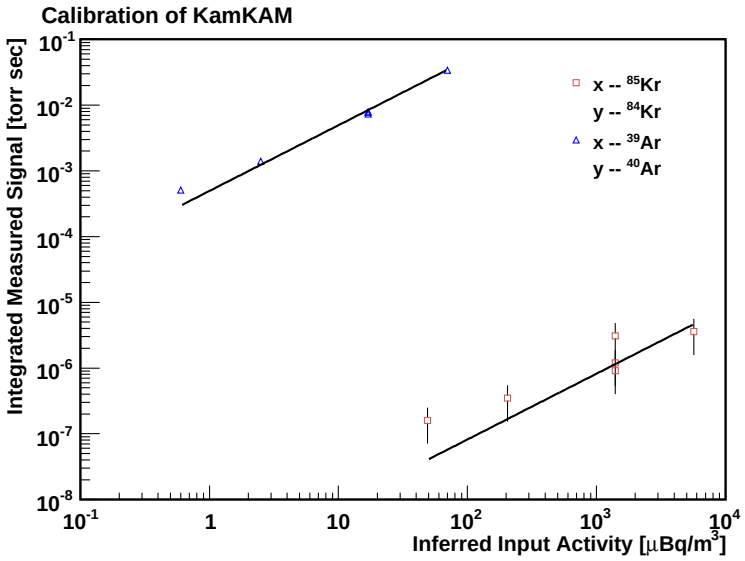

(b) Calibration

Figure A.4: (a) The partial pressure trend of different gases since the cold trap is heated up. The integrated peak areas of ^{40}Ar and ^{84}Kr are directly proportional to the amount of krypton and argon gas which were released from the cold trap. (b) The calibration of KamKAM . Known mole-amount of calibration gas is inserted into the system and the measured signals are plotted against the inferred input ^{39}Ar and ^{85}Kr activities. A linear relation is assumed and the fitted linear constant is used for conversion.

the time since the the cold trap is heated up. An example plot is shown in Fig. A.4(a). The building-up and pumping-down of ^{40}Ar and ^{84}Kr partial pressure is clear, while the rather constant pressure of other gases shows the effectiveness of the sublimation pumping. The integrated areas of ^{40}Ar and ^{84}Kr (in units of torr·sec) are directly proportional to the amount of krypton and argon gas which were originally dissolved in the liquid scintillator and the proportionality constant is periodically calibrated. Pure $^{\rm nat}$Kr and $^{\rm nat}$Ar gas are used for large signal calibrations. For small signal calibrations, however, precise low-mole pure $^{\rm nat}$Kr and $^{\rm nat}$Argon samples are difficult to prepare. Instead we use air for calibration and assume that the $^{\rm nat}$Kr and $^{\rm nat}$Ar concentration in the atmosphere are 1.099 ppm and 0.933%, as shown in Table A.1. The mole-amount of $^{\rm nat}$Kr and $^{\rm nat}$Ar are converted to the activity of ^{85}Kr and ^{39}Ar in units of μBq/m^3 (the LS sample used for each measurement is always 5 liter), a quantity that most concerns KamLAND, from the values given in Table A.1. The calibration plot is shown in Fig. A.4(b), from which the activity of ^{85}Kr and ^{39}Ar in the measured LS sample can be directly interpreted. The uncertainty from the fitted linear constant is 26% for krypton and 4% for argon.

Another systematic uncertainty comes from the reproducibility of each measurement, which incorporates uncertainties from gas trapping efficiency, gas releasing efficiency, hysteresis effects etc. Same mole-amount of calibration gases are measured several times and the variation on the results shows the uncertainty being 53% for krypton and 1% for argon. Combining all together, the total systematic uncertainty of the KamKAM measurements is 78% for ^{85}Kr and 10% for ^{39}Ar. The contributions to the systematic uncertainty are summarized in Table A.2.

The sensitivity of the KamKAM system scales up linearly with the amount of liquid scintillator sample taken and is essentially limited by the air leak rate of the sampler and gas sparging system. With five liters of LS sample for each measurement, the on-site KamKAM system achieved the sensitivity of 10^{-13}g/g for $^{\rm nat}$Kr in LS and

Table A.2: Estimated systematic uncertainties (%) of KamKAM measurements.

Description	^{85}Kr	^{39}Ar
Gas extraction efficiency	8	8
Linear calibration	26	4
reproducibility	53	1
Isotope abundance	50	4
Total systematic uncertainty	78	10

4×10^{-8}g/g for $^{\mathrm{nat}}$Ar in LS. This corresponds to the sensitivity of 30 μBq/m^3 for ^{85}Kr in LS and 0.3 μBq/m^3 for ^{39}Ar in LS.

A.3 On-site Measurements

KamKAM was installed as a part of the KamLAND purification facilities in the spring of 2007 and started daily operation. During the first purification campaign, all the KamKAM measurement results from the LS samples right after the purification system showed no sign of krypton and argon at the sensitivity level (30μBq/m^3 for ^{85}Kr in LS and 0.3μBq/m^3 for ^{39}Ar in LS). This is the first strong indication that a great reduction factor was achieved by the purification ($> 2 \times 10^4$ for ^{85}Kr). Fitting the data from KamLAND, on the other hand, only showed a reduction factor of $\sim$40 for ^{85}Kr. The inconsistency led us to believe that there are possible air leaks around the KamLAND detector chimney region, and that the convection of the LS during and after the filling is strong which caused the mixing of the new and old liquid scintillators.

A second purification campaign was then started in Jun 2008 following important improvements to minimizing these effects, including an ultra-pure nitrogen over-pressured tent around the detector chimney, a heat exchanger to precisely control the LS temperature, and a new bottom-filling scheme to minimize the LS convection. All the KamKAM measurement results during the second campaign again showed no sign of krypton and argon at the sensitivity level from the LS samples right after

the purification system. The results from the spectral fitting of the KamLAND data showed the decreasing activity of ^{85}Kr after each full-detector-volume LS transfer, indicating the effects of LS convection. Three full-detector-volume LS transfers were done at the end of the second purification. The ^{85}Kr activity in the cleanest region ($\sim$100 m^3 in the center) of the KamLAND detector from the spectrum fitting is on the order of 10 μBq/m^3. Detailed data analysis is on the way [92].

During the second purification, a new KamKAM LS sampling system was constructed which can sample the LS from the return line before it goes into the purification system. This LS comes directly out of the KamLAND detector and a measurement from this would provide an independent check on the ^{85}Kr and ^{39}Ar activity from the spectral fitting methods. One measurement has been performed on such a sample on Aug 30, 2008. The result (11.4 mBq/m^3 for ^{85}Kr in LS and 38.0μBq/m^3 for ^{39}Ar in LS) agrees well with the spectral fitting result around that time period. Unfortunately because of the maintenance work of the KamKAM system, no following measurements were performed in later periods. Nevertheless, this shows that an independent physical measurement of ^{85}Kr and ^{39}Ar background level in the detector is possible, which is very important to low energy solar neutrino and other low background experiments.

Appendix B Decay Chains of Selected Isotopes

^{238}U, ^{232}Th and ^{40}K have long half-lives and are natural radioactive background for KamLAND experiment. Tables B.1 and B.2 summarize the decay chains of ^{238}U and ^{232}Th. The α decays are indicated with symbol "$\swarrow$" and β^- decays with "$\rightarrow$." Only decays with visible energy higher than 100 KeV or branching ratio more than 0.5% are listed. Effects of internal conversions are not included as they have negligible effects for KamLAND. The most intensive transition γ-rays accompanying the decays are also listed. Some isotopes have multiple β decay branches and in those cases only the highest Q-value decay branch and the (next) most probable decay branch are shown, with a "†" symbol attached to the end reminding one to look up the nuclear database (e.g. Ref. [128]) for the full decay branches. The branching ratio is normalized to per ^{238}U or ^{232}Th decay, assuming the state of secular equilibrium being kept during the decaying chains. Care should be taken when doing calculation since possible thermal or chemical processing of the intermediate daughter could result in a break in the secular equilibrium. An example is the concentration of radon in ore-bearing rocks.

The decays of ^{40}K are summarized in Table B.3. The electron capture decay branch dominates the β^+ decay branch (0.001%) and is indicated by the symbol "$\leftarrow$ (EC)."

^{85}Kr and ^{39}Ar also have long half-lives and are potential backgrounds for solar ^{7}Be neutrino detection. Their decay schemes are summarized in Table B.4 and Table B.4.

Table B.1: ^{238}U Decay Chain

Isotope (half life) & Decay Mode	E_α [KeV]	Q_β [KeV]	E_γ [KeV]	Branching Ratio [/ ^{238}U Decay]
^{238}U (4.5×10^9 y)				
↙	4198	-	-	0.790
↙	4151	-	50	0.210
^{234}Th (24.1 d)				
→	-	273	-	0.703
→	-	181	92	0.192†
^{234}Pa (1.2 m)				
→	-	2290	-	0.977
→	-	1224	1001	0.010†
^{234}U (2.5×10^5 y)				
↙	4775	-	-	0.714
↙	4722	-	53	0.286
^{230}Th (7.5×10^4 y)				
↙	4688	-	-	0.763
↙	4621	-	68	0.237
^{226}Ra (1600 y)				
↙	4784	-	-	0.944
↙	4602	-	186	0.056
^{222}Rn (3.8 d)				
↙	5490	-	-	1.000
^{218}Po (3.1 m)				
↙	6002	-	-	1.000
^{214}Pb (26.8 m)				
→	-	1019	-	0.110
→	-	667	352	0.460†
^{214}Bi (19.9 m)				
→	-	3272	-	0.191
→	-	1540	1120	0.176†
^{214}Po (164 μs)				
↙	6902	-	800	0.0001
↙	7687	-	-	0.9999
^{210}Pb (22 y)				
→	-	64	-	0.160
→	-	17	47	0.840
^{210}Bi (5.0 d)				
→	-	1163	-	1.000
^{210}Po (138 d)				
↙	5304	-	-	1.000
^{206}Pb (stable)				

Table B.2: ^{232}Th Decay Chain

Isotope (half life) & Decay Mode	E_α [KeV]	Q_β [KeV]	E_γ [KeV]	Branching Ratio [/ ^{232}Th Decay]
^{232}Th (1.4×10^{10} y)				
↙	4013	-	-	0.779
↙	3954	-	64	0.221
^{228}Ra (5.8 y)				
→	-	46	-	1.000
^{228}Ac (6.1 h)				
→	-	2069	58	0.008
→	-	1158	969	0.299†
^{228}Th (1.9 y)				
↙	5423	-	-	0.715
↙	5340	-	84	0.285
^{224}Ra (3.7 d)				
↙	5685	-	-	0.949
↙	5449	-	241	0.051
^{220}Rn (56 s)				
↙	6288	-	-	1.000
^{216}Po (0.145 s)				
↙	6778	-	-	1.000
^{212}Pb (11 h)				
→	-	574	-	0.123
→	-	335	239	0.825†
^{212}Bi (61 m)				
64.1% / 35.9%				
→	-	2252	-	0.554
→	-	1525	727	0.045†
↙	6090	-	-	0.098
↙	6050	-	40	0.262
^{212}Po (299 ns) / ^{208}Tl (3.1 m)				
↙ / →	8784	-	-	0.640
→	-	1801	2615	0.175
→	-	1525	2615	0.026†
^{208}Pb (stable)				

Table B.3: ^{40}K Decay

Isotope (half life) & Decay Mode		E_α [KeV]	Q_β [KeV]	E_γ [KeV]	Branching Ratio [/ ^{40}K Decay]
^{40}K (1.3×10^9 y)					
89%	11%				
→		-	1311	-	0.893
	← (EC)	-	-	1461	0.106
^{40}Ar (stable)	^{40}Ca (stable)				

Table B.4: ^{85}Kr Decay

Isotope (half life) & Decay Mode	E_α [KeV]	Q_β [KeV]	E_γ [KeV]	Branching Ratio [/ ^{85}Kr Decay]
^{85}Kr (10.8 y)				
→	-	687	-	0.9956
→	-	173	514	0.0043
^{85}Rb (stable)				

Table B.5: ^{39}Ar Decay

Isotope (half life) & Decay Mode	E_α [KeV]	Q_β [KeV]	E_γ [KeV]	Branching Ratio [/ ^{39}Ar Decay]
^{39}Ar (269 y)				
→	-	565	-	1.000
^{39}K (stable)				

Appendix C Event Category

C.1 Low Level Event Classification

Events can be first classified by some low level information independent of their energy and position reconstructions. Two especially useful variables are the total number of photoelectrons on all 17-inch PMTs ($N_{p.e}^{\text{total}}$) and the standard deviation of the number of photoelectrons between PMTs ($\sigma_{N_{p.e.}}$), defined as:

$$\sigma_{N_{p.e.}}^2 = \frac{1}{N_{p.e}^{\text{total}}} \sum_{i}^{\text{PMTs}} (N_{p.e}^i - \langle N_{p.e.} \rangle)^2 \tag{C.1}$$

A plot of $\sigma_{N_{p.e.}}$ v.s. $N_{p.e}^{\text{total}}$ for a typical one-day's data in KamLAND is shown in Fig. C.1. There are some distinct regions on this plot, based on which a few event categories can be defined:

PMT Flasher $N_{p.e}^{\text{total}} > 10^3$ and $\sigma_{N_{p.e.}}^2 > 2$. These are events with very large signals collected in a single PMT or a small group of PMTs, and are not correlated with physical events.

Oil Muon $10^3 < N_{p.e}^{\text{total}} < 10^{4.8}$ and $\sigma_{N_{p.e.}}^2 > 0.015$. These are muons that pass through the buffer oil region without entering the LS region. The lights collected from oil muons are mostly from Cherenkov radiation.

LS Muon $10^{4.8} < N_{p.e}^{\text{total}} < 7 \times 10^5$. These are muons that deposit a significant amount of energy in the LS region, and are associated with high light yields.

Shower Muon $N_{p.e}^{\text{total}} > 7 \times 10^5$. These are a subset of LS Muons, which have the highest light yields. Shower muons are expected to deposit more energy than

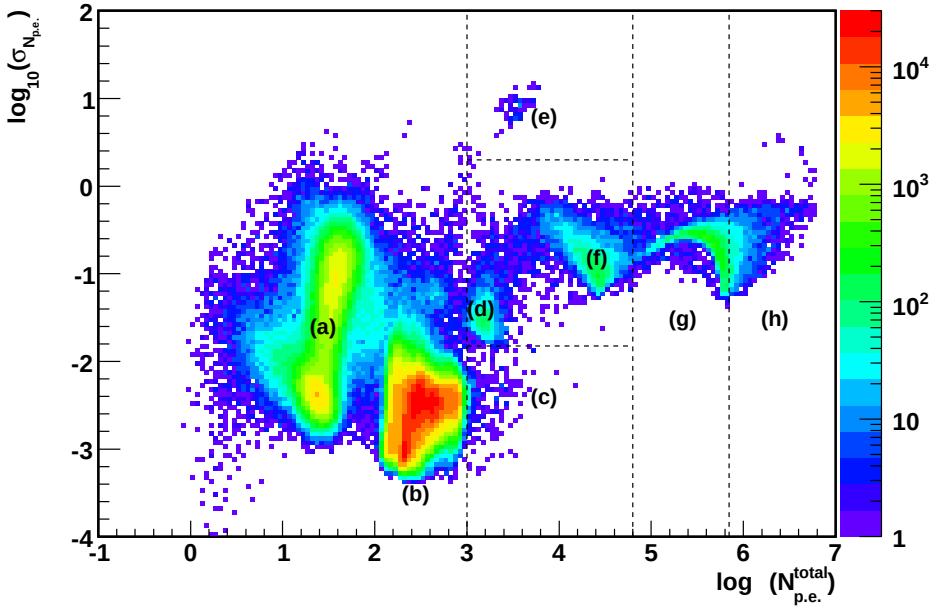

Figure C.1: Distribution of events in a typical one-day's data (run 6756) (events occurring within 50 μs after a LS muon are not included). The two variables $\sigma_{N_{p.e.}}$ and $N_{p.e}^{\text{total}}$ discriminates a few event classes: (a) background light in the ID, from low threshold ID trigger events; (b) low energy physics events; (c) higher energy physics events, mostly from ^{12}B; (d) residual post-muon noise; (e) PMT flasher events; (f) muons pass through BO only; (g) muons pass through LS; (h) shower muons which are a subset of LS muons that have highest light output.

minimum ionizing, and are found to create more spallation products.

ID Muon Events tagged as either "Oil Muon," "LS Muon" or "Shower Muon." All of these muons deposit a significant amount of energy in the inner detector.

Low Threshold Background Events Events in region (a) of Fig. C.1. These events are acquired from lower-threshold ID trigger for monitoring the background in KamLAND. These events include the muons that pass though outer detector only, acquired from the OD-to-ID trigger [79].

Candidate Physics Events Events in region (b) and (c) of Fig. C.1. These events are mostly from low energy (< 15 MeV) particle interactions, and are candidate for $\bar{\nu}_e$ events. Region (b) are mostly from radioactive decays of impurities in the LS such as ^{210}Pb and ^{85}Kr. Region (c) are mostly from higher energy events as spallation ^{12}B decays.

A few event categories can be classified with other low-level variables as well:

OD Muon OD nsummax > 10. These are muons events that are detected by the outer detector PMTs. OD muon tagging is independent of inner detector.

Muon Events that are tagged as either ID muon or OD muon.

Post Muon Noise Events that occurring within 50 μs after LS muons. These are mostly from after-pulses from electronics after a large muon signal.

Candidate Spallation Events Events that occur within 2 seconds after ID muons. These are mostly from decays of spallation radioactive isotopes created by the muons, and can be further categorized into short-lived ($\Delta t < 2$ ms, e.g. neutrons), medium-lived ($\Delta t < 200$ ms, e.g. ^{12}B) and long-lived ($\Delta t < 2$ s, e.g. ^{9}Li).

Coincidence Multiplet Events are added into a multiplet if it occurs within 1.5 ms of the previous event. A multiplet group thus contains events with temporal coincidences, including the $\bar{\nu}_e$ inverse beta decay events.

C.2 Radioactive Calibration Source Events

The radioactive calibration source events are trivially selected spatially by requiring their reconstructed positions to be within 1 m from the deployed source position, which is known accurate to 3 mm. Other selection rules for each source are defined below:

- ^{203}Hg: $0.1\text{MeV} < E_{\text{vis}} < 0.4\text{MeV}$
- ^{137}Cs: $0.4\text{MeV} < E_{\text{vis}} < 0.9\text{MeV}$
- ^{68}Ge: $0.7\text{MeV} < E_{\text{vis}} < 1.1\text{MeV}$
- ^{65}Zn: $0.9\text{MeV} < E_{\text{vis}} < 1.3\text{MeV}$
- ^{60}Co: $2\text{MeV} < E_{\text{vis}} < 3\text{MeV}$
- ^{241}Am^{9}Be: require a prompt-delay event pair, $\Delta T_{p-d} < 1.2$ ms, $\Delta R_{p-d} < 3$ m, $\Delta R_{p-\text{source}} < 2$ m, $1.9\text{MeV} < E_d < 2.7\text{MeV}$ (neutron capture on ^{1}H), $4.5\text{MeV} < E_d < 6.0\text{MeV}$ (neutron capture on ^{12}C)
- ^{210}Po^{13}C: require a prompt-delay event pair, $\Delta T_{p-d} < 1.2$ ms, $\Delta R_{p-d} < 3$ m, $\Delta R_{p-\text{source}} < 2$ m, $1.9\text{MeV} < E_d < 2.7\text{MeV}$ (neutron capture on ^{1}H), $4.3\text{MeV} < E_p < 5.5\text{MeV}$ (^{12}C excited state), $6.1\text{MeV} < E_p < 7.2\text{MeV}$ (^{16}O excited states)

Fig. C.2 shows the reconstructed energy of various calibration sources from selected typical center calibration runs. The energy resolution is $6.8\%/\sqrt{E_{\text{vis}}}$ in Period

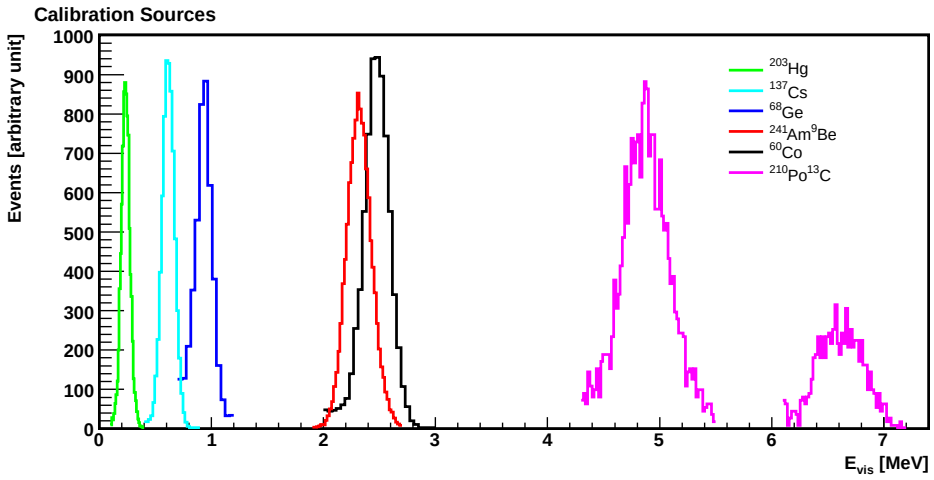

Figure C.2: The reconstructed energy of calibration sources from selected center calibration runs. The energy resolution is 6.8% in Period I and 7.6% in Period II.

I and $7.6\%/\sqrt{E_{\rm vis}}$ in Period II. The energy reconstruction variation along the z-axis has been shown in Fig. 3.5 and its volume average is ∼1%. The time variation of the source reconstructed energy has been shown in Fig. 3.8 and the average time variation is ∼0.5%. The source reconstructed energies are used to determine the energy scale parameters of the detector, except for the ^{241}Am^{9}Be and ^{210}Po^{13}C due to the biases caused by the capsule shadowing. The γ's from spallation neutrons are used instead at similar energies. Details have been discussed in Section 3.4.

Fig. C.3 shows an example of reconstructed positions from a series of z-axis ^{60}Co calibration runs performed on 09/21/2006. The vertex reconstruction resolution is ∼20 cm along the z-axis. The reconstructed vertex bias has been shown in Fig. 3.4, and is typically less than 3 cm along the z-axis. Details have been discussed in Section 3.3.

C.3 Alpha Particle Events

Alpha particles in KamLAND detector mostly come from the decay chains of ^{232}Th and ^{238}U (Appendix B), or their out-of-equilibrium daughter nuclei. α particles gen-

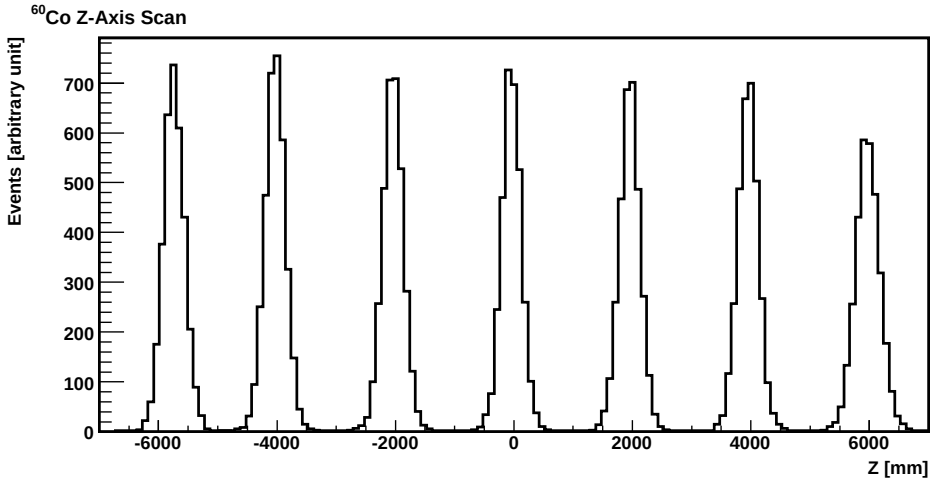

Figure C.3: The reconstructed positions from a series of z-axis ^{60}Co calibration runs (performed on 09/21/2006). The vertex resolution is ∼20 cm.

erally have energies higher than 4 MeV. However, due to their high stopping power, thery are highly quenched down to below 1 MeV in visible energy, as can be calculated from Eqn. 3.10. Alpha events are hardly identifiable in singles spectrum except for ^{210}Po α decays because of ^{210}Po's higher concentrations (not in equilibrium with ^{238}U). Coincidence techniques however can be used to cleanly select ^{214}Po and ^{212}Po α decay events.

C.3.1 ^{214}Po Alpha Decay

^{214}Po alpha decays with a half-life $\tau_{1/2} = 164\mu$s. The energy of the α particle is 7.687 MeV, but is quenched down to ∼0.63 MeV in visible energy. It is preceded by the beta decay from ^{214}Bi with an end point at 3.272 MeV. This creates a prompt-delayed coincidence event pair which can be selected by:

- $5\mu s < \Delta T_{p-d} < 505\mu s$ (signal window)
- $505\mu s < \Delta T_{p-d} < 905\mu s$ (background window for subtraction)
- $\Delta R_{p-d} < 1$ m

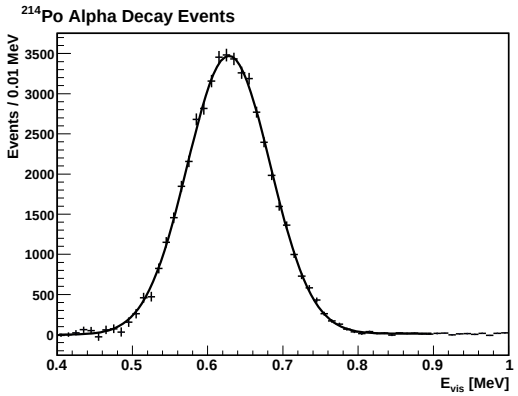

(a) ^{214}Po α Energy Spectrum

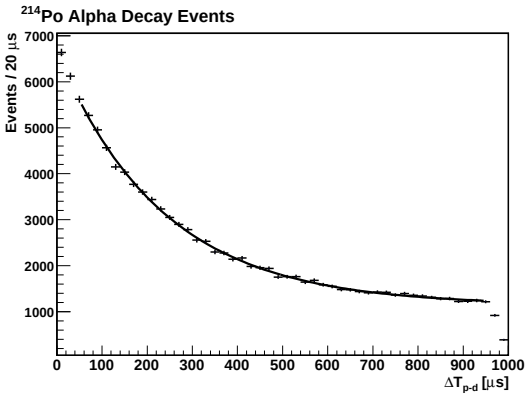

(b) ^{214}Po Decay Time

Figure C.4: The energy and time distribution of ^{214}Po α decay events (from all runs in Period I inside 6m fiducial volume). (a) The background subtracted (from background time window) energy spectrum. A fit to Gaussian plus a linear background yields mean energy at 0.6281 $\pm$ 0.0004 MeV, with χ^2/ndf = 39.5/45. (b) The distribution of time to previous ^{214}Bi β decay event. A fit to an exponential decay function plus a flat background yields the half-life 162.2 $\pm$ 2.7 μs, with χ^2/ndf = 34.0/43. This agrees with the ^{214}Po half-life ($\tau_{1/2} = 164\mu$s).

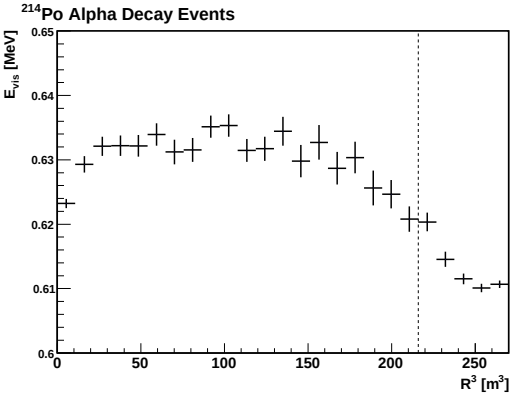

(a) Volume Variation of E_{vis}

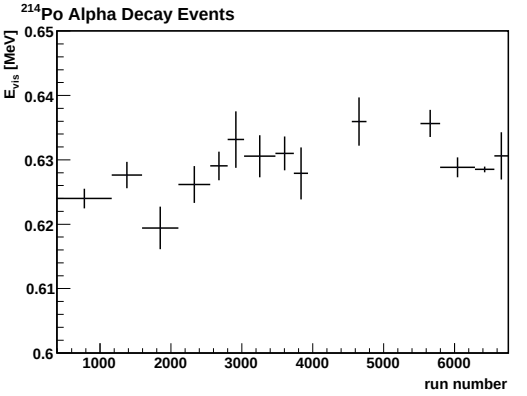

(b) Time Variation of E_{vis}

Figure C.5: The position and time variation of reconstructed energy of ^{214}Po α decay events (from all runs in Period I). (a) Each bin has a same volume of 10.8 m^3. The radial variation of E_{vis} variation inside the 6m fiducial volume (dotted line) is 0.61%. (b) Each bin has the same integrated live time. The time variation of E_{vis} in Period I is 0.67%.

- 1.8MeV $< E_p <$ 4.0MeV

- 0.4MeV $< E_d <$ 0.9MeV

The energy and time distribution of ^{214}Po α decay events are shown in Fig. C.4. Events in the background time window are statistically subtracted from the events in the signal window in order to get the correct energy spectrum of ^{214}Po α decay, as shown in Fig. C.4(a). The fit to the distribution of time to previous ^{214}Bi β decay event, shown in Fig. C.4(b), yields the the half-life 162.2 $\pm$ 2.7 μs, which agrees with ^{214}Po half-life (164 μs).

The ^{214}Po α reconstructed energy is used to calibrate the energy scale parameters discussed in Section 3.4.3. Its mean value in the fiducial volume, volume variation and time variation (e.g. Fig. C.5) are estimated for Period I and II separately and are summarized in Table 3.2

C.3.2 ^{212}Po Alpha Decay

^{212}Po alpha decays with a half-life $\tau_{1/2} = 0.299\mu$s. The energy of the α particle is 8.784 MeV, but is quenched down to $\sim$0.83 MeV in visible energy. It is preceded by the beta decay (branching ratio 64.1%) from ^{212}Bi with an end point at 2.252 MeV. This creates a prompt-delayed coincidence event pair which can be selected by:

- $0.5\mu s < \Delta T_{p-d} < 2.5\mu s$ (signal window)
- $2.5\mu s < \Delta T_{p-d} < 4.5\mu s$ (background window for subtraction)
- $\Delta R_{p-d} < 1$ m
- 1.0MeV $< E_p <$ 3.0MeV
- 0.6MeV $< E_d <$ 1.0MeV

The energy and time distribution of ^{212}Po α decay events are shown in Fig. C.6. Events in the background time window are statistically subtracted from the events in the signal window in order to get the correct energy spectrum of ^{212}Po α decay, as shown in Fig. C.6(a). The fit to the distribution of time to previous ^{212}Bi β decay

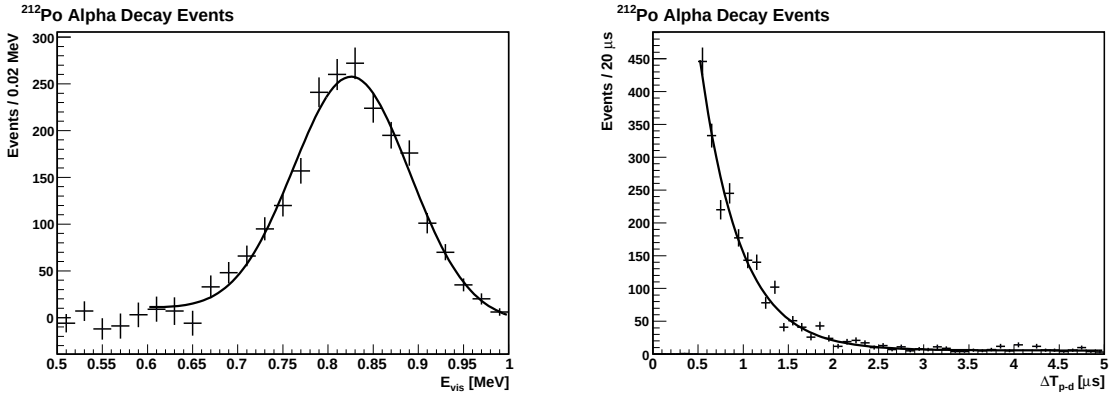

(a) ^{212}Po α Energy Spectrum (b) ^{212}Po Decay Time

Figure C.6: The energy and time distribution of ^{212}Po α decay events (from all runs in Period I inside 6m fiducial volume). (a) The background subtracted (from background time window) energy spectrum. A fit to Gaussian plus a linear background yields mean energy at 0.826 $\pm$ 0.002 MeV, with χ^2/ndf = 16.2/15. (b) The distribution of time to previous ^{212}Bi β decay event. A fit to an exponential decay function plus a flat background yields the half-life 0.305 $\pm$ 0.008 μs, with χ^2/ndf = 82.1/41. The relatively high χ^2 probably reflects the electronics biases at such short time scale. The fitted half-life agrees with the ^{212}Po half-life ($\tau_{1/2} = 0.299\mu$s).

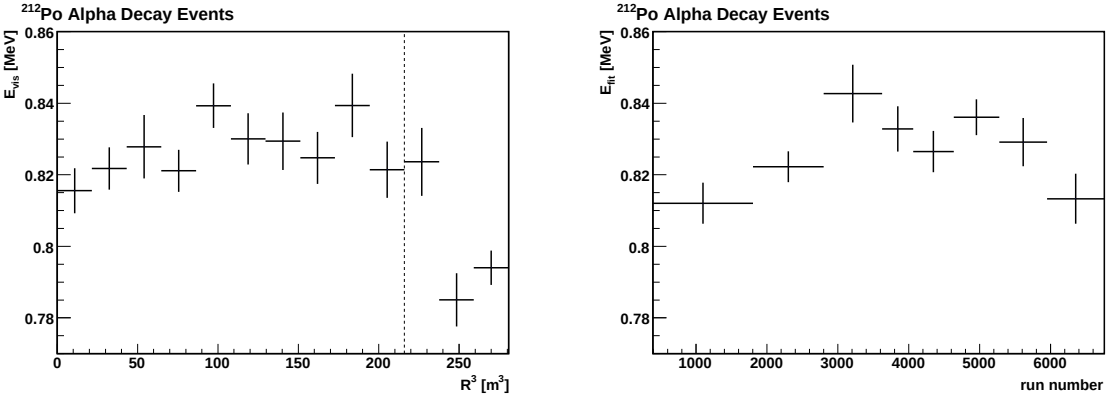

(a) Volume Variation of E_{vis} (b) Time Variation of E_{vis}

Figure C.7: The position and time variation of reconstructed energy of ^{212}Po α decay events (from all runs in Period I). (a) Each bin has a same volume of 21.6 m^3. The radial variation of E_{vis} variation inside the 6m fiducial volume (dotted line) is 0.90%. (b) Each bin has the same integrated live time. The time variation of E_{vis} in Period I is 1.21%.

event, shown in Fig. C.6(b), yields the the half-life 0.305 ± 0.008 μs, which agrees with ^{212}Po half-life (0.299 μs).

The ^{212}Po α reconstructed energy is also used to calibrate the energy scale parameters discussed in Section 3.4.3. Its mean value in the fiducial volume, volume variation and time variation (e.g. Fig. C.7) are estimated for Period I and II separately and are summarized in Table 3.2.

C.3.3 ^{210}Po Alpha Decay

^{210}Po alpha decays with a half-life of 138 days. The energy of the α particle is 5.304 MeV, but is quenched down to ∼0.3 MeV in visible energy. The ^{210}Po contribute to more than 99% of the α activity in KamLAND detector [108], and is visible from daily singles spectrum (e.g. Fig. 2.8). Because of known poor reconstruction efficiency and bias at visible energies below 0.4 MeV, the ^{210}Po alpha decay events are not used to calibrate the energy scale parameters discussed in Section 3.4.3. The absolute ^{210}Po decay rate however need to be measured because its high activity makes ^{13}C(α,n)^{16}O background significant in KamLAND. The rate of ^{210}Po decay inside the 6m fiducial volume is measured to be 0.19 ± 0.03 Bq/m^3 in Period I and 0.05 ± 0.01 Bq/m^3 in Period II. Its high activity even after the purification of LS, which removed orders of magnitude more ^{210}Bi, suggests that it is out of equilibrium from not only the ^{238}U decay chain but also the ^{210}Pb decay chain[1]. Details of ^{210}Po event selection and estimation of ^{13}C(α,n)^{16}O background has been discussed in Section 5.4.

C.4 Muon Spallation Events

As described in Appendix C.1, events that occurring within 2 seconds after ID muons are considered candidate spallation events. These events are mostly from decays of

[1]Similar effect has been observed in the Borexino experiment [42]

spallation radioactive isotopes created by the muons, and can be further categorized into short-lived ($\Delta t < 2$ ms, e.g. neutrons), medium-lived ($\Delta t < 200$ ms, e.g. ^{12}B) and long-lived ($\Delta t < 2$ s, e.g. ^{9}Li) spallation products.

C.4.1 Spallation Neutron

KamLAND receives spallation neutrons in the LS volume at a rate of ∼3000/day. The large daily sample of spallation neutron events and their spacial uniformity make them ideal for monitoring the detector stability over time and scintillator properties over the entire active volume of the detector. The neutron capture events happen relatively close to the preceding muons (∼206 μs). However, a large muon signal is often correlated with high event multiplicity following the muon, which causes the overload on individual electronics resulting waveform loss and dead time of the detector, extending as long as a few hundred micro-seconds after the large muon signal. This could cause biases in the energy reconstruction or neutron capture time study. Following selection rules are applied to select a relatively clean sample of spallation neutrons:

- multiplicity (number of evets within 0.15 – 10 ms following a muon) < 75
- $0.4ms < \Delta T_{n-\mu} < 1.4ms$ (signal window)
- $1.4ms < \Delta T_{n-\mu} < 5.4ms$ (background window for subtraction)

This selection window is shown in Fig. C.8(a). High multiplicity muons or events too close in time after a muon are rejected to avoid the electronics biases.

The distribution of spallation neutron events is uniform inside the LS volume, as can be seen from Fig. C.8(b). This uniformity can be used to calculate the 6m fiducial volume size, as discussed in Section 4.4. The fiducial volume ratio $R_{\rm fv}$ from spallation neutrons is calculated to be 0.784(±0.27%), and is used as a cross check

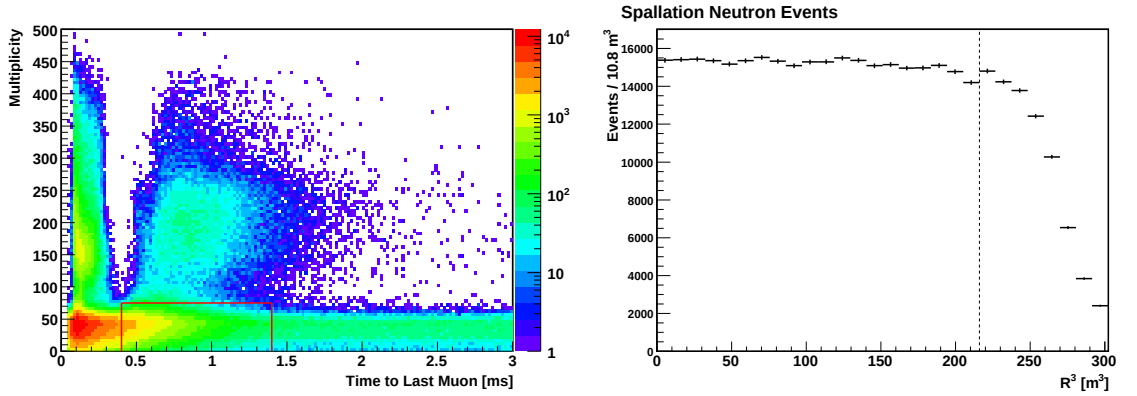

(a) Spallation Neutron Event Selection (b) Spallation Neutron Vertex Distribution

Figure C.8: (a) Spallation neutron event selection window (red box). High multiplicity (> 75) muons or events too close in time after a muon (< 0.4 ms) are rejected to avoid the electronics bias. Events inside 1.4 – 5.4 ms window are used for background subtraction. (b) The vertex distribution of spallation neutron (background subtracted). The distribution is flat inside the 6m fiducial volume (dashed line).

with the result from spallation ^{12}B, which is free from electronic bias and covers a larger energy range.

The uniformity and abundance of spallation neutron events are utilized to check the energy reconstruction bias over the whole scintillator volume. Details have been discussed in Section 3.4. Spallation neutron events are also used for determining the neutron capture time discussed in Section 4.6. The mean neutron capture time from the spallation neutron is 206.4 ± 1.3 μs (Fig. C.9(b)).

Both spallation neutron capture γ-rays (on ^{1}H and ^{12}C) are evident from the energy spectrum shown in Fig. C.9(a). Their reconstructed energies are used to calibrate the energy scale parameters discussed in Section 3.4.3. The mean value in the fiducial volume, volume variation and time variation (e.g. Fig. C.10, C.11) are estimated for Period I and II separately and are summarized in Table 3.2.

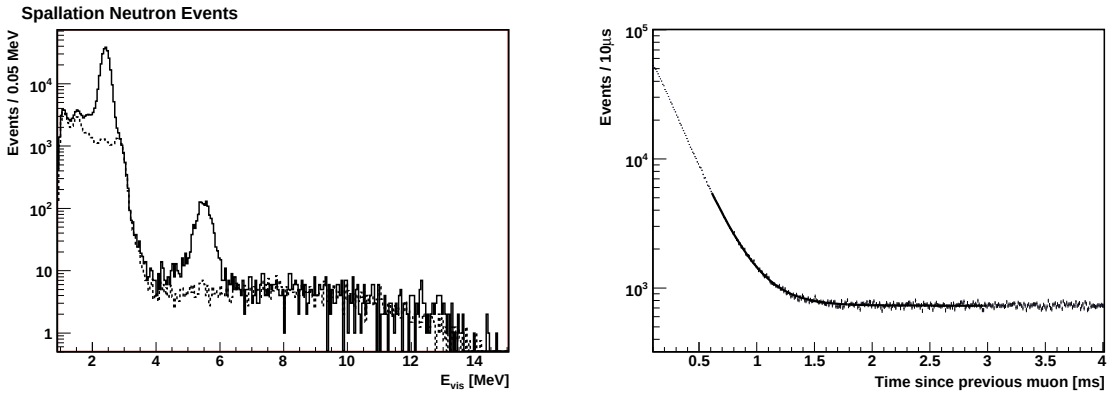

(a) Spallation Neutron Energy Spectrum (b) Spallation Neutron Capture Time

Figure C.9: Energy spectrum and capture Time of spallation neutron events (from all runs in Period I inside 6m fiducial volume): (a) Energy spectrum in the signal window (solid line) and background window (dashed line, statistically scaled). The two peaks correspond to γ-rays from neutron capture on ^{1}H and on ^{12}C. The fit to a Gaussian plus linear background yield the mean energy of the peak at 2.424 ± 0.001 MeV and 5.499 ± 0.008 MeV. (b) The distribution of time to the previous muon. A fit from 0.6 ms to 3 ms to exponential distribution plus a flat background results the mean neutron capture time $\tau = 206.4 \pm 1.3\mu s$. The χ^2/ndf from the fit is 227/237.

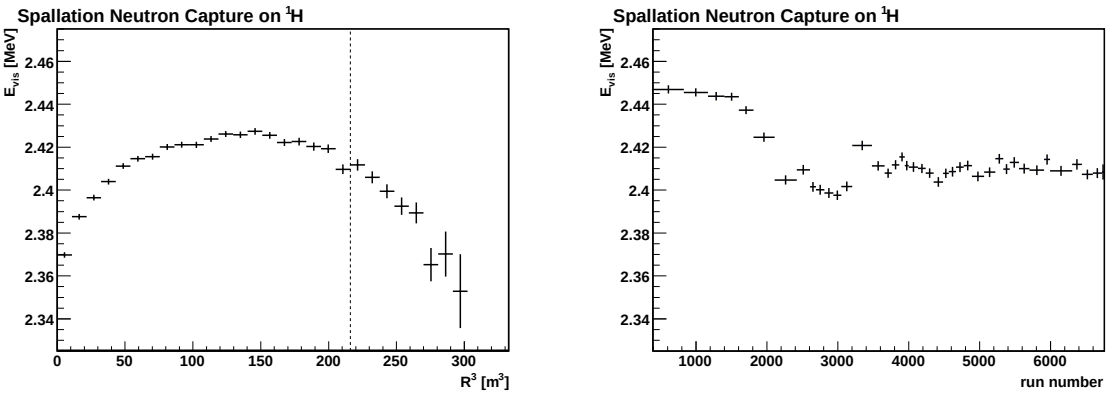

(a) Volume Variation of E_{vis} (b) Time Variation of E_{vis}

Figure C.10: The position and time variation of reconstructed energy of spallation neutron capture on ^{1}H events (from all runs in Period I). (a) Each bin has a same volume of 10.8 m^3. The radial variation of E_{vis} variation inside the 6m fiducial volume (dotted line) is 0.60%. (b) Each bin has the same integrated live time. The time variation of E_{vis} in Period I is 0.52%.

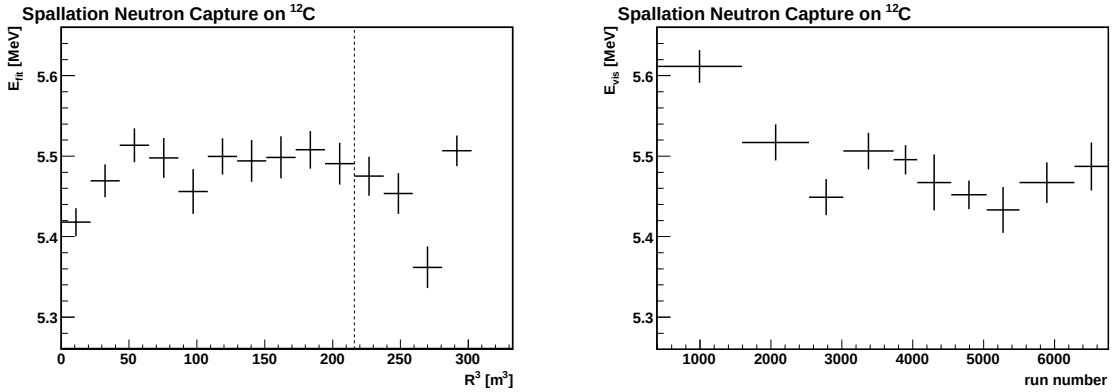

(a) Volume Variation of E_{vis}

(b) Time Variation of E_{vis}

Figure C.11: The position and time variation of reconstructed energy of spallation neutron capture on ^{12}C events (from all runs in Period I). (a) Each bin has a same volume of 21.6 m^3. The radial variation of E_{vis} variation inside the 6m fiducial volume (dotted line) is 0.50%. (b) Each bin has the same integrated live time. The time variation of E_{vis} in Period I is 0.88%.

C.4.2 Spallation ^{12}B

The spallation product ^{12}B beta decays with half-life $\tau_{1/2} = 20.2$ ms. The end point of the β spectrum is 13.4 MeV. They are the most abundant spallation isotopes at high energies above 4 MeV. They can be selected from the time correlation with preceding muon events as follows:

- The preceding muon is an isolated muon (previous and next muon are at least 1 second away).
- $2ms < \Delta T_{B-\mu} < 52ms$ (signal window)
- $300ms < \Delta T_{B-\mu} < 500ms$ (background window for subtraction)
- OD nsummax < 10 (Event itself is not an OD muon)
- 4MeV $< E_B <$ 14MeV (only high energy part of the β spectrum)

The distribution of time of ^{12}B to the previous muon is shown in Fig. C.12(b). The distribution is fitted to the sum of two exponential decay functions, including a

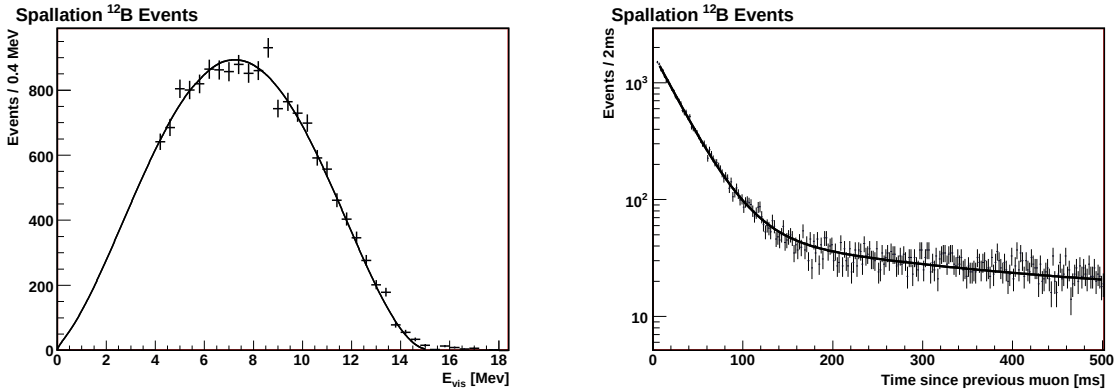

(a) Spallation ^{12}B Energy Spectrum

(b) Spallation ^{12}B Decay Time

Figure C.12: Energy spectrum and decay Time of spallation ^{12}B events (from all runs in Period I inside 6m fiducial volume): (a) Energy spectrum fitted to the expected ^{12}B beta decay visible energy spectrum from 4–14 MeV. The χ^2/ndf from the fit is 37.4/25. (b) The distribution of time to the previous muon. The distribution is fitted to the sum of two exponential decay functions, including a long-lived ^{9}Li component with fixed half-life $\tau_{1/2} = 178.3$ ms, and a flat background. The ^{12}B half life from the fit is 20.0 ± 0.2 ms. The χ^2/ndf from the fit is 383/394.

long-lived ^{9}Li component with fixed half-life $\tau_{1/2} = 178.3$ ms, and a flat background. The ^{12}B half time from the fit is 20.0 ± 0.2 ms, which agrees with the expected value (20.2 ms).

The visible energy spectrum of spallation ^{12}B is shown in Fig. C.12(a). This spectrum is fitted to the expected ^{12}B beta decay visible energy spectrum from 4–14 MeV. The χ^2/ndf from the fit is 37.4/25. The ^{12}B visible energy spectrum is used to cross-check the validity of energy scale at high energies, since the other highest calibration point is only 4.9 MeV (from spallation neutron capture on ^{12}C).

The spallation ^{12}B events are used to determine the fiducial volume of the analysis and its systematic errors, details discussed in Section 4.4. Spallation ^{12}B events are also used to determine the inefficiency of the 3-m cylinder cut along the LS muon track, which has been discussed in Section 5.5.

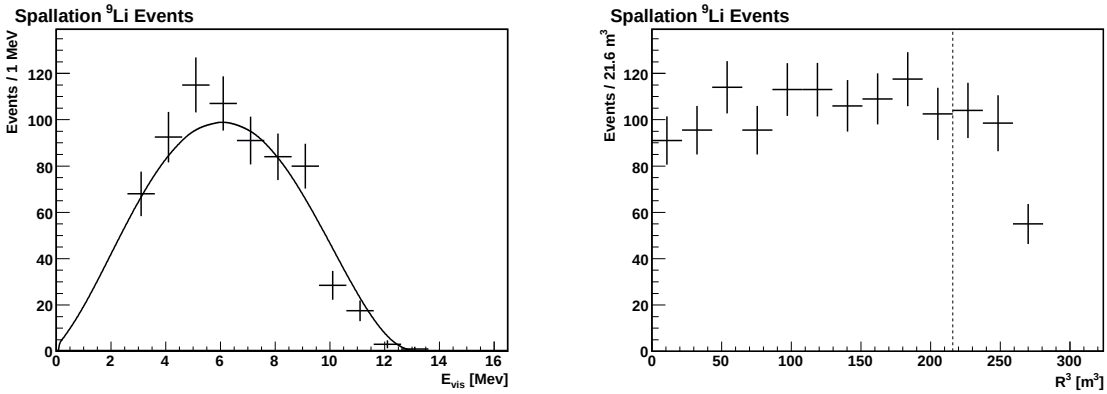

(a) Spallation ^{9}Li Energy Spectrum

(b) Spallation ^{9}Li Radial Distribution

Figure C.13: Spallation ^{9}Li events are selected from all runs in Period I inside 6m fiducial volume: (a) Background subtracted energy spectrum fitted to the expected ^{9}Li beta decay visible energy spectrum from 2.6–14.6 MeV. The χ^2/ndf from the fit is 19.1/11. (b) The vertex distribution of spallation ^{9}Li (background subtracted). The dotted line indicate the 6m fiducial volume boundary.

C.4.3 Spallation ^{9}Li

The spallation product ^{9}Li beta decays with half-life $\tau_{1/2} = 178.3$ ms. The end point of the β spectrum is 13.6 MeV. The excited states of the daughter nuclei ^{9}Be are neutron unstable and could decay to ^{8}Be and emit a neutron. As a consequence they are potential background for $\bar{\nu}_e$ detection.

The selection of Spallation ^{9}Li events and the muon veto efficiency in removing ^{9}Li background has been discussed in detail in Section 5.5. The energy spectrum and vertex distribution of spallation ^{9}Li are shown in Fig. C.13. In both figures, the signal window is from 2 ms to 0.5 s after the associated muon and the background window is from 0.5 s to 1.5 s.

Bibliography

[1] J. M. Herndon, "Feasibility of a nuclear fission reactor at the center of the Earth as the energy source for the geomagnetic field," *Journal of Geomagnetism and Geoelectricity* **45** (1993) 423–437.

[2] W. Pauli. Letter to a physicist's gathering at Tubingen, 1930.

[3] C. Cowan, F. Reines, F. Harrison, H. Kruse, and A. Mcguire, "Detection of the Free Neutrino - Confirmation," *Science* **124** (1956), no. 3212, 103–104.

[4] G. Danby *et al.*, "Observation of High-Energy Neutrino Reactions and the Existence of Two Kinds of Neutrinos," *Phys. Rev. Lett.* **9** (Jul, 1962) 36–44.

[5] **DONUT** Collaboration, T. Patzak, "First direct observation of the tau neutrino," *Europhysics News* **32** (mar, 2001) 56–57.

[6] B. Pontecorvo, "Neutrino Experiments and the Question of Leptonic-Charge Conservation," *Zh. Eksp. Teor. Fiz.* **53** (1967) 1717.

[7] **Particle Data Group** Collaboration, C. Amsler *et al.*, "The review of particle physics," *Physics Letters B667, 1* (2008).

[8] U. Seljak *et al.*, "Cosmological parameters from combining the Lyman-alpha forest with CMB, galaxy clustering and SN constraints," *JCAP* **0610** (2006) 014.

[9] J. Lesgourgues and S. Pastor, "Massive neutrinos and cosmology," *Phys. Rept.* **429** (2006) 307–379.

[10] H. V. Klapdor-Kleingrothaus *et al.*, "Evidence for Neutrinoless Double Beta Decay," *Mod. Phys. Lett.* **A16** (2001) 2409–2420.

[11] H. V. Klapdor-Kleingrothaus *et al.*, "Neutrino mass spectrum and neutrinoless double beta decay," *Phys. Rev.* **D63** (2001) 073005.

[12] P. Lipari, "Neutrinos, a Different Way to Look at the Sky," *Acta Physica Polonica Series B* **27** (2006), no. 8, 2411–2418.

[13] K. Eguchi *et al.*, "A high sensitivity search for $\bar{\nu}_e$'s from the sun and other sources at KamLAND," *Phys. Rev. Lett.* **92** (2004) 071301.

[14] W. C. Haxton and W. Lin, "The very low energy solar flux of electron and heavy-flavor neutrinos and antineutrinos," *Physics Letters B* **486** (2000), no. 3-4, 263 – 271.

[15] **Kamiokande** Collaboration, K. S. Hirata *et al.*, "Observation in the Kamiokande-II detector of the neutrino burst from supernova SN1987A," *Phys. Rev. D* **38** (Jul, 1988) 448–458.

[16] **IMB** Collaboration, C. B. Bratton *et al.*, "Angular distribution of events from sn1987a," *Phys. Rev. D* **37** (Jun, 1988) 3361–3363.

[17] **Super-Kamiokande** Collaboration, M. Malek *et al.*, "Search for Supernova Relic Neutrinos at Super-Kamiokande," *Phys. Rev. Lett.* **90** (Feb, 2003) 061101.

[18] W. F. McDonough and S. s. Sun, "The composition of the earth," *Chemical Geology* **120** (1995), no. 3-4, 223 – 253.

[19] M. J. Jackson and H. N. Pollack, "On the sensitivity of parameterized convection to the rate of decay of internal heat sources," *J. Geophys. Res.* **89** (1984) 10103–10108.

[20] F. Richter, "Regionalized models for the thermal evolution of the earth," *Earth Planet. Sci. Lett.* **68** (1984) 471–484.

[21] **KamLAND** Collaboration, T. Araki *et al.*, "Experimental investigation of geologically produced antineutrinos with KamLAND," *Nature* **436** (2005), no. 7050, 499–503.

[22] **KamLAND** Collaboration, S. Abe *et al.*, "Precision Measurement of Neutrino Oscillation Parameters with KamLAND," *Physical Review Letters* **100** (2008), no. 22, 221803.

[23] M. Honda *et al.*, "Calculation of atmospheric neutrino flux using the interaction model calibrated with atmospheric muon data," *Physical Review D* **75** (2007), no. 4, 043006.

[24] **IceCube** Collaboration, R. Abbasi *et al.*, "Search for point sources of high energy neutrinos with final data from AMANDA-II," *Physical Review D* **79** (2009), no. 6, 062001.

[25] **Antares** Collaboration, J. A. Aguilar *et al.*, "First results of the instrumentation line for the deep-sea ANTARES neutrino telescope," *Astropart. Phys.* **26** (2006) 314–324.

[26] S. W. Barwick *et al.*, "Constraints on Cosmic Neutrino Fluxes from the Antarctic Impulsive Transient Antenna Experiment," *Physical Review Letters* **96** (2006), no. 17, 171101.

[27] S. P. Mikheev and A. Y. Smirnov, "Resonance enhancement of oscillations in matter and solar neutrino spectroscopy," *Sov. J. Nucl. Phys.* **42** (1985) 913–917.

[28] L. Wolfenstein, "Neutrino oscillations in matter," *Phys. Rev. D* **17** (May, 1978) 2369–2374.

[29] **Kamiokande-II** Collaboration, K. S. Hirata *et al.*, "Experimental Study of the Atmospheric Neutrino Flux," *Phys. Lett.* **B205** (1988) 416.

[30] T. Kajita and Y. Totsuka, "Observation of atmospheric neutrinos," *Rev. Mod. Phys.* **73** (Jan, 2001) 85.

[31] **K2K** Collaboration, M. H. Ahn *et al.*, "Measurement of neutrino oscillation by the K2K experiment," *Physical Review D* **74** (2006), no. 7, 072003.

[32] **MINOS** Collaboration, D. G. Michael *et al.*, "Observation of Muon Neutrino Disappearance with the MINOS Detectors in the NuMI Neutrino Beam," *Physical Review Letters* **97** (2006), no. 19, 191801.

[33] H. A. Bethe, "Energy production in stars," *Phys. Rev.* **55** (Mar, 1939) 434–456.

[34] J. N. Bahcall and M. H. Pinsonneault, "What do we (not) know theoretically about solar neutrino fluxes?," *Phys. Rev. Lett.* **92** (2004) 121301, `astro-ph/0402114`.

[35] R. Davis *et al.*, "Search for Neutrinos from the Sun," *Phys. Rev. Lett.* **20** (May, 1968) 1205–1209.

[36] J. N. Abdurashitov *et al.*, "Measurement of the solar neutrino capture rate by SAGE and implications for neutrino oscillations in vacuum," *Phys. Rev. Lett.* **83** (1999) 4686–4689.

[37] M. Altmann *et al.*, "Complete results for five years of GNO solar neutrino observations," *Phys. Lett.* **B616** (2005) 174–190.

[38] **Kamiokande** Collaboration, Y. Fukuda *et al.*, "Solar Neutrino Data Covering Solar Cycle 22," *Phys. Rev. Lett.* **77** (Aug, 1996) 1683–1686.

[39] **Super-Kamiokande** Collaboration, J. Hosaka *et al.*, "Solar neutrino measurements in Super-Kamiokande-I," *Phys. Rev.* **D73** (2006) 112001.

[40] **Super-Kamiokande** Collaboration, J. P. Cravens *et al.*, "Solar neutrino measurements in Super-Kamiokande-II," *Phys. Rev.* **D78** (2008) 032002.

[41] **SNO** Collaboration, B. Aharmim *et al.*, "Electron energy spectra, fluxes, and day-night asymmetries of B-8 solar neutrinos from the 391-day salt phase SNO data set," *Phys. Rev.* **C72** (2005) 055502.

[42] **Borexino** Collaboration, C. Arpesella *et al.*, "Direct Measurement of the Be-7 Solar Neutrino Flux with 192 Days of Borexino Data," *Phys. Rev. Lett.* **101** (2008) 091302.

[43] G. L. Fogli *et al.*, "Getting the most from the statistical analysis of solar neutrino oscillations," *Phys. Rev. D* **66** (Sep, 2002) 053010.

[44] J. N. Bahcall *et al.*, "Solar neutrinos before and after KamLAND," *JHEP* **02** (2003) 009.

[45] **KamLAND** Collaboration, K. Eguchi *et al.*, "First results from KamLAND: Evidence for reactor anti-neutrino disappearance," *Phys. Rev. Lett.* **90** (2003) 021802.

[46] **KamLAND** Collaboration, T. Araki *et al.*, "Measurement of neutrino oscillation with KamLAND: Evidence of spectral distortion," *Phys. Rev. Lett.* **94** (2005) 081801.

[47] H. Kwon *et al.*, "Search for Neutrino Oscillations at a Fission Reactor," *Phys. Rev.* **D24** (1981) 1097–1111.

[48] G. Zacek *et al.*, "Neutrino Oscillation Experiments at the Gosgen Nuclear Power Reactor," *Phys. Rev.* **D34** (1986) 2621–2636.

[49] A. I. Afonin *et al.*, "Anti-Electron-Neutrino Spectra at Two Distances from the Reactor of the Rovno Nuclear Power Plant: Search for Oscillations," *JETP Lett.* **45** (1987) 247–251.

[50] Y. V. Kozlov *et al.*, "Antineutrino deuteron experiment at Krasnoyarsk reactor," *Phys. Atom. Nucl.* **63** (2000) 1016–1019.

[51] B. Achkar *et al.*, "Comparison of anti-neutrino reactor spectrum models with the Bugey-3 measurements," *Phys. Lett. B* **374** (1996) 243–248.

[52] **CHOOZ** Collaboration, M. Apollonio *et al.*, "Limits on Neutrino Oscillations from the CHOOZ Experiment," *Phys. Lett.* **B466** (1999) 415–430.

[53] **CHOOZ** Collaboration, M. Apollonio *et al.*, "Search for neutrino oscillations on a long base-line at the CHOOZ nuclear power station," *Eur. Phys. J.* **C27** (2003) 331–374.

[54] **PALO VERDE** Collaboration, F. Boehm *et al.*, "Search for Neutrino Oscillations at the Palo Verde Nuclear Reactors," *Phys. Rev. Lett.* **84** (Apr, 2000) 3764–3767.

[55] J. M. Herndon, "Nuclear georeactor origin of oceanic basalt 3He/4He, evidence, and implications," *Proceedings of the National Academy of Sciences of the United States of America* **100** (2003), no. 6, 3047–3050.

[56] J. M. Herndon, "Substructure of the inner core of the Earth," *Proceedings of the National Academy of Sciences of the United States of America* **93** (1996), no. 2, 646–648.

[57] A. M. Dziewonski and D. L. Anderson, "Preliminary reference Earth model," *Physics of the Earth and Planetary Interiors* **25** (June, 1981) 297–356.

[58] B. Lemley, "Nuclear Planet," *Discover* (2002).

[59] J. M. Herndon and D. A. Edgerley, "Background for terrestrial antineutrino investigations: Radionuclide distribution, georeactor fission events, and boundary conditions on fission power production," `hep-ph/0501216`.

[60] D. F. Hollenbach and J. M. Herndon, "Deep-Earth Reactor: Nuclear Fission, Helium, and the Geomagnetic Field," *Proc. Nat. Acad. Sci.* **98** (2001) 11085–11090.

[61] U. N. R. Commission. and O. R. N. Laboratory., *SCALE, a modular code system for performing standardized computer analyses for licensing evaluation*. The Commission : Supt. of Docs., U.S. G.P.O. , Washington, DC, version 4.4; rev. 6. ed., 2000.

[62] V. D. Rusov *et al.*, "Geoantineutrino spectrum, He-3/He-4 ratio radial distribution and slow nuclear burning on the boundary of the liquid and solid phases of the earth's core,".

[63] M. Maurette, "Fossil nuclear reactors," *Annual Review of Nuclear Science* **26** (1976), no. 1, 319–350.

[64] D. Anderson, *Theory of the Earth*. Blackwell Scientific Publications, Brookline Village, MA, 1989.

[65] D. Gubbins, "Energetics of Earths Core," *Journal of Geophysics* **43** (1977), no. 1-2, 453–464.

[66] G. A. Glatzmaier and P. H. Roberts, "Rotation and Magnetism of Earth's Inner Core," *Science* **274** (1996), no. 5294, 1887–1891.

[67] W. Clarke *et al.*, "Excess 3He in the sea: evidence for terrestrial primordial helium," *Earth Planet. Sci. Lett.* **6** (1969) 213–220.

[68] R. O. Pepin and P. Signer, "Primordial Rare Gases in Meteorites," *Science* **149** (1965), no. 3681, 253–265.

[69] H. N. Pollack *et al.*, "Heat flow from the Earth's interior: analysis of the global data set," *Rev. Geophys.* **31** (1993) 267–280.

[70] A. Hofmeister and R. Criss, "Earth's heat flux revised and linked to chemistry," *Tectonophysics* **395** (2005), no. 3-4, 159 – 177.

[71] J. Maricic, *Setting Limits On The Power Of A Geo-Reactor With KamLAND Detector*. PhD thesis, Hawaii Univ., 2005.

[72] G. L. Fogli *et al.*, "KamLAND neutrino spectra in energy and time: Indications for reactor power variations and constraints on the georeactor," *Physics Letters B* **623** (2005) 80.

[73] P. Vogel and J. F. Beacom, "Angular distribution of neutron inverse beta decay, $\bar{\nu}_e + p \to e^+ + n$," *Phys. Rev. D* **60** (Jul, 1999) 053003.

[74] D. Wilkinson, "Analysis of neutron beta-decay," *Nuclear Physics A* **377** (1982), no. 2-3, 474 – 504.

[75] P. Vogel, "Analysis of the antineutrino capture on protons," *Phys. Rev. D* **29** (May, 1984) 1918–1922.

[76] S. A. Fayans, "Radiative Corrections and Recoil Effects in the Reaction Anti-Electron-Neutrino + p $\to$ n + e^+ at Low-Energies," *Sov. J. Nucl. Phys.* **42** (1985) 590.

[77] S. Fukuda *et al.*, "The Super-Kamiokande detector," *Nuclear Instruments and Methods in Physics Research Section A* **501** (2003), no. 2-3, 418 – 462.

[78] F. Suekane *et al.*, "An Overview of the KamLAND 1-kiloton Liquid Scintillator," `arXiv:physics/0404071v2`.

[79] N. Tolich, *Experimental Study of Terrestrial Electron Anti-Neutrinos with KamLAND.* PhD thesis, Stanford Univ., 2005.

[80] J. B. Benziger *et al.*, "A scintillator purification system for a large scale solar neutrino experiment," *Nuclear Instruments and Methods in Physics Research Section A* **417** (1998), no. 2-3, 278 – 296.

[81] http ://general.krl.caltech.edu/KamLAND/radioassay/NAA/index.html, 2001. KamLAND Collaboration Internal Document.

[82] H. Kume *et al.*, "20 inch diameter photomultiplier," *Nuclear Instruments and Methods in Physics Research* **205** (1983), no. 3, 443 – 449.

[83] S. Kleinfelder, "Gigahertz waveform sampling and digitization circuit design and implementation," *Nuclear Science, IEEE Transactions on* **50** (Aug., 2003) 955–962.

[84] K. Tolich, *Measurement of Neutrino Oscillation Parameters and Investigation of Uranium and Thorium Abundances in the Earth Using Anti-neutrinos.* PhD thesis, Stanford Univ., 2007.

[85] D. A. Dwyer, *Precision Measurement of Neutrino Oscillation Parameters with KamLAND.* PhD thesis, University of California, Berkeley, 2007.

[86] S. Enomoto, *Neutrino Geophysics and Observation of Geo-Neutrinos at KamLAND.* PhD thesis, Tohoku Univ., 2005.

[87] D. W. McKee *et al.*, "A C-13(alpha,n)O-16 calibration source for KamLAND," *NUCL.INSTRUM.METH.A* **527** (2008) 272.

[88] **KamLAND** Collaboration, B. E. Berger *et al.*, "The KamLAND full-volume calibration system," *Journal of Instrumentation* **4** (2009), no. 04, P04017.

[89] **Super-Kamiokande** Collaboration, Y. Gando *et al.*, "Search for $\bar{\nu}_e$ from the Sun at Super-Kamiokande-I," *Phys. Rev. Lett.* **90** (May, 2003) 171302.

[90] **KamLAND** Collaboration, T. Araki *et al.*, "Search for the invisible decay of neutrons with KamLAND," *Phys. Rev. Lett.* **96** (2006) 101802.

[91] **KamLAND** Collaboration, S. Abe *et al.*, "Production of radioactive isotopes through cosmic muon spallation in KamLAND," *Phys. Rev. C* **81** (Feb, 2010) 025807.

[92] K. Nakajima *et al.*, "Detection of ^{7}Be solar neutrino by KamLAND." KamLAND Internal Collaboration Meeting, unpublished, 2009.

[93] A. Savitzky and M. J. E. Golay, "Smoothing and Differentiation of Data by Simplified Least Squares Procedures.," *Analytical Chemistry* **36** (05, 1964) 1627–1639.

[94] http://lcgapp.cern.ch/project/cls/work-packages/mathlibs/minuit/. Minuit Project.

[95] J. B. Birks, Proc. Phys. Soc. (London) A64, 874 (1951).

[96] http://www.srim.org/. SRIM Project.

[97] http://www.irs.inms.nrc.ca/EGSnrc/EGSnrc.html. EGSnrc Project.

[98] C. N. Chou, "The nature of the saturation effect of fluorescent scintillators," *Phys. Rev.* **87** (1952), no. 5, 904–905.

[99] A. Tang *et al.*, "Muon simulations for Super-Kamiokande, KamLAND, and CHOOZ," *Physical Review D* **74** (2006), no. 5, 053007.

[100] V. Kudryavtsev, "Muon simulation codes MUSIC and MUSUN for underground physics," *Computer Physics Communications* **180** (2009), no. 3, 339 – 346.

[101] D.J.H. and R.B.S., "Neutron cross sections: Bnl-325," *Journal of Nuclear Energy (1954)* **7** (1958), no. 3-4, 228 – 228.

[102] http://geant4.web.cern.ch/geant4/. GEANT4 Project.

[103] Z. Djurcic *et al.*, "Uncertainties in the Anti-neutrino Production at Nuclear Reactors," *J. Phys.* **G36** (2009) 045002.

[104] A. Hahn *et al.*, "Anti-neutrino spectra from Pu-241 and Pu-239 thermal neutron fission products," *Phys. Lett. B* **218** (1989) 365.

[105] K. Schreckenbach *et al.*, "Determination of the anti-neutrino spectrum from U-235 thermal neutron fission products up to 9.5-MeV," *Phys. Lett. B* **160** (1985) 325.

[106] P. Vogel *et al.*, "Reactor antineutrino spectra and their application to antineutrino-induced reactions. II," *Phys. Rev. C* **24** (Oct, 1981) 1543–1553.

[107] Y. Declais, "Study of reactor anti-neutrino interaction with proton at Bugey nuclear power plant," *Phys. Lett. B* **338** (1994) 383–389.

[108] K. Ichimura, *Precise Measurement of Neutrino Oscillation Parameters with KamLAND*. PhD thesis, Tohoku Univ., 2008.

[109] K. Nakajima *et al.*, "A simple model of reactor cores for reactor neutrino flux calculations for the KamLAND experiment," *NUCL.INSTRUM.METH.A* **569** (2006) 837.

[110] http://wwwndc.jaea.go.jp/ftpnd/jendl/jendl-an-2005.html.

[111] R. B. Walton *et al.*, "Interaction of Neutrons with Oxygen and a Study of the $C13(\alpha, n)O16$ Reaction," *Phys. Rev.* **107** (Aug, 1957) 1065–1075.

[112] G. W. Kerr *et al.*, "Energy levels of 17O from 13C(α,α0)13C and 13C(α,n)16O," *Nuclear Physics A* **110** (1968), no. 3, 637 – 656.

[113] http://www.fluka.org/. FLUKA Project.

[114] L. A. Winslow, *First Solar Neutrinos from KamLAND: A Measurement of the B8 Solar Neutrino Flux*. PhD thesis, University of California, Berkeley, 2008.

[115] D. Dwyer and R. McKeown, "Calculation of Atmospheric Neutrino Background in KamLAND." KamLAND Collaboration Internal Document, 2007.

[116] L. A. Ahrens *et al.*, "Measurement of neutrino-proton and antineutrino-proton elastic scattering," *Phys. Rev. D* **35** (Feb, 1987) 785–809.

[117] **SNO** Collaboration, B. Aharmim *et al.*, "Independent Measurement of the Total Active ^{8}B Solar Neutrino Flux Using an Array of ^{3}He Proportional Counters at the Sudbury Neutrino Observatory," *Physical Review Letters* **101** (2008), no. 11, 111301.

[118] http://www.sno.phy.queensu.ca/sno/papers/ncd_chi2/.

[119] A. Stuart *et al.*, *Kendall's Advanced Theory of Statistics*, vol. 2A. Wiley, 6th ed., 2009.

[120] G. J. Feldman and R. D. Cousins, "Unified approach to the classical statistical analysis of small signals," *Phys. Rev. D* **57** (Apr, 1998) 3873–3889.

[121] A. Rocholl and K. Jochum, "Th, U and other trace elements in carbonaceous chondrites: Implications for the terrestrial and solar-system Th/U ratios," *Earth and Planetary Science Letters* **117** (1993), no. 1-2, 265 – 278.

[122] C. Sutour *et al.*, "Determination of the argon concentration in ambient dry air for the calculation of air density," *Metrologia* **44** (2007), no. 6, 448–452.

[123] N. Aoki and Y. Makide, "The Concentration of Krypton in the Atmosphere—Its Revision after Half a Century—," *Chemistry Letters* **34** (2005), no. 10, 1396–1397.

[124] P. Collon *et al.*, "Tracing noble gas radionuclides in the environment," *Annual Review of Nuclear and Particle Science* **54** (2004), no. 1, 39–67.

[125] M. Hirota *et al.*, "Spatial and temporal variations of atmospheric ^{85}kr observed during 1995-2001 in japan: Estimation of atmospheric ^{85}kr inventory in the northern hemisphere," *Journal of Radiation Research* **45** (2004), no. 3, 405–413.

[126] D. N. McKinsey and C. Orzel, "Radioactive krypton background evaluation using atom counting," *Nucl. Instrum. Meth.* **A545** (2005) 524–531.

[127] M. C. Cowen *et al.*, "Nonlinearities in sensitivity of quadrupole partial pressure analyzers operating at higher gas pressures," *Journal of Vacuum Science Technology A* **12** (1994), no. 1, 228–234.

[128] http://www.nndc.bnl.gov/.